Continuum modeling of brittle and ductile damage: theory and computational frameworks

von der Fakultät Maschinenbau
der Technischen Universität Dortmund
zur Erlangung des akademischen Grades

Doktor-Ingenieur (Dr.-Ing.)

genehmigte Dissertation

von

Kai Langenfeld

aus Lünen

Referent:	Prof. Dr.-Ing. J. Mosler
Korreferenten:	Prof. Dr.-Ing. D. Balzani
	Prof. Dr.-Ing. U. A. Handge
Tag der Einreichung:	30.08.2022
Tag der mündlichen Prüfung:	24.02.2023

Bibliografische Information Der Deutschen Bibliothek
Die Deutsche Bibliothek verzeichnet diese Publikation in der Deutschen Nationalbibliografie; detaillierte bibliografische Daten sind im Internet über **http://dnb.ddb.de** abrufbar.

Bibliographic information published by Die Deutsche Bibliothek
Die Deutsche Bibliothek lists this publication in the Deutsche Nationalbibliografie; detailed bibliographic data is available in the Internet at **http://dnb.ddb.de**.

Schriftenreihe des Instituts für Mechanik

Herausgeber: Institut für Mechanik
Fakultät Maschinenbau
Technische Universität Dortmund
Leonhard-Euler-Str. 5
D-44227 Dortmund

Druck: Koffler DruckManagement GmbH

Als Manuskript gedruckt. Printed in Germany.

ISSN 2191-0022
ISBN 978-3-947323-41-8

"Theories are nets cast to catch what we call 'the world': to rationalize, to explain, and to master it."

Karl Raimund Popper (1902–1994)

Acknowledgements

This thesis has been developed during my time as a PhD student at the Institute of Mechanics at TU Dortmund University. The past years have been the reason why I have matured both as a person and scientifically. Therefore I would like to take this opportunity to thank the people who have supported me during this time.

First and foremost, I would like to thank my mentor and doctoral supervisor Prof. Jörn Mosler. He welcomed me in his team in April 2017 and inspired me from the very beginning with his scientific thinking. Thank you for giving me this opportunity, for always taking the time for discussions and for encouraging me to develop and pursue my own ideas.

I also would like to express my gratitude to Prof. Daniel Balzani for his sincere interest in my work and for accepting to act as the co-referee of this thesis. Furthermore, I would like to thank Prof. Ulrich A. Handge and Prof. Andreas Brümmer for kindly agreeing to serve as the third referee and as the chairman of the examination committee, respectively.

As part of my work in the CRC/TRR 188, I would like to thank all members for the interesting bi-annual discussions as well as for the opportunity to gain insights into interdisciplinary fields of science.

Special thanks to the whole team at the Institute of Mechanics, without whom this time would only have been half as enjoyable. Particularly, I would like to express my gratitude to Prof. Andreas Menzel for his significant contribution to the very pleasant working atmosphere, to Kerstin Walter and Tina McDonagh for their administrative support, for proofreading my manuscripts and for organizing various social events apart from the daily work routine as well as to Matthias Weiss for the professional maintenance of the hardware and software at the institute. I also would like to thank Dr. Patrick Kurzeja for opening an additional scientific point of view and for inspiring me with his enthusiasm as well as with his innovative yet careful approach to science.

Many thanks to my (former) office partners Henning Lammen and Dr. Christian Sievers. I genuinely enjoyed sharing an office with both of you. Moreover, I would like to thank all colleagues for the serious and for the not-so-serious discussions in the kitchen of the institute, which frequently led to new ideas or, atleast, to a good mood. Therefore, I would like to thank Dr. Serhat Aygün, Dr. Thorsten Bartel, Merlin Bödecker, Klas Feike, Volker Fohrmeister, Tim Furlan, Gian-Luca Geuken, Dilek Güzel, Marius Harnisch, Dr. Tim Heitbreder, Dr. Tobias Kaiser, Alexander Niehüser, Isabelle Noll, Felix Rörentrop, Dr. Lars Rose, Markus Schewe, Robin Schulte, Lennart Sobisch, Leon Sprave, Tillmann Wiegold, Hendrik Wilbuer and Carina Witt. Special thanks also to

all participants of the after work sport events. I always enjoyed that exhausting time, whether it was jogging, bouldering or football. I hope we stay in touch.

Last but not least, I would like to thank my friends and family for their support. They were always there for me when I needed them and always made it possible to take a break from formulas and equations. In particular, I would like to thank my parents Birgit and Dieter for paving the way for this thesis through their support during my early educational process.

Dortmund, March 2023 Kai Langenfeld

Zusammenfassung

Das Ziel der vorliegenden Arbeit ist es im Rahmen des Sonderforschungsbereichs TRR188 einen Modellierungsansatz auf kontinuumsmechanischer Basis zur Bewertung von Schädigungszuständen zu entwickeln. Die Bewertung der Strukturen erfolgt mittels Finite-Elemente-Simulationen. Dabei kann der zugrundeliegende Schädigungsmechanismus in Abhängigkeit der aufgeprägten Lastamplitude duktilen (im Kurzzeitfestigkeitsbereich) oder spröden (im Langzeitfestigkeitsbereich) Ursprungs sein. Aus diesem Grund werden in der vorliegenden Arbeit sowohl kontinuumsmechanische Materialmodelle für spröde als auch für duktile Schädigung ausgearbeitet.

Bei der Modellierung der spröden Schädigung ist ein Schwerpunkt und im Kontext der Finite-Elemente-Methode die Berechnung netzunabhängiger und somit objektiver Simulationsergebnisse. Beim Vergleich verschiedener Regularisierungsverfahren wird eine Krümmungsabhängigkeit gradientenbasierter Modelle aufgezeigt, die sowohl analytisch als auch numerisch untersucht wird. Anschließend werden zwei Methoden zur gezielten Kontrolle dieser Krümmungseffekte erarbeitet.

Für eine objektive Modellierung anisotroper, duktiler Schädigungsevolution wird ein aus der Literatur bekanntes, lokales Materialmodell mikromorph gradientenerweitert. Da der Standardansatz der mikromorphen Regularisierung sich als ungeeignet erweist, wird eine Erweiterung vorgeschlagen. Anschließend wird das Modell auf Basis experimenteller Daten erweitert und kalibriert. Diese Modellerweiterungen beinhalten überlagerte lineare und nicht-lineare isotrope und kinematische Verfestigung, thermomechanische Kopplungseffekte sowie ein neues Kriterium zur Vorhersage der Schädigungsinitiierung unter zyklischer Belastung.

Abstract

The goal of the present work is the development of an anisotropic damage model suitable for the numerical analysis of structures undergoing cyclic loading. The structures are numerically analyzed by means of the finite-element method, where the underlying damage mechanism can be ductile (in the low cycle fatigue range) or brittle (in the high cycle fatigue range). For this reason, continuum mechanics based material models suitable for both brittle and ductile damage are elaborated in the present work.

For modeling brittle damage by means of the finite element method, one focus lies on the calculation of mesh-independent and thus objective results. By comparing different regularization methods, a curvature dependence of gradient-based models is shown, which is investigated analytically and numerically. Subsequently, two methods are elaborated in order to control this effect.

For an objective modeling approach of anisotropic, ductile damage evolution, an established local material model is gradient-enhanced in line with the so-called micromorphic approach. Since the standard micromorphic regularization proves to be unsuitable, it is extended. The final model is calibrated based on experimental data. It accounts for superposed linear and non-linear isotropic and kinematic hardening, thermomechanical interactions, and a new criterion for damage initiation under cyclic loading.

Publications

Key parts of this thesis are based on peer-reviewed journal articles, which were either published or submitted during the progress of this thesis.

1. K. Langenfeld, P. Junker, J. Mosler: *Quasi-brittle damage modeling based on incremental energy relaxation combined with a viscous-type regularization*, Continuum Mechanics and Thermodynamics, 30: 1125–1144, 2018 [89].

2. K. Langenfeld, J. Mosler: *A micromorphic approach for gradient-enhanced anisotropic ductile damage*, Computer Methods in Applied Mechanics and Engineering, 360(1): 112717, 2020 [88].

3. K. Langenfeld et al.: *Influence of anisotropic damage evolution on cold forging*, Production Engineering, 14, 2020 [91].

4. K. Langenfeld, P. Kurzeja, J. Mosler: *How regularization concepts interfere with (quasi-)brittle damage: A comparison based on a unified variational framework*, Continuum Mechanics and Thermodynamics, 34: 1517–1544, 2022 [92].

5. K. Langenfeld, P. Kurzeja, J. Mosler: *On the curvature dependence of gradient damage models: control and opportunities*, Computer Methods in Applied Mechanics and Engineering, 410: 115987, 2023 [90].

Some parts of the contents of the listed articles as well as some figures have been partly modified in order to avoid unnecessary repetitions and to connect the essential parts of this thesis. The author of this thesis contributed essential aspects with regard to the outline of the theory, carried out all numerical implementations and simulations, and prepared the journal articles.

Contents

Notation

The notation used in this work becomes obvious from its context. However, the following essential relations are collectively provided for the sake of the reader's convenience.

Tensors In a three-dimensional Euclidean space spanned by the Cartesian basis vectors $\{\boldsymbol{e}_i\}, i = 1, 2, 3$, tensors of first, second and fourth order are expressed in terms of their coefficients $(\bullet)_i$ following Einstein's summation convention, namely

$$\begin{aligned}
&\boldsymbol{u} = u_i\,\boldsymbol{e}_i \quad , && \text{(first-order tensor, i.e. vector)}\\
&\boldsymbol{S} = S_{ij}\,\boldsymbol{e}_i \otimes \boldsymbol{e}_j \quad , && \text{(second-order tensor)}\\
&\mathbb{T} = \mathsf{T}_{ijkl}\,\boldsymbol{e}_i \otimes \boldsymbol{e}_j \otimes \boldsymbol{e}_k \otimes \boldsymbol{e}_l \quad . && \text{(fourth-order tensor)}
\end{aligned}$$

Here and in the following, we use non-bold letters for scalars, bold-face lower-case italic letters for vectors, bold-face upper-case italic letters for second-order tensors and bold-face upper-case sans-serif letters for fourth-order tensors.

Inner tensor products Inner tensor products are denoted by dots where the number of dots characterises the number of contractions, i.e.

$$\begin{aligned}
&\boldsymbol{u} \cdot \boldsymbol{v} = u_i\,v_i \quad ,\\
&\boldsymbol{S} \cdot \boldsymbol{u} = S_{ij}\,u_j\,\boldsymbol{e}_i \quad ,\\
&\boldsymbol{S} \cdot \boldsymbol{T} = S_{ij}\,T_{jk}\,\boldsymbol{e}_i \otimes \boldsymbol{e}_k \quad ,\\
&\boldsymbol{S} : \boldsymbol{T} = S_{ij}\,T_{ij} \quad ,\\
&\mathbb{S} : \boldsymbol{T} = \mathsf{S}_{ijkl}\,T_{kl}\,\boldsymbol{e}_i \otimes \boldsymbol{e}_j \quad .
\end{aligned}$$

An n-fold contraction of two nth-order tensors always results in a scalar.

Outer tensor products Outer tensor products—also referred to as dyadic products—are represented by the classical symbol $\otimes$ as well as by the non-standard symbols $\overline{\otimes}$ and $\underline{\otimes}$ using the definitions

$$\boldsymbol{u} \otimes \boldsymbol{v} = u_i\,v_j\,\boldsymbol{e}_i \otimes \boldsymbol{e}_j \quad ,$$

$$
\begin{aligned}
\boldsymbol{S} \otimes \boldsymbol{T} &= S_{ij}\, T_{kl}\, \boldsymbol{e}_i \otimes \boldsymbol{e}_j \otimes \boldsymbol{e}_k \otimes \boldsymbol{e}_l \quad , \\
\boldsymbol{S} \mathbin{\overline{\otimes}} \boldsymbol{T} &= S_{ik}\, T_{jl}\, \boldsymbol{e}_i \otimes \boldsymbol{e}_j \otimes \boldsymbol{e}_k \otimes \boldsymbol{e}_l \quad , \\
\boldsymbol{S} \mathbin{\underline{\otimes}} \boldsymbol{T} &= S_{il}\, T_{jk}\, \boldsymbol{e}_i \otimes \boldsymbol{e}_j \otimes \boldsymbol{e}_k \otimes \boldsymbol{e}_l \quad ,
\end{aligned}
$$

The dyadic product of two first-order tensors, i.e. vectors, results in second-order tensors, whereas the dyadic products of two second-order tensors result in fourth-order tensors.

Identity tensors The second-order identity tensor $\boldsymbol{I}$ and the fourth-order symmetric, volumetric and deviatoric identity tensors, $\mathsf{I}^{\mathrm{sym}}$, $\mathsf{I}^{\mathrm{vol}}$ and $\mathsf{I}^{\mathrm{dev}}$, respectively, are defined as

$$
\begin{aligned}
\boldsymbol{I} &= \delta_{ij}\, \boldsymbol{e}_i \otimes \boldsymbol{e}_j \quad , \\
\mathbb{I}^{\mathrm{sym}} &= \frac{1}{2} \left[\boldsymbol{I} \mathbin{\overline{\otimes}} \boldsymbol{I} + \boldsymbol{I} \mathbin{\underline{\otimes}} \boldsymbol{I} \right] , \\
\mathbb{I}^{\mathrm{vol}} &= \frac{1}{3} \left[\boldsymbol{I} \otimes \boldsymbol{I} \right] \quad , \\
\mathbb{I}^{\mathrm{dev}} &= \mathsf{I}^{\mathrm{sym}} - \mathsf{I}^{\mathrm{vol}} \quad ,
\end{aligned}
$$

with the Kronecker delta symbol $\delta_{ij} = \boldsymbol{e}_i \cdot \boldsymbol{e}_j$.

1 Introduction

1.1 Motivation

The analysis as well as the prediction of failure in structures is still one of the most fundamental problems in engineering. On a macroscopic scale, failure is often accompanied by the formation of cracks or shear bands which evolve in time and space until the ultimate collapse of the structure is observed. Failure of components and structures occurs in various areas. Quite recent examples are the collapsed bridges in Genoa (2018) and Pittsburgh (2022). A case study of damage related accidents of airplanes and a case study of damage related transportation accidents highlight the relevance even further [149, 158]. It underlines the continuing necessity of understanding and predicting damage and failure. Although there are now numerous criteria for predicting service life and failure, the estimations are often limited to monotonous load paths and focus on minimizing damage in general. For this reason, a naive strategy would be to avoid failure and the prior material damage completely.

Within the scope of CRC/TRR 188 in Germany and similar research projects in other countries, a different approach is pursued. To be more precise, the goal is not to minimize damage in general, but to optimize the damage distribution in the components in an application-specific manner. For that purpose, it is important to predict the distribution of damage within the structure through the whole lifetime cycle of the material and the structure. Both, prediction and evaluation of the damage distribution can be performed with damage models based on continuum mechanics. Compared to experimental evaluation, modeling is clearly more cost-efficient, although experiments can certainly not be avoided completely.

Within the CRC/TRR 188 the focus lies on metals. They are often manufactured by forming technologies. During the forming process, ductile damage, i.e., damage with accompanying plasticity, is often the underlying damage mechanism. In contrast, damage can be either brittle or ductile in the case of cyclic loading – usually relevant to the real service conditions. At high load amplitudes, the failure mode is rather ductile, while at low load amplitudes, it is rather brittle.

The main objective of this thesis is the development of constitutive models in order

to evaluate damage distributions of extruded components with respect to cyclic loading. For that reason, both brittle damage and ductile damage have to be considered.

Independent whether ductile or brittle damage is considered, material degradation is usually an anisotropic process. Clearly, the models have to account for this. Furthermore, the irreversibility accompanying damage is oftentimes difficult to estimate in experiments. One possibility to monitor the dissipation resulting from irreversible process is the analysis of the corresponding temperature increase. By summarizing the aforementioned points, the first goal of the present thesis is

- the development of an anisotropic, thermomechanically coupled (ductile) damage model suitable for the analysis of metals undergoing cyclic loading.

A special focus lies on the objective, i.e., regularized description of material softening in order to obtain finite element simulations objective with respect to the underlying spatial discretization. Therefore, frequently applied regularization methods are compared with respect to their numerical feasibility and physical soundness. Particularly, the following novel contributions are presented in this thesis:

- analysis of regularization methods based on a unified variational framework
- and extension of an anisotropic, ductile damage model towards the objective simulation of fatigue tests.

1.2 State of the art

1.2.1 Continuum damage mechanics

Since the prediction of cracks and shear bands in solids is one of the most important issues in engineering, several theoretical and numerical methods have been advocated. If cracks are modeled as sharp evolving material interfaces (with a zero thickness), fracture mechanics represents a suitable framework, cf. [7, 63, 68]. Because cracking is a mathematically and numerically challenging so-called free discontinuity problem, fracture mechanics has to be combined with advanced numerical approaches. Two such approaches are the so-called EXtended Finite Element Method (X-FEM [175]) or the embedded Strong Discontinuity Approach (SDA [145, 167]). Alternatively, interface elements can be embedded into the discretization between bulk elements [129]. In order to eliminate the mesh bias induced by the initial discretization, interface elements should be combined with suitable adaptive schemes, cf. [111].

Cracks do not have to be necessarily modeled as sharp interfaces, but they can also be approximated in a smeared fashion with a finite thickness (or in physical terms, by means of homogenization [128, 156]). Such approximations lead to continuum damage mechanics. In continuum damage mechanics the degrading effect of damage on the elastic and plastic properties of the material is taken into account [29], thus the (effective)

stiffness of the considered material decreases. Continuum damage mechanics is based on the pioneering work by *Kachanov*, who was the first to introduce a scalar integrity measure b in the range of 1 and 0 for the time to rupture under creep conditions [75]. This variable is interpreted as the remaining load carrying effective area, in the sense, that $b = 1$ denotes fully intact material points while $b = 0$ corresponds to completely broken material points. Later on, the damage variable $d = 1 - b$ was introduced and interpreted as the loss of load carrying effective area [144]. In a homogenized manner, the effect of damage on the macroscale results in a degradation of the elastic properties, e.g., the Young's modulus [30]. In order to incorporate this observation into continuum damage mechanics, several principles based on the introduction of a fictitious undamaged configuration have been developed. One such principle goes back to *Kachanov* and is called the principle of strain equivalence, also known as effective stress concept [75], see Fig. 1.1 for a graphical representation. This principle states that identical strains

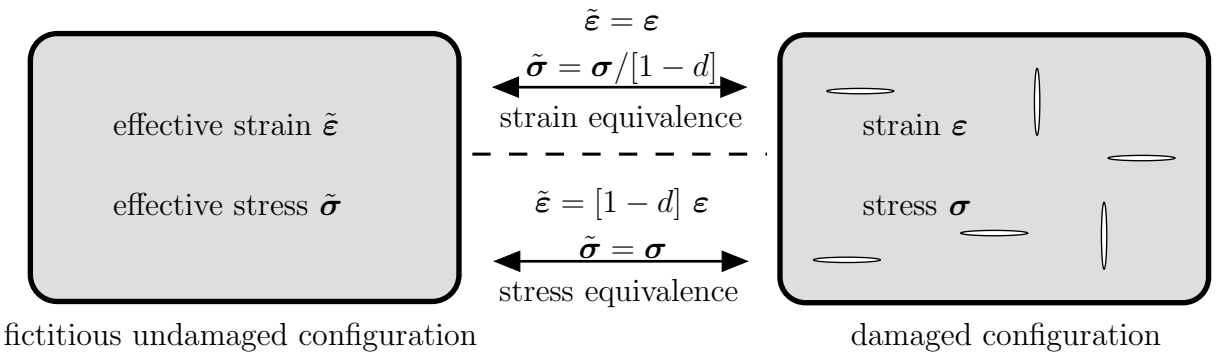

Figure 1.1: Schematic illustration of the homogenization principles strain energy equivalence and stress energy equivalence between the damaged configuration and a fictitious undamaged configuration.

are associated with the damaged configuration ($\bullet$) and with the fictitious undamaged configuration ($\tilde{\bullet}$), cf. [94, 121, 168]. The stresses are adjusted via $\tilde{\boldsymbol{\sigma}} = \boldsymbol{\sigma}/[1-d]$ due to the reduced cross-section area. An alternative principle in continuum damage mechanics is the principle of stress equivalence or effective strain concept, cf. [41, 168]. The stress tensors are assumed to be identical and the strains are adjusted via $\tilde{\boldsymbol{\varepsilon}} = [1-d]\,\boldsymbol{\varepsilon}$. The emerging crack induces a discontinuity in the displacements and thus decreases the strains in the damaged configuration. The strain tensor in the fictitious undamaged configuration is decreased in order to take this into account. The third principle is the principle of strain energy equivalence, cf. [41, 93, 99, 174], which assumes identical strain energies for both configurations, i.e., $\psi = \tilde{\psi}$. This principle can be fulfilled in several ways. One approach, in the spirit of finite strain plasticity, see [51, 106], is shown in detail in Chapter 6. The three principles mentioned are the most common, but not the only ones. For example, the principle of reciprocity is introduced in [170].

Up to this point, damage was captured by a scalar variable, which automatically

leads to the assumption of isotropic damage and thus leads to a non-changing Poisson's ratio [74]. Depending on the required physical accuracy, damage can also be modeled in an anisotropic manner. By doing so, the anisotropy can be captured through several scalar damage variables [103] or by means of higher order tensors. Thereby, the order should be of even nature, such that the dependence on the sign of the surface normal vector cancels out [122]. Frequent choices are second-order tensors [76, 84, 123, 174] and fourth-order tensors [33, 74, 84, 188], but also eighth-order damage tensors can be found in the literature [27].

Continuum damage mechanics can be further divided into the underlying damage mechanisms: brittle damage, ductile damage, creep, fatigue and spall damage [122]. In the following, the modeling theory regarding brittle damage, ductile damage and fatigue in the framework of continuum damage mechanics is concisely introduced.

Brittle damage Brittle damage (Fig. 1.2(a)) is a material degradation without plastic deformation. It occurs through the loss of interatomic bonding on the atomic level and leads ultimately to the formation of cracks on the macro level. This damage mechanism is typically observed in brittle materials such as rocks, concrete and ceramics [84] and can often be identified by means of a smooth crack surface [120]. The commonly used relation to determine the fracture of cracked, brittle solids dates back to *Griffith* [62]. He states that the loss of potential bulk energy of the solid is equal to the dissipated energy through formation of new surfaces, i.e., cracks. From a modeling point of view, this is taken into account by coupling the evolution of the damage variable (or damage tensor) to the energy release rate [29, 41, 56]. Alternative options for brittle damage evolution are strain-based evolution equations [22, 136, 168] and stress-based evolution equations [168]. A detailed overview of modeling of brittle material degradation is given in [84].

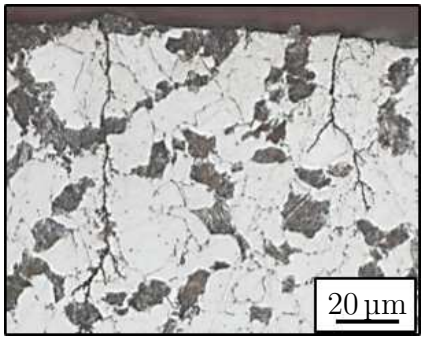

(a) Micro cracks in dual-phase steel DP800

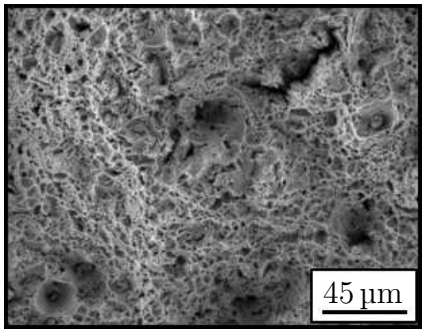

(b) Fracture surface of case-hardened steel 16MnCrS5

Figure 1.2: Comparison of brittle (a) and ductile (b) fracture surfaces. Taken from CRC/TRR 188, project C01.

Ductile damage In contrast to brittle damage, ductile damage (Fig. 1.2(b)) occurs in combination with plasticity. This type of damage typically occurs in ductile metals and is caused by the formation, growth and coalescence of voids. In general, the void formation is caused by the detachment of the matrix material from hard inclusions or by the fracture of inclusions [122]. These voids then grow due to plastic deformation and eventually coalesce in the form of micro cracks [57], which typically lead to dimpled fracture surfaces [120]. In order to incorporate these observations into a continuum damage mechanics model, the damage evolution is coupled to the evolution of plasticity. The first modeling approaches reach back to *McClintock* [104] and *Rice* [148] who proposed the first evolution equations for the growth of voids. Later on, a micromechanics-based model by *Gurson* [64] was proposed in order to also account for void nucleation. That model is analyzed by *Tvergaard and Needleman* [181, 182], who modified the original yield surface in order to obtain a better fit to experiments [180]. The first phenomenological model in the spirit of continuum damage mechanics was proposed by *Lemaitre* [94]. In that model the damage evolution depends on the energy release rate (similar to brittle damage), but is activated only simultaneously with the evolution of plasticity. Therefore, the energy release rate alone does not trigger inelastic deformations. In contrast to the GTN-model [180], the model in [94] also affects the elastic properties of the material – in line with the proposed framework by *Kachanov* [75]. A thorough overview of ductile damage and modeling approaches is given in [18].

Fatigue Mechanical fatigue can be described as damage induced by application of fluctuating stresses and strains [79]. The first reported fatigue test already dates back to the 19th century and was performed in order to examine the failure of steel chain ropes with respect to cyclic loading [3]. Since then there have been a variety of studies, cf. [14, 35, 134, 147, 185] among others. A detailed historical overview is given in [161, 176]. One way to categorize fatigue is by the number of cycles till failure into either low cycle fatigue (LCF) or high cycle fatigue (HCF). In general, the change from LCF to HCF occurs between 10^4 [95], 10^5 [122] and 10^6 [79] cycles. Focusing on steels, LCF leads to the nucleation of micro cavities as a result of irreversible plastic deformation [122]. Therefore the underlying failure mechanism might be considered as ductile damage. In contrast thereto, failure associated with HCF might be considered as brittle damage, since it occurs almost without any accompanying plasticity [122]. However, both brittle and ductile damage modes can also occur simultaneously.

From a modeling perspective, there are different techniques in order to predict the lifetime of components subject to cyclic loading. The so-called critical plane approach is a well established method, see [77] for a review. It is based on the experimental observation, that fatigue life is usually dominated by crack growth along either shear planes or tensile planes, i.e., the critical plane. Amplitude and mean value are then calculated from the cyclic stresses and strains on such planes and compared to experimentally measured Coffin-Manson-curves [169]. To proportional load cases, this method is successful. For non-proportional load cases, i.e., paths where the orientation of the principal axes

change, on the other hand, it is significantly less accurate, since the interactions between different strain components are not considered accurate enough [100, 169].

By way of contrast, continuum damage mechanics is a suitable tool in order to consider the interactions associated with non-proportional load paths. One of the first continuum damage models is the model by *Chaboche and Lesne* [28], where the damage evolution is coupled to the mean stress and to the maximum stress of each cycle. Other models are found in [95] and in [96], where the fatigue process is divided into a micro crack nucleation and crack growth phase. In order to distinguish between both phases from a modeling point of view, a damage initiation criterion has been proposed. FE^2, cf. [160] for a review, has also been applied to fatigue simulations [19, 47]. Furthermore, a continuum damage mechanics theory based on an endurance surface in the stress space has been proposed by *Ottosen et al.* [132]. That surface may move and evolve similar to plasticity theories and is the criterion for damage initiation. Stress states outside of the surface are admissible and lead to the evolution of damage. More recently, phase field models for fracture [56] are applied to fatigue damage. The phase-field model is combined with a durability concept, i.e., the fracture toughness of the phase-field model is reduced by means of an additional cyclic damage variable [4, 162].

1.2.2 Numerical regularizations

Independent of the considered constitutive model the mathematical problem associated with standard time-independent local damage models becomes ill-posed and numerical simulations show the pathological mesh dependence, if standard finite elements are employed, cf. [17, 138].

Various different approaches have been elaborated in the engineering community in order to regularize this problem. All approaches share the idea of incorporating a certain length scale into the formulation. By doing so, the width of the zone showing localized inelastic deformations (e.g., cracks or shear bands) is prescribed and part of the overall model. In the following several regularization methods are briefly reviewed.

The first one to mention is the so-called fracture energy concept (also known as crack-band theory), cf. [15, 151] among others. The material parameters are chosen in accordance to the characteristic length of the underlying finite element mesh, such that each element has the same fracture energy. Clearly, this length also depends on the orientation of the element to the cracking path which lead to the development of advanced calculation methods of the characteristic length [126, 127]. By doing so, the loading behavior and the fracture energy are unaffected by mesh refinements. In contrast, the distribution of the damage variable still localizes in only one element row and therefore remains dependent on the underlying discretization [73].

Viscous regularization constitutes an alternative concept [50]. It is applied to a broad range of materials, e.g., to the modeling of quasi-brittle damage [58] or softening elastoplasticity [44]. The key idea is the incorporation of a time dependence into the constitutive equations. By choosing that time dependence to be sufficiently large, the softening

behavior becomes mainly dependent on the time step and no longer on the mechanical behavior, i.e., the strains and stresses. Hence, the mechanical tangent remains positive definite [89]. On the one hand, this leads to mesh-independent loading behavior as well as to mesh-independent distributions of the damage variable. On the other hand, the results are now additionally influenced by the loading rate, which can be heterogeneous within the structure and which can interfere with additional time-dependent processes.

Non-local theories are a third option for the purpose of regularization [17, 138]. The relevant variables are averaged over a certain spatial domain, which exceeds the dimension of one individual finite element. As a result, a length scale defining the crack width is introduced into the constitutive model. This also leads to mesh-independent results.

Based on non-local theories, the gradient regularization has been developed [136]. It results from the non-local theory through a Taylor series expansion up to the second derivative [16, 138]. The key idea is to include the gradient of the softening variable into the constitutive framework. Penalization of these gradients hinders localization into one element row. The neighboring elements will also show softening behavior in order to flatten the gradient. The gradient regularization hence introduces a spatial length scale into the constitutive framework.

Alternatively, the gradient regularization might be approximated in a micromorphic manner [48, 54]. This is often beneficial from an implementation point of view, since it preserves the structure of the underlying local model. It is based on the introduction of an additional global field, which is coupled to the softening variable. Instead of penalizing the gradient of the damage variable directly, the gradient of the global additional field is considered. Similar to the viscous regularization, the micromorphic regularization is applied to a broad range of materials being isotropic brittle damage [48], anisotropic brittle damage [52] crystal plasticity and phase transformation [55], isotropic ductile damage [80, 154] and anisotropic ductile damage [88] to mention but a few.

1.3 Structure of the thesis

The thesis starts with the fundamentals of continuum mechanics in Chapter 2. This will set the basis for the derivation of further theories. Apart from the kinematics and the balance equations, it recapitulates the variational formulation based on incremental energy minimization [40, 130, 140] and presents two prototype models suitable for isotropic, brittle material degradation. The fist one is a local, and thus ill-posed model, and the second one is a non-local phase-field model [56, 110]. Both prototype models are based on the principle of incremental energy minimization and will be analyzed and extended in the following chapters.

In Chapter 3 the regularization methods fracture energy concept, viscous regularization and micromorphic regularization will be analyzed in terms of their numerical feasibility, their mutual compatibility and their distinctive limitations. Subsequently, the approaches are compared to each other. In particular, the comparison will focus

on the variational structure, the well-posedness and the characteristic response (loading behavior, damage field, fracture energy).

Since the (micromorphic) gradient regularization turns out to be the most promising regularization method for the chosen prototype model, it will be further analyzed in Chapter 4. While the incorporation of a length scale certainly regularizes the local model, it leads to an undesired curvature dependence. This chapter aims at opening a new view of this phenomenon by exploring when and how the curvature influence affects the physical behavior. It approaches these goals by a dimensional analysis followed by analytical and numerical examples with a focus on brittle fracture.

Building on the previous chapter, both prototype models suitable for regularized, isotropic, brittle damage will be extended in order to control the curvature dependence in Chapter 5. For that purpose, two methods are elaborated. They are based on a double micromorphic approach. To be more precise, in addition to the gradient, the Hessian is also considered within the model.

The second main part of this thesis focuses on ductile material degradation and starts with Chapter 6. A model suitable for anisotropic, ductile damage evolution is presented [51, 106]. Since this model is based on the principle of Generalized Standard Materials [67, 112] and on the principle of strain energy equivalence [105, 174], those principles are concisely reviewed first. The prototype model is extended to account for non-linear isotropic and non-linear kinematic hardening and forms the basis for the subsequent chapters.

In Chapter 7 it is shown that the standard approach of the micromorphic regularization is not suitable in order to regularize the underlying prototype model. Moreover, it is shown that the micromorphic regularization in its standard form is not suitable for ductile damage models of *Lemaitre*-type in general. The origin is elaborated in detail and an extended version of the micromorphic regularization is proposed.

Chapter 8 aims at modeling LCF. For that purpose an energetic based damage initiation criterion, cf. [96], is extended to account for different load amplitudes. Furthermore, the underlying ductile damage model is extended towards thermomechanics. Since temperature evolution is directly connected to the model's dissipation, it allows the evaluation of the overall anisotropic damage distribution by means of a scalar quantity. By doing so, the dissipation inequality is discussed, since it is also affected by the micromorphic regularization. The thermomechanical model is then applied to tensile specimens subject to tensile loading and subsequently to LCF-tests.

2 Fundamentals

The purpose of this chapter is to concisely review the fundamentals of continuum mechanics upon which this thesis is based. Although some of these fundamentals have been known for decades, or even centuries, they are repeated in order to clarify the notation. This chapter includes, apart from the kinematics and the well known balance equations, the principle of energy minimization as a method to derive constitutive models as well as two prototype models suitable for isotropic, brittle damage. These models will serve as a basis for analyses and extensions in the subsequent chapters.

2.1 Kinematics

Let $\boldsymbol{u}(\boldsymbol{X})$ be the displacement field of all points $\boldsymbol{X}$ belonging to the reference configuration $\mathcal{B}$.

Geometrically linearized theory Total strain tensor $\boldsymbol{\varepsilon}$ is defined as

$$\boldsymbol{\varepsilon} = \frac{1}{2}\left[\nabla \boldsymbol{u} + \nabla^T \boldsymbol{u}\right] \ , \tag{2.1}$$

where ∇ is the gradient operator with respect to $\boldsymbol{X}$. For modeling plasticity, total strain tensor $\boldsymbol{\varepsilon}$ is additively decomposed in an incompatible manner into an elastic part and a plastic part, i.e.,

$$\boldsymbol{\varepsilon} = \boldsymbol{\varepsilon}^{\mathrm{e}} + \boldsymbol{\varepsilon}^{\mathrm{p}} \tag{2.2}$$

where the superscripts e and p distinguish between the elastic, i.e., reversible, strains and the plastic, i.e., irreversible, strains.

Geometrically exact theory In the geometrically exact formulation, the deformation gradient is defined as

$$\boldsymbol{F} = \frac{\partial \boldsymbol{x}}{\partial \boldsymbol{X}} = \frac{\partial \left[\boldsymbol{X} + \boldsymbol{u}\right]}{\partial \boldsymbol{X}} = \boldsymbol{I} + \nabla \boldsymbol{u} \ . \tag{2.3}$$

This allows the computation of the right Cauchy-Green deformation tensor

$$\boldsymbol{C} = \boldsymbol{F}^T \cdot \boldsymbol{F} \ , \tag{2.4}$$

from which the family of generalized strains, see [163], is computed as

$$\boldsymbol{E}^m = \begin{cases} \dfrac{1}{2\,m} \left[\boldsymbol{C}^m - \boldsymbol{I}\right] \ , & \text{if } m \neq 0 \\ \dfrac{1}{2} \ln\left(\boldsymbol{C}\right) \ , & \text{else .} \end{cases} \tag{2.5}$$

These generalized strains can be decomposed additively into an elastic and a plastic part as [61]

$$\boldsymbol{E} = \boldsymbol{E}^{\mathrm{e}} + \boldsymbol{E}^{\mathrm{p}} \ . \tag{2.6}$$

This analogy to the linearized theory allows the extension constitutive models to finite strains without changing its local structure.
Certainly, the aforementioned sketched theory is not the only theory for modeling elasto-plastic deformations undergoing large deformations. An alternative approach is based on a multiplicative decomposition of the deformation gradient as

$$\boldsymbol{F} = \boldsymbol{F}^{\mathrm{e}} \cdot \boldsymbol{F}^{\mathrm{p}} \ , \tag{2.7}$$

which can be interpreted as the introduction of an intermediate configuration associated with plastic deformations [93]. A second alternative is the additive decomposition of the deformation rate tensor into

$$\boldsymbol{d} = \boldsymbol{d}^{\mathrm{e}} + \boldsymbol{d}^{\mathrm{p}} \ , \tag{2.8}$$

associated with hypo-elasto-plastic theories [179].

2.2 Balance laws

Balance laws describe the most fundamental principles in physics. Nowadays, they can be found in several textbooks, cf. [186] among others.

Balance of linear momentum The axiom of balance of linear momentum states that the change of linear momentum in time is equal to the sum of all external forces acting on the body [186]. Let $\boldsymbol{L}$ be the linear momentum of the body with respect to reference configuration $\mathcal{B}$. Then the balance of linear momentum is then expressed as

$$\dot{\boldsymbol{L}} = \boldsymbol{F}_A + \boldsymbol{F}_V \tag{2.9}$$

where $\dot{\bullet}$ denotes the material time derivative. The external forces are separated into forces acting on the surface $\boldsymbol{F}_A$ and forces acting in the volume $\boldsymbol{F}_V$, both given in integral format as

$$\boldsymbol{F}_A = \int_{\partial\mathcal{B}} \boldsymbol{t}\,\mathrm{d}A\ , \qquad \boldsymbol{F}_V = \int_{\mathcal{B}} \rho\,\boldsymbol{b}\,\mathrm{d}V\ . \tag{2.10}$$

Here, ρ denotes the mass density, $\boldsymbol{t}$ denotes surface tractions and $\rho\,\boldsymbol{b}$ denotes forces per volume. By considering linear momentum $\boldsymbol{L}$ as well as its time derivative $\dot{\boldsymbol{L}}$ in their integral format as

$$\boldsymbol{L} = \int_{\mathcal{B}} \rho\,\dot{\boldsymbol{x}}\,\mathrm{d}V\ , \qquad \dot{\boldsymbol{L}} = \int_{\mathcal{B}} \rho\,\ddot{\boldsymbol{x}}\,\mathrm{d}V \tag{2.11}$$

leads by insertion of (2.10) and (2.11) into axiom (2.9) to

$$\int_{\mathcal{B}} \rho\,\ddot{\boldsymbol{x}}\,\mathrm{d}V = \int_{\partial\mathcal{B}} \boldsymbol{t}\,\mathrm{d}A + \int_{\mathcal{B}} \rho\,\boldsymbol{b}\,\mathrm{d}V \tag{2.12}$$

as the integral format of balance of linear momentum. Utilizing *Cauchy*'s postulate, resulting in $\boldsymbol{\sigma}\cdot\boldsymbol{n} = \boldsymbol{t}$ with $\boldsymbol{\sigma}$ being the stress tensor of second order and $\boldsymbol{n}$ the outward facing normal vector of the body with respect to reference configuration $\mathcal{B}$, enables the reformulation of balance equation (2.12) into

$$\int_{\mathcal{B}} \rho\,\ddot{\boldsymbol{x}}\,\mathrm{d}V = \int_{\mathcal{B}} \mathrm{div}\,(\boldsymbol{\sigma})\ \mathrm{d}V + \int_{\mathcal{B}} \rho\,\boldsymbol{b}\,\mathrm{d}V\ . \tag{2.13}$$

Its local format follows as

$$\rho\,\ddot{\boldsymbol{x}} = \mathrm{div}\,(\boldsymbol{\sigma}) + \rho\,\boldsymbol{b} \tag{2.14}$$

known as the strong form of equilibrium.

Balance of angular momentum Analogously to the axiom of balance of linear momentum, the axiom of balance of angular momentum states that the change of angular momentum in time with respect to fixed point in time and space $\boldsymbol{x}_0$ is equal to the sum of all moments stemming from external volume and surface forces with respect to point $\boldsymbol{x}_0$, see [186]. It reads

$$\dot{\boldsymbol{M}} = \boldsymbol{M}_A + \boldsymbol{M}_V\ , \tag{2.15}$$

with $\boldsymbol{M}_A$ and $\boldsymbol{M}_V$ being the external moments

$$\boldsymbol{M}_A = \int_{\partial\mathcal{B}} [\boldsymbol{x} - \boldsymbol{x_0}] \times \boldsymbol{t}\, \mathrm{d}A \,, \qquad \boldsymbol{M}_V = \int_{\mathcal{B}} \rho\, [\boldsymbol{x} - \boldsymbol{x_0}] \times \boldsymbol{b}\, \mathrm{d}V \,. \tag{2.16}$$

with respect to point $\boldsymbol{x}_0$. The angular momentum $\boldsymbol{M}$ and its material time derivative $\dot{\boldsymbol{M}}$ read

$$\boldsymbol{M} = \int_{\mathcal{B}} \rho\, [\boldsymbol{x} - \boldsymbol{x}_0] \times \dot{\boldsymbol{x}}\, \mathrm{d}V \,, \qquad \dot{\boldsymbol{M}} = \int_{\mathcal{B}} \rho\, [\boldsymbol{x} - \boldsymbol{x}_0] \times \ddot{\boldsymbol{x}}\, \mathrm{d}V \,. \tag{2.17}$$

By inserting both eq. (2.16) and eq. (2.17) into axiom (2.15) leads to its integral format

$$\int_{\mathcal{B}} \rho\, [\boldsymbol{x} - \boldsymbol{x}_0] \times \ddot{\boldsymbol{x}}\, \mathrm{d}V = \int_{\partial\mathcal{B}} [\boldsymbol{x} - \boldsymbol{x_0}] \times \boldsymbol{t}\, \mathrm{d}A + \int_{\mathcal{B}} \rho\, [\boldsymbol{x} - \boldsymbol{x_0}] \times \boldsymbol{b}\, \mathrm{d}V \,, \tag{2.18}$$

which is reformulated into

$$\begin{aligned} \int_{\mathcal{B}} \rho\, [\boldsymbol{x} - \boldsymbol{x}_0] \times \ddot{\boldsymbol{x}}\, \mathrm{d}V = &\int_{\mathcal{B}} [\boldsymbol{x} - \boldsymbol{x_0}] \times \operatorname{div}(\boldsymbol{\sigma}) + \nabla [\boldsymbol{x} - \boldsymbol{x_0}] \times \boldsymbol{\sigma}\, \mathrm{d}V \\ &+ \int_{\mathcal{B}} \rho\, [\boldsymbol{x} - \boldsymbol{x_0}] \times \boldsymbol{b}\, \mathrm{d}V \,. \end{aligned} \tag{2.19}$$

By considering balance of linear momentum (2.13) and using identity $\nabla [\boldsymbol{x} - \boldsymbol{x_0}] = \boldsymbol{I}$ the balance equation is reduced to

$$\int_{\mathcal{B}} \boldsymbol{I} \times \boldsymbol{\sigma}\, \mathrm{d}V = \boldsymbol{0} \,. \tag{2.20}$$

Therefore, balance of angular momentum is fulfilled in a point wise manner, if stress tensor $\boldsymbol{\sigma}$ is symmetric.

Balance of micro forces The balance of micro forces, see [65], is a generalized balance law. The general equation of this framework reads

$$\int_{\partial\mathcal{B}} \boldsymbol{\Omega} \cdot \boldsymbol{n}\, \mathrm{d}A + \int_{\mathcal{B}} [\gamma - \omega]\, \mathrm{d}V = 0 \,, \tag{2.21}$$

where $\boldsymbol{\Omega}$ is a micro stress vector and ω and γ internal and external micro forces. This balance equation is concerned, for instance, with non-local fields of gradient continua. Similar to the balance of linear momentum and the balance of angular momentum, the

strong form is obtained by means of the divergence theorem and the localization theorem as

$$\operatorname{div}(\boldsymbol{\Omega}) + \gamma = \omega \ . \tag{2.22}$$

1st law of thermodynamics Considering continuum mechanics, a mathematical representation of the first law reads

$$\dot{E} = P + Q \ , \tag{2.23}$$

where E denotes the total energy of the system, P external mechanical power and Q the heat supply. The total energy E consists of kinetic energy K as well as internal energy U given in integral format together with their corresponding time derivatives as

$$K = \frac{1}{2} \int_{\mathcal{B}} \rho \, \dot{\boldsymbol{x}} \cdot \dot{\boldsymbol{x}} \, \mathrm{d}V \ , \qquad \dot{K} = \int_{\mathcal{B}} \rho \, \dot{\boldsymbol{x}} \cdot \ddot{\boldsymbol{x}} \, \mathrm{d}V \ , \tag{2.24}$$

$$U = \int_{\mathcal{B}} u \, \mathrm{d}V \ , \qquad \dot{U} = \int_{\mathcal{B}} \dot{u} \, \mathrm{d}V \ . \tag{2.25}$$

Considering continuum mechanics, the volume specific internal energy u is given in terms of the Helmholtz free energy ψ, the temperature Θ and the entropy s as

$$u = \psi + \Theta \, s \ , \qquad \dot{u} = \dot{\psi} + \dot{\Theta} \, s + \Theta \, \dot{s} \ . \tag{2.26}$$

Thus, only the external power and the heat supply remain to be specified. Starting with the external power, which is divided into mechanical part P^{mec} and part P^{mic} associated with micro force field φ as

$$P^{\mathrm{mec}} = \int_{\partial\mathcal{B}} \boldsymbol{t} \cdot \dot{\boldsymbol{x}} \, \mathrm{d}A + \int_{\mathcal{B}} \rho \, \boldsymbol{b} \cdot \dot{\boldsymbol{x}} \, \mathrm{d}V \ , \tag{2.27}$$

$$P^{\mathrm{mic}} = \int_{\partial\mathcal{B}} \boldsymbol{\Omega} \cdot \boldsymbol{n} \, \dot{\varphi} \, \mathrm{d}A + \int_{\mathcal{B}} \gamma \, \dot{\varphi} \, \mathrm{d}V. \tag{2.28}$$

Likewise, the heat supply consists of a surface flux term $\boldsymbol{q}$ and a volume specific source term r as

$$Q = -\int_{\partial\mathcal{B}} \boldsymbol{q} \cdot \boldsymbol{N} \, \mathrm{d}A + \int_{\mathcal{B}} \rho \, r \, \mathrm{d}V \ . \tag{2.29}$$

After insertion of eq. (2.24) – (2.29) into balance law (2.23), application of the divergence theorem to all surface quantities and truncation of balance of linear momentum (2.13) as well as balance of micro forces (2.22) leads to the strong form of balance of energy as

$$\dot{\psi} + \dot{\Theta}\, s + \Theta\, \dot{s} = \boldsymbol{\sigma} : \nabla \dot{\boldsymbol{x}} + \boldsymbol{\Omega} \cdot \nabla \dot{\varphi} + \omega\, \dot{\varphi} - \operatorname{div}(\boldsymbol{q}) + \rho\, r \; . \tag{2.30}$$

2nd law of thermodynamics The second law of thermodynamics deals with the direction of processes and the generated entropy thereof. Following [186], the rate of entropy is specified as

$$\dot{S} = \frac{\mathrm{d}}{\mathrm{d}t} \int\limits_{\mathcal{B}} s \, \mathrm{d}V + \int\limits_{\partial\mathcal{B}} \frac{1}{\Theta}\, \boldsymbol{q} \cdot \boldsymbol{N} - \int\limits_{\mathcal{B}} \frac{\rho\, r}{\Theta} \, \mathrm{d}V \; . \tag{2.31}$$

In thermodynamic processes the entropy never decreases. Mathematically speaking, $\dot{S} \geq 0$ has to hold for every thermodynamic process. Processes with $\dot{S} = 0$ are referred to as reversible and processes with $\dot{S} > 0$ are referred to as irreversible. By applying the divergence theorem and multiplying with Θ, the rate of entropy is transformed into dissipation inequality

$$\mathcal{D} = \Theta\, \dot{s} + \operatorname{div}(\boldsymbol{q}) - \rho\, r - \frac{1}{\Theta}\, \boldsymbol{q} \cdot \nabla \Theta \geq 0 \; . \tag{2.32}$$

By inserting eq. (2.26), the dissipation inequality is reformulated in terms of the Helmholtz energy ψ as

$$\mathcal{D} = \boldsymbol{\sigma} : \nabla \dot{\boldsymbol{x}} + \boldsymbol{\Omega} \cdot \nabla \dot{\varphi} + \omega\, \dot{\varphi} - \left[\dot{\psi} + \dot{\Theta}\, s \right] - \frac{1}{\Theta}\, \boldsymbol{q} \cdot \nabla \Theta \geq 0 \; . \tag{2.33}$$

For isothermal process, i.e., $\Theta = \text{const.} > 0\, K$, the dissipation inequality simplifies to

$$\mathcal{D} = \boldsymbol{\sigma} : \nabla \dot{\boldsymbol{x}} + \boldsymbol{\Omega} \cdot \nabla \dot{\varphi} + \omega\, \dot{\varphi} - \dot{\psi} \geq 0 \tag{2.34}$$

and by additionally vanishing micro forces to

$$\mathcal{D} = \boldsymbol{\sigma} : \nabla \dot{\boldsymbol{x}} - \dot{\psi} \geq 0 \; . \tag{2.35}$$

2.3 Variational formulation

The variational framework of incremental energy minimization can be traced back to, at least, *Petryk* [140], *Comi and Perego* [40], *Ortiz and Repetto* [130] and *Carstensen et al.* [26]. Since then, the topic has been strongly promoted by *Francfort and Marigo* [56], *Ortiz and Stainier* [131], *Miehe and Lambrecht* [109], *Petryk* [141] and *Mosler* [118], among others. The key idea is the introduction of potential $\mathcal{I}$ and its rate $\dot{\mathcal{I}}$. After

adding powers due to external forces, balance and evolution equations follow jointly through stationarity. In order to recall the nomenclature and structure as briefly as necessary, the rate potential is chosen as

$$\dot{\mathcal{I}} = \dot{\psi} + D \,, \tag{2.36}$$

$$\psi = \psi^{\mathrm{loc}}(\boldsymbol{\varepsilon},\, q,\, \varphi) + \psi^{\mathrm{nloc}}(q,\, \varphi,\, \nabla\varphi) \,, \tag{2.37}$$

$$D = D^{\mathrm{ri}}\,(q,\, \dot{q}) + D^{\mathrm{rd}}\,(q,\, \dot{q}) + D^{\mathrm{nloc}}(\varphi,\, \dot{\varphi},\, \nabla\varphi,\, \nabla\dot{\varphi}) \,. \tag{2.38}$$

Helmholtz energy ψ depends on linearized strain tensor $\boldsymbol{\varepsilon}$, scalar internal variable q and non-local field φ. It is split into two parts: ψ^{loc} defines solely the local model and ψ^{nloc} accounts for non-local extensions, e.g., in terms of the micromorphic gradient regularization, cf. [48, 54]. The state dependent (dependence on q and $\dot{q}$) dissipation function is split in a similar manner. D^{ri} defines the rate-independent part of the model and is homogeneous of degree one in $\dot{q}$. D^{rd} is a rate-dependent extension in order to include viscous effects and D^{nloc} is a non-local dissipative extension analogously to its energetic counterpart ψ^{nloc}. It allows for instance the derivation of the phase-field model [56] by means of the variational approach. In what follows, the time-continuous case will be specified first, followed by its time-discrete counterpart.

2.3.1 Time-continuous setting

According to *Petryk* [141], *Ortiz and Repetto* [130], *Carstensen et al.* [26] and *Miehe and Lambrecht* [109], among others, a global rate potential $\dot{\mathcal{E}}$ can be defined as

$$\dot{\mathcal{E}} = \int_{\mathcal{B}} \dot{\mathcal{I}}\, \mathrm{d}V - \int_{\mathcal{B}} \rho\, \boldsymbol{b} \cdot \dot{\boldsymbol{u}}\, \mathrm{d}V - \int_{\partial\mathcal{B}} \boldsymbol{t} \cdot \dot{\boldsymbol{u}}\, \mathrm{d}A \,, \tag{2.39}$$

where $\dot{\mathcal{I}}$ is the local rate potential presented in eq. (2.36), $\boldsymbol{u}$ is the displacement field, ρ is the density of the material and $\rho\,\boldsymbol{b}$ and $\boldsymbol{t}$ are forces acting in body $\mathcal{B}$ and on its surface $\partial\mathcal{B}$, respectively. The choice of potential (2.39) is not mandatory. It is also admissible to apply external loads with respect to non-local field φ, as it is done for instance in [153]. The stationarity condition of potential (2.39) reads

$$\delta\dot{\mathcal{E}} = \delta_{\dot{\boldsymbol{u}}}\dot{\mathcal{E}} \cdot \delta\dot{\boldsymbol{u}} + \delta_{\dot{\varphi}}\dot{\mathcal{E}}\, \delta\dot{\varphi} + \partial_{\dot{q}}\dot{\mathcal{E}}\, \delta\dot{q} = 0 \tag{2.40}$$

and, thus, leads to the balance laws and the evolution equation as

$$\delta_{\dot{\boldsymbol{u}}}\dot{\mathcal{E}} \cdot \delta\dot{\boldsymbol{u}} = \boldsymbol{0} \,, \qquad \delta_{\dot{\varphi}}\dot{\mathcal{E}}\, \delta\dot{\varphi} = 0 \,, \qquad \partial_{\dot{q}}\dot{\mathcal{E}}\, \delta\dot{q} = 0 \,. \tag{2.41}$$

Here, operator $\partial_{\dot{q}}\dot{\mathcal{E}}$ denotes the subdifferential with respect to $\dot{q}$. Starting with balance of linear momentum, i.e., $\delta_{\dot{\boldsymbol{u}}}\dot{\mathcal{E}} \cdot \delta\dot{\boldsymbol{u}} = 0$, yields

$$\begin{aligned} \delta_{\dot{\boldsymbol{u}}}\dot{\mathcal{E}} \cdot \delta\dot{\boldsymbol{u}} &= \int_{\mathcal{B}} \boldsymbol{\sigma} : \delta_{\dot{\boldsymbol{u}}}\dot{\boldsymbol{\varepsilon}}\, \mathrm{d}V - \int_{\mathcal{B}} \rho\, \boldsymbol{b} \cdot \delta\dot{\boldsymbol{u}}\, \mathrm{d}V - \int_{\partial\mathcal{B}} \boldsymbol{t} \cdot \delta\dot{\boldsymbol{u}}\, \mathrm{d}A = 0 \\ \Leftrightarrow \quad & \int_{\mathcal{B}} \left[\operatorname{div}(\boldsymbol{\sigma}) + \rho\, \boldsymbol{b}\right] \cdot \delta\dot{\boldsymbol{u}}\, \mathrm{d}V = \int_{\partial\mathcal{B}} \left[\boldsymbol{\sigma} \cdot \boldsymbol{n} - \boldsymbol{t}\right] \cdot \delta\dot{\boldsymbol{u}}\, \mathrm{d}A\,, \end{aligned} \tag{2.42}$$

where $\boldsymbol{\sigma}$ is the Cauchy stress tensor in the framework of linearized kinematics following from Helmholtz energy (2.37) as $\boldsymbol{\sigma} = \partial_{\boldsymbol{\varepsilon}}\psi$. The weak form of balance of linear momentum (2.42) is transformed by means of the localization theorem into its strong form

$$\begin{aligned} \operatorname{div}(\boldsymbol{\sigma}) &= -\rho\, \boldsymbol{b} \quad \text{in } \mathcal{B}\,, \\ \boldsymbol{\sigma} \cdot \boldsymbol{n} &= \boldsymbol{t} \qquad \text{on } \partial\mathcal{B}\,. \end{aligned} \tag{2.43}$$

The equivalence between eq. (2.43) and (2.14) becomes obvious by neglecting contributions due to inertia. Following the same line of thought the balance equation associated with non-local field φ is derived as

$$\begin{aligned} \delta_{\dot{\varphi}}\dot{\mathcal{E}}\, \delta\varphi &= \int_{\mathcal{B}} \omega\, \delta\dot{\varphi} + \ \boldsymbol{\Omega} \cdot \delta_{\dot{\varphi}} \nabla\dot{\varphi}\, \mathrm{d}V = 0 \\ \Leftrightarrow \quad & \int_{\mathcal{B}} \left[\operatorname{div}(\boldsymbol{\Omega}) - \omega\right]\, \delta\dot{\varphi}\, \mathrm{d}V = \int_{\partial\mathcal{B}} \boldsymbol{\Omega} \cdot \boldsymbol{n}\, \delta\dot{\varphi}\, \mathrm{d}A\,, \end{aligned} \tag{2.44}$$

which is known as the balance of micro forces, cf. [65]. Here, $\omega = \partial_{\varphi}\mathcal{I}$ and $\boldsymbol{\Omega} = \partial_{\nabla\varphi}\mathcal{I}$ follow as derivatives from Helmholtz energy (2.37) and dissipation function (2.38). For the special case $D^{\mathrm{nloc}} \equiv 0$, ω and $\boldsymbol{\Omega}$ are fully defined in terms of Helmholtz energy (2.37) as $\omega = \partial_{\varphi}\psi$ and $\boldsymbol{\Omega} = \partial_{\nabla\varphi}\psi$. By, once again, applying the localization theorem to weak form (2.44), the strong form of the balance of micro forces results in

$$\begin{aligned} \operatorname{div}(\boldsymbol{\Omega}) &= \omega \quad \text{in } \mathcal{B}\,, \\ \boldsymbol{\Omega} \cdot \boldsymbol{n} &= 0 \quad \text{on } \partial\mathcal{B}\,. \end{aligned} \tag{2.45}$$

By neglecting parts associated with volume force, i.e., $\gamma = 0$, the equivalence between eq. (2.45) and (2.22) becomes also apparent. The evolution equation of internal variable q is left to be determined. It follows from stationarity of potential (2.39) with respect to $\dot{q}$, resulting in Biot's equation, cf. [21], as

$$\partial_{\dot{q}}\dot{\mathcal{E}}\, \delta\dot{q} = \int_{\mathcal{B}} \left[-Q + \partial_{\dot{q}} D\right]\, \delta\dot{q}\, \mathrm{d}V \ni 0 \tag{2.46}$$

or in its local format as

$$Q \in \partial_{\dot{q}} D \quad \text{in } \mathcal{B} \,. \tag{2.47}$$

Q denotes the energetic dual quantity to internal variable q and follows from Helmholtz energy (2.37) as $Q = -\partial_q \psi$. Evolution equation (2.47) can be recast in terms of an elastic domain, whose boundary is characterized by $\delta_{\dot{q}} \dot{\mathcal{I}} = 0$ and internal variable q evolves, if the boundary of the elastic domain is reached (or exceeded within the trial step). A further restriction to the evolution equation follows from the second law of thermodynamics. The stress power associated with the model is

$$\mathcal{P} = \boldsymbol{\sigma} : \dot{\boldsymbol{\varepsilon}} + \omega \, \dot{\varphi} + \boldsymbol{\Omega} \cdot \nabla \dot{\varphi} \,, \tag{2.48}$$

thus leading to dissipation inequality

$$\begin{aligned} \mathcal{D} = \mathcal{P} - \dot{\psi} = \left[\boldsymbol{\sigma} - \frac{\partial \psi}{\partial \boldsymbol{\varepsilon}} \right] : \dot{\boldsymbol{\varepsilon}} + \left[\omega - \frac{\partial \psi}{\partial \varphi} \right] \dot{\varphi} + \left[\boldsymbol{\Omega} - \frac{\partial \psi}{\partial \nabla \varphi} \right] \cdot \nabla \dot{\varphi} - \frac{\partial \psi}{\partial q} \, \dot{q} \geq 0 \\ \Leftrightarrow \quad \frac{\partial D^{\mathrm{nloc}}}{\partial \dot{\varphi}} \, \dot{\varphi} + \frac{\partial D^{\mathrm{nloc}}}{\partial \nabla \dot{\varphi}} \cdot \nabla \dot{\varphi} + Q \, \dot{q} \geq 0 \,. \end{aligned} \tag{2.49}$$

The dissipation inequality is a priori fulfilled, if dissipation function (2.38) is non-negative, convex in its rates and contains the origin. For the special case $D^{\mathrm{nloc}} \equiv 0$ dissipation inequality (2.49) simplifies to $\mathcal{D} = Q \, \dot{q} \geq 0$.

2.3.2 Time-discrete setting

The time discrete formulation is not only required for the numerical implementation but also turns the variational framework into a minimization problem. The time discretization of $\dot{\boldsymbol{u}}$, $\dot{\varphi}$ and $\dot{q}$ are chosen in implicit manner as

$$\dot{\boldsymbol{u}} = \frac{\boldsymbol{u} - \boldsymbol{u}_n}{\Delta t} \,, \qquad \dot{\varphi} = \frac{\varphi - \varphi_n}{\Delta t} \,, \qquad \dot{q} = \frac{q - q_n}{\Delta t} \,. \tag{2.50}$$

The time index $n+1$ is omitted for easier readability, i.e., $\boldsymbol{u} \coloneqq \boldsymbol{u}_{n+1}$ for instance. Inserting approximations (2.50) into potentials (2.36) and (2.39) and subsequently performing a time integration leads to incremental potentials

$$\mathcal{I} = \int_{t_n}^{t_{n+1}} \dot{\mathcal{I}} \, \mathrm{d}t = \psi - \psi_n + \int_{t_n}^{t_{n+1}} D \, \mathrm{d}t \,, \tag{2.51}$$

$$\mathcal{E} = \int_{t_n}^{t_{n+1}} \dot{\mathcal{E}} \, \mathrm{d}t = \int_{\mathcal{B}} \mathcal{I} \, \mathrm{d}V - \int_{\mathcal{B}} \rho \, \boldsymbol{b} \cdot [\boldsymbol{u} - \boldsymbol{u}_n] \, \mathrm{d}V - \int_{\partial\mathcal{B}} \boldsymbol{t} \cdot [\boldsymbol{u} - \boldsymbol{u}_n] \, \mathrm{d}A \, . \tag{2.52}$$

$\psi_n = \psi(\boldsymbol{\varepsilon}_n, \varphi_n, q_n)$ denotes the Helmholtz energy of the previous time step and where $\psi = \psi(\boldsymbol{\varepsilon}, \varphi, q)$ denotes the Helmholtz energy of the current time step. In contrast to rate potential (2.36), incremental potential (2.51) depends only on $\boldsymbol{u}$, φ, q and no longer on the rates $\dot{\boldsymbol{u}}$, $\dot{\varphi}$ and $\dot{q}$. Similar to Subsection 2.3.1, the balance and evolution equations follow jointly through stationarity of potential (2.52), i.e.,

$$\delta\mathcal{E} = \delta_{\boldsymbol{u}}\mathcal{E} \cdot \delta\boldsymbol{u} + \delta_{\varphi}\mathcal{E} \, \delta\varphi + \partial_q \mathcal{E} \, \delta q = 0 \tag{2.53}$$

has to hold. The first term results in balance of linear momentum

$$\begin{aligned} \delta_{\boldsymbol{u}}\mathcal{E} \cdot \delta\boldsymbol{u} &= \int_{\mathcal{B}} \boldsymbol{\sigma} : \delta_{\boldsymbol{u}}\boldsymbol{\varepsilon} \, \mathrm{d}V - \int_{\mathcal{B}} \rho \, \boldsymbol{b} \cdot \delta\boldsymbol{u} \, \mathrm{d}V - \int_{\partial\mathcal{B}} \boldsymbol{t} \cdot \delta\boldsymbol{u} \, \mathrm{d}A = \boldsymbol{0} \\ \Leftrightarrow \quad & \int_{\mathcal{B}} [\operatorname{div}(\boldsymbol{\sigma}) + \rho \, \boldsymbol{b}] \cdot \delta\boldsymbol{u} \, \mathrm{d}V = \int_{\partial\mathcal{B}} [\boldsymbol{\sigma} \cdot \boldsymbol{n} - \boldsymbol{t}] \cdot \delta\boldsymbol{u} \, \mathrm{d}A \end{aligned} \tag{2.54}$$

which is equivalent to time-continuous variation (2.42) and, thus, equivalent to (2.14). Consequently, the local format of this balance law is equivalent to the strong form of balance of linear momentum (2.43) at time step t_{n+1}. A straightforward calculation of the second expression in total variation (2.53) yields

$$\begin{aligned} \delta_{\varphi}\mathcal{E} \, \delta\varphi &= \int_{\mathcal{B}} \omega \, \delta\varphi + \boldsymbol{\Omega} \cdot \delta_{\varphi}\nabla\varphi \, \mathrm{d}V = 0 \\ \Leftrightarrow \quad & \int_{\mathcal{B}} [\operatorname{div}(\boldsymbol{\Omega}) - \omega] \, \delta\varphi \, \mathrm{d}V = \int_{\partial\mathcal{B}} [\boldsymbol{\Omega} \cdot \boldsymbol{n}] \, \delta\varphi \, \mathrm{d}A \end{aligned} \tag{2.55}$$

which locally yields balance of microforces (2.45) at time t_{n+1}. The equivalence to the time-continuous counterpart again becomes obvious. The remaining variation results in Biot's equation associated with internal variable q. It is given in its integral format as

$$\partial_q \mathcal{E} \, \delta q = \int_{\mathcal{B}} \left[-Q + \partial_q \int_{t_n}^{t_{n+1}} D \, \mathrm{d}t \right] \delta q \, \mathrm{d}V = 0 \tag{2.56}$$

and in its local format as

$$Q \in \partial_q \int_{t_n}^{t_{n+1}} D \, \mathrm{d}t \quad \text{in } \mathcal{B} \, . \tag{2.57}$$

The additional constraint due to the second law of thermodynamics is transformed in an analogous manner into a constraint for the evolution equation. It results in

$$\int_{t_n}^{t_{n+1}} \mathcal{D}\,\mathrm{d}t = \int_{\varphi_n}^{\varphi_{n+1}} \frac{\partial D^{\mathrm{nloc}}}{\partial \varphi}\,\mathrm{d}\varphi + \int_{\nabla\varphi_n}^{\nabla\varphi_{n+1}} \frac{\partial D^{\mathrm{nloc}}}{\partial \nabla\varphi}\,\mathrm{d}\nabla\varphi + \int_{q_n}^{q_{n+1}} Q\,\mathrm{d}q \geq 0\,, \tag{2.58}$$

which is also a priori fulfilled for non-negative, convex and origin-containing dissipation functions. It simplifies for $D^{\mathrm{nloc}} \equiv 0$ to

$$\int_{t_n}^{t} \mathcal{D}\,\mathrm{d}t = \int_{q_n}^{q} Q\,\mathrm{d}q \geq 0\,. \tag{2.59}$$

2.3.3 Determining well-posedness for local models

Due to the time-discrete variational framework, an analysis of the convexity properties of the global incremental energy $\mathcal{E}$ is sufficient to characterize the boundary value problem. Since potential $\mathcal{E}$ differs only in terms of linear expressions from potential $\mathcal{I}$, the convexity properties of potential $\mathcal{E}$ are identical to the convexity properties of potential $\mathcal{I}$, which allows te shift of the analysis of the convexity properties to potential $\mathcal{I}$. Following *Miehe and Lambrecht* [109] among others, the global quantities $\boldsymbol{\sigma}$, ω and $\boldsymbol{\Omega}$ are given as

$$\boldsymbol{\sigma} = \frac{\partial \mathcal{I}}{\partial \boldsymbol{\varepsilon}} = \frac{\partial \mathcal{I}}{\partial \boldsymbol{\varepsilon}} + \underbrace{\frac{\partial \mathcal{I}}{\partial q}\,\frac{\mathrm{d}q}{\mathrm{d}\boldsymbol{\varepsilon}}}_{=\mathbf{0}} = \frac{\mathrm{d}\mathcal{I}}{\mathrm{d}\boldsymbol{\varepsilon}}\,, \tag{2.60}$$

$$\omega = \frac{\partial \mathcal{I}}{\partial \varphi} = \frac{\partial \mathcal{I}}{\partial \varphi} + \underbrace{\frac{\partial \mathcal{I}}{\partial q}\,\frac{\mathrm{d}q}{\mathrm{d}\boldsymbol{\varepsilon}}}_{=\mathbf{0}} = \frac{\mathrm{d}\mathcal{I}}{\mathrm{d}\varphi}\,, \tag{2.61}$$

$$\boldsymbol{\Omega} = \frac{\partial \mathcal{I}}{\partial \nabla\varphi} = \frac{\mathrm{d}\mathcal{I}}{\mathrm{d}\nabla\varphi} \tag{2.62}$$

and hence, follow as total derivatives of the incremental energy. The product $\partial_q \mathcal{I}\,\mathrm{d}_{\boldsymbol{\varepsilon}} q$ vanishes, since $\partial_q \mathcal{I} = 0$ if internal variable q evolves and otherwise $\mathrm{d}_{\boldsymbol{\varepsilon}} q = \mathbf{0}$. By focusing on local models only, i.e., by neglecting ψ^{nloc}, D^{nloc} and thus φ, the analysis of well-posedness is reduced to the analysis of the convexity properties of local potential $\mathcal{I}(\boldsymbol{u})$ or $\mathcal{I}(\boldsymbol{\varepsilon})$, respectively. In this case, the Hessian follows as

$$\frac{\mathrm{d}^2\mathcal{I}}{\mathrm{d}\boldsymbol{\varepsilon}^2} = \frac{\partial^2 \mathcal{I}}{\partial \boldsymbol{\varepsilon}^2} + \left[\frac{\partial^2 \mathcal{I}}{\partial \boldsymbol{\varepsilon}\,\partial q} + \underbrace{\frac{\partial^2 \mathcal{I}}{\partial q\,\partial \boldsymbol{\varepsilon}} + \frac{\partial^2 \mathcal{I}}{\partial q^2}\,\frac{\mathrm{d}q}{\mathrm{d}\boldsymbol{\varepsilon}}}_{=\mathbf{0}}\right] \otimes \frac{\mathrm{d}q}{\mathrm{d}\boldsymbol{\varepsilon}} + \underbrace{\frac{\partial \mathcal{I}}{\partial q}\,\frac{\mathrm{d}^2 q}{\mathrm{d}\boldsymbol{\varepsilon}^2}}_{=\mathbf{0}} = \frac{\mathrm{d}\boldsymbol{\sigma}}{\mathrm{d}\boldsymbol{\varepsilon}}\,. \tag{2.63}$$

Thus, the condition for well-posedness (neglecting degree of freedom φ) reduces to

$$\det\left(\frac{\mathrm{d}^2\mathcal{I}}{\mathrm{d}\boldsymbol{\varepsilon}^2}\right) = \det\left(\frac{\mathrm{d}\boldsymbol{\sigma}}{\mathrm{d}\boldsymbol{\varepsilon}}\right) > 0\,, \tag{2.64}$$

i.e., $\mathrm{d}_{\boldsymbol{\varepsilon}}\boldsymbol{\sigma}$ has to be positive definite.

2.3.4 Localized incremental step

Since the analysis in Subsec. 2.3.3 is only applicable to local models, this subsection shows a unified framework in order to determine the well-posedness of variationally derived constitutive models at specific time steps. The approximation of the evolution equations by an incremental step will later allow an analytical investigation of well-posedness. For that reason, we simplify it further by assuming a localized variation for a spatially homogeneous problem, e.g., for a homogeneous bar under tension, and focus solely on the critical time step at which the softening process starts, i.e., when $\partial_q\mathcal{I} = 0$ is reached for the first time. The incremental step for a quadratic approximation of $\delta\mathcal{I} = 0$ then reads

$$\delta_{\boldsymbol{\varepsilon}}\mathcal{I} = \boldsymbol{\sigma} - \mathcal{L}_{\mathrm{ext}} = 0 \quad \forall\delta\boldsymbol{\varepsilon} \tag{2.65}$$

$$\delta_q\mathcal{I} = 0 \quad \forall\delta q \tag{2.66}$$

$$\delta_\varphi\mathcal{I} = 0 \quad \forall\delta\varphi, \tag{2.67}$$

where $\mathcal{L}_{\mathrm{ext}}$ accounts for the influence of external loads. The first linearization with respect to time can be written as

$$\boldsymbol{A}\cdot\tilde{\boldsymbol{\Xi}} + \boldsymbol{G}_\Delta\cdot\Delta\tilde{\boldsymbol{\Xi}} + \boldsymbol{b}_{\mathrm{total}} = \boldsymbol{0} \quad \left(+\mathcal{O}(\tilde{\boldsymbol{\Xi}}^2,\, \Delta\tilde{\boldsymbol{\Xi}}^2\right)\,, \tag{2.68}$$

with symbol $\tilde{\boldsymbol{\Xi}} = (\tilde{\boldsymbol{\varepsilon}},\, \tilde{q},\, \tilde{\varphi})^T$ representing the summary of all variables. Increments are denoted as $\tilde{\bullet}$, the starting equilibrium configuration is denoted as $\bar{\bullet}$ and Kelvin notation is assumed for interpretation of the products. Matrix $\boldsymbol{A}$ follows as a partial derivative of the incremental energy as

$$\boldsymbol{A} \coloneqq \frac{\partial^2\mathcal{I}}{\partial\boldsymbol{\Xi}^2} = \begin{bmatrix} \overline{\partial^2\mathcal{I}_{\boldsymbol{\varepsilon}\boldsymbol{\varepsilon}}} & \overline{\partial^2\mathcal{I}_{\boldsymbol{\varepsilon}q}} & \overline{\partial^2\mathcal{I}_{\boldsymbol{\varepsilon}\varphi}} \\ & \overline{\partial^2\mathcal{I}_{qq}} & \overline{\partial^2\mathcal{I}_{q\varphi}} \\ \mathrm{sym} & & \overline{\partial^2\mathcal{I}_{\varphi\varphi}} \end{bmatrix}\,. \tag{2.69}$$

Similarly, matrix $\boldsymbol{G}_\Delta$ contains the partial derivatives with respect to Laplacian $\Delta\tilde{\boldsymbol{\Xi}} = (\Delta\tilde{\boldsymbol{\varepsilon}},\, \Delta\tilde{q},\, \Delta\tilde{\varphi})^T$. Since the incremental step relies on a quadratic approximation of $\mathcal{I}$, matrix $\boldsymbol{G}_\Delta$ follows as

$$\boldsymbol{G}_\Delta \coloneqq \frac{\partial^2 \mathcal{I}}{\partial \Delta \boldsymbol{\Xi}^2} = \begin{bmatrix} \boldsymbol{0} & \boldsymbol{0} & \boldsymbol{0} \\ & 0 & 0 \\ \text{sym} & & -l_q \end{bmatrix} . \tag{2.70}$$

Lastly, vector $\boldsymbol{b}_{\text{total}}$ is left to be determined. It contains external loads $\boldsymbol{z}_{\text{ext}}$, the variation evaluated at the last converged time step and boundary terms of $\nabla\varphi$ that are typically assumed to vanish at the body's boundaries. Thus, it reads

$$\boldsymbol{b}_{\text{total}} = \left[\begin{pmatrix} \overline{\partial \mathcal{I}_{\boldsymbol{\varepsilon}}} \\ \overline{\partial \mathcal{I}_q} \\ \overline{\partial \mathcal{I}_\varphi} \end{pmatrix} + \begin{pmatrix} \boldsymbol{z}_{\text{ext}} \\ 0 \\ 0 \end{pmatrix} + \begin{pmatrix} \boldsymbol{0} \\ 0 \\ -l_q\, \Delta\overline{\varphi} \end{pmatrix} \right] . \tag{2.71}$$

Linearization (2.68) shall be used to analyze, whether and how regularization methods provide well-posedness. According to the underlying variational structure, all matrices in (2.68) are defined by means of derivatives of the potential $\mathcal{I}$. This analysis is limited to the one-dimensional, incremental approximation of the respective models for the sake of analytical accessibility.

2.4 Prototype models for isotropic, brittle damage model

In this section, constitutive models are introduced in order to capture isotropic and (quasi-)brittle material degradation. First, a local model will be presented and afterwards a phase field model adopted from [56, 110].

2.4.1 Local, isotropic, (quasi-)brittle damage

Following the variational formulation presented in Section 2.3, the constitutive equations are derived from incremental potential $\mathcal{I}$, which consists of Helmholtz energy ψ and dissipation function D. They are defined as

$$\psi = \psi^{\text{loc}}(\boldsymbol{\varepsilon},\, \alpha) \coloneqq f(\alpha)\, \psi_0(\boldsymbol{\varepsilon}) , \tag{2.72}$$

$$D = D^{\text{ri}}(\alpha,\, \dot{\alpha}) \coloneqq -\frac{\alpha}{c_E}\, f'(\alpha)\, |\dot{\alpha}| , \tag{2.73}$$

neglecting parts ψ^{nloc}, D^{rd} and D^{nloc}. Here, ψ_0 denotes the Helmholtz energy of an undamaged elastic solid and f is a degradation function. f is assumed to be strictly

monotonous and bounded between 1 and 0, i.e., $f = 1$ denotes virgin material points while $f \to 0$ denotes fully damaged material points. A frequently made choice is

$$\psi_0(\boldsymbol{\varepsilon}) = \frac{\lambda}{2} \operatorname{tr}(\boldsymbol{\varepsilon})^2 + \mu\, \boldsymbol{\varepsilon} : \boldsymbol{\varepsilon} = \frac{1}{2}\, \boldsymbol{\varepsilon} : \mathbb{E} : \boldsymbol{\varepsilon} \,, \tag{2.74}$$

$$f(\alpha) = c_0 + [1 - c_0] \exp\left(\frac{\alpha_0 - \alpha^p}{\alpha_u}\right) \,, \tag{2.75}$$

where λ and μ are the Lamé parameters, $c_0 \approx 0$ is the lower bound of the degradation function, α_0 is the threshold value for damage initiation and where α_u and p are parameters defining the fracture energy and the softening response of the material. Insertion of both Helmholtz energy (2.72) and dissipation function (2.73) into incremental potential (2.51) results in

$$\mathcal{I} = f\, \psi_0 - \psi_n + \int_{t_n}^{t_{n+1}} D \,\mathrm{d}t = f\, \psi_0 - \psi_n - \int_{\alpha_n}^{\alpha_{n+1}} \frac{\alpha}{c_E}\, f' \operatorname{sign}(\alpha - \alpha_n) \,\mathrm{d}\alpha \,. \tag{2.76}$$

Since balance laws (2.54) and (2.55) are independent of the specific choice of the dissipation function, only the derivation of the evolution equation remains to be of interest. A straightforward computation of Biot's equation (2.57) leads to

$$f'\, \psi_0 = \frac{\alpha}{c_E}\, f' \begin{cases} \operatorname{sign}(\alpha - \alpha_n) & \text{if } \alpha \neq \alpha_n \\ [-1, 1] & \text{else} \,. \end{cases} \tag{2.77}$$

By considering the second law of thermodynamics in incremental format, i.e.,

$$\int_{t_n}^{t_{n+1}} \mathcal{D} \,\mathrm{d}t = \int_{\alpha_n}^{\alpha_{n+1}} -f'\, \psi_0 \,\mathrm{d}\alpha \geq 0 \quad \Rightarrow \quad \alpha \geq \alpha_n \,, \tag{2.78}$$

the additional constraint $\alpha \geq \alpha_n$ has to be enforced. Due to the time-discrete setting, both equations (2.77) and (2.78) can be combined into

$$\alpha = \max(\alpha_n,\, c_E\, \psi_0) \tag{2.79}$$

as the final evolution equation. The definition of Helmholtz energy (2.72) and dissipation function (2.73) specify the total energy of the system as

$$E = \int_{\mathcal{B}} \dot{\psi} + D \,\mathrm{d}t \,\mathrm{d}V = \int_{\mathcal{B}} \int_0^\infty \boldsymbol{\sigma} : \dot{\boldsymbol{\varepsilon}} \,\mathrm{d}t \,\mathrm{d}V + \int_{\mathcal{B}} \int_0^\infty \underbrace{\left[\partial_\alpha \psi - f' \frac{\alpha}{c_E} \operatorname{sign}(\dot{\alpha})\right]}_{=0} \dot{\alpha} \,\mathrm{d}t \,\mathrm{d}V$$

$$= \int_{\mathcal{B}} \int_{0}^{\infty} \boldsymbol{\sigma} : \dot{\boldsymbol{\varepsilon}} \, \mathrm{d}t \, \mathrm{d}V \ . \tag{2.80}$$

2.4.2 Phase-field model for fracture

Following [56, 110] the Helmholtz energy and the dissipation function, also known as surface energy density [6], are specified as

$$\psi = \psi^{\mathrm{loc}} = f(\varphi) \, \psi_0(\boldsymbol{\varepsilon}) \ , \tag{2.81}$$

$$D = D^{\mathrm{nloc}} = \frac{g_c}{l_\varphi} \left[\varphi \, \dot{\varphi} + l_\varphi^2 \, \nabla\varphi \cdot \nabla\dot{\varphi} \right] \ . \tag{2.82}$$

ψ_0 is the Helmholtz energy adopted from eq. (2.74) and degradation function f is chosen as

$$f = c_0 + [1 - c_0] \, [1 - \varphi]^2 \ , \tag{2.83}$$

where c_0 once again acts as the lower bound for the degradation function. Material parameters g_c and l_φ in dissipation function (2.82) denote the Griffith-type critical energy release rate and the internal length scale, respectively. By following the variational framework in Section 2.3, the balance equations follow as

$$\delta_{\dot{\boldsymbol{u}}} \dot{\mathcal{E}} \cdot \delta\dot{\boldsymbol{u}} = 0 \ , \qquad \delta_{\dot{\varphi}} \dot{\mathcal{E}} \cdot \delta\dot{\varphi} = 0 \tag{2.84}$$

where the first equation results in balance of linear momentum (2.13), while the latter equation yields balance of micro forces associated with non-local damage field φ. By defining $\omega = \partial_{\dot{\varphi}} \mathcal{I} = f' \, \psi_0 + g_c / l_\varphi \, \varphi$ and $\boldsymbol{\Omega} = \partial_{\nabla\dot{\varphi}} \mathcal{I} = g_c \, l_\varphi \, \nabla\varphi$, it reads

$$\begin{aligned} \delta_{\dot{\varphi}} \mathcal{E} \, \delta\dot{\varphi} &= \int_{\mathcal{B}} \omega \, \delta\dot{\varphi} + \boldsymbol{\Omega} \, \delta\nabla\dot{\varphi} \, \mathrm{d}V = 0 \\ \Leftrightarrow \quad & \int_{\mathcal{B}} \left[\mathrm{div}\,(\boldsymbol{\Omega}) - \omega \right] \, \delta\dot{\varphi} \, \mathrm{d}V = \int_{\partial\mathcal{B}} \left[\boldsymbol{\Omega} \cdot \boldsymbol{n} \right] \, \delta\dot{\varphi} \, \mathrm{d}A \ . \end{aligned} \tag{2.85}$$

Thermodynamic driving force ω is frequently modified into

$$\omega = f' \, [\mathcal{H} - \mathcal{H}_0] + \frac{g_c}{l_\varphi} \, \varphi \ , \tag{2.86}$$

$$\mathcal{H} = \max\left(\psi_0, \, \mathcal{H}_n\right) \ , \qquad \mathcal{H}(t = 0) = \mathcal{H}_0 \tag{2.87}$$

where $\mathcal{H}$ is an additional, monotonic increasing internal variable and $\mathcal{H}_0$ a threshold value for damage initiation. This modification prevents a reduction of non-local damage variable φ, and thus, prevents healing of the material. Similar to the previous prototype

model leads the definition of Helmholtz energy (2.81) and dissipation function (2.82) to the system's total energy as

$$\begin{aligned} E &= \int_{\mathcal{B}} \int_{0}^{\infty} \dot{\psi} + D \,\mathrm{d}t \,\mathrm{d}V = \int_{\mathcal{B}} \int_{0}^{\infty} \boldsymbol{\sigma} : \dot{\boldsymbol{\varepsilon}} \,\mathrm{d}t \,\mathrm{d}V + \underbrace{\int_{\mathcal{B}} \int_{0}^{\infty} \omega \,\dot{\varphi} + \boldsymbol{\Omega} \cdot \nabla \dot{\varphi} \,\mathrm{d}t \,\mathrm{d}V}_{=0} \\ &= \int_{\mathcal{B}} \int_{0}^{\infty} \boldsymbol{\sigma} : \dot{\boldsymbol{\varepsilon}} \,\mathrm{d}t \,\mathrm{d}V \ . \end{aligned} \tag{2.88}$$

3 Numerical regularizations of damage models: a comparison based on a unified variational framework

In this chapter three regularization methods are applied to prototype model 2.4.1 suitable for isotropic, (quasi-)brittle damage evolution and compared to one another. The variational derivation of material models in terms of incremental energy minimization will be used as a unifying framework for the analytical comparison of the regularization methods. The comparison focuses on

- highlighting how well-posedness is achieved via the respective coefficient tensors of the incremental step,
- the physics predicted by the regularized models
- and their numerical feasibility.

First the ill-posedness of prototype model 2.4.1 is pointed out. Subsequently, the fracture energy concept [15, 151], the viscous regularization [50] and the micromorphic gradient regularization [48, 54] will be applied to the prototype model. Numerical tests are performed on the basis of two illustrative boundary value problems: a pre-cracked plate and an L-shaped specimen.

3.1 Ill-posedness of the prototype model for isotropic (quasi-)brittle damage

Following Subsection 2.3.4, well-posedness (or the lack thereof) is illustrated for the incremental approximation of an initially homogeneous bar under tension. For this reason a one-dimensional approximation is used. In this case, Helmholtz energy (2.74) simplifies to $\psi_0 = 1/2\, E\, \varepsilon^2$. Stationarity for the local prototype model reads

$$\boldsymbol{A}^{\text{pro}} \cdot \boldsymbol{\Xi}^{\text{pro}} + \mathbf{b}^{\text{pro}}_{\text{total}} = \mathbf{0}, \quad \boldsymbol{A}^{\text{pro}} = \begin{bmatrix} \bar{f}\, E & \bar{f}'\, E\, \bar{\varepsilon} \\ \bar{f}'\, E\, \bar{\varepsilon} & -\dfrac{1}{c_E}\, \bar{f}' \end{bmatrix}, \quad \boldsymbol{\Xi}^{\text{pro}} = \begin{pmatrix} \tilde{\varepsilon} \\ \tilde{\alpha} \end{pmatrix}. \tag{3.1}$$

The solution to this equation is obtained by inverting matrix $\boldsymbol{A}^{\mathrm{pro}}$ as long as it is regular. The eigenvalues read

$$\Lambda_{1,2}^{\mathrm{pro}} = f\,\hat{\Lambda}_{1,2}^{\mathrm{pro}} \quad \text{with} \tag{3.2}$$
$$\hat{\Lambda}_{1,2}^{\mathrm{pro}} = \frac{c_E\,E\,\alpha_u + p\,\bar{\alpha}^{p-1}}{2\,c_E\,\alpha_u} \pm \sqrt{\left[\frac{c_E\,E\,\alpha_u + p\,\bar{\alpha}^{p-1}}{2\,c_E\,\alpha_u}\right]^2 + \frac{E\,p}{\alpha_u\,c_E}\bar{\alpha}^{p-1}\,\left[\frac{2\,p}{\alpha_u}\,\bar{\alpha}^{p} - 1\right]}\,.$$

At the beginning, both eigenvalues are real and positive for small ε and α. $\boldsymbol{A}^{\mathrm{pro}}$ thus starts to be regular and the problem starts to be well-posed. A change in sign occurs for one eigenvalue, though, at $\alpha = c_E\,\psi_0 = [\alpha_u/[2\,p]]^{1/p}$ and defines the onset of softening – rendering the model ill-posed. The other eigenvalue remains always positive and corresponds to the evolution of α that remains well-defined itself.
Alternatively, the incremental energy can be analyzed according to Subsec. 2.3.3. For the inelastic region, the tangent follows as

$$\frac{\mathrm{d}^2\mathcal{I}}{\mathrm{d}\varepsilon^2} = \frac{\mathrm{d}\sigma}{\mathrm{d}\varepsilon} = f\,E\,\left[1 - \frac{2\,p}{\alpha_u}\,\alpha^p\right]\,. \tag{3.3}$$

Thus, as soon as $\alpha > [\alpha_u/[2\,p]]^{1/p}$ the model becomes ill-posed. The ill-posedness is highlighted numerically by a one-dimensional example in appendix A.1. The aim of the subsequent regularization techniques is to recover well-posedness.

3.2 Fracture energy concept

The fracture energy concept is not a regularization method from a mathematical point of view, since the underlying equations remain ill-posed. In contrast to modifying the governing equations, the fracture energy concept adapts the solution scheme to fit the physical response. More precisely, the material parameters are chosen in dependence on the underlying finite element discretization. Therefore it is preferable for the physical properties of the model, i.e., the maximum stress and the systems total energy per unit volume, to be known beforehand. Otherwise, the calibration has to be done numerically. For prototype model 2.4.1 the relevant properties can be derived in a closed format.

3.2.1 Fracture energy of prototype model 2.4.1

The system's total energy per unit volume is given as

$$g_f = \int_{t=0}^{\infty} \boldsymbol{\sigma} : \dot{\boldsymbol{\varepsilon}}\,\mathrm{d}t\,. \tag{3.4}$$

By utilizing the variational structure of the prototype model, the system's energy per unit volume can be reformulated into

$$g_f = \int_{t=0}^{\infty} D \, \mathrm{d}t \; , \tag{3.5}$$

since identity

$$\begin{aligned} \int_{t=0}^{\infty} \boldsymbol{\sigma} : \dot{\boldsymbol{\varepsilon}} \, \mathrm{d}t + \underbrace{\int_{t=0}^{\infty} \partial_\alpha \psi \, \dot{\alpha} + D \, \mathrm{d}t}_{=0} &= \int_{t=0}^{\infty} \dot{\psi} + D \, \mathrm{d}t \\ &= \underbrace{\psi(t=\infty)}_{=0} - \underbrace{\psi(t=0)}_{=0} + \int_{t=0}^{\infty} D \, \mathrm{d}t \end{aligned} \tag{3.6}$$

holds for all dissipation functions D being homogeneous of degree one in $\dot{\alpha}$. A subsequent calculation leads to

$$g_f = \int_{t=0}^{\infty} D \, \mathrm{d}t = - \int_{\alpha_0^{1/p}}^{\infty} \frac{\alpha}{c_E} \, f' \, \mathrm{d}\alpha = \underbrace{- \Big[\frac{\alpha}{c_E} \, f \Big]_{\alpha_0^{1/p}}^{\infty}}_{=: g_f^1} + \underbrace{\int_{\alpha_0^{1/p}}^{\infty} \frac{1}{c_E} \, f \, \mathrm{d}\alpha}_{=: g_f^2} \tag{3.7}$$

and, thus, to

$$g_f^1 = \frac{1}{c_E} \, \alpha_0^{1/p} \; . \tag{3.8}$$

Expression g_f^2 varies in dependence of material parameter p. Therefore, it is given in Tab. 3.1 for selected parameters p. Due to the prototype models isotropy, a one-dimensional setting is considered for further analysis. The stress-strain relation follows then as

$$\sigma = \exp\left(\frac{\alpha_0 - \alpha^p}{\alpha_u} \right) E \, \varepsilon \qquad \text{with} \qquad \alpha = \max\left(\alpha_n, \, \frac{1}{2} \, c_E \, E \, \varepsilon^2 \right) \; , \tag{3.9}$$

where $c_0 = 0$ has been inserted. The model behaves elastic as long as inequality $\varepsilon^2 < 2 \, \alpha_0^{1/p} / [c_E \, E]$ holds. By choosing material parameter $\alpha_u \leq 2 \, \alpha_0 \, p$ the stress decreases

p	$c_E\, g_f^2$
1	α_u
1/2	$2\,\left[\alpha_0\,\alpha_u + \alpha_u^2\right]$
1/4	$4\,\left[6\,\alpha_u^4 + 6\,\alpha_0\,\alpha_u^3 + 3\,\alpha_0^2\,\alpha_u^2 + \alpha_0^3\,\alpha_u\right]$
1/8	$8\,\big[\,5040\,\alpha_u^8 + 5040\,\alpha_0\,\alpha_u^7 + 2520\,\alpha_0^2\,\alpha_u^6 + 840\,\alpha_0^3\,\alpha_u^5$ $+210\,\alpha_0^4\,\alpha_u^4 + 42\,\alpha_0^5\,\alpha_u^3 + 7\,\alpha_0^6\,\alpha_u^2 + \alpha_0^7\,\alpha_u\big]$

Table 3.1: Analytical solution of integral g_f^2 in eq. (3.7) in dependence of parameter p

immediately after exceeding the elastic region. Therefore, the maximum stress also occurs at this transition point and reads

$$\sigma_{\max} = \left[\frac{2\,E}{c_E}\,\alpha_0^{1/p}\right]^{1/2} \quad . \tag{3.10}$$

By choosing parameter $\alpha_u > 2\,\alpha_0\,p$ the maximum stress occurs within the inelastic region and exceeds maximum stress (3.10).

3.2.2 Adaption of the fracture energy concept to ill-posedness

The fracture energy concept relies on the ill-posedness of the underlying local model in the sense, that damage localizes in one element row. This is guaranteed for the present model if inequality $\alpha_u < 2\,\alpha_0\,p$ holds. Additional constraints stem from maximum stress (3.10) (or maximum force) and from the fracture energy. The latter is connected to the system's energy per unit volume as

$$G_f = \frac{1}{A_c} \int\limits_{\mathcal{B}} g_f \,\mathrm{d}V \ . \tag{3.11}$$

The crack surface A_c, and thus, the fracture energy is connected to the dimension of the elements showing dissipative behavior and to the material parameter due to g_f. While the maximum load turns out to be independent of the underlying mesh (if inequality $\alpha_u < 2\,\alpha_0\,p$ holds), the fracture energy G_f is reformulated into

$$G_f = g_f\,d_e \ , \tag{3.12}$$

where d_e is the element's characteristic diameter. By means of a structured mesh, the element's characteristic diameter can be approximated well by the element length orthogonal to the crack surface, cf., e.g., [119].

In summary, the material parameters have to be chosen for each element separately such that (i) immediate localization is ensured, (ii) the maximum stress (3.10) as well

as (iii) the fracture energy (3.11) show identical values for each element and match the experimental observations. The problem description remains ill-posed but secondary effects such as unphysical behavior or mesh dependence are avoided by a calibration between material and numerical parameters.

3.3 Viscous regularization

3.3.1 Fundamentals

The key idea of the viscous regularization is the introduction of a time dependence into the evolution of the internal variable responsible for ill-posedness [50]. A straightforward option for models based on an incremental energy is to activate the rate dependent part in dissipation function (2.38). By doing so Helmholtz energy (2.37) and dissipation function (2.38) are now given as

$$\psi = \psi^{\mathrm{loc}}(\boldsymbol{\varepsilon},\, \alpha)\,, \tag{3.13}$$

$$D = D^{\mathrm{ri}}(\alpha,\, \dot{\alpha}) + D^{\mathrm{rd}}(\alpha,\, \dot{\alpha})\,. \tag{3.14}$$

While ψ^{loc} and D^{ri} are adopted from local prototype model 2.4.1, dissipation function

$$D^{\mathrm{rd}} \coloneqq -\frac{\alpha}{c_E}\, f'\, \frac{\eta}{2}\, \dot{\alpha}^2 \tag{3.15}$$

is appended. The quadratic rate term corresponds to the viscosity. By choosing an exponent larger than two, the viscous model is extended to power law viscosity, cf. [131]. Insertion of eq. (3.13) and (3.14) into incremental energy (2.51) leads to

$$\mathcal{I} = f\,\psi_0 - \psi_n - \int_{\alpha_n}^{\alpha_{n+1}} \frac{\alpha}{c_E}\, f' \,\mathrm{sign}(\alpha - \alpha_n)\,\mathrm{d}\alpha + \int_{t_n}^{t_{n+1}} \frac{\eta}{2\,c_E}\,\alpha\, f' \frac{[\alpha - \alpha_n]^2}{[t - t_n]^2}\mathrm{d}t\,. \tag{3.16}$$

Since the second integral cannot easily be transformed into an integral with respect to α, the integral is approximated numerically. By means of an implicit approximation, the incremental energy takes the form

$$\mathcal{I} \approx f\,\psi_0 - \psi_n - \int_{\alpha_n}^{\alpha_{n+1}} \frac{\alpha}{c_E}\, f'\,\mathrm{d}\alpha - \frac{\eta}{2\,c_E}\,\alpha\, f'\,\frac{[\alpha - \alpha_n]^2}{\Delta t}\,. \tag{3.17}$$

The additional time dependence in (3.17) affects the evolution equation of internal variable α as

$$\partial_\alpha \mathcal{I} \approx \underbrace{f'\,\psi_0 - \frac{\alpha}{c_E}\,f'\,\left[\operatorname{sign}(\alpha-\alpha_n) - \frac{\eta}{c_E}\,\frac{\alpha-\alpha_n}{\Delta t}\right]}_{\partial_{\dot\alpha}\dot{\mathcal{I}}} - \frac{\eta}{2\,c_E}\,\frac{[\alpha-\alpha_n]^2}{\Delta t}\,[f' + \alpha\,f''] \ni 0 \tag{3.18}$$

where the first part is identical to time-continuous variation $\partial_{\dot\alpha}\dot{\mathcal{I}} \ni 0$. Due to the continuity of α, the second part converges towards zero if $\Delta t \to 0$, cf. [109]. Note that the viscosity still affects the evolution of α under this approximation. A numerical demonstration is given in appendix A.2. Assuming sufficiently small time steps, the quadratic part of eq. (3.18) is thus omitted in the following, so that the evolution equation is approximated by

$$\begin{aligned} &\partial_\alpha \mathcal{I} \approx f'\,\psi_0 - \frac{\alpha}{c_E}\,f'\,\left[\operatorname{sign}(\alpha-\alpha_n) - \frac{\eta}{c_E}\,\frac{\alpha-\alpha_n}{\Delta t}\right] \ni 0 \\ \Leftrightarrow\quad &f'\,\psi_0 = \begin{cases} \dfrac{\alpha}{c_E}\,f'\,[-1,\,1] & \text{if } \alpha = \alpha_n \\ \dfrac{\alpha}{c_E}\,f'\,\left[\operatorname{sign}(\alpha-\alpha_n) + \eta\,\dfrac{\alpha-\alpha_n}{\Delta t}\right] & \text{else .} \end{cases} \end{aligned} \tag{3.19}$$

By combining (3.19) and constraint (2.78) the final form of the evolution equation results in

$$\alpha = \max\left(\alpha_n,\,\alpha^{\mathrm{tr}}\right) \quad \text{with} \quad \alpha^{\mathrm{tr}} = \frac{\alpha_n}{2} - \frac{\Delta t}{2\,\eta} + \sqrt{\left[\frac{\alpha_n}{2} - \frac{\Delta t}{2\,\eta}\right]^2 + \frac{\Delta t}{\eta}\,c_E\,\psi_0}\,. \tag{3.20}$$

The total energy predicted by this model follows as

$$\begin{aligned} E &= \int_{\mathcal{B}} \dot\psi + D\,\mathrm{d}t\,\mathrm{d}V = \int_{\mathcal{B}} \int_0^\infty \boldsymbol{\sigma} : \dot{\boldsymbol{\varepsilon}}\,\mathrm{d}t\,\mathrm{d}V + \int_{\mathcal{B}} \int_0^\infty \underbrace{[\partial_\alpha \psi + \partial_{\dot\alpha} D]}_{=0}\,\dot\alpha\,\mathrm{d}t\,\mathrm{d}V \\ &= \int_{\mathcal{B}} \int_0^\infty \boldsymbol{\sigma} : \dot{\boldsymbol{\varepsilon}}\,\mathrm{d}t\,\mathrm{d}V\,. \end{aligned} \tag{3.21}$$

3.3.2 Well-posedness of the viscous regularization

Focusing on an incremental step (see Subsec. 2.3.4), the analysis of matrices $\boldsymbol{A}$ and $\boldsymbol{G}_\Delta$ is sufficient to determine the well-posedness of the constitutive equations. Since the viscous regularization does not introduce a gradient dependence, matrix $\boldsymbol{G}_\Delta$ vanishes and only stationarity condition (2.68) has to be solved.

Clearly, the existence of a unique solution depends on the regularity of matrix $\boldsymbol{A}$, given for the one-dimensional case as

$$\boldsymbol{A}^{\text{vis}} = \begin{bmatrix} \bar{f}\, E & f'\, E\, \bar{\varepsilon} \\ \bar{f}'\, E\, \bar{\varepsilon} & -\dfrac{1}{c_E}\, \bar{f}' \left[1 + \dfrac{\eta}{\Delta t}\, [2\,\bar{\alpha} - \alpha_n]\right] \end{bmatrix} . \tag{3.22}$$

Here, the difference between matrix $\boldsymbol{A}^{\text{pro}}$ and $\boldsymbol{A}^{\text{vis}}$ is highlighted in gray color rendering the evolution equation of α time-dependent. A straightforward computation of the eigenvalues results in

$$\begin{aligned} \Lambda_{1,2}^{\text{vis}} &= f\, \hat{\Lambda}_{1,2}^{\text{vis}} \quad \text{with} \\ \hat{\Lambda}_{1,2}^{\text{vis}} &= \frac{c_E\, E\, \alpha_u + p\, \bar{\alpha}^{p-1} \left[1 + \dfrac{\eta}{\Delta t}\, [2\,\bar{\alpha} - \alpha_n]\right]}{2\, c_E\, \alpha_u} \\ &\quad \pm \sqrt{\begin{aligned} &\left[\frac{c_E\, E\, \alpha_u + p\, \bar{\alpha}^{p-1} \left[1 + \dfrac{\eta}{\Delta t}\, [2\,\bar{\alpha} - \alpha_n]\right]}{2\, c_E\, \alpha_u}\right]^2 \cdots \\ &\cdots - \frac{E\, p}{\alpha_u\, c_E}\, \bar{\alpha}^{p-1} \left[1 + \frac{\eta}{\Delta t}\, [2\,\bar{\alpha} - \alpha_n] - 2\, \frac{p}{\alpha_u}\, \bar{\alpha}^{p-1}\, c_E\, \bar{\psi}_0\right] \end{aligned}} . \end{aligned} \tag{3.23}$$

Again, the eigenvalue belonging to the evolution equation of α remains unconditionally positive. The sign of the eigenvalue belonging to ε depends on the time step Δt. It remains positive as long as

$$\begin{aligned} & 1 + \frac{\eta}{\Delta t}\, [2\,\bar{\alpha} - \alpha_n] - \frac{2\, c_E\, p}{\alpha_u}\, \bar{\alpha}^{p-1}\, \bar{\psi}_0 > 0 \\ \Leftrightarrow \quad & \Delta t < \eta\, \alpha_u\, \frac{2\,\bar{\alpha} - \alpha_n}{2\, c_E\, p\, \bar{\alpha}^{p-1}\, \bar{\psi}_0 - 1} \;=: \Delta t_{\text{crit}}. \end{aligned} \tag{3.24}$$

By the estimate of $2\,\bar{\alpha} - \bar{\alpha}_n > \bar{\alpha} > \alpha_0^{1/p}$ a lower bound for the critical time step can thus be specified as

$$\Delta t_{\text{crit}} > \frac{\eta\, \alpha_u}{2\, c_E\, p\, \bar{\psi}_0}\, \alpha_0^{[2-p]/p} , \tag{3.25}$$

since effective energy $\bar{\psi}_0$ is limited due to the boundary value problem. As a consequence, the viscous regularization guarantees well-posedness, if the time step is chosen smaller than the critical one.

Alternatively, the well-posedness is investigated according to Subsec. 2.3.3. Considering inelastic loading, the tangent follows as

$$\frac{\mathrm{d}^2\mathcal{I}}{\mathrm{d}\varepsilon^2} = \frac{\mathrm{d}\sigma}{\mathrm{d}\varepsilon} = f\,E\,\left[1 - \frac{\Delta t}{\eta}\,\psi_0\,\frac{p}{\alpha_u}\,\alpha^{p-1}\,\left[\left[\frac{\alpha_n}{2} - \frac{\Delta t}{2\,\eta}\right]^2 + \frac{\Delta t}{\eta}\,c_E\,\psi_0\right]^{1/2}\right]\,, \tag{3.26}$$

which converges for $\Delta t \to 0$ to

$$\lim_{\Delta t \to 0} \frac{\mathrm{d}\sigma}{\mathrm{d}\varepsilon} = f\,E > 0\,. \tag{3.27}$$

Since a lower bound for the time step is specified in eq. (3.25), the viscous example model is thus well-posed. Again, a detailed numerical analysis of the viscous regularization on the basis of the one-dimensional bar is given in appendix A.1. It highlights the numerical evolution of eigenvalues and eigenmodes.

3.4 Micromorphic gradient regularization

3.4.1 Fundamentals

The by now classic form of a gradient-enhanced continuum is

$$\psi = \psi^{\mathrm{loc}}(\boldsymbol{\varepsilon},\,\alpha) + \psi^{\mathrm{nloc}}(\nabla\alpha)\,, \quad \psi^{\mathrm{nloc}} = \frac{l_\alpha^2}{2}\,||\nabla\alpha||^2\,, \tag{3.28}$$

where the non-local energy contribution ψ^{nloc} is appended to Helmholtz energy (2.72) of the prototype model and where l_α is a model parameter which implicitly defines the length of the zone showing localized material damage. To be more precise, penalization of gradient $\nabla\alpha$ hinders localization into one element row. The neighboring elements also show softening behavior in order to flatten the gradient. This changes the structure of the underlying material model by shifting the evolution equations to the global/non-local level. Alternatively, a gradient regularization can be approximated in a micromorphic manner. By following *Forest* [54] and also *Dimitrijevic and Hackl* [48], the non-local Helmholtz energy contribution (3.28) is approximated as

$$\psi = \psi^{\mathrm{loc}}(\boldsymbol{\varepsilon},\,\alpha) + \psi^{\mathrm{nloc}}(\alpha,\,\varphi,\,\nabla\varphi)\,, \quad \psi^{\mathrm{nloc}} = \frac{c_\alpha}{2}\,[\varphi - \alpha]^2 + \frac{c_\alpha\,l_\alpha^2}{2}\,||\nabla\varphi||^2\,. \tag{3.29}$$

Internal variable α is coupled to additional global auxiliary field φ and the latter gradient is penalized instead. The evolution equation for α remains at the local level. If, furthermore, penalty parameter c_α is chosen as sufficiently large, φ converges towards α and energy (3.29) becomes a sound approximation of (3.28). The specific choice of prefactor $c_\alpha\,l_\alpha^2$ renders l_α a physical length and allows to adjust the localization width

and the penalty contribution independently.
Starting from the local prototype model, i.e., $D = D^{\mathrm{ri}}$, the micromorphic extension yields an incremental energy of the form

$$\mathcal{I} = f\,\psi_0 + \frac{c_\alpha}{2}\,[\varphi - \alpha]^2 + \frac{c_\alpha\,l_\alpha^2}{2}\,||\nabla\varphi||^2 - \psi_n - \int_{\alpha_n}^{\alpha_{n+1}} \frac{\alpha}{c_E}\,f'\,\mathrm{sign}(\alpha - \alpha_n)\,\mathrm{d}\alpha\,. \tag{3.30}$$

This extension does not alter any balance equations but the evolution equation. It is given by Biot's equation (2.57) as

$$f'\,\psi_0 - c_\alpha\,[\varphi - \alpha] = \frac{\alpha}{c_E}\,f' \begin{cases} [-1,\,1] & \text{if } \alpha = \alpha_n \\ \mathrm{sign}(\alpha - \alpha_n) & \text{else}\,. \end{cases} \tag{3.31}$$

By considering the second law of thermodynamics with an associated stress power of the type $\mathcal{P} = \boldsymbol{\sigma} : \dot{\boldsymbol{\varepsilon}} + \omega\,\dot{\varphi} + \boldsymbol{\Omega}\cdot\nabla\dot{\varphi}$, the dissipation inequality follows as

$$\int_{t_n}^{t_{n+1}} \mathcal{D}\,\mathrm{d}t = \int_{\alpha_n}^{\alpha_{n+1}} Y\,\mathrm{d}\alpha \geq 0 \tag{3.32}$$

with $Y = -\dfrac{\partial\psi}{\partial\alpha} = -f'\,\psi_0 + c_\alpha\,[\varphi - \alpha]$. A sufficiently large penalty parameter c_α enforces identity $\alpha \approx \varphi$ and, thus, dissipation inequality (3.32) is approximated by

$$\int_{t_n}^{t_{n+1}} \mathcal{D}\,\mathrm{d}t = \int_{\alpha_n}^{\alpha_{n+1}} \underbrace{-f'\,\psi_0}_{=Y^{\mathrm{loc}}}\,\mathrm{d}\alpha \geq 0\,. \tag{3.33}$$

This dissipation inequality is formally identical to the dissipation inequality of the underlying local prototype model and thus constraint $\alpha \geq \alpha_n$ has also to be complied with for the micromorphic gradient-enhanced model. Evolution equation (3.31) and constraint (3.32) are combined by means of Karush-Kuhn-Tucker-conditions with indicator function Φ as

$$\Phi = f'\,[\alpha - c_E\,\psi_0] + c_\alpha\,[\varphi - \alpha] \leq 0 \qquad \dot{\alpha} \geq 0 \qquad \Phi\,\dot{\alpha} = 0\,. \tag{3.34}$$

The system's total energy E will later be evaluated during post-processing and follows from the definition of Helmholtz energy (3.29) and dissipation function (2.73) as

$$E = \int_{\mathcal{B}} \int_0^\infty \dot{\psi} + D\,\mathrm{d}t\,\mathrm{d}V$$

$$= \int_{\mathcal{B}} \int_0^\infty \boldsymbol{\sigma} : \dot{\boldsymbol{\varepsilon}} \, \mathrm{d}t \, \mathrm{d}V + \underbrace{\int_{\mathcal{B}} \int_0^\infty \omega \, \dot{\varphi} + \boldsymbol{\Omega} \cdot \nabla \dot{\varphi} \, \mathrm{d}t \, \mathrm{d}V}_{=0} + \int_{\mathcal{B}} \int_0^\infty \underbrace{\left[\partial_\alpha \psi - f' \, \frac{\alpha}{c_E} \operatorname{sign}(\dot{\alpha}) \right]}_{=0} \dot{\alpha} \, \mathrm{d}t \, \mathrm{d}V$$

$$= \int_{\mathcal{B}} \int_0^\infty \boldsymbol{\sigma} : \dot{\boldsymbol{\varepsilon}} \, \mathrm{d}t \, \mathrm{d}V \tag{3.35}$$

3.4.2 Well-posedness of the micromorphic gradient regularization

The coefficient matrices of the quadratically approximated incremental potential (2.68) read, until reaching the point of ill-posedness,

$$\begin{aligned} \boldsymbol{A}^{\mathrm{mic}} &= \begin{bmatrix} \bar{f} \, E & -\bar{f}/\alpha_u \, E \, \bar{\varepsilon} & 0 \\ -\bar{f}/\alpha_u \, E \, \bar{\varepsilon} & \bar{f}/(c_E \, \alpha_u) + c_\alpha & -c_\alpha \\ 0 & -c_\alpha & c_\alpha \end{bmatrix}, \\ \boldsymbol{G}_\Delta &= \begin{bmatrix} 0 & 0 & 0 \\ 0 & 0 & 0 \\ 0 & 0 & -c_\alpha \, l_\alpha^2 \end{bmatrix}, \quad \boldsymbol{b}_{\mathrm{total}} = \begin{bmatrix} -\tilde{\sigma}^* \\ 0 \\ 0 \end{bmatrix}. \end{aligned} \tag{3.36}$$

Overbars ($\bar{\bullet}$) indicate values of the starting point of the incremental step while a tilde ($\tilde{\bullet}$) indicates the incremental difference. The differences compared to the underlying prototype model are highlighted in gray color.

A trivial solution to the micromorphic problem is exactly the solution of the local prototype model, as long as $\boldsymbol{A}^{\mathrm{mic}}$ is regular. More precisely speaking, $\boldsymbol{\Xi}^{\mathrm{mic}} = -\boldsymbol{A}^{\mathrm{mic}-1} \cdot \boldsymbol{b}_{\mathrm{total}}$ with $\varphi = \alpha = c_E \, \psi_0$. For the sake of simplicity, we assume the exponent $p = 1$ for the local prototype model. Also well-posedness of the local prototype model and its micromorphic regularization are equivalent in this case ($\det(\boldsymbol{A}^{\mathrm{pro}}) \neq 0 \Leftrightarrow \det(\boldsymbol{A}^{\mathrm{mic}}) \neq 0$).

The regularization now becomes effective at the point of ill-posedness. It appears for $\varepsilon = \sqrt{\alpha_u / [E \, c_E]} \Leftrightarrow \alpha = \alpha_u / 2$. We now focus on how the micromorphic regularization affects the evolution of the solution. We started from an initially homogeneous, uniaxial problem for the sake of illustration. At the onset of ill-posedness, the system attains $\varepsilon = \sigma^* / [f \, E]$, $\alpha = 1/2 \, c_E \, E \, \varepsilon^2$ and $\varphi = \alpha$. Neither $\boldsymbol{A}^{\mathrm{mic}}$ nor $\boldsymbol{G}_\Delta$ have full rank to allow for a classic solution, though. To find a solution, we have to split the problem. First, it can be shown that the upper part of the equation system applying to ε and α can be stated as

$$\boldsymbol{A}^{2\times 3} \cdot \tilde{\boldsymbol{\Xi}} + \boldsymbol{b}_{\mathrm{total}}^{2\times 1} = -\boldsymbol{G}_\Delta^{2\times 3} \cdot \Delta \tilde{\boldsymbol{\Xi}} = \boldsymbol{0}. \tag{3.37}$$

Moreover, the parameter $c_\alpha > 0$ of the gradient extension causes $\operatorname{rank}(\mathbf{A}^{2\times 3}) = \dim(\mathbf{b}_{\mathrm{total}}^{2\times 1}) = \dim(\varepsilon) + \dim(\alpha) = 2$. Given this equation system, there is thus a lin-

ear reformulation such that $\tilde{\varepsilon} = [\ldots]\,\tilde{\varphi}$ and $\tilde{\alpha} = [\ldots]\,\tilde{\varphi}$. The latter can be used to reformulate the last line of the first variation of the equilibrium condition as

$$\gamma\,\tilde{\varphi} + b_{\text{total},\varphi} - c_\alpha\,l_\alpha^2\,\Delta\tilde{\varphi} = 0\;, \tag{3.38}$$

where $b_{\text{total},\varphi}$ denotes the third component of $\boldsymbol{b}_{\text{total}}$. A one-dimensional stress σ^* results in the boundary condition term b being $b = \sigma^*\sqrt{\alpha_u\,c_E\,E}$. The value of γ is $\gamma = -c_\alpha^2\,\left[c_\alpha + \bar{f}\,\alpha_u^{-1}\,\left[c_E^{-1} - E\,\bar{\varepsilon}^2\,\alpha_u^{-1}\right]\right]^{-1}$ for a homogeneous state. As the state becomes heterogeneous once damage localization appears, extra terms add to γ due to the gradients at the damage region. The role of γ will thus be discussed after we clarified the requirements for the respective solution structure.

As an intermediate result regarding well-posedness is that the incremental micromorphic problem can be reduced to a second-order PDE of the auxiliary variable $\tilde{\varphi}$. According to the previous linear relationships, $\tilde{\varepsilon}$ and $\tilde{\alpha}$ can be back calculated. Finding a solution, nevertheless, still requires further reformulations and considerations. Notably, the problem description so far is still ill-posed as a substantial condition is yet missing, namely, localization. This becomes obvious by two properties of the mathematical structure. First of all, simply inserting the parameters of the softening state into the pure reformulation, i.e. performing the quadratic incremental approximation just around the softening point, yields $\gamma = 0 \;\Rightarrow\; \Delta\tilde{\varphi} = \text{const}$. Assuming homogeneous Neumann boundary conditions $\nabla\,\varphi = 0$, the solution only reaches $\varphi = \text{const}$. Damage localization as observed in experiments is clearly missing, rendering the solution unphysical. A second indicator for an unphysical solution is the lack of a unique position for damage localization.

To achieve a regularized localization we must further assume two things, in addition to the micromorphic regularization scheme. Firstly, an imperfection to uniquely locate the onset of damage localization and, secondly, a function space large enough to describe its shape. The imperfection can be artificially generated by a heterogeneous initial damage field or geometry, for instance. The description by piecewise solution functions is required mathematically, because a single function cannot solve the governing equation in this example, since $\gamma = 0$ and $\nabla\varphi = 0$ enforce a single function to remain spatially constant. Only a split into piecewise functions allows a localized damage progression. To be more precise, a split allows for a combination of trigonometric wave solutions with decaying exponential functions and for non-zero gradients at their transition points. This is well explained in the example found in [137], which provides an accessible (yet also extensive) analytical solution of a simpler problem. This split into piecewise functions can also be seen in phase-field problems, e.g., by a discontinuity in the non-zero gradient at the position of damage localization, cf. [110]. Non-academic examples typically do not show this particular need for triggering localization. Applying the regularization scheme suffices, because heterogeneity is usually given in more realistic problems.

Eventually, the piecewise solution for the increment of φ can be split into a particular solution and a harmonic one. The particular solution $\tilde{\varphi}_p$ can simply be a constant in this

example. The harmonic solution $\tilde{\varphi}_h$ adds the regularization property. By exploiting its harmonic nature with $\Delta\tilde{\varphi}_h = \lambda^2\tilde{\varphi}_h$, the incremental problem statement can be rewritten as

$$\underbrace{\left[\boldsymbol{A}^{\mathrm{mic}} + \begin{pmatrix} 0 & 0 & 0 \\ 0 & 0 & 0 \\ 0 & 0 & \gamma - c_\alpha\, l_\alpha^2\, \lambda^2 \end{pmatrix}\right]}_{\boldsymbol{A}_h^{\mathrm{mic}}} \cdot \begin{pmatrix} \tilde{\varepsilon} \\ \tilde{\alpha} \\ \tilde{\varphi}_h \end{pmatrix} + \boldsymbol{b}_{\mathrm{total}} = \boldsymbol{0} \tag{3.39}$$

which is well-posed. This can indeed be seen as a new, convex(ified) variational formulation of the harmonic micromorphic problem. In view of the elaborated derivations in [137] for an even simpler study, we omit a further detailed analytic discussion and refer to the illustrative example given therein. The two important conditions to make the problem finally well-posed – in addition to the micromorphic extension – are the introduction of an imperfection and giving up the previous assumption of a perfectly homogeneous problem. A detailed numerical analysis of the (harmonic) evolution of the eigenvalues and eigenmodes associated to the one-dimensional bar is given in appendix A.1.

3.5 Comparison of the regularization approaches

The variational approach allows the comparison of the three regularization concepts in a unified mathematical structure, see Tab. 3.2 for a summarized juxtaposition. By apply-

General Helmholtz energy	$\psi = f\,\psi_0 + \frac{c_\alpha}{2}\,[\varphi - \alpha]^2 + \frac{c_\alpha\, l_\alpha^2}{2}\,[\nabla\varphi \cdot \nabla\varphi]$	
General dissipation function	$D = -\frac{\alpha}{c_E}\, f'\,\left[\lvert\dot{\alpha}\rvert + \eta\,\dot{\alpha}^2\right]$	
	Material parameter	stress power
Local prototype	$\eta = 0,\ c_\alpha = 0$	$\mathcal{P} = \boldsymbol{\sigma} : \dot{\boldsymbol{\varepsilon}}$
Fracture energy	$\eta = 0,\ c_\alpha = 0$	$\mathcal{P} = \boldsymbol{\sigma} : \dot{\boldsymbol{\varepsilon}}$
Viscous regularization	$\eta > 0,\ c_\alpha = 0$	$\mathcal{P} = \boldsymbol{\sigma} : \dot{\boldsymbol{\varepsilon}}$
Gradient regularization	$\eta = 0,\ c_\alpha > 0$	$\mathcal{P} = \boldsymbol{\sigma} : \dot{\boldsymbol{\varepsilon}} + \omega\,\dot{\varphi} + \boldsymbol{\Omega} \cdot \nabla\boldsymbol{\varphi}$

Table 3.2: Generalized potential to obtain the three example models by different choices of material parameters.

ing a general Helmholtz energy and a general dissipation function, each regularization concept can be derived from a specific combination of material parameters η and c_α. The local prototype model is derived by choosing viscosity $\eta = 0$ and penalty parameter $c_\alpha = 0$ – as well as the model regularized with respect to the fracture energy. The model

becomes rate dependent by choosing penalty parameter $c_\alpha = 0$ and a viscosity $\eta > 0$. The internal variable is coupled to additional field φ by choosing penalty parameter c_α sufficiently large. Since the gradient of φ enters the constitutive behavior, the gradient of α also implicitly enters the constitutive behavior. Analogously, the well-posedness of the regularized models can be compared in terms of the localized incremental step, i.e., by comparing the matrices $\mathbf{A}$. They are given here again for the sake of readability as

$$\boldsymbol{A}^{\text{pro}} = \begin{bmatrix} \bar{f}\,E & \bar{f}'\,E\,\bar{\varepsilon} \\ \bar{f}'\,E\,\bar{\varepsilon} & -\dfrac{1}{c_E}\,\bar{f}' \end{bmatrix}, \qquad \boldsymbol{A}^{\text{vis}} = \begin{bmatrix} \bar{f}\,E & f'\,E\,\bar{\varepsilon} \\ \bar{f}'\,E\,\bar{\varepsilon} & -\dfrac{1}{c_E}\,\bar{f}'\left[1+\dfrac{\eta}{\Delta t}\,[2\,\bar{\alpha}-\alpha_n]\right] \end{bmatrix},$$

$$\boldsymbol{A}^{\text{mic}} = \begin{bmatrix} \bar{f}\,E & -\bar{f}/\alpha_u\,E\,\bar{\varepsilon} & 0 \\ -\bar{f}/\alpha_u\,E\,\bar{\varepsilon} & -\dfrac{1}{c_E}\,\bar{f}'+c_\alpha & -c_\alpha \\ 0 & -c_\alpha & c_\alpha+\gamma-c_\alpha\,l_\alpha^2\,\lambda^2 \end{bmatrix}. \tag{3.40}$$

It is clear that the example models contain the equations of the local models – only the parts highlighted in gray color are different. They belong to derivative $\partial_{\alpha\alpha}\mathcal{I}$, responsible for the evolution of internal variable α. Thus, both the viscous regularization and the micromorphic gradient regularization exclusively modify the evolution equation associated with internal variable α in order to render the model well-posed.

3.6 Numerical Results

The three regularization concepts are now examined numerically by two illustrative boundary value problems, a pre-cracked plate and an L-shaped specimen. The properties of interest cover, among others, mesh objectivity, fracture energy, unloading behavior, crack shape, computation time and transferability of model parameters to other boundary value problems.

3.6.1 Pre-cracked plate

Boundary value problem and numerical setup The pre-cracked plate has a height and a width of 500 mm, see Fig. 3.1. The initial crack is located on the left side with a length of 125 mm. A linearly distributed prescribed displacement $\bar{u}_{\max} = 0.01\,\text{mm}$ ($\dot{\bar{u}} = 0.01\,\text{mm}\,\text{s}^{-1}$) is applied to the top and bottom. The assumption of plane stress is made for each calculation, cf. appendix A.3. Starting from an initial mesh consisting of 16×16 elements, the area of interest is refined recursively. The two meshes after three and four refinements will be used for evaluation, Fig. 3.7. The model parameters are given in Tab. 3.3. The fracture energy is computed in a post-processing step for each element according to eq. 3.11 and summed up orthogonal to the emerging crack.

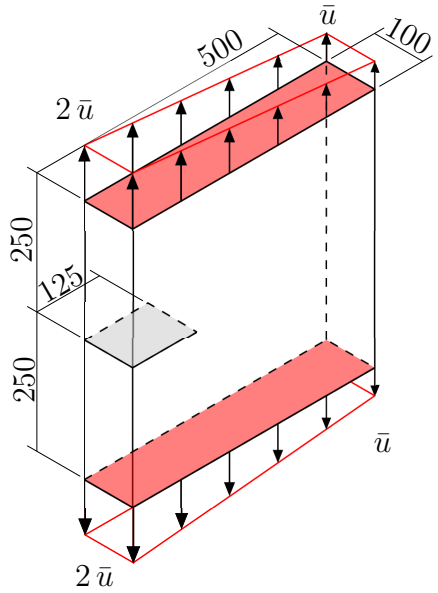

Figure 3.1: Pre-cracked plate: geometry and boundary conditions. Plane stress conditions are assumed. Homogeneous Neumann boundary conditions are assumed as far as the gradient-enhanced model is concerned.

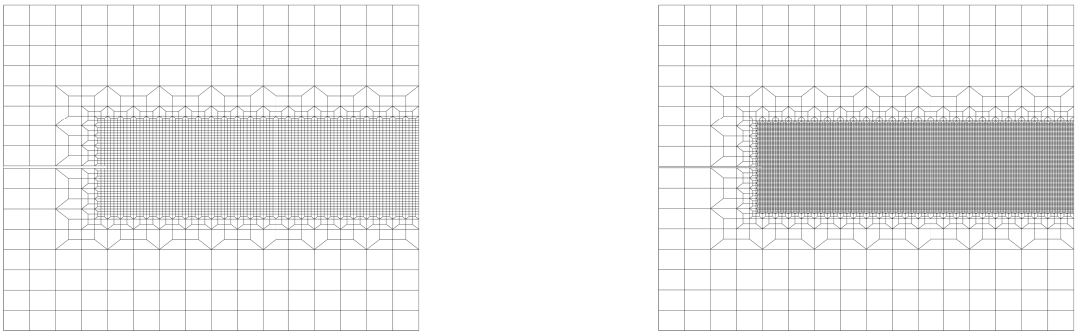

(a) 3 refinements – 4468 elements

(b) 4 refinements – 14936 elements

Figure 3.2: Pre-cracked plate: recursively refined discretizations.

Results and discussion The material parameters of the regularized models are chosen so that they match the same peak load and integrated fracture energy, to make comparability as fair as possible. Consequently, the parameters differ from model to model except for the elastic parameters.

As a first result, a simple transferability between the models is not available and the regularization of a model involves a subsequent parameter adjustment. Moreover, the fracture energy concept requires mesh-dependent material parameters. Here, only α_u needs to be adjusted for the selected prototype models, cf. Tab. 3.3. This is due to the

Name	Symbol	Value frac. eng.	Value visc.	Value micr.	Unit
Young's Modulus	E	21000	21000	21000	[MPa]
Poisson's ratio	ν	0.2	0.2	0.2	[–]
damage threshold	α_0	0.25	0.08	0.4	[MPa]
damage slope	α_u	0.055/0.066	0.072	1	[–]
damage exponent	p	0.125	0.5	1	[–]
energy scaling factor	c_E	0.75	500	20000	[–]
viscosity	η	—	2	—	[1/s]
penalty parameter	c_α	—	—	100	[MPa]
length parameter	l_α	—	—	0.1	[mm]

Table 3.3: Pre-cracked plate and L-shaped specimen: material parameters associated with the three example models.

fact that the crack emerges exclusively in the refined area. Apart from that, the loading behavior of the micromorphic model (Fig. 3.4 (c)) and of the prototype model (Fig. 3.4 (a)) agrees qualitatively and quantitatively. Both models show a fast softening behavior up to a load below 2 kN, where the load-displacement diagram shows a kink and slowly converges towards zero, as it is expected for degradation functions of exponential type. In contrast to the prototype model and the micromorphic example model, the viscous model (Fig. 3.4 (b)) does not show any change in the softening behavior caused by the exponential function. All three regularization methods eventually yield mesh-objective load-displacement diagrams.

The crack orientation also coincides in all simulations considering the distribution of degradation function f, cf. Fig. 3.3. The damage distribution for the fracture energy concept localizes into one element row. This behavior is neither observed for the viscous example model (Fig. 3.4 (b)) nor for the micromorphic example model (Fig. 3.4 (c)). Both show a mesh-independent crack width. However, the viscous example model shows a spatially varying crack width. This is due to the dependence of the model on the strain rate, which varies within the structure.

The fracture energy follows from the model-specific energy E and the corresponding fracture surface $A_c = l_c\, T$ with T being the thickness as

$$G_f = \frac{E}{A_c}\,. \tag{3.41}$$

The fracture energy concept shows a spatially constant fracture energy. This is expected as the material and numerical parameters have been adjusted accordingly. Also the micromorphic prototype model shows an (almost) constant fracture energy with deviations below 9%. The fracture energy predicted by the viscous prototype model, on the contrary, is far from constant. This unphysical influence is also caused by the heterogeneous

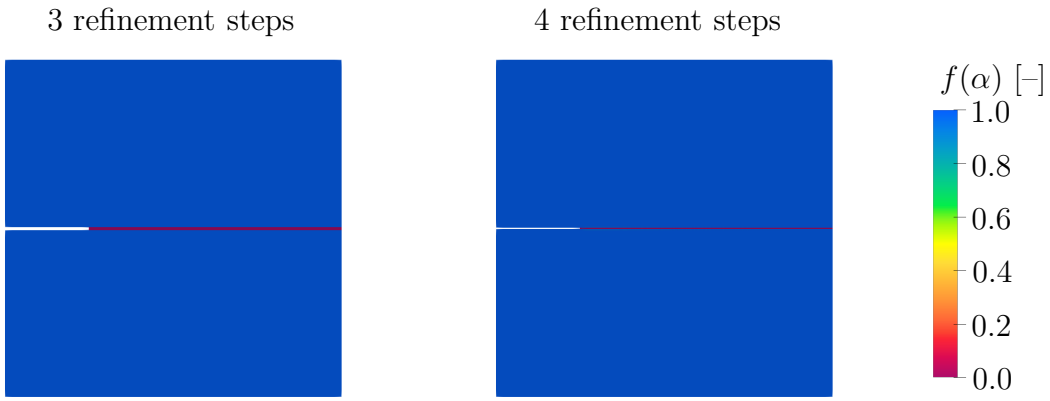

(a) Fracture energy concept

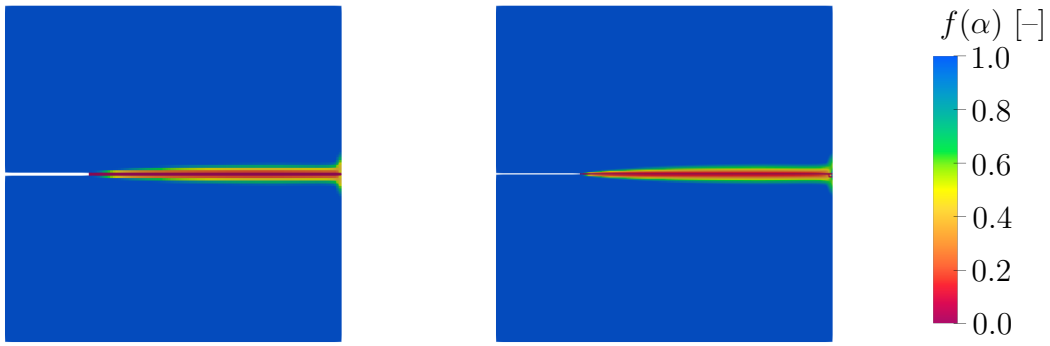

(b) Viscous regularization

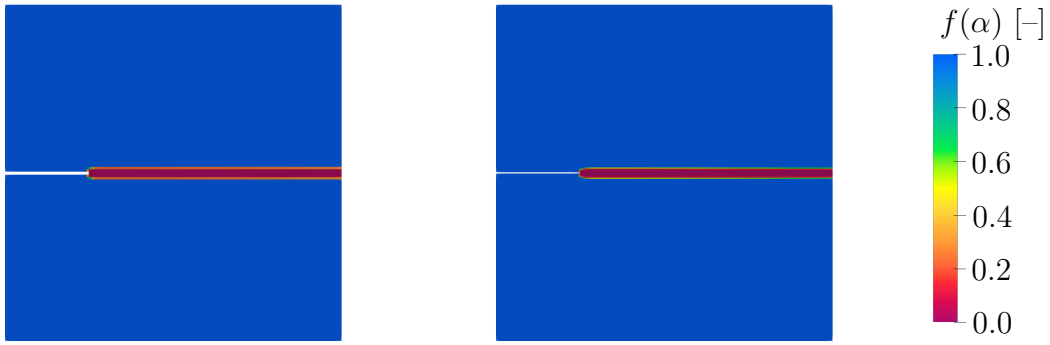

(c) Micromorphic gradient regularization

Figure 3.3: Pre-cracked plate: distribution of degradation function for the three example models and 3 and 4 recursive mesh refinements.

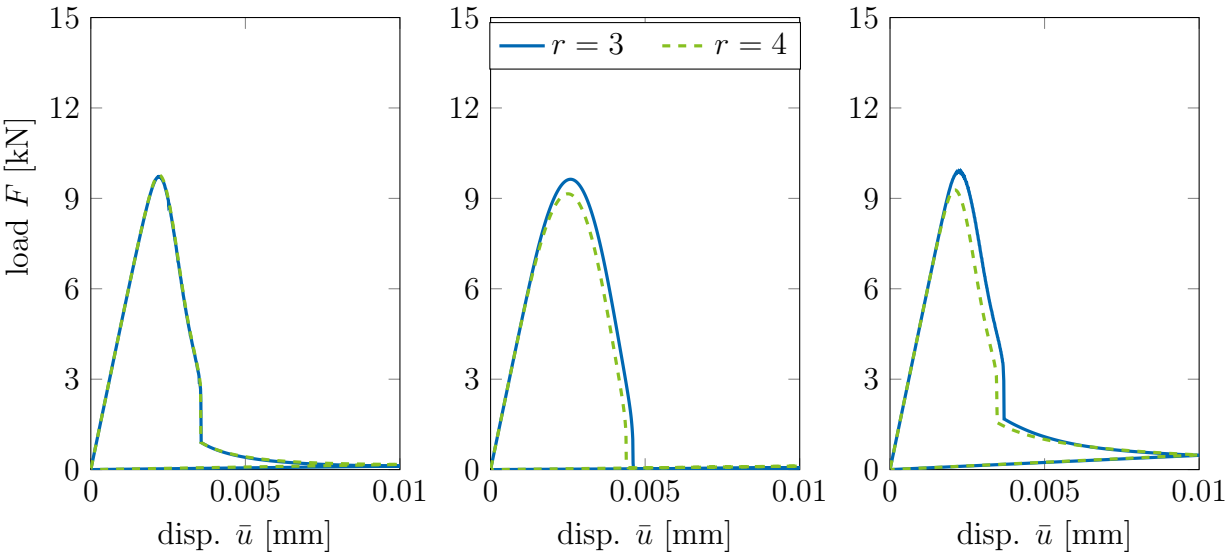

(a) Fracture energy concept **(b)** Viscous regularization **(c)** Micromorphic gradient regularization

Figure 3.4: Pre-cracked plate: load-displacement diagrams for the three example models.

strain rates within the structure, which already influenced the width of the emerging crack.

3.6.2 L-shaped plate

Boundary value problem and numerical setup The L-shaped plate is fixed at the top edge and loaded at the bottom right edge in vertical direction in dependence on prescribed displacement $\bar{u}_{\max} = 0.05\,\mathrm{mm}$ ($\dot{\bar{u}} = 0.05\,\mathrm{mm\,s^{-1}}$), Fig. 3.6. The assumption of plane stress has been made, cf. appendix A.3. Starting from the initial mesh with three regions of 8×8 elements each, the area of interest is refined recursively, see examples in Fig. 3.7. Compared to the previous example, two further mesh refinements have been studied due to higher sensitivity regarding mesh-dependence. The finest mesh consists of 54532 elements after six refinements. The material parameters have been adopted from Subsection 3.6.1, cf. Tab. 3.3.

Results and discussion A major difference is the unloading behavior of the viscous model (Fig. 3.8 (b)). While both the micromorphic example model (Fig. 3.8 (c)) and its local counterpart (Fig. 3.8 (a)) show purely linear elastic unloading, this is not the case for the viscous model. This is due to the introduced time dependence of the evolution equation, which leads to further evolution of damage even when the Helmholtz energy – the mechanical driving force of internal variable α, cf. (3.20) – decreases. Apart from

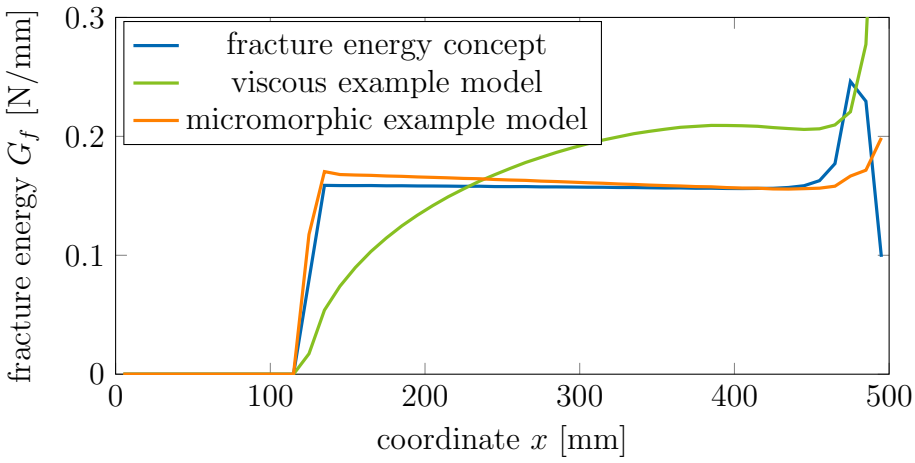

Figure 3.5: Pre-cracked plate: fracture energy of the propagating crack based on 4 recursive mesh refinements.

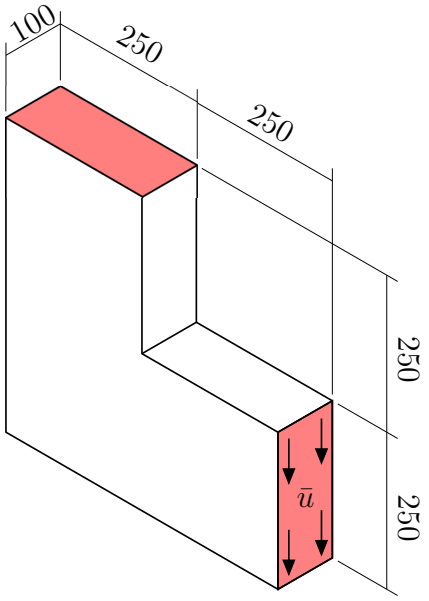

Figure 3.6: L-shaped specimen: geometry and boundary conditions. Plane stress conditions are assumed. Homogeneous Neumann boundary conditions are assumed as far as the gradient-enhanced model is concerned.

this, the findings regarding the load-displacement diagram agree with those observed in the previous example. The micromorphic regularization (Fig. 3.8 (c)) agrees qualitatively with its local counterpart (Fig. 3.8 (a)). However, the peak loads deviate by approximately 18%. A larger deviation of approximately 20% of the peak load is observed between the viscous and the local example model. The peak load of the viscous model is thereby strongly influenced by external loading rate $\dot{\bar{u}}$. Although being a mod-

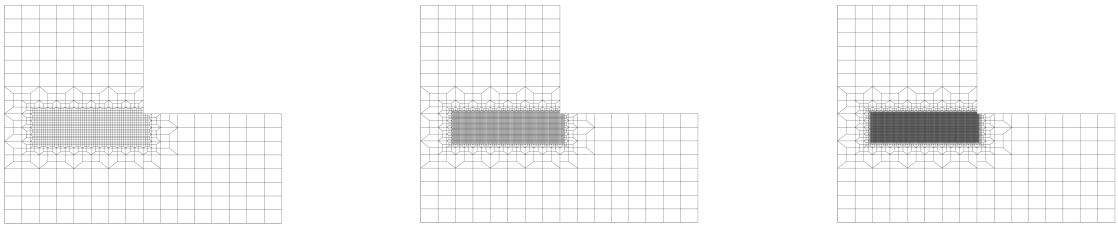

(a) 3 refinements – 1587 elements

(b) 4 refinements – 4558 elements

(c) 5 refinements – 15081 elements

Figure 3.7: L-shaped specimen: recursively refined discretizations.

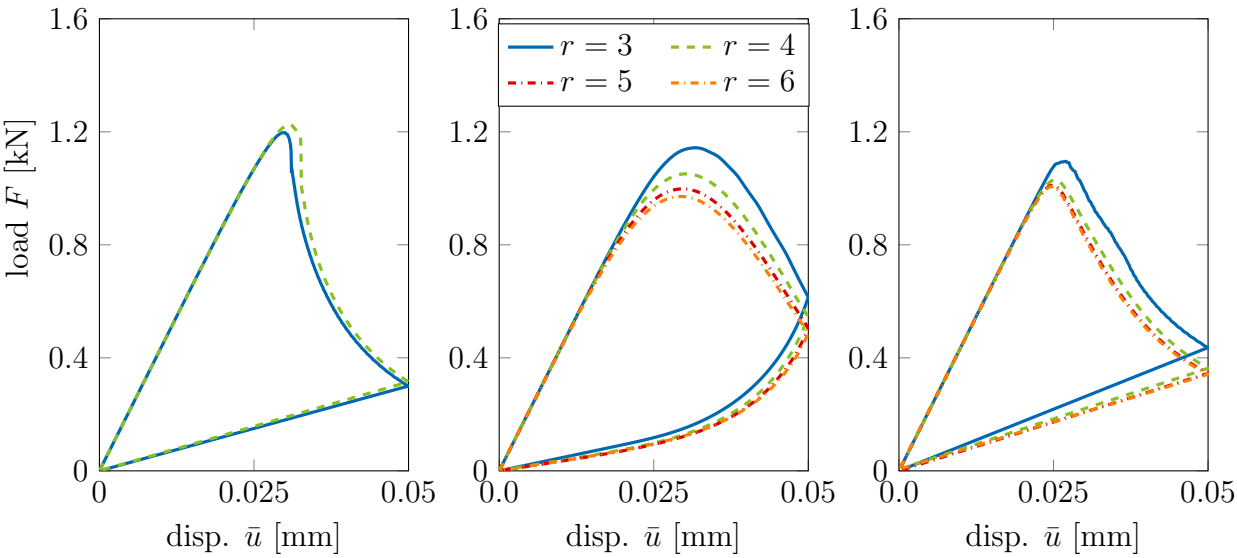

(a) Fracture energy concept

(b) Viscous regularization

(c) Micromorphic gradient regularization

Figure 3.8: L-shaped specimen: load-displacement diagrams for the three example models.

est deviation compared to other influences, it indicates the limited transferability of calibrated model parameters from one boundary value problem to the other. A possible explanation lies in the shape of the emerging cracks that may induce additional effects due to their curvature, see Fig. 3.9.

The regularization methods prove again that they can reliably provide mesh-objective results. Similar to the pre-cracked plate, the fracture energy concept results in a crack band width of one element, highlighting the ill-posed equations. Furthermore, the fracture energy concept yields an (almost) horizontal crack orientation. This is in significant contrast to the viscous regularization and the micromorphic regularization. Both show

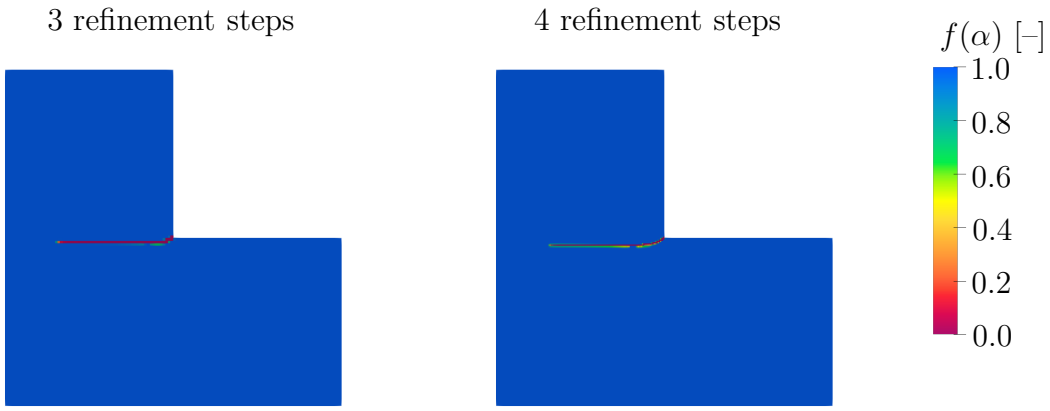

(a) Fracture energy concept

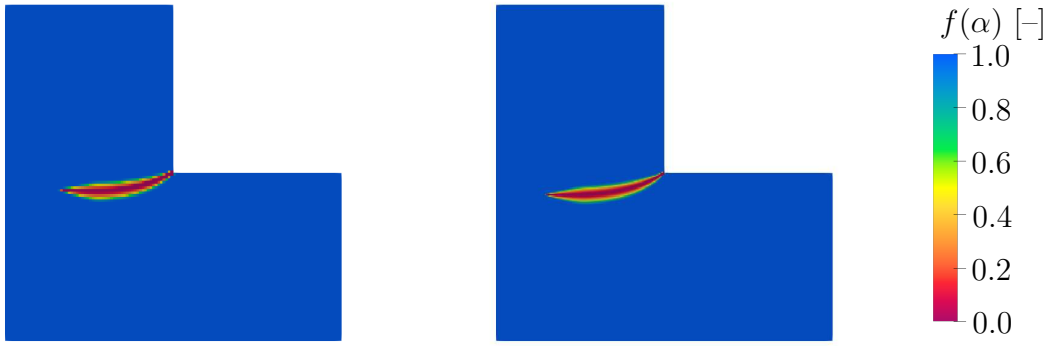

(b) Viscous regularization

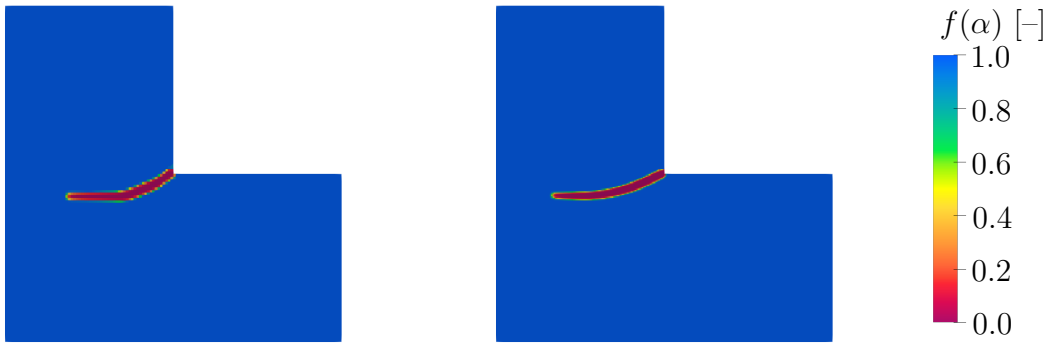

(c) Micromorphic gradient regularization

Figure 3.9: L-shaped specimen: distribution of degradation function for the three example models and 3 and 4 recursive mesh refinements.

a curved crack path as observed in experiments, cf. [184]. The viscous model, however, causes a varying crack thickness, indicating again the unphysical dependence on the heterogeneous strain rate within the structure.

3.6.3 Implications for predictions of (quasi-)brittle damage

In summary, all three regularization techniques provide mesh-objective load-displacement diagrams. Deviations for the presented examples can reach moderate amounts, though, such as 20% deviation regarding the peak load. The damage field is only mesh-objective for the viscous and the micromorphic regularization. Considering the fracture energy concept, the damage width is related to the underlying element aspect discretization and requires an adaption of material parameter α_u. Furthermore, the fracture energy concept also shows the least reproducibility of the crack path geometry as it does not accurately capture the curved crack for the L-shape problem, see also [119].

Further influences can be seen in the physical properties, e.g., the fracture energy, which is supposed to be constant for (quasi-)brittle materials. This only holds for the fracture energy concept, since the parameters are specifically chosen for that purpose. It is also almost constant for the micromorphic example model. If fracture energy is a key observation to be made, the viscous regularization shows the least accuracy. This is explained by the spatially heterogeneous strain rate distribution. The artificial viscosity moreover causes an unphysical crack width and inelastic unloading behavior. This may be of increased relevance when modeling fatigue.

Aiming for the least interference with the actual damage physics, the micromorphic regularization seems to be most promising. The numerical effort of the micromorphic example model, however, by far exceeds that of the other two example models. It is based on an additional global field and increases the system of equations by the number of nodes. In terms of the computation time the L-shaped specimen with four refinements times took $\sim$25 minutes for the fracture energy concept and the viscous regularization and $\sim$92 minutes for the micromorphic model. The fracture energy concept and the gradient model, moreover, would allow for further improvement by choosing much larger time steps during unloading. Note that the implementation effort of the micromorphic approach is increased due to the implicit form of its evolution equation. The restrictions of the fracture energy concept and the viscous regularization, on the other hand, require a substantial amount of cumbersome corrections to achieve the reliability of the micromorphic approach.

A Appendix

A.1 Numerical Analysis – One-dimensional bar

The present numerical framework highlights the damage evolution by monitoring the eigenvalues and the eigenmodes of the one-dimensional problem, respectively. The one-dimensional bar has a length of 20 mm, is fixed on the left side and loaded on the right side. The material parameters are taken from Tab. 3.3 and an imperfection in form of a lowered threshold value α_0 is applied at coordinate $x = 10\,\text{mm}$. The fracture energy concept shows a change of sign in the lowest eigenvalue at the onset of damage-induced softening, see Fig. 3.10 (a), where the eigenmode corresponding to the negative eigenvalue changes from a continuous mode (associated to the previous elastic domain) to a discontinuous mode (Fig. 3.10 (b)). This mode leads to a change of sign of the displacement field at the imperfection. Hence, it leads to a discontinuous displacement field and to a damage field, which localizes solely in the imperfect element.

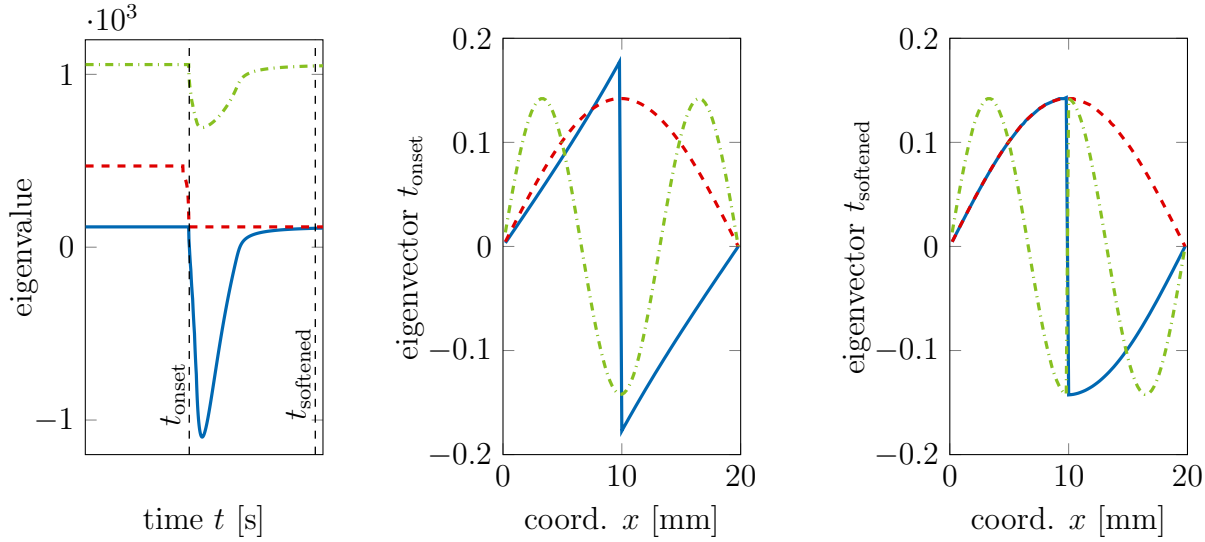

(a) Evolution of the lowest three eigenvalues

(b) Corresponding eigenmodes at t_{onset}

(c) Corresponding eigenmodes at t_{softened}

Figure 3.10: One-dimensional bar: fracture energy concept. Evolution of the lowest three eigenvalues and corresponding eigenmodes at the onset of softening and at a fully softened state.

The viscous example model shows a different behavior. The evolution of the eigenvalues and the corresponding eigenmodes are shown in Fig. 3.11. In contrast to the local model, no instantaneous changes of the eigenvalues and the corresponding eigenmodes is observed for the viscous example model. Furthermore, the eigenvalues decrease

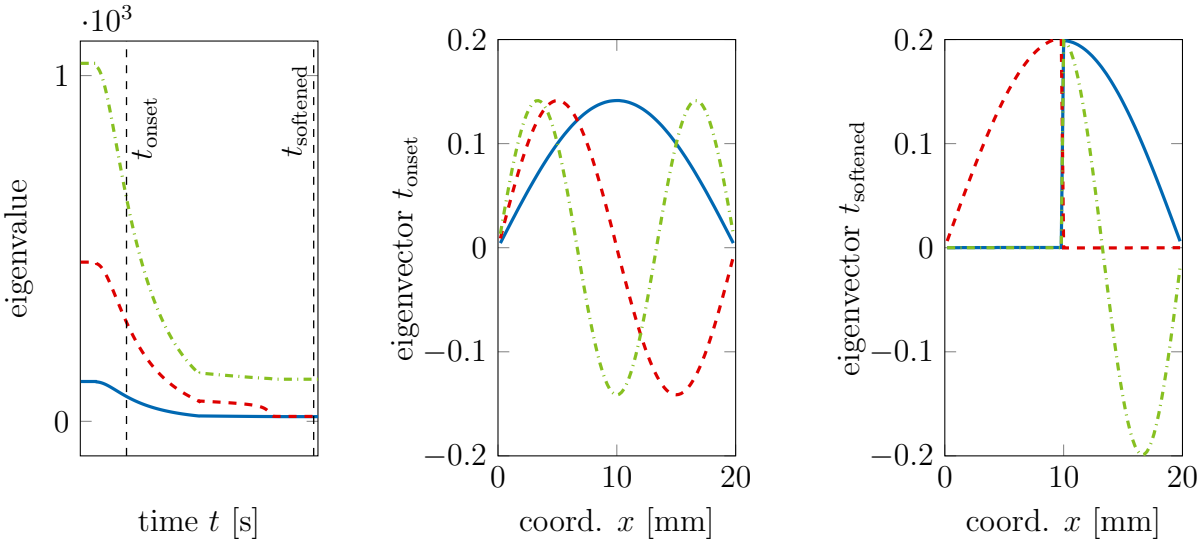

(a) Evolution of the lowest three eigenvalues

(b) Corresponding eigenmodes at t_{onset}

(c) Corresponding eigenmodes at t_{softened}

Figure 3.11: One-dimensional bar: viscous regularization. Evolution of the lowest three eigenvalues and corresponding eigenmodes at the onset of softening and at a fully softened state.

slowly towards zero (but remain positive) (Fig. 3.11 (a)), such that even at the onset of softening the eigenmodes (Fig. 3.11 (b)) are identical to those associated to the elastic region. Unfortunately, this is associated with a degradation of all elements of the one-dimensional bar. The eigenmodes develop a discontinuity at the imperfection with further decreasing eigenvalues. These discontinuities do not appear instantaneously (as for the local model), but continuously until they obtain the final form associated with a completely softened state, cf. Fig. 3.11 (c). At this state, almost all elements show identical material degradation. Only the imperfect element is softened a little further, where the difference between these values is dependent on the size of the applied imperfection.

The micromorphic example model shows again a different behavior, see Fig. 3.12. The eigenvalues decrease instantaneously at the onset of softening towards zero (but remain positive), cf. Fig. 3.12 (a). The eigenmodes associated with the displacement field at the onset of softening qualitatively agree with those for the elastic region and (more important) do not show any discontinuities (Fig. 3.12 (b)). Even at a fully softened state, Fig. 3.12 (c) does not show any discontinuities but a consistent localization width. Furthermore, the transition of the eigenmodes from those in Fig. 3.12 (b) to the ones in Fig. 3.12 (c) takes place in a continuous manner.

Well-posedness was investigated by means of the governing coefficient matrices and their eigenvalues. Within a finite element framework based on a Bubnov-Galerkin ansatz, pos-

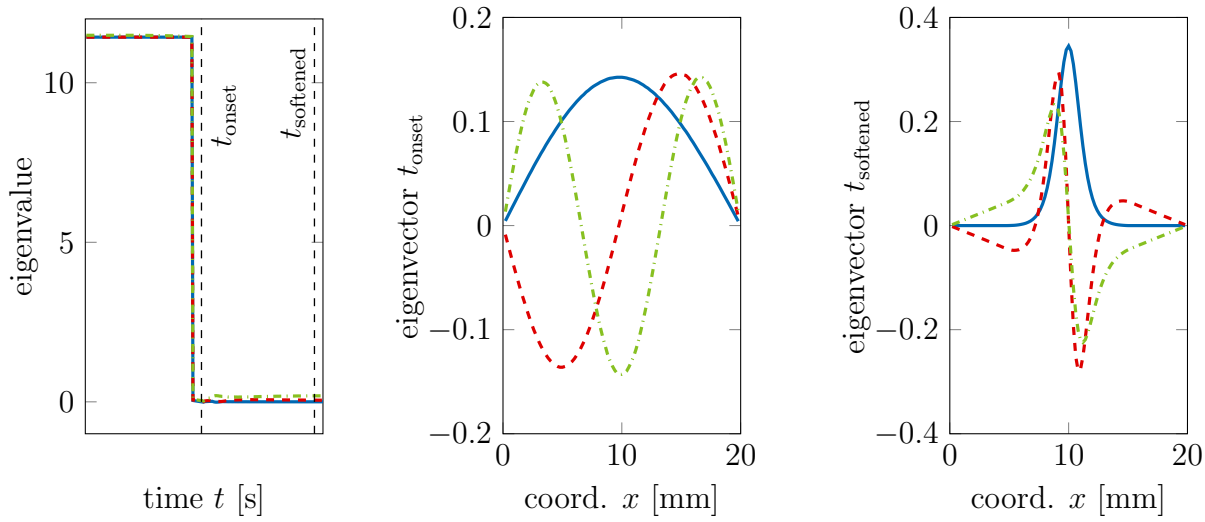

(a) Evolution of the lowest three eigenvalues

(b) Corresponding eigenmodes at t_{onset}

(c) Corresponding eigenmodes at t_{softened}

Figure 3.12: One-dimensional bar: micromorphic gradient regularization. Evolution of the lowest three eigenvalues and corresponding eigenmodes at the onset of softening and at a fully softened state.

itive eigenvalues of theses matrices result in positive eigenvalues of the stiffness matrix. Hence, the transition of the smallest eigenvalue of the local model from a positive to a negative sign highlights again the ill-posedness of this model – in contrast to the viscous and the micromorphic relaxed models for which the eigenvalues remain positive.

A.2 Difference between the time-continuous and the time-discrete variation

As shown in Section 3.3, the evolution equation for the time-continuous case has been further approximated. In order to quantify the difference, both evolution equations – the continuous one $\partial_{\dot{\alpha}} D\, \partial \dot{\alpha} = 0$ and the time discrete one $\partial_{\alpha} D\, \partial \alpha = 0$ – have been applied to a one-dimensional example. The error intrinsic to this approximation is numerically analyzed here. The material parameters have been chosen according to Table 3.3 and the strain rate is set to $\dot{\varepsilon} = 10^{-3}\,\mathrm{s}^{-1}$. The results are shown in terms of degradation function f (Fig. 3.13 (a)) and in terms of the relative difference with respect to the time-continuous variation (Fig. 3.13 (b)). The black graph provides the reference and corresponds to the time-continuous variation with a chosen time step of $\Delta t = 10^{-4}\,\mathrm{s}$. The blue, green and red graphs belong to the time-discrete counterpart and are calculated with different time steps. The evolution of degradation function f (Fig. 3.13 (a)) only differs marginally. According to Fig. 3.13 (b) the relative difference decreases with a decreasing time step. For a time step of $\Delta t = 10^{-3}\,\mathrm{s}$ the relative difference is below 1 %

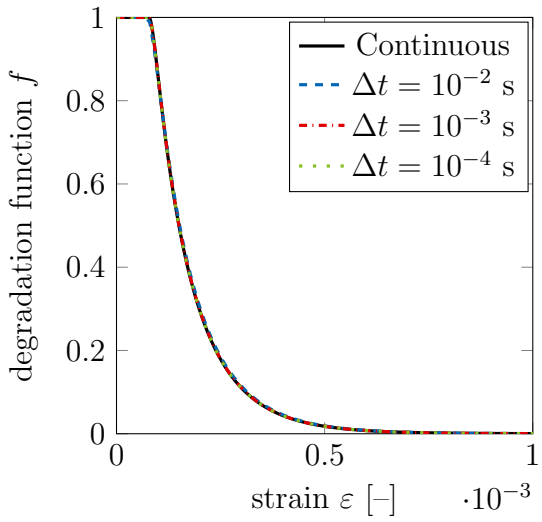

(a) Evolution of the degradation function f. Time discretization based on different time steps.

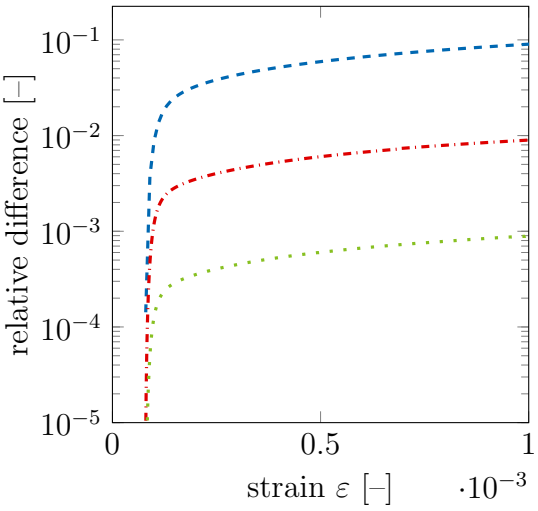

(b) Relative error of degradation function f with respect to the time-continuous evolution equation.

Figure 3.13: One-dimensional bar: viscous regularization. Time-continuous evolution equation vs time-discrete evolution equation.

and for a time step of $\Delta t = 10^{-4}\,\mathrm{s}$ even below 0.1 %. Thus, the time-discrete evolution equation indeed converges to the time-continuous one.

A.3 Plane stress element formulation – linearized theory

Oftentimes simulations are simplified by utilizing symmetries of the boundary value problems into the finite element formulation. An often made assumption when modeling components with large ratios between the cross-sectional area and the thickness is the assumption of plane stress. This means, that the stress connected to the thickness direction – here z – is assumed to be zero, such that the stress tensor reduces to two dimensions. Usually the strain components ε_{xx}, ε_{xy}, ε_{yx} and ε_{yy} are explicitly given on the local level. The remaining components of the strain tensor $\boldsymbol{\varepsilon}$ act as additional degrees of freedom. To be more precise, the equation

$$\{\sigma_{xz},\, \sigma_{yz},\, \sigma_{zx},\, \sigma_{zy},\, \sigma_{zz}\} = f\left(\varepsilon_{xz},\, \varepsilon_{yz},\, \varepsilon_{zx},\, \varepsilon_{zy},\, \varepsilon_{zz}\right) = \mathbf{0} \tag{3.42}$$

has to be solved. In general, this is connected to an additional iteration process on the local level. Dependent on the strain measurement, i.e., if $\boldsymbol{\varepsilon}$ is symmetric, eq. (3.42) may be reduced to three unknowns as

$$\{\sigma_{xz},\, \sigma_{yz},\, \sigma_{zz}\} = f\left(\varepsilon_{xz},\, \varepsilon_{yz},\, \varepsilon_{zz}\right) = \mathbf{0}\,. \tag{3.43}$$

If additionally the constitutive relations are isotropic, the shear stress only depends on the co-axial shear strain. Hence, $\sigma_{\bullet z} = 0$ is equivalent to $\varepsilon_{\bullet z} = 0$ and no longer needs to be considered in the local optimization process. The remaining equation is

$$\sigma_{zz} = f\left(\varepsilon_{zz}\right) = 0 \,. \tag{3.44}$$

Dependent on the constitutive relation this equation may be solved in closed format. For instance, when hooke's law is considered as the constitutive equation the stress component σ_{zz} is linearly dependent on the strain component ε_{zz} and the solution of eq. (3.44) is written as

$$\sigma_{zz} = \lambda \operatorname{tr}\left(\boldsymbol{\varepsilon}\right) + 2\,\mu\,\varepsilon_{zz} = 0 \quad \Leftrightarrow \quad \varepsilon_{zz} = -\frac{\lambda}{\lambda + 2\,\mu}\left[\varepsilon_{xx} + \varepsilon_{yy}\right] \tag{3.45}$$

with λ and μ being the Lamé parameter. Since ε_{zz} affects at least σ_{xx} and σ_{yy}, the tangent for a finite element implementation – meaning $\mathrm{d}_{\boldsymbol{\varepsilon}}\boldsymbol{\sigma}$ – is also affected. It may be computed by utilizing the chain rule as

$$\frac{\mathrm{d}\boldsymbol{\sigma}}{\mathrm{d}\boldsymbol{\varepsilon}} = \frac{\partial\boldsymbol{\sigma}}{\partial\boldsymbol{\varepsilon}} + \frac{\partial\boldsymbol{\sigma}}{\partial\varepsilon_{zz}} : \frac{\mathrm{d}\varepsilon_{zz}}{\mathrm{d}\boldsymbol{\varepsilon}} \,, \tag{3.46}$$

where the derivative $\mathrm{d}_{\boldsymbol{\varepsilon}}\varepsilon_{zz}$ is given in matrix format as

$$\frac{\mathrm{d}\varepsilon_{zz}}{\mathrm{d}\boldsymbol{\varepsilon}} = -\frac{\lambda}{\lambda + 2\,\mu}\begin{pmatrix} 1 & 0 & 0 \\ 0 & 1 & 0 \\ 0 & 0 & 0 \end{pmatrix} \,. \tag{3.47}$$

In the case that eq. (3.42) cannot be solved in closed format, the change in the tangent can also not be given in closed format. It can be computed utilizing the total variation of eq. (3.42), i.e., by solving

$$\mathrm{d}\left\{\sigma_{xz},\, \sigma_{yz},\, \sigma_{zx},\, \sigma_{zy},\, \sigma_{zz}\right\} = \mathbf{0} \tag{3.48}$$

and extracting the corresponding submatrix.

4 Curvature dependence of gradient continua

4.1 Motivation of gradient continua

Gradient models are nowadays frequently found in the literature. On the one hand, gradient models are used to capture physical phenomena, on the other hand, the gradient is incorporated into a model for the purpose of numerical regularization, i.e., in order to regularize local material models showing softening behavior.

4.1.1 Gradient and curvature-dependent models for physical phenomena

Representative examples for the consideration of gradient-based formulations are higher-order strain gradient theories [114, 164], e.g., bending of fibers in reinforced materials [11], generalized gradient continua [5], e.g., gradient plasticity [53, 152], homogenization of microstructures covering rotational degrees of freedom [124] and also topology optimization [13]. Phase-transition zones constitute another setting where gradient-enhanced models are used, e.g., to capture geometries and energies of interfaces [24, 69, 72], such as those between fluid and solid phases [116]. Band formations in metals [66], metallic glasses [82], granular media [20] and architected materials [34, 133] often involve instabilities and bifurcation and can be described by gradient-enhanced approaches, too.

Moreover, a multitude of different physical systems shows a combination of curvature (which can be captured by the second gradient) and gradient-related formulations. The design of microstructures with tailored effective properties can be dictated by curvature-driven evolution [183]. Another indication for the relevance of curvature on smaller scales is the delay of shear localization in metallic glasses [82]. A famous small-scale effect of curvature is also found for fluid-fluid interfaces. While surface tension induces curved shapes, it is usually considered invariant itself with respect to curvature on the

mm-scale. It nevertheless requires curvature corrections when reaching the scale of the so-called Tolman-length [178]. This is due to a change of the energy potential across interfaces that deviate from a perfect plane. Further curvature phenomena that are related to gradient-extensions or general regularization problems involve surface elasticity theories [32, 172], optimal image segmentation [78, 159] , signal processing [60] with applications to bio-medical systems [43], the regularity of solutions to partial differential equations of various physical problems [23, 49, 117, 142] and optimization in machine learning algorithms [135].

Curvature is also relevant in continuum damage mechanics. Notch curvature and void shape can already affect the nucleation and evolution of damage [177]. Complex stress states and geometry change under loading and interfere with curved damage paths. Fracture toughness can also depend on the sample size and shape or can interact with a heterogeneous microstructure [157]. Macroscopically observed curvature does not necessarily transfer to the microcurvature, though [125]. A curved crack path evolution can hence be a desired physical property in such situations.

4.1.2 Gradient models for numerical regularization

Another key motivation for gradient extensions is the ill-posedness of mere local models [17, 138, 167] as outlined in the previous chapter. A typical application of gradient-based models in solid mechanics is the description of brittle damage. The gradient extension then allows to control the localization width – independent with respect to the spatial discretization as far as numerics are concerned [52, 56, 80, 110]. A single curved crack can be observed, depending on the load case (Fig. 4.1(a)), while kinked or intersecting straight patterns are also possible. Ductile damage with plastic deformation can be captured by gradient-enhanced modeling from the typical component size [171] down to the scale of crystal plasticity [153]. A gradient-enhanced formulation accordingly adds one degree of freedom together with an extra material parameter. More specifically for one spatial dimension, the potential and the governing term in the corresponding stationarity condition are enhanced by the gradient as for instance shown in [48, 102], see also eq. (3.28) and (3.29):

$$\begin{array}{lll} \underline{\text{1d gradient :}} & \underline{\text{1d potential } \psi_{\text{grad}} \text{ :}} & \underline{\text{1d stationarity } \delta\psi_{\text{grad}} \text{ :}} \\ \nabla\varphi \text{ (scalar)} & \dfrac{l^2}{2}\left\|\nabla\varphi\right\|^2 = \dfrac{l^2}{2}\left(\nabla\varphi\nabla\varphi\right) & \dfrac{l^2}{2}\left(\nabla\nabla\varphi\right) \end{array} \tag{4.1}$$

The characteristic length of the gradient term, l, then typically relates to the crack width. Many pioneering and recent works indeed use this one-dimensional interpretation and prominent analytical solutions are then given in the form of exponential functions, see [110, 137] and Fig. 4.2 that sketches the conceptual idea of this chapter. The parameter l clearly dictates the length of the damage zone and regularizes ill-posed local models that would otherwise yield mesh-dependent results. This phenomenologi-

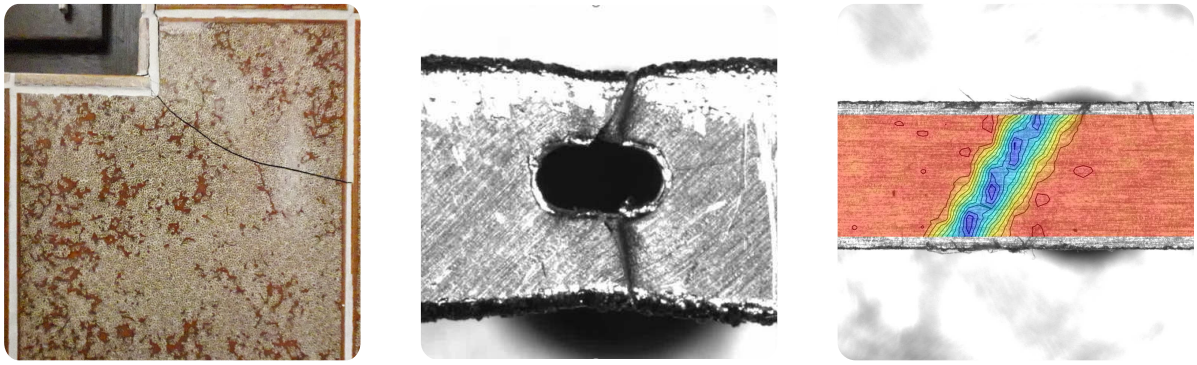

(a) Curved crack in a ceramic tile

(b) Ductile damage in aluminum

(c) Lüders band in aluminum

Figure 4.1: Selected mechanical systems with a length scale suitable for gradient regularization.

cal and illustrative approach is documented for a large class of gradient-based methods, including micromorphic implementations based on an auxiliary variable [48, 54] and phase-field models [56]. The typical exponential solution even motivated the choice of appropriate exponential shape functions [85]. While the one-dimensional analysis allows for a convenient physical interpretation and calibration, the naive extension to three dimensions induces a new side effect, namely, the influence of curvature. The sharp-interface limit, as known from Γ-convergence in phase-field models [115], can suppress a methodological curvature influence but is practically limited by the required numerical spatial resolution. Therefore, this often unintended side effect and its impact on the predicted physical behavior will be the very focus of this chapter. Taking a closer look on the responsible terms in three dimensions

$$\begin{array}{lll} \underline{\text{3d gradient :}} & \underline{\text{3d potential : } \psi^{\text{grd}}} & \underline{\text{3d stationarity : } \delta\psi^{\text{grd}}} \\ \nabla\varphi =: \|\nabla\varphi\|\,\boldsymbol{n}_\varphi & \dfrac{l^2}{2}\,\|\nabla\varphi\|^2 & \dfrac{l^2}{2}\,\underbrace{(\nabla\|\nabla\varphi\|)\cdot\boldsymbol{n}_\varphi}_{\overset{1d}{\to}\nabla\nabla\varphi} + \dfrac{l^2}{2}\,\|\nabla\varphi\|\,\underbrace{\operatorname{div}(\boldsymbol{n}_\varphi)}_{=:\,-2\,\kappa} \end{array} \tag{4.2}$$

shows that a new curvature influence arises from the spatial change of the normalized gradient direction ($\boldsymbol{n}_\varphi = \nabla\varphi/\|\nabla\varphi\|$). More specifically, the mean curvature is defined by half of its negative divergence, $\kappa = -\operatorname{div}(\boldsymbol{n}_\varphi)/2$. The new term superposes the initially intended regularization along the gradient direction, compare the two cases depicted in Fig 4.2. Needless to say, that these findings will also apply to two dimensions such as regularized contact lines embedded into a surface.

Despite the appearance and importance of curvature in selected applications, it is clearly considered an undesired methodological influence in the present context of gradient-enhanced models because of three reasons. Firstly, most gradient-based reg-

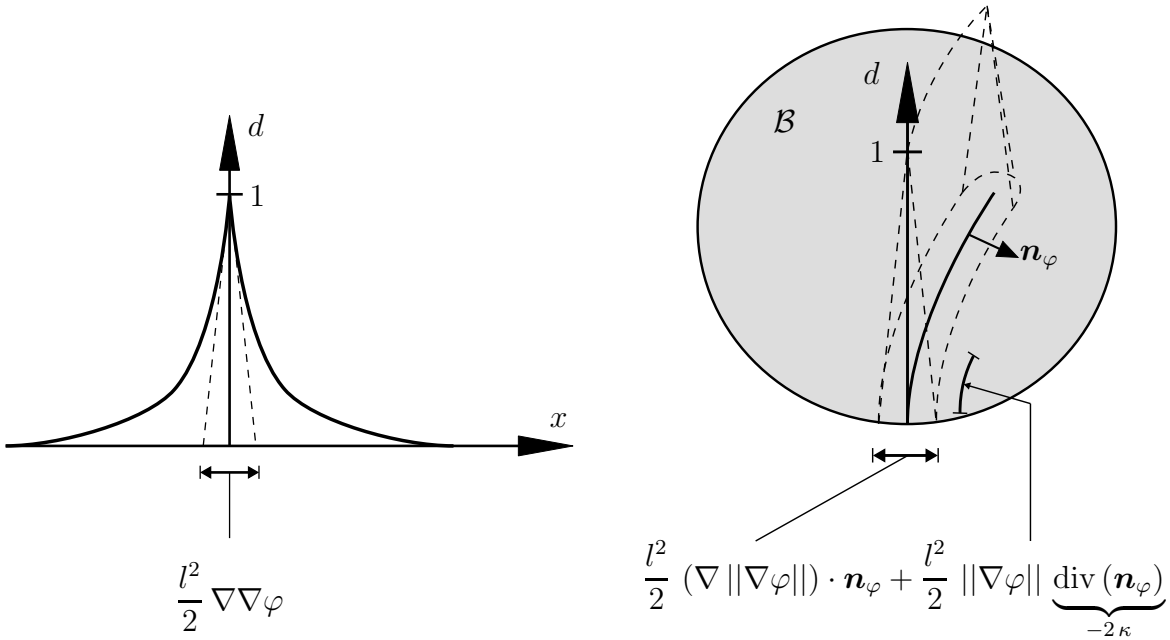

(a) One-dimensional gradient-enhancement **(b)** Three-dimensional gradient-enhancement

Figure 4.2: Length scales induced by one-dimensional (a) and three-dimensional (b) gradient-enhancement. Associated terms of the stationarity condition are connected by lines.

ularizations usually attempt to control only one of the two terms in (4.2). For example, they either determine the width of a damage zone [80] or capillary-induced curvature [45]. Secondly, the above mentioned physical influences of curvature usually differ from the restricted mathematical structure provided by the term ($||\nabla\varphi||^2$) or higher orders thereof [97]. For example, curved water droplets even originate from a more simple, constant interface energy [45, 86] and curved metallic surfaces can be affected by more complex, anisotropic surface properties [165]. Thirdly and most importantly, the curvature influence based on naive gradient-extension in three dimensions is coupled to the same material parameter l as the initial curvature-free regularization, which cannot be granted in most cases.

In conclusion, the methodological curvature influence that accompanies standard, three-dimensional gradient extensions can pose an unintended side effect in many situations. The intention of traditional models often relies on the control of the curvature-free regularization and a single length scale. The present work thus aims at opening a new view on this phenomenon by exploring the superposed curvature influence with the following questions

- When does the additional curvature term have significant influence?
- How does the curvature term influence the physical behavior?

It approaches these questions by a dimensional analysis followed by analytical and numerical examples with a focus on brittle fracture for illustration.

4.2 Dimensionless split

It may be helpful to first split the gradient extension and cast it into a dimensionless format to systematically address the role of the curvature term. For this reason, it is assumed that the problem is governed by a single characteristic length of the problem geometry, L_{prob}. It might be a characteristic width or a diameter. For the sake of simplicity, it is also assumed that a numerical method is characterized by a single mesh size L_{mesh} and that the variable φ is already made dimensionless into $\tilde{\varphi}$, e.g., a strain measure or a dimensionless damage variable. One may otherwise scale the gradient-enhanced equation by an appropriate inverse energy or the like.

The two terms of the three-dimensional gradient extension are split by assigning two individual material parameters, l_{reg} and l_{curv}, in order to highlight the curvature influence. They are associated with the regular, curvature-free term and the curvature-related term, respectively. The gradient extension can then be reformulated as

$$\begin{aligned} \frac{l^2}{2}\nabla\cdot\nabla\varphi \quad &\xrightarrow[\text{parameters}]{\text{split of}} \quad \frac{l_{\mathrm{reg}}^2}{2}\left(\nabla\|\nabla\varphi\|\right)\cdot\boldsymbol{n}_\varphi - l_{\mathrm{curv}}^2\,\|\nabla\varphi\|\,\kappa \\ &\xrightarrow[\text{format}]{\text{dimensionless}} \quad \frac{\Pi_{\mathrm{reg}}^2}{2}\left(\tilde{\nabla}\|\tilde{\nabla}\tilde{\varphi}\|\right)\cdot\boldsymbol{n}_\varphi - \Pi_{\mathrm{reg}}\,\Pi_{\mathrm{split}}\,\|\tilde{\nabla}\tilde{\varphi}\|\,\tilde{\kappa} \end{aligned} \tag{4.3}$$

with dimensionless parameters summarized in Tab. 4.1. Note that not all dimensionless parameters are independent of each other and are listed for comprehensibility. Alternative combinations and representations are furthermore possible.

The regular, curvature-free part of the gradient extension is weighted by the dimensionless number Π_{reg}. It determines the width of the gradient-regularized zone with respect to the overall specimen size. Brittle fracture models, for instance, tend to minimize this value for a sharp-crack limit, while maintaining a reasonable lower bound for $\Pi_{\mathrm{reg}}/\Pi_{\mathrm{mesh}}$ for sufficient spatial discretization. The curvature-free part is moreover dictated by the second spatial derivative of the gradient-enhanced variable, motivating the well-known exponential solutions in one dimension as explained above. The curvature-related part in the presented formulation is also weighted by Π_{reg} and additionally by factor Π_{split}. The special case $\Pi_{\mathrm{split}} = 1$ yields the traditional gradient extension with equal weighting of curvature-free and curvature-related terms. The curvature influence moreover scales with the amplitude of the first gradient, $\|\tilde{\nabla}\tilde{\varphi}\|$, and with curvature $\tilde{\kappa}$ itself. The role of the first gradient in this product becomes clearer by imagining a gradient in, e.g., damage, strain or phase concentration. The coupling with curvature then implies a change of orientation, e.g., a rotating concentration gradient. The combined product $(\|\tilde{\nabla}\tilde{\varphi}\|\,\tilde{\kappa})$ thus particularly accounts for localized concentration and is in close agreement with the small-scale observations described above, for instance, curvature de-

pendence of kinking or surface tension on smaller scales. Curvature fixed to that format, however, also constrains the options of controlling arbitrary curvature effects of different mathematical structure.

The dimensionless formulation lastly also reveals the restrictions of naive, three-dimensional gradient formulations from a numerical modeling perspective. Dimensionless curvature $\tilde{\kappa}$ becomes relevant as curvature κ approaches the length scale $l_{\mathrm{curv}} = l_{\mathrm{reg}}$ in standard gradient extensions. At the same time, it must not fall below the order of the mesh size in numerical simulations ($\Pi_{\mathrm{reg}}/\Pi_{\mathrm{mesh}} > 0$). Numerical control of the curvature term is accordingly limited by this lower bound.

In conclusion, the dimensionless split anticipates a physical interpretation and restrictions of the curvature-related term. The mathematical structure constrains the curvature influence to a fixed format and couples it to the regularization length parameter $l_{\mathrm{curv}} = l_{\mathrm{reg}}$. The need for sufficient numerical resolution poses a lower bound for this parameter. The following analytical example will explore the impact of two constraints by relaxing them, namely, eliminating the regularization length of the curvature term and avoiding a spatial discretization.

dimensionless parameter	expression	comment
$\tilde{\boldsymbol{x}}$	$\boldsymbol{x}/L_{\mathrm{prob}}$	dimensionless coordinate
$\tilde{\nabla}$	$L_{\mathrm{prob}}\,\nabla$	dimensionless gradient operator
$\tilde{\varphi}$	$\varphi/\ldots$	dimensionless variable of choice
$\tilde{\kappa}$	$l_{\mathrm{curv}}\,\kappa$	dimensionless curvature
Π_{reg}	$l_{\mathrm{reg}}/L_{\mathrm{prob}}$	curv.-free reg. length to geometry ratio
Π_{curv}	$l_{\mathrm{curv}}/L_{\mathrm{prob}}$	curv.-related reg. length to geometry ratio
Π_{split}	$l_{\mathrm{curv}}/l_{\mathrm{reg}}$	curv.-related over curvature-free reg. length
Π_{mesh}	$l_{\mathrm{mesh}}/L_{\mathrm{prob}}$	characteristic numerical mesh to geometry ratio

Table 4.1: Dimensionless variables and numbers of the gradient-enhanced terms.

4.3 Analytical example: quasi-brittle twisted cylinder

4.3.1 Problem statement

A twisted cylinder undergoing quasi-brittle damage will allow to quantify the influence of the curvature-related term analytically. The setting is based on the bifurcation analysis in [98], while the governing equations are adopted from [92] and [39]. Despite some necessary simplifications, the analytical solution benefits strongly from the fact that the results are independent of a numerical mesh size that could affect the regularization or the curvature resolution. A cylinder with radius R and length L is fixed at one end and twisted by angle γ on the other, see the sketch in Fig. 4.3. The focus lies

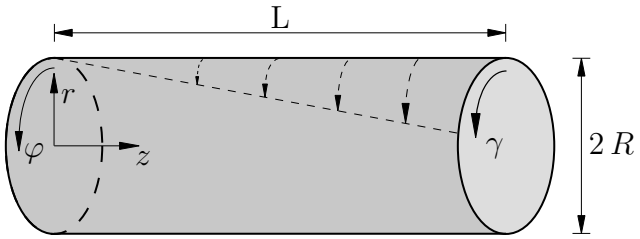

Figure 4.3: Quasi-brittle twisted cylinder: geometry and boundary conditions.

on the role of curvature during the onset of damage without further influences such as ultimate structural failure or bifurcation. The only characteristic length of the problem is R, because strain, stress and damage evolution will not change in axial direction. Length L will only implicitly enter a combined coefficient of the resulting equation. The constitutive relations are adopted from Section 3.4 and for the purpose of analytical ease of use slightly simplified. Thus, the material is linear elastic and isotropic with shear modulus μ. Quasi-brittle damage φ evolves immediately and proportional to the elastic energy ψ_0 with proportionality factor c_E. Degradation function f or integrity, respectively, declines linearly with damage φ. Tab. 4.2 provides an explicit summary of the relationships and assumptions. They can be finally combined into a single differential equation in terms of the damage variable $\varphi(r)$, reading

$$\varphi - l_{\text{reg}}^2 \frac{\partial^2 \varphi}{\partial r^2} - l_{\text{curv}}^2 \frac{\partial \varphi}{\partial r} \frac{1}{r} = c\, r^2 \quad \text{with } c = c_E\, \mu\, \frac{1}{2}\, \frac{\gamma^2}{L^2}, \tag{4.4a}$$

$$\frac{\partial \varphi}{\partial r} = 0 \qquad \text{at boundaries } r \in \{0,\, R\}. \tag{4.4b}$$

The curvature term becomes apparent by the factor $1/r$ and is accordingly scaled by the first spatial derivative of the damage variable. Note that $l_{\text{reg}} = l_{\text{curv}}$ for a traditional gradient extension while here l_{reg} drops independently to segregate the curvature influence. The boundary conditions of $\partial_r \varphi$ also apply only to gradient-enhanced models and are associated to their extra degree of freedom. The damage variable φ itself is implicitly linked to the boundary conditions of strain or stress, respectively.

4.3.2 Solution for local and gradient models with curvature modification

The solution to problem (4.4) shall be discussed for unit-free starting values of $l = l_{\text{reg}} = l_{\text{curv}} = c = R = 1$. For the damage model, this can be realized, for instance, by $l = l_{\text{reg}} = l_{\text{curv}} = 1$ [mm], c = 10^{-6} [Nm^{-4}] and $R = 1$ [mm] or by $l = l_{\text{reg}} = l_{\text{curv}} = 1$ [m], c = 1 [Nm^{-4}] and $R = 1$ [m]. The latter (more academic setting) allows omitting units for clarity in the following results without the need for scaling between [mm] and [m]. Also, this combination is a setting just between low and high sensitivity regarding

curvature influence. As a first variation, the three cases of the gradient-regularization length are distinguished: the pure local model, the traditional gradient extension and a gradient extension with suppressed curvature influence. Moreover, the radius of the twisted cylinder R is varied to study the influence of the specimen size. The analytical solution shall not only be visualized but first written out to allow a comparison of the mathematical structure (omitting units):

- local model without gradient extension ($l_{\mathrm{reg}} = 0$, $\Pi_{\mathrm{split}} = l_{\mathrm{curv}}/l_{\mathrm{reg}} = 1$):

$$\varphi = r^2 \tag{4.5}$$

- traditional gradient extension ($l_{\mathrm{reg}} = 1$, $\Pi_{\mathrm{split}} = l_{\mathrm{curv}}/l_{\mathrm{reg}} = 1$)

$$\begin{aligned}\varphi = \frac{J_0(ir)}{4\,J_1(iR)} i\pi[& - R^3 J_0(iR)Y_0(-iR) - 2R^3 J_1(iR)Y_1(-iR) \\ & + R^3 J_0(iR)Y_2(-iR) + R^3 Y_0(-iR)I_4(R) \\ & + 2iR^3 Y_1(-iR)I_3(R) - 4iR^2 J_1(iR)Y_0(-iR) \\ & - 2iR^2 J_0(iR)Y_1(-iR) + 8R^2 Y_0(-iR)I_3(R) \\ & + R^3 Y_0(-iR)I_2(R) - 4RJ_0(iR)Y_0(-iR)I_2(R) \\ & + 8RY_0(-iR)I_2(R) + 4iR^2 Y_1(-iR)I_2(R) \\ & + 2r^3 J_1(iR)Y_1(-ir) + 2ir^3 J_1(iR)Y_0(-ir)I_3(r)/J_0(ir) \\ & + 4ir^2 J_1(iR)Y_0(-ir) + 4ir^2 J_1(iR)Y_0(-ir)I_2(r)/J_0(ir) \\ & + 4RJ_0(iR)Y_0(-iR) - 8RJ_1(iR)Y_1(-iR) \\ & + 4RJ_0(iR)Y_2(-iR) - 8iJ_0(iR)Y_1(-iR) \\ & + 8rJ_1(iR)Y_1(-ir) + 8RJ_1(iR)Y_1(-iR)I_0(R) \\ & - 4RJ_0(iR)Y_2(-iR)I_0(R) + 2(R(R + 4iJ_1(iR)) \\ & - 4J_0(iR))Y_0(-iR)I_1(R) - 8irJ_1(iR)Y_0(-ir)I_1(r) \\ & + 8iJ_0(iR)Y_1(-iR)I_0(R) - 8rJ_1(iR)Y_1(-ir)I_0(r) \quad].\end{aligned} \tag{4.6}$$

This solution was obtained using the computer algebra system [1]. J_n is the Bessel function of the first kind, Y_n is the Bessel function of the second kind, I_n is the modified Bessel function of the first kind and $i = \sqrt{-1}$. Also note that $r \geq 0$, the material parameters are assumed to be strictly positive and some settings may lead to (unphysical) imaginary parts that have been neglected in the present case.

- gradient-extension with suppressed curvature influence ($l_{\mathrm{reg}} = 1$, $\Pi_{\mathrm{split}} = l_{\mathrm{curv}}/l_{\mathrm{reg}} = 0$):

$$\varphi = 2 + r^2 + 2R\frac{e^R}{1 - e^{2R}}\left[e^r + e^{-r}\right] \tag{4.7}$$

type	original	reduced to brittle cylinder	comments and simplifications
kinematics	$\boldsymbol{\varepsilon} = \left[\nabla \boldsymbol{u} + \nabla^T \boldsymbol{u}\right]/2$	$\varepsilon := \varepsilon_{z\theta} = \varepsilon_{\theta z} = \partial_z u/2$	only circumferential $u =: u_\theta$
			symmetry yields $\varepsilon = \varepsilon(r)$
damage variable	φ	$\varphi = \varphi(\varepsilon(r))$	no healing $\dot{\varphi} \geq 0$
local rate potential	$\dot{\mathcal{I}} = \dot{\psi} + D$		stationarity dictates $\delta\dot{\mathcal{I}} = 0$
Helmholtz energy	$\psi = f\,\psi_0 + l^2\,\|\|\nabla\varphi\|\|^2/2$		
dissipation	$D = -\partial_\varphi f\,\varphi\,\|\dot{\varphi}\|/c_E$		
linear-isotropic elasticity	$\psi_0 = \frac{1}{2}\lambda\,(\mathrm{tr}\boldsymbol{\varepsilon})^2 + \mu\,\boldsymbol{\varepsilon} : \boldsymbol{\varepsilon}$		λ, μ Lamé parameters
stresses	$\boldsymbol{\sigma} = f\,\boldsymbol{\sigma}_0 = f\,\partial_{\boldsymbol{\varepsilon}}\psi_0$	$\sigma_{z\varphi} = \sigma_{\varphi z} = f\,\mu\,\partial_z u$	$\nabla f \cdot \boldsymbol{\sigma}_0 = \boldsymbol{0}$
linear degradation	$f(\varphi) = 1 - c_E\,\varphi$	$f = f(r) \in [0,1]$	$\partial_z f = 0$, no damage threshold
momentum balance	$\mathrm{div}\,(\boldsymbol{\sigma}) = \boldsymbol{0}$	$u_{,zz} = 0$	$\rightarrow u = h(r)\,z + g(r)$, from $\delta_{\boldsymbol{u}}\dot{\mathcal{I}} = 0$
damage evolution	$\varphi - l^2 \mathrm{div}\,(\nabla\varphi) = c_E\,\psi_0(\boldsymbol{\varepsilon})$		from $\delta_{\dot{\varphi}}\dot{\mathcal{I}} = 0$
boundary conditions		$u = 0$, $u_r = u_z = 0$	$z = 0 \rightarrow g(r) = 0$
		$u = \gamma\,r$, $u_r = u_z = 0$	$z = L \rightarrow h(r) = \gamma\,r/L$
		$\boldsymbol{\sigma} \cdot \boldsymbol{n} = \boldsymbol{0}$	$r = R \cup z = L$
		$\nabla\varphi \cdot \boldsymbol{n} = 0$	$r = R \cup z \in \{0,\, L\}$
		$\partial_r \varphi = 0$	$r = 0$ (avoid singularity of $\partial_r\varphi$)

Table 4.2: Quasi-brittle twisted cylinder: governing equations and simplifications. The central equation is the damage evolution, in which the simplifications and $\psi_0(\varepsilon(u(h(r))))$ are combined.

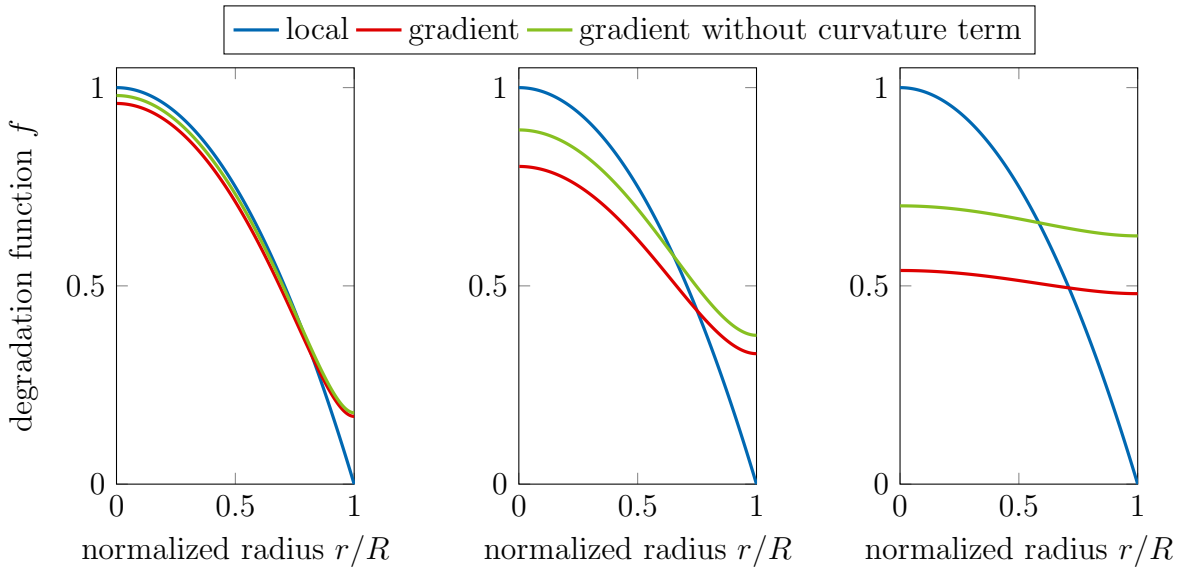

(a) $\Pi_{\text{reg}} = l/R = 0.1$ **(b)** $\Pi_{\text{reg}} = l/R = 0.25$ **(c)** $\Pi_{\text{reg}} = l/R = 1$

Figure 4.4: Quasi-brittle twisted cylinder: damage distribution for different ratios Π^{reg} and three models.

It becomes obvious from the solution formulas that the traditional gradient extension does not provide the exponential damage distribution as expected from the one-dimensional, phenomenological interpretation (see eq. (4.6)). This underlines the introductory motivation of this work that the curvature influence indeed breaks the convenient physical interpretation. Only removing the curvature term allows for the well-known exponential damage distribution (see eq. (4.7)). From a quantitative perspective, all solutions are close if the ratio of regularization length to cylinder radius is small ($\Pi_{\text{reg}} \ll 1$), see Fig. 4.4. The local solution differs the most from the gradient-enhanced models on the outer boundary, because it naturally does not enforce a vanishing gradient there. The relative deviation between the traditional gradient extension and its curvature-free modification ($\Pi_{\text{split}} = 1$ vs $\Pi_{\text{split}} = 0$) is largest at the center of the cylinder (-50 % damage without curvature influence) and smallest at its boundary (-1 %). It must nevertheless be noted, that the relatively large deviation in the center corresponds to a small absolute difference (only twice as large as compared to the boundary).

Curvature becomes a dominant influence as soon as the regularization length approaches the specimen size, cf. the middle and right graph in Fig. 4.4. While the local model keeps its shape with a mere scaling of the damage values, the gradient-enhanced approaches flatten out and deviate more from another. In case of equal characteristic lengths ($\Pi_{\text{reg}} = 1$), elimination of the curvature term results in less damage, -35 % at the center and -28 % at the boundary. This significant deviation continues for smaller radii of the quasi-brittle cylinder.

Processes with regularization gradients comparable to the geometry size, e.g. nucleation processes or microstructural interaction, are hence highly susceptible to the observed methodological curvature influence. Although this influence weakens on larger scales, it can remain relevant where accuracy is of importance, e.g., calibration or bifurcating fracture paths. Also, reaching the sometimes desirable sharp-interface limit ($\Pi_{\mathrm{reg}} \to 0$) may be restricted numerically due to higher computational costs. It therefore requires careful control, whether and how curvature shall influence the physical behavior predicted by the model. Given these general theoretical findings, the numerical examples will now continue with insights for more specific and complex geometries and loading conditions.

4.4 Numerical examples

The following examples assess the role of curvature by the example of regularized quasi-brittle damage in systems of increasing complexity. For that purpose, first the origin of the curvature dependence in the constitutive equations of both gradient damage models the micromorphic gradient damage model 3.4 and the phase-field model 2.4.2 is highlighted.

4.4.1 Curvature dependence of gradient damage models

The starting point is the analysis of balance of micro forces (2.55). Its mathematical structure is similar for the micromorphic and the phase-field description, despite its different origin in Helmholtz energy and dissipation, respectively. Both descriptions show different prefactors, though, which will be combined by means of generalized length parameter $l^\bullet$ (micromorphic model: $l^\bullet = c_\alpha\, l_\alpha^2$, phase-field model: $l^\bullet = g_c\, l_\varphi$). The multiplicative split of $\boldsymbol{\Omega}$ into its absolute value and its direction

$$\boldsymbol{\Omega} = l^\bullet\, \nabla\varphi = l^\bullet\, ||\nabla\varphi||\, \boldsymbol{n}_\varphi \tag{4.8}$$

allows to reformulate the balance of micro forces as

$$\begin{aligned} \int_{\mathcal{B}} l^\bullet \underbrace{\Big[\boldsymbol{n}_\varphi \cdot \nabla\, ||\nabla\varphi|| + \underbrace{\operatorname{div}(\boldsymbol{n}_\varphi)}_{-2\,\kappa}\, ||\nabla\varphi|| \Big]}_{\operatorname{div}(\boldsymbol{\Omega})} \delta\varphi \,\mathrm{d}V - \int_{\mathcal{B}} \omega\, \delta\varphi \,\mathrm{d}V \\ = \int_{\partial\mathcal{B}} l^\bullet\, ||\nabla\varphi||\, \boldsymbol{n}_\varphi \cdot \boldsymbol{n}\, \delta\varphi \,\mathrm{d}V\ . \end{aligned} \tag{4.9}$$

Accordingly, both approaches also share a similar role of the additional influence of curvature κ. If and how this influence appears in specific boundary value problems will be visualized and quantified by the subsequent examples.

4.4.2 Radial stretch of a disc

Problem focus The radial stretch of a disc (Fig. 4.5) constitutes a valuable testing case for the start, because damage initiates at the outer boundary. The associated curvature is thus naturally determined by the disc radius R. The latter is the key variation of this example. This opens the possibility to review whether and how the characteristic curvature $1/R$ interacts with regularization length $l^\bullet$, for both the micromorphic and the phase-field prototype model. The fracture energy G_f is the key parameter of interest to be extracted from the simulations. It relates the system's total energy E in eqs. (2.88) and (3.35) to the fracture surface A_c. This energy used to create the fracture surface is supposed to be a material constant but not a priori fixed by the model's parameters. It will hence be processed from the simulation output and reviewed with respect to potential curvature-related biases. For the radial-symmetric problem with thickness t, the fracture energy reads

$$G_f = \frac{E}{A_c} = \frac{1}{2\,\pi\,R\,t} \int_0^t \int_0^R \int_0^{2\,\pi} \int_0^\infty \boldsymbol{\sigma} : \dot{\boldsymbol{\varepsilon}}\, r \,\mathrm{d}t \,\mathrm{d}\theta \,\mathrm{d}r \,\mathrm{d}z = \frac{1}{R} \int_0^R \int_0^\infty \boldsymbol{\sigma} : \dot{\boldsymbol{\varepsilon}} \,\mathrm{d}t \, r \,\mathrm{d}r \,. \tag{4.10}$$

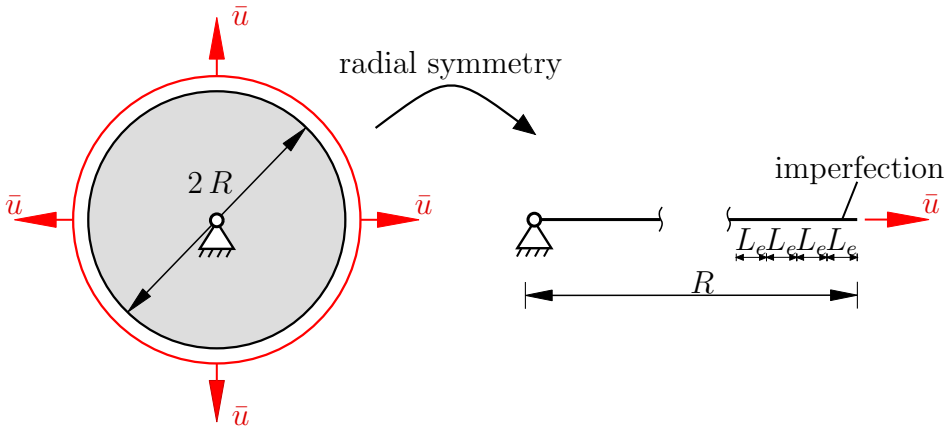

Figure 4.5: Radial stretch of a disc: geometry, boundary conditions and discretization.

Numerical setup The disc is loaded in radial direction along the surface and fixed at its center. The surface displacement $\bar{u}$ is increased up to 0.04 mm and withdrawn thereafter. Due to the symmetry of the system, the calculations are reduced to the one-dimensional case as shown in Fig. 4.5. The disc radius R varies between 15 mm and 100 mm, while the elements' length L_e in the softening zone is fixed at 0.05 mm for numerical comparability. The damage threshold α_0 of the outermost element is reduced by 10 % to trigger localization. Further material parameters are given in Tab. 4.3 for the micromorphic framework and in Tab. 4.4 for the phase-field framework.

Name	Symbol	Unit	Value Stretched disc	Value L-shape
Young's Modulus	E	[MPa]	21000	21000
Poisson's ratio	ν	[–]	0.2	0.2
residual stiffness factor	c_0	[–]	10^{-7}	10^{-7}
damage threshold	α_0	[MPa]	0.4	0.4
damage slope	α_u	[–]	0.5	1
energy scaling factor	c_E	[–]	200	20000
penalty parameter	c_α	[MPa]	100	100
regularization length	l_α	[mm]	0.1	varying

Table 4.3: Radial stretch of a disc: material parameters associated with the micromorphic gradient damage model.

Name	Symbol	Unit	Value Stretched disc	Value Pre-cracked strip
Young's Modulus	E	[MPa]	21000	21000
Poisson's ratio	ν	[–]	0.2	0.2
residual stiffness factor	c_0	[–]	10^{-7}	10^{-7}
damage threshold	$\mathcal{H}_0$	[MPa]	0.05	0.0
crit. energy release rate	g_c	[N/mm]	0.2	0.2
regularization length	l_φ	[mm]	2	varying

Table 4.4: Radial stretch of a disc: material parameters associated with the phase-field model.

The solutions are determined by a finite-element implementation with linear shape functions for both the displacement field and the micromorphic field. The radial symmetry has been accounted for by an axisymmetric element formulation (see Appendix F.1) and the observed snap-back behavior is captured through an arc-length method [42] (see Appendix B.1). The fracture energy G_f is one parameter of interest to be extracted from the simulations by integration of the resulting stress-strain relation in each element. The damage distribution is additionally characterized by the damage width that is defined here by a degradation cutoff of $f < 0.95$. Note that interface integrals along the circumferential direction benefit from utilizing radial symmetry as they are determined analytically and independent of numerical, spatial discretization.

Results and discussion The fracture energy, being a key property in quasi-brittle damage, and the damage distribution converge for large radii, Fig. 4.6. This behavior matches the previous dimensionless and the analytical analysis as the disc size becomes much larger than the regularization length. The maximum radius analyzed is 100 mm and compares to a regularization length scale of $l_\alpha = 0.1$ mm (micromorphic) and 2 mm

(phase-field), respectively. The convergence observed for larger systems is desired, e.g. for benchmarking, considering the role of fracture energy as a material constant that is supposed to be independent of specimen size and shape. For small radii, however,

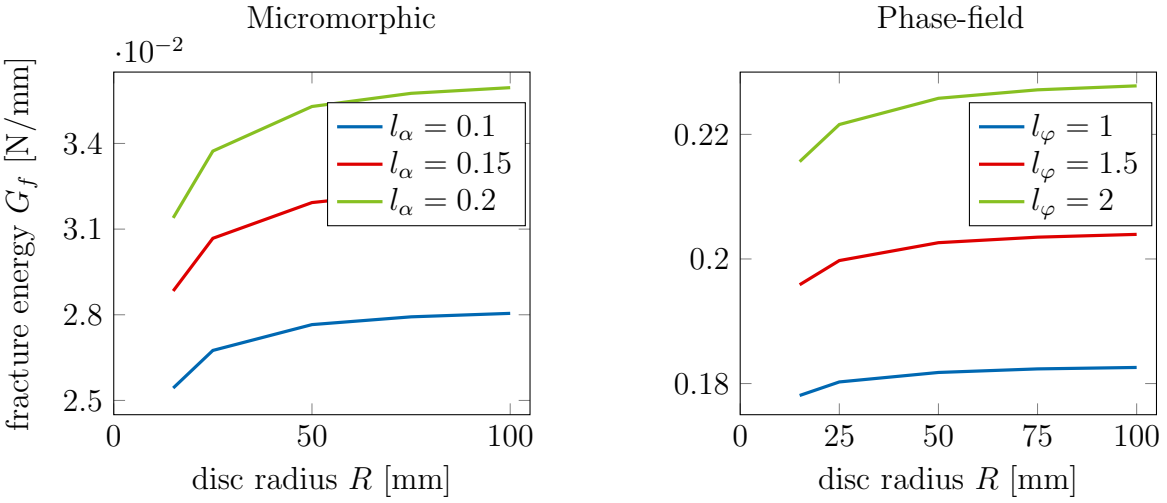

(a) Fracture energy for varying radii

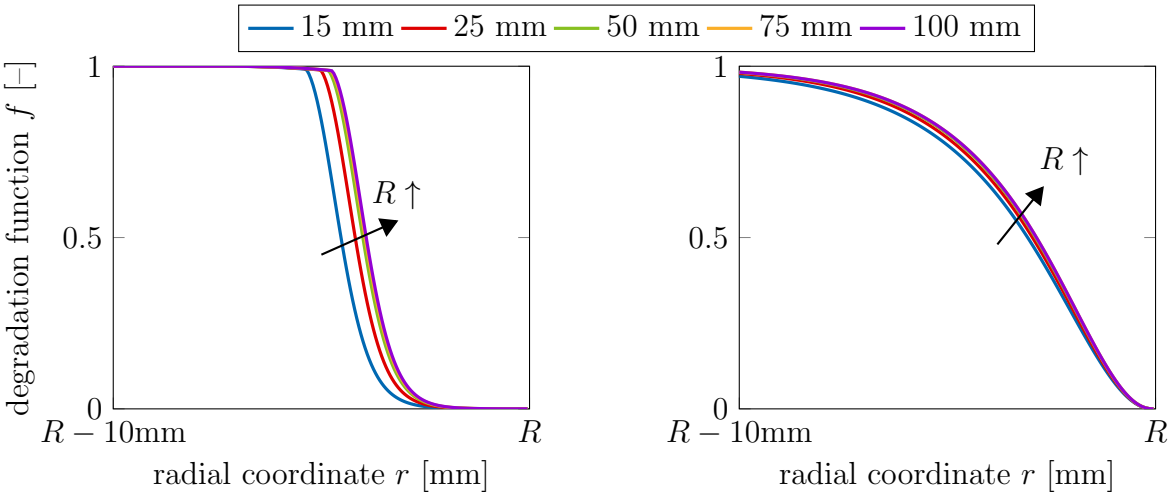

(b) Degradation function for varying radii

Figure 4.6: Radial stretch of a disc: micromorphic gradient damage model and phase-field model. Fracture energy and degradation function at the outermost 10 mm.

the fracture energy and the damage distribution deviate from their large-scale plateau. Reducing the disc radius from 100 mm to 15 mm, the damage width increases by more than 10 % (11.6 % micromorphic, 10.4 % phase-field), while maintaining the shape qualitatively. Turning the view towards the fracture energy, smaller-sized bodies are weaker in micromorphic simulations. The back-calculated fracture energy is reduced by 5.8 %, which is clearly an undesired effect for a material parameter. Even worse, this influence is

reversed in the phase-field predictions. The same size reduction increases the resistance against quasi-brittle damage now by raising fracture energy by 4.1 %. These observations clearly demonstrate that the influence of the disc's curvature prevents a physically sound interpretation once the problem size approaches the regularization length – or even an order of magnitude larger. Other geometrical influences are excluded by limitation to a single physical length scale. Numerical comparability is moreover given by utilizing radial symmetry and identical meshing in the damage zone. In addition, the impact is inconsistent between the micromorphic and the phase-field approach and thus requires appropriate consideration when curvature effects become relevant.

4.4.3 L-Shape

Problem focus The L-Shape is a well-proven system for evaluating quasi-brittle damage models [184] and shall be reanalyzed for more detailed assessment of the micromorphic prototype model, see Fig. 3.6. It provides three practical extensions compared to the disc system above. Firstly, it allows a free crack path inside the body. Secondly, damage is initiated by a stress singularity at the bend. Thirdly, the size of the L-Shape turns the view towards macroscopic problems with higher relevance for practical applications. For that reason, the specimen size will remain constant, while the regularization length will be varied. The response of major interest now becomes the curvature of the evolving damage zone.

Numerical setup The L-shaped specimen is fixed at the top and loaded in vertical direction at the lower outer face by displacement $\bar{u}$. Plane stress conditions are assumed and homogeneous Neumann boundary conditions are employed with respect to the micromorphic auxiliary variable. The finite element simulations have been performed with linear shape functions and a monolithic solution strategy. The underlying mesh consists of 10651 elements, which are mainly located in the damage-prone area. The material parameters are given in Tab. 4.3. They are closely based on the values used for the disc setup and slightly modified to achieve immediate softening and best comparability of the respective parameter studies.

The parameter of interest, l_α, is varied, while all remaining parameters are kept constant. The numerical results are given in terms of the distribution of degradation function f. More specifically, a circle is fitted to the evolving crack path and its curvature is compared for different regularization lengths. This has been done through an analytical calculation of the radius and the center point in dependence on the most-left, the central and the most-right coordinate of the crack path. Subsequently, by means of a least-square minimization, the final radius and the final center point were calculated with respect to all coordinates of the crack path.

Results and discussion All regularization lengths show the expected curved crack pattern with different crack widths, Fig. 4.7 (a)-(c). The different regularization lengths

also result in different peak loads, which range between 917 N and 1248 N, Fig. 4.7 (d). This behavior is known and documented, for instance, in [80].

Upon closer examination of the new aspect, the curvatures of the cracks also clearly change as highlighted in Fig. 4.7 (e). As far as this prototype model is representative for the micromorphic regularization, the curvature is implicitly connected to the numerical width of the emerging crack. A larger regularization length penalizes a curved damage evolution, which also agrees well with the mathematical formulation and the split of the curvature-related term before. The smallest regularization length allows for the largest curvature of the initial crack path ($0.0042\,\mathrm{mm}^{-1}$ for $l_\alpha^2 = 0.005\,\mathrm{mm}^2$). The largest regularization length reduces the curvature by almost 25 % ($0.003\,\mathrm{mm}^{-1}$ for $l_\alpha^2 = 0.03\,\mathrm{mm}^2$). As one result, the cracks propagate on paths that are clearly distinguishable on a macroscopic basis and may be critical for sensitive environments that require accurate predictions.

While this standard example clearly indicates the impact of a classic micromorphic regularization on the crack's curvature, the influence of the curvature term is likely superposed by further influences. The crack width itself can alter the stress field and the follower load differs due to the different peaks in the load-displacement progression. These may be further influences on the curvature of the crack path that cannot be simply eliminated. Therefore, the next numerical example directly dictates the crack path evolution by a fixed hole and constantly oriented boundary conditions.

4.4.4 Punched and precracked strip

Problem focus A punched and precracked strip connects the previous examples by allowing a free damage evolution yet governing the starting and end point of the crack, Fig. 4.8. The strip is pulled apart (out of plane) and damage will initiate at the tip of the pre-crack. The crack propagates downwards and can eventually deviate once it interferes with the stress field around the punched hole. This problem is found to be a well-proven benchmark for phase-field models and adopted from [9] and [59]. The response of the present phase-field prototype model is investigated for various regularization lengths.

Numerical setup The two halves of the top boundary are sheared out-of-plane with a prescribed displacement. All other boundaries are stress-free in the basis example adopted from literature references. As the punched hole does not always interact with the damage field, depending on the numerical parameters, a second setup with a fixed bottom which forces the crack to deviate is investigated. Plane stress conditions are assumed and homogeneous Neumann boundary conditions are employed with respect to the phase-field auxiliary variable. The material parameters are given in Tab. 4.4.

The phase-field model has been implemented based on linear shape function, where the resulting system of equations has been solved in a staggered manner.

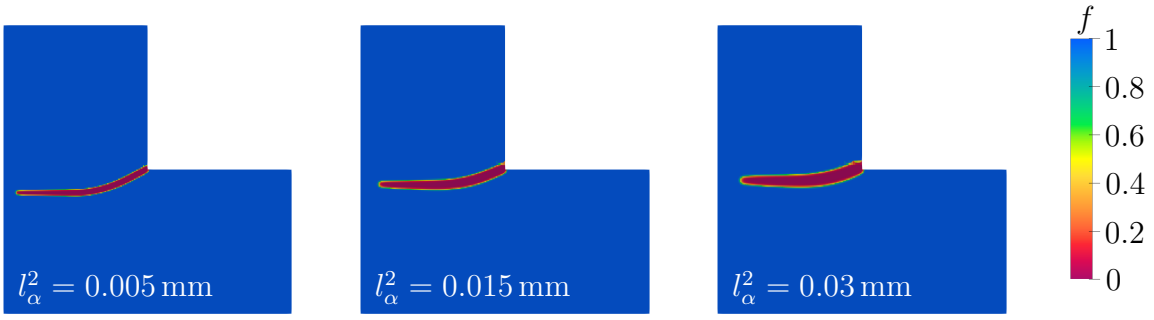

(a) Distribution of the degradation function

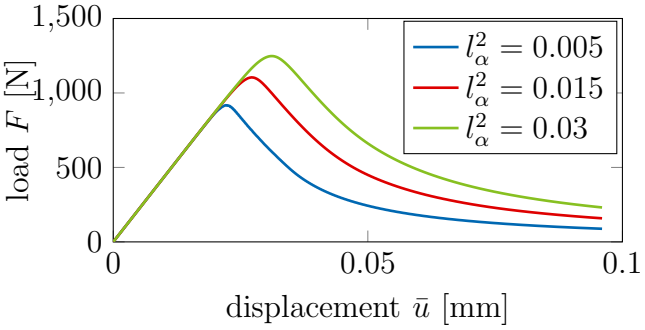

(b) Load-displacement diagrams

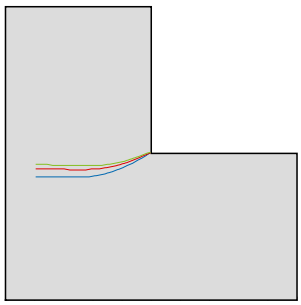

(c) Central crack path

Figure 4.7: L-shaped specimen: micromorphic gradient damage model. Degradation function, load-displacement diagrams and central crack patch for varying length parameter l_α.

Results and discussion Starting with the literature case of a free lower boundary, the strip cracks in a straight line from top to bottom for small regularization lengths l_φ, Fig. 4.9. The damage width is too small for interference with the punched hole then. Once a critical width is reached, though, the crack will snap into the hole. Analyzing only these curved paths, they tend to flatten for larger regularization lengths. They take a shorter and more direct route as l_φ increases. The relationship between regularization length and crack length is hence not monotonic. The crack length first increases due to deviation towards the hole (from 150.0 mm to 156.9 mm for $l_\varphi = 2$ mm and 3 mm). Caused by the penalization of curvature, nevertheless, the crack length decreases afterwards once the hole is intersected (from 152.7 mm to 143.1 mm for $l_\varphi = 4$ mm and 5 mm). Thus, both influences crack width and crack curvature are observed in this higher-dimensional problem. Interestingly, both have opposed impact on the final crack length.

Fixing the bottom allows us to further reduce the influence of the crack width, because it forces the crack to deviate sideways independent of its width, Fig. 4.10. The focus on curvature becomes even more pronounced due to the systematic and significant

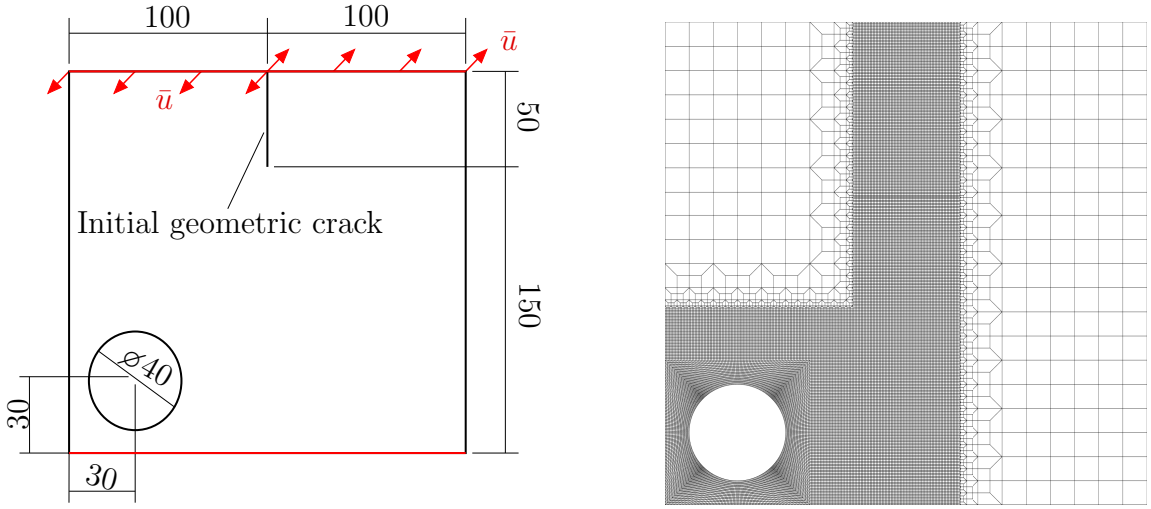

(a) Dimensions and boundary conditions **(b)** Mesh with 37012 elements

Figure 4.8: Punched and pre-cracked strip: geometry, boundary conditions and discretization.

decrease of total crack length for larger l_φ. This can be well explained by the former insights. Larger regularization lengths allow for less curvature (e.g., $0.0277\,\mathrm{mm}^{-1}$ for $l_\varphi = 2\,\mathrm{mm}$ compared to $0.0314\,\mathrm{mm}^{-1}$ for $l_\varphi = 1\,\mathrm{mm}$) and the crack path must deviate earlier to reach the hole and becomes shorter (e.g., 143.7 mm compared to 179.8 mm, respectively). Vice versa, smaller regularization lengths allow larger curvature and thus a later and more severe turning point of the crack path. The lowest point of the damage zone hence becomes another distinctive implication of the inherent, methodological curvature influence. As a result, the regularization length determines whether the crack path affects the region below the hole (up to $l_\varphi \approx 1\,\mathrm{mm}$) or whether it remains free of degradation.

Finally, it shall be emphasized that the regularization length l_φ remained small compared to the specimen size in this example, e.g., $l_\varphi = 2\,\mathrm{mm}$ corresponds to 1 % of the system size. The often unintended curvature influence of the gradient method is hence twofold. On the local scale, it directly affects crack evolution such as turning points. On the global scale, it indirectly affects the crack length and the position of damaged regions. The curvature influence thus becomes decisive for both microscopic and macroscopic systems with uncertain or crucial crack paths.

4.5 Experiment: Bending of a drilled and notched plate

Problem focus An experimental test shall finally evaluate the gradient-induced curvature influence on quasi-brittle damage as previously demonstrated analytically and numerically. It involves a cooled plate of dark chocolate with a hole and a notch similar

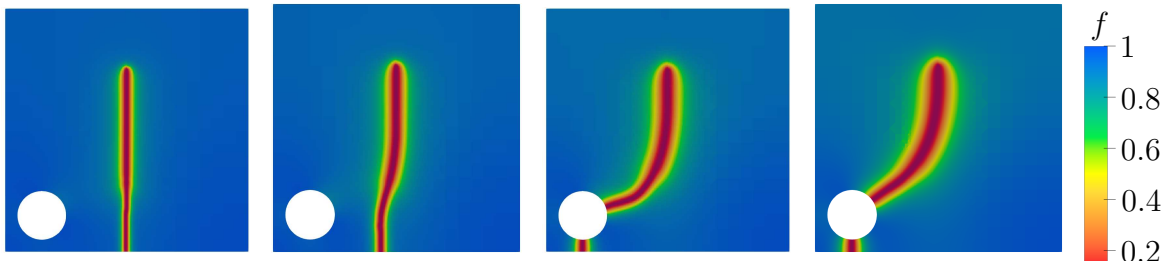

$l_\varphi = 2\,\mathrm{mm}$, $L_{\mathrm{crack}} = 150\,\mathrm{mm}$ | $l_\varphi = 3\,\mathrm{mm}$, $L_{\mathrm{crack}} = 156.9\,\mathrm{mm}$ | $l_\varphi = 4\,\mathrm{mm}$, $L_{\mathrm{crack}} = 152.7\,\mathrm{mm}$ | $l_\varphi = 5\,\mathrm{mm}$, $L_{\mathrm{crack}} = 143.1\,\mathrm{mm}$

Figure 4.9: Punched and precracked strip with free bottom: phase-field model. Degradation function for varying length parameter l_φ. The crack length L_{crack} is measured without the contribution within the hole.

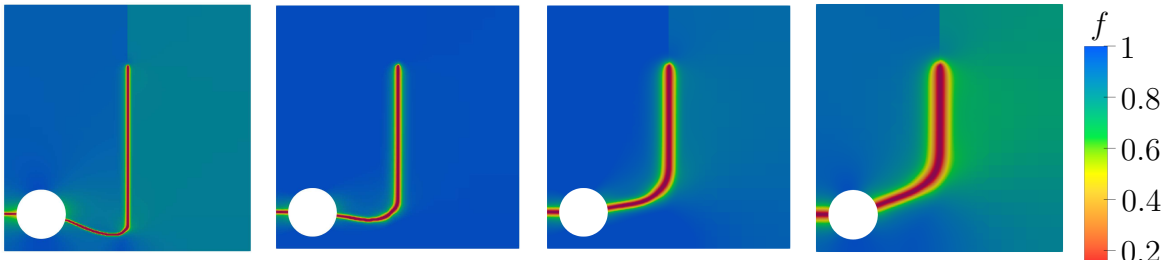

$l_\varphi = 0.5\,\mathrm{mm}$, $L_{\mathrm{crack}} = 197.7\,\mathrm{mm}$ | $l_\varphi = 1\,\mathrm{mm}$, $L_{\mathrm{crack}} = 179.8\,\mathrm{mm}$ | $l_\varphi = 2\,\mathrm{mm}$, $L_{\mathrm{crack}} = 143.7\,\mathrm{mm}$ | $l_\varphi = 3\,\mathrm{mm}$, $L_{\mathrm{crack}} = 137.1\,\mathrm{mm}$

Figure 4.10: Punched and precracked strip with fixed bottom: phase-field model. Degradation function for varying length parameter l_φ. The crack length L_{crack} is measured without the contribution within the hole.

to the out-of-plane shear problem, but adds significant bending stiffness. The focus of this analysis is on the crack path and how the experiment compares to different regularization lengths that affect the curvature evolution in simulations.

Experimental setup The material used to capture quasi-brittle behavior is cooled dark chocolate with 70 % cocoa at 3° C. It has been chosen due to its recyclability, casting ability in 3d-printed molds and the reduction of splinters that may damage experimental equipment. A chocolate plate of $100\,\mathrm{mm} \times 100\,\mathrm{mm} \times 5\,\mathrm{mm}$ was cast, drilled and notched as shown in Fig. 4.11. One half separated by the notch has been clamped. A calibrated weight was attached by a string to the other half and lowered slowly to induce cracking that occurred for forces between 5 N and 7.5 N.

Numerical setup The plate has an initial geometric crack that starts in the middle of the top edge. The plate is fixed on the right side of the crack and loaded in out-of-

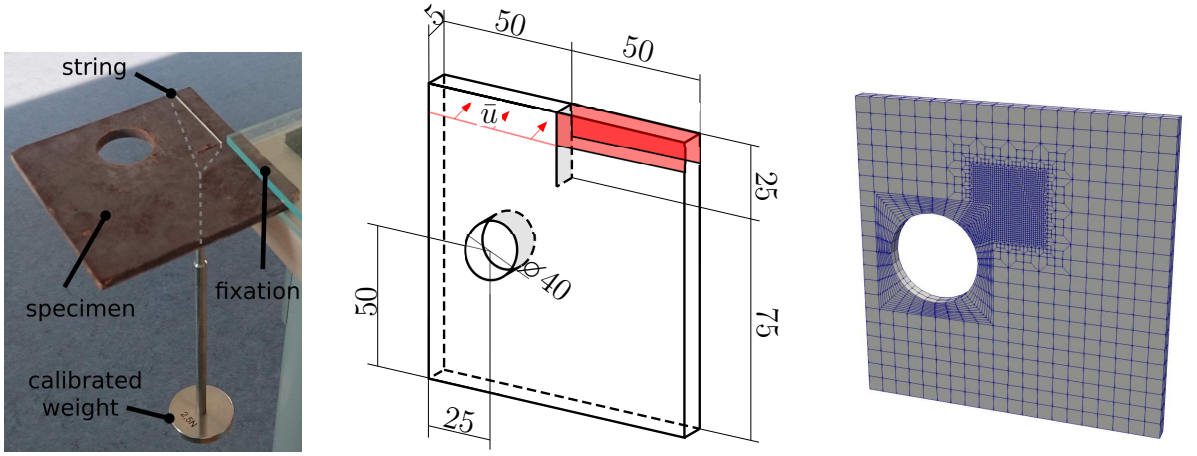

(a) Experimental setup **(b)** Dimensions and boundary conditions **(c)** Mesh with 4948 elements

Figure 4.11: Cracking experiment of cooled dark chocolate: experimental and numerical setup.

Name	Symbol	Unit	Value Plate bending
Young's Modulus	E	[MPa]	26.9
Poisson's ratio	ν	[–]	0.4
residual stiffness factor	c_0	[–]	10^{-7}
damage threshold	$\mathcal{H}_0$	[MPa]	0
crit. energy release rate	g_c	[Nmm]	0.01995
regularization length	l_φ	[mm]	varying

Table 4.5: Cracking experiment of cooled dark chocolate: material parameters associated with the phase-field model.

plane direction on the left side of the crack. The mesh is refined below the crack tip and on the right side of the punched hole; along the expected cracking path. In order to capture the bending behavior of the experiment, the calculations are performed in a three-dimensional setting with two layers of elements. The discretization in thickness direction has been chosen as a compromise between accuracy and calculation time. The material parameters are given in Tab. 4.5 and the calculations are performed by means of a staggered solution scheme.

Results and discussion All four specimens show a very similar, straight crack path, Fig.4.12. The crack length is 18.597 ± 1.687 mm. Here, $\bullet \pm \bullet$ indicates mean $\pm$ population standard deviation.. The crack shape resembles a straight line with a coefficient of determination $r^2_{\text{det}} = 0.983$. This underlines that the notch and the hole reliably govern

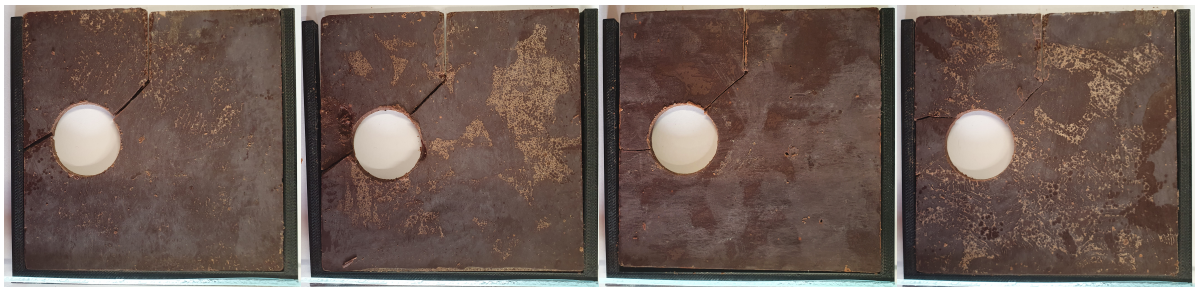

Figure 4.12: Cracking experiment of cooled dark chocolate: experimental specimens after cracking.

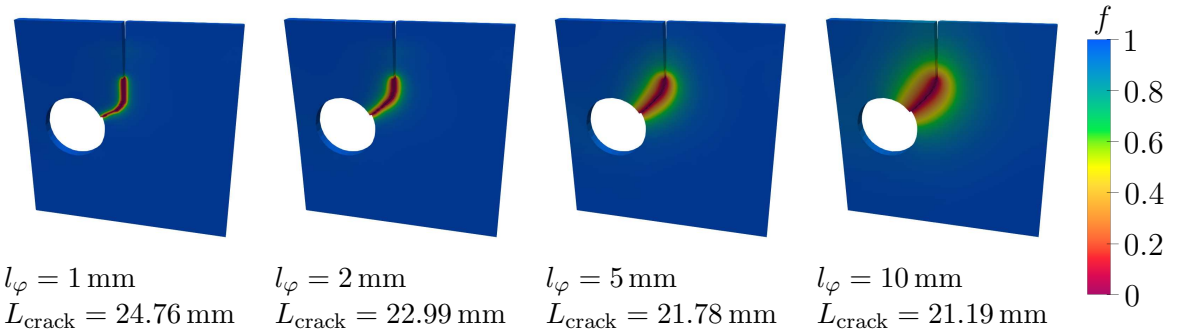

Figure 4.13: Cracking experiment of cooled dark chocolate: phase-field model. Distribution of degradation function for varying regularization length l_φ.

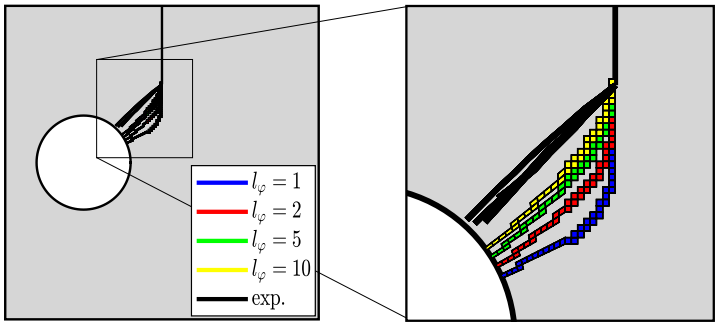

Figure 4.14: Cracking experiment of cooled dark chocolate: comparison of the crack path between simulation and experiments.

the crack evolution and yield reproducible results despite the fast propagation process and inaccuracies in fabrication and boundary conditions. Note that the relatively small deviations result from variations in the crack paths but also from fabrication inaccuracies affecting the notch-hole distance.

The simulations approach the experimental observation with larger regularization lengths, see Fig. 4.13. This agrees well with the fact that a larger regularization length penalizes curvature. Agreement between experiment and simulations – in terms of crack

length – is closest for the largest regularization length involved ($l_\varphi = 1\,\mathrm{mm}$) with a relative deviation of 13.9 %. The deviation increased to 33.1 % for the smallest simulated regularization length ($l_\varphi = 1\,\mathrm{mm}$). This match between experiment and simulations also applies to the overall crack shape, Fig. 4.14.

Interestingly, the sharp-interface limit evolves towards the hole at later stages of crack progression and thus tends to poorer predictions for this problem. This is in contrast to the observations of a sharp crack surface without apparent plastic deformation. It must thus be noted at this point that simplifying assumptions such as quasi-static simulations, numerical approximations and experimental inaccuracies likely prohibit a perfect match between experiment and simulation, anyway. Also, further processes superpose the curvature effect on the crack path, e.g., the interaction between stress localization around the hole and the width of the regularization zone. Thus, isolation of the mere curvature influence is again difficult for the experiment. Interpreting the regularization length as a model parameter, however, shows that it finally controls the curvature of the crack path for the present setup. The experiment hence supports the statement of a methodological, gradient-based curvature effect.

B Appendix

B.1 Arc length method

When modeling softening materials, a so called snap-back behavior in the equilibrium path might occur. To be more precise, the load-deflection might show for two or three different (equilibrium) loads the same deflection, see [25] among others. Although that behavior would not occur in reality (due to dynamical effects), it is still important form a numerical point of view. Typically, the standard solution algorithms, e.g., displacement or load controlled Newton-types, are not able to follow the load-deflection path correctly in this case. Therefore the so called arc length or path-following methods have been proposed by [42, 146, 150]. Here, neither the load nor the displacement is explicitly prescribed. Instead, a solution is searched in a domain close to the solution of the last time step. In order to do so, the residual function is modified by the additional degree of freedom λ as

$$\boldsymbol{r_u}(\boldsymbol{u},\, \lambda) = \boldsymbol{f}^{\text{int}}(\boldsymbol{u}) - \lambda\, \boldsymbol{f}^{\text{ext}} \ . \tag{4.11}$$

Furthermore the residual is enhanced by a suitable constraint function. Following [42] the constraint function is given as

$$r_\lambda(\boldsymbol{u},\, \lambda) \coloneqq f^{\text{Cris}} = \psi^2\, [\boldsymbol{u} - \boldsymbol{u}_n]^T \cdot [\boldsymbol{u} - \boldsymbol{u}_n] + [\lambda - \lambda_n]^2\ \boldsymbol{f}^{\text{ext}^T} \cdot \boldsymbol{f}^{\text{ext}} - \Delta s^2 \ , \tag{4.12}$$

where ψ is a scaling parameter for the displacements, Δs the actual arc length and the variables with subscript n belong to the last converged time step. The constraint equation (4.12) can be interpreted as an ellipsoid around the solution of the last time step. A straightforward linearization of residua (4.11) and (4.12) yield

$$\begin{bmatrix} \boldsymbol{r_u} \\ r_\lambda \end{bmatrix} + \begin{bmatrix} \boldsymbol{K_{uu}} & \boldsymbol{K_{u\lambda}} \\ \boldsymbol{K_{\lambda u}} & K_{\lambda\lambda} \end{bmatrix} \cdot \begin{bmatrix} \Delta\boldsymbol{u} \\ \Delta\lambda \end{bmatrix} = \begin{bmatrix} \boldsymbol{0} \\ 0 \end{bmatrix} \tag{4.13}$$

as the system of equation which has to be solved. Typically, this system is not solved monolithically but with the help of partitioning, cf. [186]. Within this scheme, each iteration starts with solving for the displacement field in dependence of increment $\Delta\lambda$ as

$$\Delta\boldsymbol{u} = \underbrace{-\boldsymbol{K}_{\boldsymbol{uu}}^{-1} \cdot \boldsymbol{r_u}}_{=:\Delta\boldsymbol{u}^{\boldsymbol{u}}} \underbrace{-\boldsymbol{K}_{\boldsymbol{uu}}^{-1} \cdot \boldsymbol{K_{u\lambda}}}_{=:\Delta\boldsymbol{u}^{\lambda}} \Delta\lambda \ . \tag{4.14}$$

Afterwards constraint equation (4.12) has to hold even for the updated degrees of freedom

$$\boldsymbol{u} \leftarrow \boldsymbol{u} + \Delta\boldsymbol{u}^{\boldsymbol{u}} + \Delta\boldsymbol{u}^{\lambda}\,\Delta\lambda \tag{4.15}$$

$$\lambda \leftarrow \lambda + \Delta\lambda\ . \tag{4.16}$$

Therefore updated displacement (4.15) and updated load factor (4.16) are inserted into the constraint equation (4.12). After rearrangement, the constraint equation (4.12) can be written as

$$\begin{aligned} f^{\mathrm{Cris}} = &\left[\psi^2\,\Delta\boldsymbol{u}^{\lambda^T}\cdot\Delta\boldsymbol{u}^{\lambda} + \boldsymbol{f}^{\mathrm{ext}^T}\cdot\boldsymbol{f}^{\mathrm{ext}}\right]\Delta\lambda^2 \\ &+ 2\left[\psi^2\,\left[\boldsymbol{u}+\Delta\boldsymbol{u}^{\boldsymbol{u}}-\boldsymbol{u}_n\right]^T\cdot\Delta\boldsymbol{u}^{\lambda}+\lambda-\lambda_n\right]\Delta\lambda \\ &+ \psi^2\,\left[\boldsymbol{u}+\Delta\boldsymbol{u}^{\boldsymbol{u}}-\boldsymbol{u}_n\right]^T\cdot\left[\boldsymbol{u}+\Delta\boldsymbol{u}^{\boldsymbol{u}}-\boldsymbol{u}_n\right]+\left[\lambda-\lambda_n\right]^2-\Delta s^2 \end{aligned} \quad . \tag{4.17}$$

and solved in closed format. Since eq. (4.17) has usually two distinct solutions, the suitable solution has to be chosen. They can be represented in terms of generalized vectors $\boldsymbol{s}$ as

$$\boldsymbol{s}_1 = \begin{bmatrix}\psi\,\left[\boldsymbol{u}_1-\boldsymbol{u}_n\right]\\ \lambda_1-\lambda_n\end{bmatrix}\ , \qquad \boldsymbol{s}_2 = \begin{bmatrix}\psi\,\left[\boldsymbol{u}_2-\boldsymbol{u}_n\right]\\ \lambda_2-\lambda_n\end{bmatrix}\ , \qquad \boldsymbol{s}_n = \begin{bmatrix}\psi\,\left[\boldsymbol{u}_n-\boldsymbol{u}_{nn}\right]\\ \lambda_n-\lambda_{nn}\end{bmatrix}\ , \tag{4.18}$$

where $\boldsymbol{s}_n$ denotes the solution increment of the last time step. A suitable criterion in order to choose the intended solution is the angle criterion. Here, the deviation between $\boldsymbol{s}_1$ and $\boldsymbol{s}_n$ is compared to the deviation between $\boldsymbol{s}_2$ and $\boldsymbol{s}_n$. The chosen solution is the one which deviates less. Mathematically speaking, the solution which shows the smaller angle α_i according to

$$\cos\left(\alpha_1\right) = \left(\frac{\boldsymbol{s}_1\cdot\boldsymbol{s}_n}{||\boldsymbol{s}_1||\ ||\boldsymbol{s}_n||}\right)\ , \qquad \cos\left(\alpha_2\right) = \left(\frac{\boldsymbol{s}_2\cdot\boldsymbol{s}_n}{||\boldsymbol{s}_2||\ ||\boldsymbol{s}_n||}\right)\ . \tag{4.19}$$

This scheme is repeated until the residual function (4.11) fulfills the desired tolerance.

5 Direct control of the curvature of gradient continua

Although curvature effects have been studied in connection with various topics, there is hardly any literature on curvature dependence in damage modeling. Instead, size effects have been studied, cf. [98, 139, 187]. For instance, *Peerlings et al.* [139] investigated the effect of the internal length scale compared to the structure's size, and *Zhang et al.* [187] analyzed size effects with a vanishing internal length scale. However, no curved crack paths were considered in these analyses.

A first step towards curvature dependence of gradient damage models has been performed by *Li and Maurini* [97]. They investigated anisotropic fracture surface energies and crack kinking within a phase-field model and therefore incorporated the second derivative of the phase field parameter into the fracture surface energy density. Hence, they introduced a physically motivated curvature influence in order to describe anisotropic behavior. In contrast, the focus of the present paper lies on the methodological curvature dependence stemming from the balance equation associated with non-local field φ as pointed out in the previous chapter.

5.1 Origin of the curvature effect and control possibilities

The origin of the curvature dependence has been traced back to balance of micro forces (2.21), cf. Subsection 4.4.1. In order to control both the localization width and the curvature simultaneously, a single length parameter is not sufficient. Using the split of $\operatorname{div}(\boldsymbol{\Omega})$ (eq. (4.9)) and by introducing an additional length parameter $l_\kappa^\bullet$ for the part depending on the curvature as

$$\operatorname{div}\left(\widetilde{\boldsymbol{\Omega}}\right) \coloneqq l^\bullet \, \boldsymbol{n}_\varphi \cdot \nabla \, ||\nabla\varphi|| + l_\kappa^\bullet \operatorname{div}(\boldsymbol{n}_\varphi) \, ||\nabla\varphi|| \tag{5.1}$$

both parts (absolute value and curvature) can be controlled separately. Similar to prefactor $l^\bullet$, prefactor $l_\kappa^\bullet$ differs in dependence of the underlying model (micromorphic:

$l^\bullet_\kappa = c_\alpha\, l^2_\kappa$, phase-field: $l^\bullet_\kappa = g_c\, l_\kappa$). The key idea is thus to scale length parameter $l^\bullet_\kappa$ independently of length parameter $l^\bullet$. However, in this case

$$l^\bullet \neq l^\bullet_\kappa \quad \Rightarrow \quad \int_{\mathcal{B}} \operatorname{div}\left(\widetilde{\boldsymbol{\Omega}}\right) \delta\varphi \,\mathrm{d}V \neq \int_{\partial\mathcal{B}} \widetilde{\boldsymbol{\Omega}} \cdot \boldsymbol{n}\, \delta\varphi \,\mathrm{d}A - \int_{\mathcal{B}} \widetilde{\boldsymbol{\Omega}} \cdot \nabla\delta\varphi \,\mathrm{d}V \tag{5.2}$$

and the expressions $\nabla\,||\nabla\varphi||$ and $\operatorname{div}(\boldsymbol{n}_\varphi)$ of eq. (5.1) have to be calculated explicitly. By starting with the first part of eq. (5.1), which transforms into

$$l^\bullet\, \boldsymbol{n}_\varphi \cdot \nabla\,||\nabla\varphi|| = l^\bullet\, \boldsymbol{n}_\varphi \cdot \nabla^2\,\varphi \cdot \boldsymbol{n}_\varphi \,. \tag{5.3}$$

The second part of eq. (5.1) results analogously in

$$l^\bullet_\kappa \operatorname{div}(\boldsymbol{n}_\varphi)\; ||\nabla\varphi|| = l^\bullet_\kappa \operatorname{div}(\nabla\varphi) - l^\bullet_\kappa\, \boldsymbol{n}_\varphi \cdot \nabla^2\,\varphi \cdot \boldsymbol{n}_\varphi \,. \tag{5.4}$$

Insertion of both eq. (5.3) and (5.4) back into eq. (5.1) leads to

$$\operatorname{div}\left(\widetilde{\boldsymbol{\Omega}}\right) = l^\bullet_\kappa \operatorname{div}(\nabla\varphi) + [l^\bullet - l^\bullet_\kappa]\; \boldsymbol{n}_\varphi \cdot \nabla^2\,\varphi \cdot \boldsymbol{n}_\varphi \,. \tag{5.5}$$

By choosing $l^\bullet = l^\bullet_\kappa$ the second part of eq. (5.5) cancels out and the usual form of balance of micro forces is obtained. Using identity $\operatorname{div}(\nabla\varphi) = \operatorname{tr}(\nabla^2\varphi)$ allows to further reformulate eq. (5.5) into

$$\begin{aligned} \operatorname{div}\left(\widetilde{\boldsymbol{\Omega}}\right) &= l^\bullet \operatorname{div}(\nabla\varphi) + [l^\bullet - l^\bullet_\kappa]\; \left[\boldsymbol{n}_\varphi \cdot \nabla^2\varphi \cdot \boldsymbol{n}_\varphi - \operatorname{tr}\left(\nabla^2\varphi\right)\right] \\ &= \operatorname{div}(\boldsymbol{\Omega}) + [l^\bullet - l^\bullet_\kappa]\; \left[\boldsymbol{n}_\varphi \cdot \nabla^2\varphi \cdot \boldsymbol{n}_\varphi - \operatorname{tr}\left(\nabla^2\varphi\right)\right] \end{aligned} \tag{5.6}$$

which yields an explicit expression for the term that relates to the curvature dependence of the underlying gradient damage models:

$$r_\kappa \coloneqq \boldsymbol{n}_\varphi \cdot \nabla^2\varphi \cdot \boldsymbol{n}_\varphi - \operatorname{tr}\left(\nabla^2\varphi\right) \,. \tag{5.7}$$

5.1.1 Potential-based model: consideration of a curvature-dependent Helmholtz energy

The first approach follows the variational formulation by appending additional curvature-dependent contribution to the underlying model's Helmholtz energy as

$$\psi = \psi^{\mathrm{pro}} + \psi^{\mathrm{curv}}(\nabla\varphi,\, \nabla^2\varphi) \,. \tag{5.8}$$

Helmholtz energy ψ^{pro} denotes the Helmholtz energy from the underlying gradient damage model, i.e., from micromorphic gradient damage model 3.4 or from phase-field model 2.4.2. A suitable choice for contribution ψ^{curv} is

$$\psi^{\text{curv}} = \frac{L_\kappa}{2} \left[||\nabla\varphi||^2 \, r_\kappa \right]^2 \,, \tag{5.9}$$

where r_κ is precisely the curvature expression defined in eq. (5.7).

From an implementation point of view and concerning $\mathcal{C}^0$-continuous finite elements, the expression $\nabla^2\varphi$ cannot be integrated correctly, since $\mathcal{C}^0$-continuous finite elements violate the continuity requirements as pointed out in [189]. One possibility is to use $\mathcal{C}^1$-continuous finite elements. Another one is to adopt the idea from strain gradient elasticity, see [113, 164], and to approximate the second derivative by means of an additional micromorphic enhancement, cf. [48, 54]. Following the latter, additional field variable $\boldsymbol{\chi}$ is introduced. The associated balance equation then follows jointly from the variational framework through stationarity as

$$\delta\mathcal{E} = \delta_{\boldsymbol{u}}\mathcal{E} \cdot \delta\boldsymbol{u} + \delta_\varphi\mathcal{E}\,\delta\varphi + \delta_\alpha\mathcal{E}\,\delta\alpha + \delta_{\boldsymbol{\chi}}\mathcal{E} \cdot \delta\boldsymbol{\chi} = 0 \,, \tag{5.10}$$

$$\delta_{\boldsymbol{u}}\mathcal{E} \cdot \delta\boldsymbol{u} = 0 \,, \qquad \delta_\varphi\mathcal{E}\,\delta_\varphi = 0 \,, \qquad \delta_\alpha\mathcal{E}\,\delta\alpha = 0 \,, \qquad \delta_{\boldsymbol{\chi}}\mathcal{E} \cdot \delta\boldsymbol{\chi} = 0 \,. \tag{5.11}$$

The balance equations associated with $\boldsymbol{u}$, φ and α remain unaltered, such that only the latter equation remains to be specified. This balance equation is associated with micromorphic field $\boldsymbol{\chi}$ and reads

$$\begin{aligned} \delta_{\dot{\boldsymbol{\chi}}}\dot{\mathcal{E}} \cdot \delta\dot{\boldsymbol{\chi}} &= \int_{\mathcal{B}} \boldsymbol{v} \cdot \delta\dot{\boldsymbol{\chi}} + \boldsymbol{\Upsilon} : \delta\nabla\dot{\boldsymbol{\chi}} \,\mathrm{d}V = 0 \\ \Leftrightarrow \quad & \int_{\mathcal{B}} \left[\operatorname{div}(\boldsymbol{\Upsilon}) - \boldsymbol{v} \right] \cdot \delta\dot{\boldsymbol{\chi}} \,\mathrm{d}V = \int_{\partial\mathcal{B}} \left[\delta\dot{\boldsymbol{\chi}} \cdot \boldsymbol{\Upsilon} \right] \cdot \boldsymbol{n} \,\mathrm{d}A \,, \end{aligned} \tag{5.12}$$

where $\boldsymbol{v} = \partial_{\boldsymbol{\chi}}\psi$ and $\boldsymbol{\Upsilon} = \partial_{\nabla\boldsymbol{\chi}}\psi$ are the energetic dual forces to $\boldsymbol{\chi}$ and $\nabla\boldsymbol{\chi}$. The localized format of balance eq. (5.12) follows as

$$\operatorname{div}(\boldsymbol{\Upsilon}) = \boldsymbol{v} \quad \text{in } \mathcal{B} \,, \tag{5.13}$$

$$\boldsymbol{\Upsilon} \cdot \boldsymbol{n} = \boldsymbol{0} \quad \text{on } \partial\mathcal{B} \,. \tag{5.14}$$

For the evaluation of Helmholtz energy contribution (5.9), $\nabla\varphi$ is coupled to $\boldsymbol{\chi}$ such that $\nabla\boldsymbol{\chi}$ replaces $\nabla^2\varphi$. For the sake of convenience $\boldsymbol{\chi}$ also replaces $\nabla\varphi$. This leads to the micromorphic transformation of energy contribution (5.9) into

$$\psi^{\text{curv}} = \frac{c_\chi}{2} \, ||\nabla\varphi - \boldsymbol{\chi}||^2 + \frac{L_\kappa}{2} \left[\boldsymbol{\chi} \cdot \nabla\boldsymbol{\chi} \cdot \boldsymbol{\chi} - ||\boldsymbol{\chi}||^2 \operatorname{tr}(\nabla\boldsymbol{\chi}) \right]^2 \,, \tag{5.15}$$

where c_χ is an additional penalty parameter and L_κ the parameter controlling the curvature. A straightforward computation of the energetically dual quantities to $\nabla\varphi$, $\boldsymbol{\chi}$ and $\nabla\boldsymbol{\chi}$ results in

$$\boldsymbol{\Omega} = \frac{\partial\psi}{\partial\nabla\varphi} = l^\bullet\,\nabla\varphi + c_\chi\,[\nabla\varphi - \boldsymbol{\chi}]\ , \tag{5.16}$$

$$\boldsymbol{v} = \frac{\partial\psi}{\partial\boldsymbol{\chi}} = c_\chi\,[\boldsymbol{\chi} - \nabla\varphi] + L_\kappa\,||\boldsymbol{\chi}||^2\,r_\kappa\,[\nabla\boldsymbol{\chi}\cdot\boldsymbol{\chi} + \boldsymbol{\chi}\cdot\nabla\boldsymbol{\chi} - 2\,\boldsymbol{\chi}\,\mathrm{tr}\,(\nabla\boldsymbol{\chi})]\ , \tag{5.17}$$

$$\boldsymbol{\Upsilon} = \frac{\partial\psi}{\partial\nabla\boldsymbol{\chi}} = L_\kappa\,||\boldsymbol{\chi}||^2\,r_\kappa\,\left[\boldsymbol{\chi}\otimes\boldsymbol{\chi} - ||\boldsymbol{\chi}||^2\,\boldsymbol{I}\right]\ . \tag{5.18}$$

5.1.2 Micro force-based model: direct modification of balance of micro forces

Another option in order to control or eliminate the curvature dependence is to extract the curvature dependence from the constitutive equations directly. This is achieved by using eq. (5.6) and replacing $\mathrm{div}\,(\boldsymbol{\Omega})$ in balance equation (2.21) by $\mathrm{div}(\widetilde{\boldsymbol{\Omega}})$. The curvature-independent counterpart of balance of micro forces then reads

$$\int_{\mathcal{B}} \left[\mathrm{div}\,(\boldsymbol{\Omega}) - \omega + [l^\bullet - l^\bullet_\kappa]\,r_\kappa\right]\,\delta\varphi\,\mathrm{d}V = \int_{\partial\mathcal{B}} [\boldsymbol{\Omega}\cdot\boldsymbol{n}]\,\delta\varphi\,\mathrm{d}A \tag{5.19}$$

with r_κ being defined in eq. (5.7). The choice $l^\bullet_\kappa = l^\bullet$ removes r_κ and balance equation (5.19) simplifies to traditional balance equation (2.21). The localized format of eq. (5.19) is obtained as

$$\mathrm{div}\,(\boldsymbol{\Omega}) + [l^\bullet - l^\bullet_\kappa]\,r_\kappa = \omega \quad \text{in } \mathcal{B} \tag{5.20}$$

$$\boldsymbol{\Omega}\cdot\boldsymbol{n} = 0 \quad \text{on } \partial\mathcal{B}\ . \tag{5.21}$$

It bears emphasis that due to contribution $c_\alpha\,[l^2_\alpha - l^2_\kappa]\,r_\kappa$, the balance equation no longer follows as a stationarity condition from a potential. By the assumption of the existence of such a potential $\tilde{\mathcal{E}}$, the stationarity condition of potential $\tilde{\mathcal{I}}$ would read

$$\frac{\partial\tilde{\mathcal{I}}}{\partial\varphi} = \omega - [l^\bullet - l^\bullet_\kappa]\,r_\kappa(\nabla\varphi,\,\nabla^2\varphi)\ , \tag{5.22}$$

$$\frac{\partial\tilde{\mathcal{I}}}{\partial\nabla\varphi} = l^\bullet\,\nabla\varphi\ , \tag{5.23}$$

$$\frac{\partial\tilde{\mathcal{I}}}{\partial\nabla^2\varphi} = \boldsymbol{0} \tag{5.24}$$

which leads to a non-symmetric Hessian, i.e.,

$$\frac{\partial \tilde{\mathcal{I}}^2}{\partial \varphi \, \partial \nabla \varphi} = -[l^\bullet - l_\kappa^\bullet] \, \frac{\partial r_\kappa}{\partial \nabla \varphi} \neq \mathbf{0} = \frac{\partial \tilde{\mathcal{I}}^2}{\partial \nabla \varphi \, \partial \varphi} \, , \tag{5.25}$$

$$\frac{\partial \tilde{\mathcal{I}}^2}{\partial \varphi \, \partial \nabla^2 \varphi} = -[l^\bullet - l_\kappa^\bullet] \, \frac{\partial r_\kappa}{\partial \nabla^2 \varphi} \neq \mathbf{0} = \frac{\partial \tilde{\mathcal{I}}^2}{\partial \nabla^2 \varphi \, \partial \varphi} \, . \tag{5.26}$$

Thus, such a potential does not exist.

Analogously to the previous model (Subsection 5.1.1) expression $\nabla^2 \varphi$ in r_κ cannot be integrated correctly with $\mathcal{C}^0$-continuous finite elements. By following the same line of thought, additional field $\boldsymbol{\chi}$ is again introduced and coupled to $\nabla \varphi$. By doing so, expressions $\boldsymbol{\chi}$ and $\nabla \boldsymbol{\chi}$ replace $\nabla \varphi$ and $\nabla^2 \varphi$ in curvature expression r_κ. Furthermore, the coupling of $\nabla \varphi$ and $\boldsymbol{\chi}$ has to be taken into account. This leads to an additional penalty contribution $\boldsymbol{\varsigma} \coloneqq c_\chi \, [\boldsymbol{\chi} - \nabla \varphi]$ in balance eq. (5.19). Thus, balance eq. (5.19) is modified to

$$\begin{aligned} & \int_{\mathcal{B}} [\boldsymbol{\Omega} - \boldsymbol{\varsigma}] \cdot \delta \nabla \varphi + [\omega - [l^\bullet - l_\kappa^\bullet] \, r_\kappa(\boldsymbol{\chi}, \, \nabla \boldsymbol{\chi})] \; \delta \varphi \, \mathrm{d}V = 0 \\ \Leftrightarrow \quad & \int_{\mathcal{B}} [\operatorname{div} (\boldsymbol{\Omega} - \boldsymbol{\varsigma}) + [l^\bullet - l_\kappa^\bullet] \, r_\kappa(\boldsymbol{\chi}, \, \nabla \boldsymbol{\chi}) - \omega] \; \delta \varphi \, \mathrm{d}V = \int_{\partial \mathcal{B}} [\boldsymbol{\Omega} - \boldsymbol{\varsigma}] \cdot \boldsymbol{n} \, \delta \varphi \, \mathrm{d}A \, , \end{aligned} \tag{5.27}$$

whose localized format reads

$$\operatorname{div} (\boldsymbol{\Omega} - \boldsymbol{\varsigma}) = \omega - [l^\bullet - l_\kappa^\bullet] \, r_\kappa \quad \text{in } \mathcal{B} \, , \tag{5.28}$$

$$[\boldsymbol{\Omega} - \boldsymbol{\varsigma}] \cdot \boldsymbol{n} = \mathbf{0} \quad \text{on } \partial \mathcal{B} \, . \tag{5.29}$$

The balance equation associated to the micromorphic field $\boldsymbol{\chi}$ reads

$$\int_{\mathcal{B}} \boldsymbol{\varsigma} \cdot \delta \boldsymbol{\chi} \, \mathrm{d}V = 0 \tag{5.30}$$

and completes the model.

Remark 1 *The potential-based method does not eliminate the curvature dependence of the underlying gradient damage model completely. This can be demonstrated by analyzing the mathematical structure of the respective balance equation, i.e.,*

$$\begin{aligned} & \delta_{\dot{\varphi}} \dot{\mathcal{E}} \, \delta \dot{\varphi} = \int_{\mathcal{B}} c_\alpha \; [\varphi - \alpha] \; \delta \dot{\varphi} + \nabla \varphi \cdot g(\nabla^2 \varphi) \cdot \delta \nabla \dot{\varphi} + h(\nabla \varphi) : \delta \nabla^2 \dot{\varphi} \, \mathrm{d}V = 0 \\ & \textit{with } g(\nabla^2 \varphi) = c_\alpha \, l_\alpha^2 \, \boldsymbol{I} + L_\kappa \operatorname{tr} \left(\nabla^2 \varphi \right) \, \boldsymbol{I} + L_\kappa \, \nabla^2 \varphi \, . \end{aligned} \tag{5.31}$$

The functions $g(\nabla^2\varphi)$ and $h(\nabla\varphi)$ occur due to additional Helmholtz energy contribution ψ^{curv}. The middle part can be reformulated into

$$\int_{\mathcal{B}} \nabla\varphi \cdot g(\nabla^2\varphi) \cdot \delta\nabla\dot{\varphi}\,\mathrm{d}V = \int_{\partial\mathcal{B}} L_\kappa\, \nabla\varphi \cdot \nabla^2\varphi \cdot \boldsymbol{n}\, \delta\dot{\varphi}\,\mathrm{d}A - \int_{\mathcal{B}} \mathrm{div}\left(\nabla\varphi \cdot g(\nabla^2\varphi)\right)\, \delta\dot{\varphi}\,\mathrm{d}V\,, \tag{5.32}$$

with

$$\begin{aligned}\mathrm{div}\left(g(\nabla^2\varphi)\cdot\nabla\varphi\right) = \quad & \underbrace{c_\alpha\, l_\alpha^2\, \mathrm{div}\left(\nabla\varphi\right)}_{\textit{(standard gradient enhancement)}} \\ & + \underbrace{L_\kappa\, \left[\mathrm{div}\left(\nabla\varphi\right)^2 + \nabla^2\varphi : \nabla^2\varphi + \mathrm{div}\left(\mathrm{tr}\left(\nabla^2\varphi\right)\, \boldsymbol{I} + \nabla^2\varphi\right)\cdot\nabla\varphi\right]}_{\textit{(potential-based extra term for curvature control)}}\,.\end{aligned} \tag{5.33}$$

The new term proposed with the potential-based approach (last term in eq. (5.33)) does add a degree of freedom to control the curvature influence of standard gradient enhancements (middle term in eq. (5.33)). The former cannot compensate for the latter exactly, though, due to the different orders of magnitude. This incomplete control capability can be explained by turning the view towards the micro force-based approach. The curvature elimination of the micro force-based approach required a non-symmetric Hessian (cf. Subsection 5.1.2), which is not possible when derived from a potential.

5.2 Numerical results

The focus lies on the following two selected boundary value problems: the stretched disc (Fig. 4.5) and the L-shaped specimen (Fig. 3.6).

5.2.1 Radial stretch of a disc

5.2.1.1 Problem focus

the fist example predetermines the crack's curvature that evolves at the disc's boundary due to an imperfection (see Fig 4.5). This allows us to vary the crack's curvature κ directly by varying the disc's radius R. It moreover allows the analysis of the curvature dependence of the extended models in terms of resulting fracture energy (4.10) and the crack width. The numerically predicted fracture energy G_f is a key property of interest. It represents the energy required to create the crack per crack surface area and is typically assumed to be a constant for brittle materials.

5.2.1.2 Numerical setup

The disc is loaded in radial direction along the surface with prescribed displacement $\bar{u}$. The final amplitude is $\bar{u} = 0.04\,\text{mm}$ for the micromorphic models and $\bar{u} = 0.014\,\text{mm}$ for the extended phase-field models. Rotational symmetry is employed and reduces the problem to one spatial dimension in radial direction (see Appendix C.4 and F.1). The radius varies between 15 mm and 100 mm (micromorphic) and 12.5 mm and 75 mm (phase-field), respectively, while the element length L_e in the softening zone is fixed to 0.05 mm. In order to trigger localization, the threshold value α_0 ($\mathcal{H}_0$ in the phase-field model) of the outermost element is reduced by 10 %. All computations are based on linear shape functions (fields $\boldsymbol{u}$, φ, $\boldsymbol{\chi}$) and the observed snap-back behavior is resolved by means of an arc-length method [42], see also Appendix B.1. The material parameters are given in Tab. 5.1 for the micromorphic gradient damage models and in Tab. 5.2 for the phase-field models.

Name	Symbol	Unit	Value (AP) Stretched disc	Value (LS) L-shape
Young's Modulus	E	[MPa]	21000	21000
Poisson's ratio	ν	[–]	0.2	0.2
residual stiffness factor	c_0	[–]	10^{-7}	10^{-7}
damage threshold	α_0	[MPa]	0.4	0.4
damage slope	α_u	[–]	0.5	1
energy scaling factor	c_E	[–]	200	20000
penalty parameter	c_α	[MPa]	100	100
length parameter	l_α	[mm]	0.1	0.1
penalty parameter	c_χ	[MPa]	10	10
curvature parameter	l_κ	[mm]	varying	varying
curvature parameter	L_κ	[Nmm^6]	varying	varying

Table 5.1: Radial stretch of a disc and L-shaped specimen: material parameters associated with curvature-enhanced micromorphic gradient damage models.

5.2.1.3 Results and discussion

The conventional gradient extension ($L_\kappa = 0$ or $l_\kappa^\bullet = l^\bullet$, respectively) clearly yields a fracture energy that depends on the radius and thus the curvature of the disc, see the lower (blue) lines in Fig. 5.2 and 5.1. Although this physically undesired behavior tends to diminish by convergence for larger disc sizes, its effect is not negligible for the entire spectrum investigated.

This undesired curvature influence can successfully be lowered by tuning parameter L_κ of the potential-based approach. See the middle (red) lines in Fig. 5.2, where the fluctuation reduces from 10 % to 2 % (micromorph) and from 6.5 % to 1.3 % (phase-field).

Name	Symbol	Unit	Value Stretched disc
Young's Modulus	E	[MPa]	21000
Poisson's ratio	ν	[–]	0.2
residual stiffness factor	c_0	[–]	10^{-7}
damage threshold	$\mathcal{H}_0$	[MPa]	0.05
crit. energy release rate	g_c	[N/mm]	0.25
length parameter	l_φ	[mm]	2
penalty parameter	c_χ	[MPa]	1
curvature parameter	l_κ	[mm]	varying
curvature parameter	L_κ	[Nmm^6]	varying

Table 5.2: Radial stretch of a disc: material parameters associated with the curvature-enhanced phase-field models.

A too large parameter L_κ can even invert the curvature-induced effect and the fracture energies decrease with increasing radius (top (green) lines in Fig. 5.2).

Curvature parameter L_κ and radius $R_{\max}$ do not only affect the fracture energy but also the resulting crack width, see Fig. 5.2 (bottom). This width shall be defined here by a degradation cutoff of $f < 0.95$. The increase of the crack width notably coincides with the increase of fracture energy. This behavior is observed for both underlying gradient damage models the micromorphic one and the phase-field model. The crack-width sensitivity is more pronounced for the micromorph gradient model, though. The deviation of the crack width between smallest and largest disc radii starts at 11.6 % for the prototype model $L_\kappa = 0$. Tuning L_κ increases the deviation to 31.4 % for $L_\kappa = 200$ (where sensitivity for of the fracture energy is mostly eliminated) and further up to 38 % for $L_\kappa = 1000$.

The potential-based approach is eventually able to control and to diminish the curvature influence on the fracture energy of both gradient-enhanced models. This control ability however also changes the width of the damage field, which usually is an artificial yet numerically relevant width for sharp cracks. The potential-based approach requires a careful calibration of the new parameter L_κ, and a complete elimination is usually not possible. The micro force-based approach also allows to modify the curvature influence and shares some qualitative characteristics of the potential-based approach. Fig. 5.1 specifically compares the conventional case ($l^\bullet_\kappa = l^\bullet$) with the modification of the micro-forces fully activated ($l^\bullet_\kappa = 0$). In contrast to the potential-based approach, it suppresses the undesired curvature influence on the fracture energy even better for the micromorphic prototype model. Interestingly, it otherwise performs worse for the phase-field prototype model. Turning the view towards its impact on the crack width, the micro force-based approach eliminates the dependence on the disc's curvature completely and model-independently. As another result, there is no proportionality left between the fracture energy and the crack width.

The model-specific behavior of both approaches to curvature control highlights the complexity of the inherent curvature dependence and underlines the need for customized solutions that may depend on the formulation and the implementation.

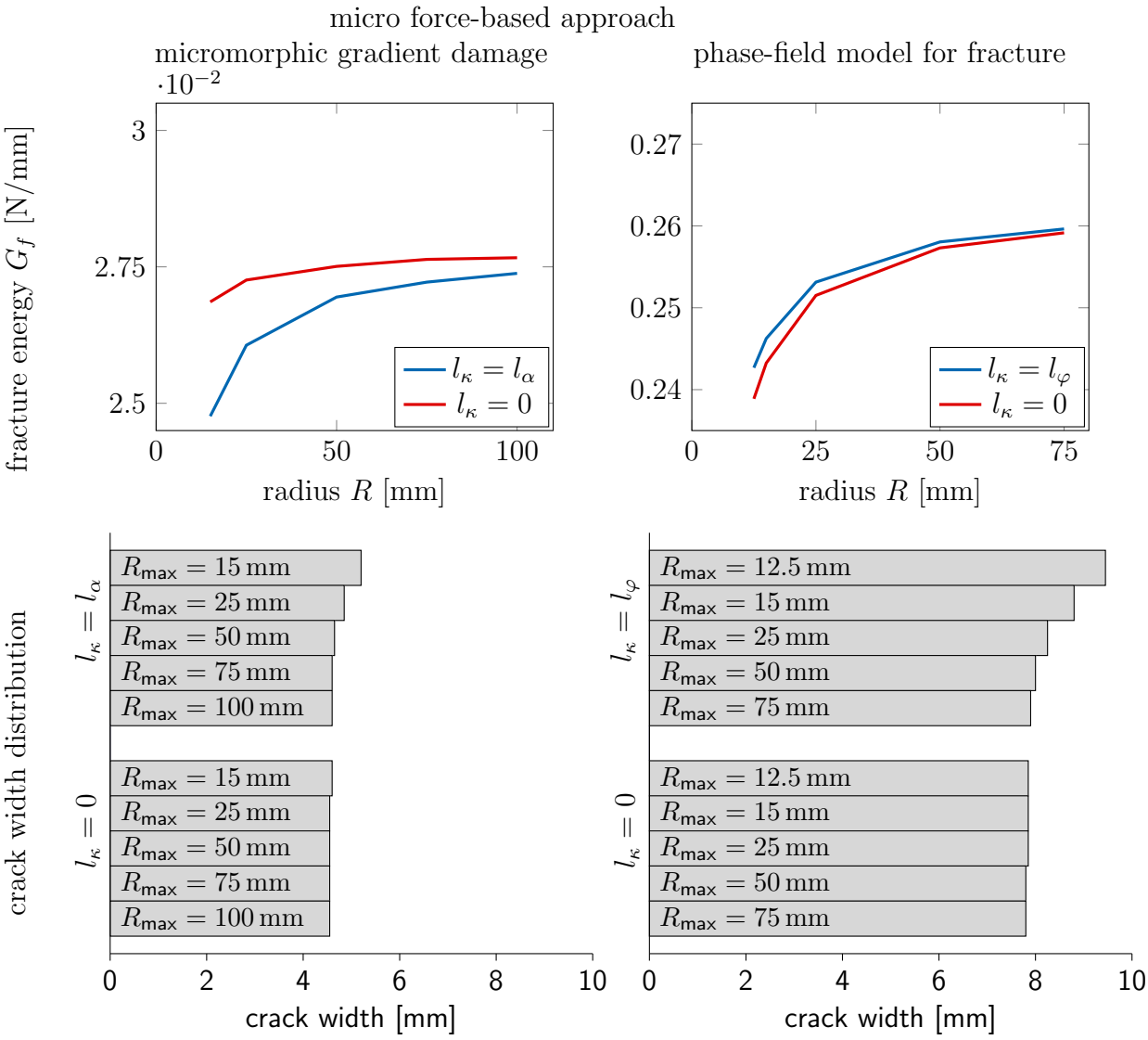

Figure 5.1: Radial stretch of a disc: micro force-based approach. Fracture energies (top) and crack width (bottom) for various radii and new length parameter L_κ. Left and right column show results for the micromorphic and the phase-field model, respectively.

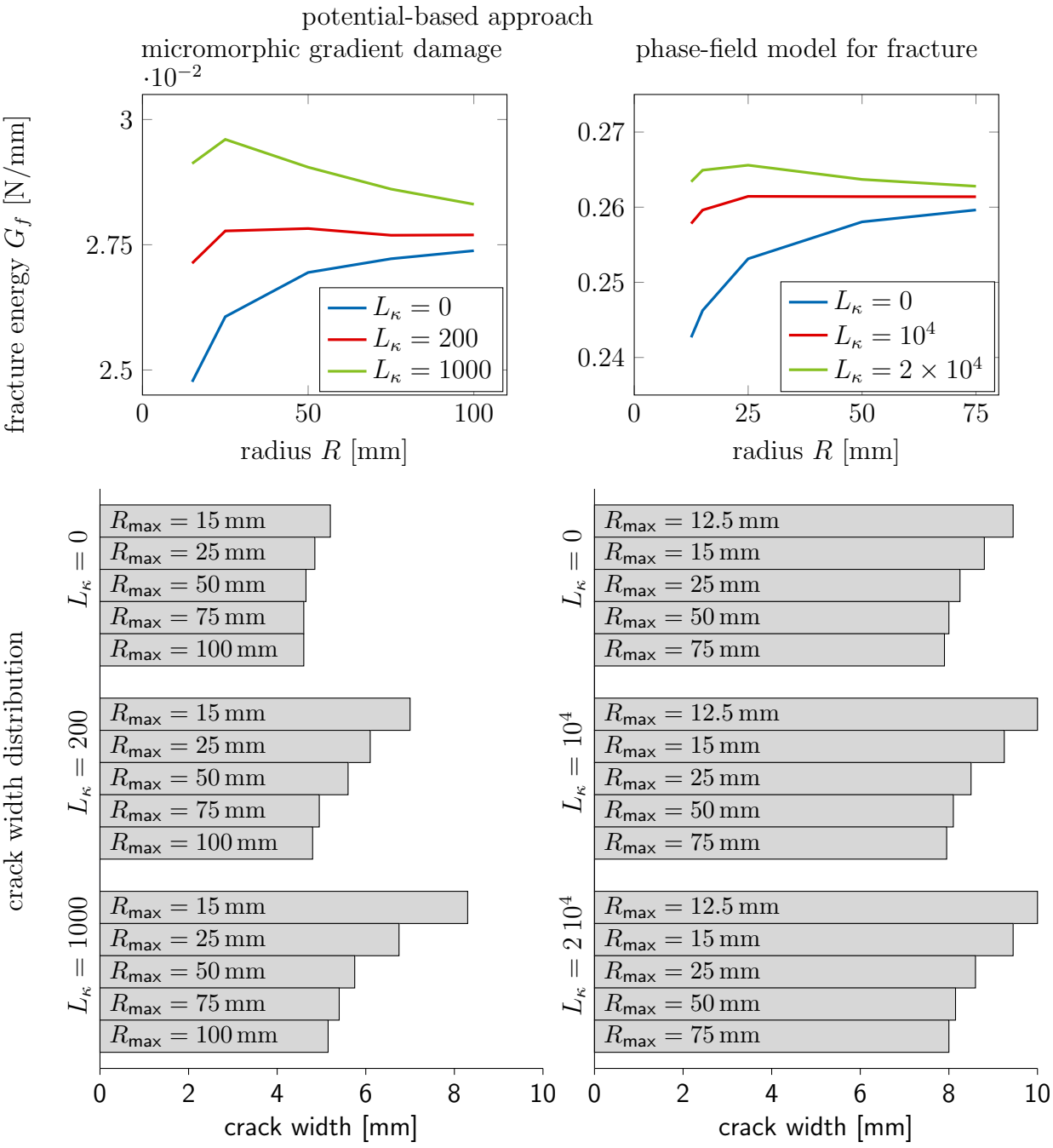

Figure 5.2: Radial stretch of a disc: potential-based approach. Fracture energies (top) and crack width (bottom) for various radii and new length parameter $l_\kappa^\bullet$. Left and right column show results for the micromorphic and the phase-field model, respectively.

5.2.2 L-shaped specimen

5.2.2.1 Problem focus

The L-shape specimen (Fig. 3.6) constitutes a well-established benchmark problem for crack propagation [184]. The crack path develops freely in this example and is therefore ideal in order to investigate the effect of varying curvature parameters $l_\kappa^\bullet$ and L_κ, respectively. While the previous example focused on a systematic study of both the micromorphic and the phase-field model, this second example will focus in more detail only on the micromorphic implementation as the qualitative implications apply to both models.

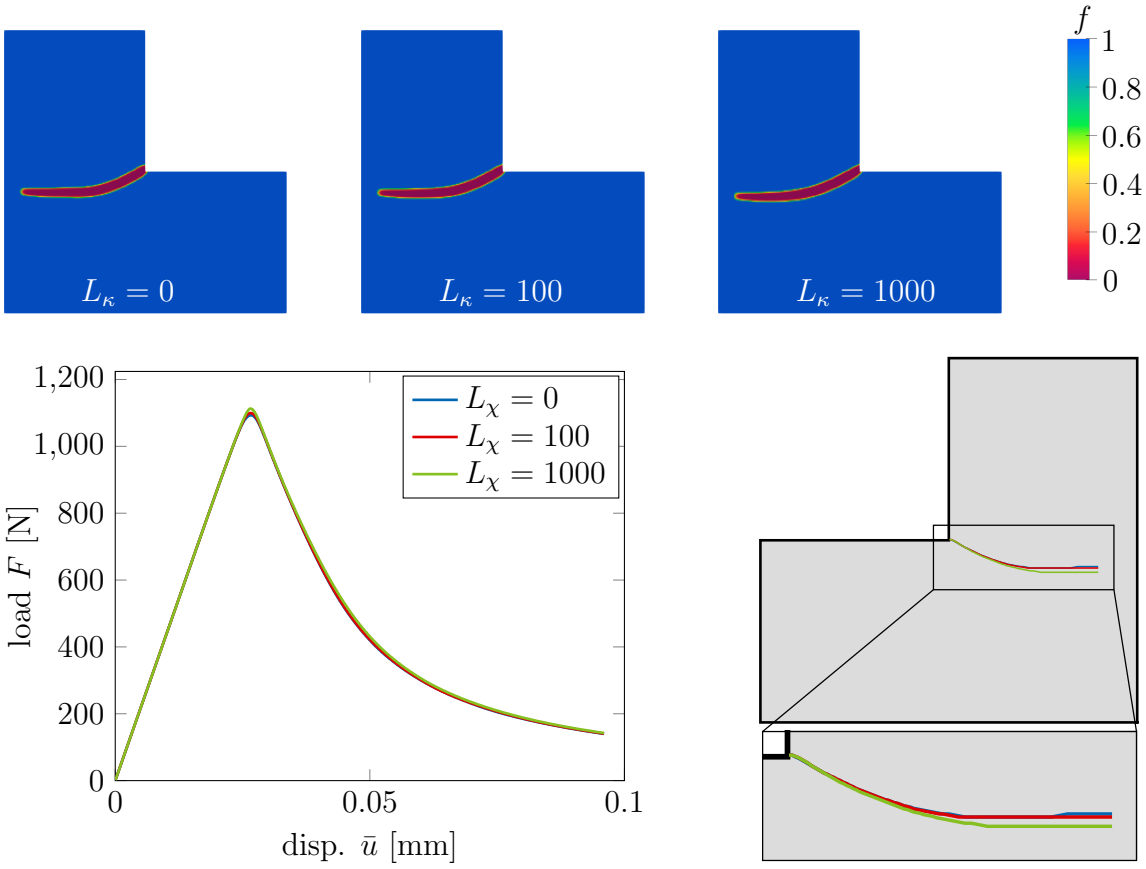

Figure 5.3: L-shaped specimen: potential-based approach (micromorphic gradient damage): distribution of degradation function, load-displacement diagram and central crack path.

5.2.2.2 Numerical setup

The L-shaped specimen is fixed at the top and loaded in vertical direction at the lower left surface by prescribed displacement $\bar{u} = 0.1\,\mathrm{mm}$. All fields ($\boldsymbol{u}$, φ, $\boldsymbol{\chi}$) are spanned by linear shape functions and plane stress conditions are assumed. Homogeneous Neumann boundary conditions are prescribed for micromorphic fields φ and $\boldsymbol{\chi}$. The underlying mesh consists of 10651 elements, which are clustered in the area of the emerging crack. The material parameters are given in Tab. 5.1.

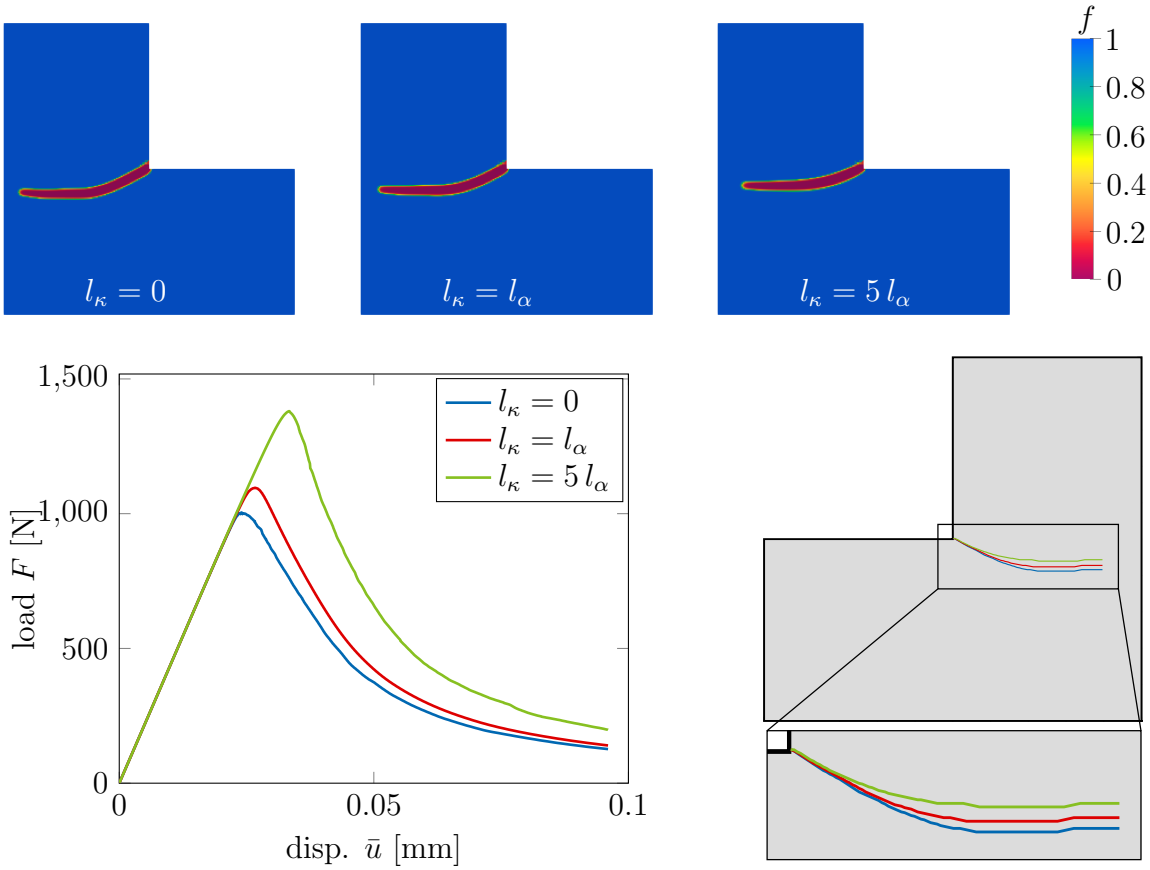

Figure 5.4: L-shaped specimen: micro force-based approach (micromorphic gradient damage): distribution of degradation function, load-displacement diagram and central crack path.

5.2.2.3 Results and discussion

It can be shown for the potential-based approach that L_κ also controls the curvature of a freely evolving crack (Fig. 5.3). For standard gradient models ($L_\kappa = 0$), the crack has a mean curvature of $1/R = 0.004\,31\,\mathrm{mm}^{-1}$, while for $L_\kappa = 1000$ the mean curvature is reduced by 6.5 % to $1/R = 0.004\,03\,\mathrm{mm}^{-1}$. However, the width of the crack remains

virtually unaffected by L_κ. Furthermore, the change of curvature does not affect the ultimate load for this example. To be more precise, the maximum load varies by less than 2 %. Thus, the potential-based approach allows to calibrate the curvature of the emerging crack without interfering with either the loading behavior nor the crack width.

The micro force-based approach also allows to control the crack's curvature without interfering with the crack width (Fig. 5.4). The crack curvatures of the presented extreme cases show a tunability of 20 %. Their values $1/R = 0.0044\,\mathrm{mm}^{-1}$ ($l_\kappa = 0$) and $1/R = 0.0035\,\mathrm{mm}^{-1}$ ($l_\kappa = 5\,l_\alpha$) enclose the case of the standard gradient approach ($l_\kappa = l_\alpha$) to show the control opportunities in both directions for this example. However, the micro force-based modification simultaneously affects the observed maximum load. The force response increases by $\sim$30 %. Thus, the model parameters have to be re-calibrated due to the interaction of curvature control and structural response to loading.

C Appendix

C.1 Approximation of global fields $\boldsymbol{u}$, φ and $\boldsymbol{\chi}$

This appendix covers implementation aspects of both the potential-based model, cf. Subsection 5.1.1, and the micro force-based model, cf. Subsection 5.1.2. Since the underlying micromorphic prototype model (see Section 3.4) as well as the phase-field model (see Subsection 2.4.2) share the same structure, the implementation aspects of the respective extended models are similar.

Starting from the mapping between physical coordinates $\boldsymbol{X}$ and natural coordinates $\boldsymbol{\xi}$ as

$$\boldsymbol{X} = \sum_{A=1}^{n_{en}} \boldsymbol{X}^A \, N^A(\boldsymbol{\xi}) \tag{5.34}$$

allows the computation of the Jacobian matrix $\boldsymbol{J}$ as

$$\boldsymbol{J} = \frac{\partial \boldsymbol{X}}{\partial \boldsymbol{\xi}} = \sum_{A=1}^{n_{en}} \boldsymbol{X}^A \otimes \frac{\partial N^A}{\partial \boldsymbol{\xi}} \, , \tag{5.35}$$

where n_{en} is the number of nodes per element and N^A is the shape function associated with node A. The derivatives of the shape functions with respect to the physical coordinates are given then by

$$\frac{\partial N^A}{\partial \boldsymbol{X}}(\boldsymbol{\xi}) = \frac{\partial N^A}{\partial \boldsymbol{\xi}} \cdot \boldsymbol{J}^{-1} \, . \tag{5.36}$$

Analogously, displacement field $\boldsymbol{u}$, micromorphic field φ, second micromorphic field $\boldsymbol{\chi}$ and their gradients are interpolated as

$$\boldsymbol{u} = \sum_{A=1}^{n_{\text{en}}} \boldsymbol{u}^A \, N^A(\boldsymbol{\xi}) \qquad \Rightarrow \qquad \nabla \boldsymbol{u} = \sum_{A=1}^{n_{\text{en}}} \boldsymbol{u}^A \otimes \frac{\partial N^A}{\partial \boldsymbol{X}}(\boldsymbol{\xi}) \, , \tag{5.37}$$

$$\varphi = \sum_{A=1}^{n_{\text{en}}} \varphi^A \, N^A(\boldsymbol{\xi}) \qquad \Rightarrow \qquad \nabla \varphi = \sum_{A=1}^{n_{\text{en}}} \varphi^A \, \frac{\partial N^A}{\partial \boldsymbol{X}}(\boldsymbol{\xi}) \, , \tag{5.38}$$

$$\boldsymbol{\chi} = \sum_{A=1}^{n_{en}} \boldsymbol{\chi}^A \, N^A(\boldsymbol{\xi}) \qquad \Rightarrow \qquad \nabla \boldsymbol{\chi} = \sum_{A=1}^{n_{en}} \boldsymbol{\chi}^A \otimes \frac{\partial N^A}{\partial \boldsymbol{X}}(\boldsymbol{\xi}) \, . \tag{5.39}$$

By employing a Bubnov-Galerkin-ansatz the variations of $\boldsymbol{u}$, φ and $\boldsymbol{\chi}$ yield

$$\delta\boldsymbol{u} = \sum_{A=1}^{n_{\text{en}}} \delta\boldsymbol{u}^A \, N^A(\boldsymbol{\xi}) \qquad \Rightarrow \qquad \delta\nabla\boldsymbol{u} = \sum_{A=1}^{n_{\text{en}}} \delta\boldsymbol{u}^A \otimes \frac{\partial N^A}{\partial \boldsymbol{X}}(\boldsymbol{\xi}) \; , \tag{5.40}$$

$$\delta\varphi = \sum_{A=1}^{n_{\text{en}}} \delta\varphi^A \, N^A(\boldsymbol{\xi}) \qquad \Rightarrow \qquad \delta\nabla\varphi = \sum_{A=1}^{n_{\text{en}}} \delta\varphi^A \, \frac{\partial N^A}{\partial \boldsymbol{X}}(\boldsymbol{\xi}) \; , \tag{5.41}$$

$$\delta\boldsymbol{\chi} = \sum_{A=1}^{n_{\text{en}}} \delta\boldsymbol{\chi}^A \, N^A(\boldsymbol{\xi}) \qquad \Rightarrow \qquad \delta\nabla\boldsymbol{\chi} = \sum_{A=1}^{n_{\text{en}}} \delta\boldsymbol{\chi}^A \, \frac{\partial N^A}{\partial \boldsymbol{X}}(\boldsymbol{\xi}) \tag{5.42}$$

C.2 Implementation details associated with the potential-based model

Inserting approximations (5.37) – (5.42) into balance equations (2.54), (2.55) and (5.12), respectively, leads to the contribution of element e as

$$\delta_{\boldsymbol{u}}\mathcal{E} \cdot \delta\boldsymbol{u} = \sum_{A=1}^{n_{en}} \int_{\mathcal{B}^e} \left[\boldsymbol{\sigma} \cdot \frac{\partial N^A}{\partial \boldsymbol{X}} \right] \cdot \delta\boldsymbol{u}^A \, \mathrm{d}V \; , \tag{5.43}$$

$$\delta_{\varphi}\mathcal{E} \, \delta\varphi = \sum_{A=1}^{n_{en}} \int_{\mathcal{B}^e} \left[\omega \, N^A + \boldsymbol{\Omega} \cdot \frac{\partial N^A}{\partial \boldsymbol{X}} \right] \delta\varphi^A \, \mathrm{d}V \; , \tag{5.44}$$

$$\delta_{\boldsymbol{\chi}}\mathcal{E} \cdot \delta\boldsymbol{\chi} = \sum_{A=1}^{n_{en}} \int_{\mathcal{B}^e} \left[\boldsymbol{\upsilon} \, N^A + \boldsymbol{\Upsilon} \cdot \frac{\partial N^A}{\partial \boldsymbol{X}} \right] \cdot \delta\boldsymbol{\chi}^A \, \mathrm{d}V \; . \tag{5.45}$$

Clearly, if body forces are present, the respective terms have to be added. Eq. (5.43) – (5.45) motivate residuals

$$\boldsymbol{R}_{\boldsymbol{u}}^{e,\,A} = \int_{\mathcal{B}^e} \boldsymbol{\sigma} \cdot \frac{\partial N^A}{\partial \boldsymbol{X}} \, \mathrm{d}V \; , \tag{5.46}$$

$$\boldsymbol{R}_{\varphi}^{e,\,A} = \int_{\mathcal{B}^e} \left[\omega \, N^A + \boldsymbol{\Omega} \cdot \frac{\partial N^A}{\partial \boldsymbol{X}} \right] \mathrm{d}V \; , \tag{5.47}$$

$$\boldsymbol{R}_{\boldsymbol{\chi}}^{e,\,A} = \int_{\mathcal{B}^e} \left[\boldsymbol{\upsilon} \, N^A + \boldsymbol{\Upsilon} \cdot \frac{\partial N^A}{\partial \boldsymbol{X}} \right] \mathrm{d}V \; . \tag{5.48}$$

An efficient method to solve the resulting non-linear system of equations (after the assembling step) is the Newton-Raphson method. It requires the linearization of residuals (5.46) – (5.48). These linearizations are given as

$$\boldsymbol{K}^{e,\,AB}_{\boldsymbol{u}\boldsymbol{u}} = \int\limits_{\mathcal{B}^e} \frac{\partial N^A}{\partial \boldsymbol{X}} \cdot \frac{\mathrm{d}\boldsymbol{\sigma}}{\mathrm{d}\boldsymbol{\varepsilon}} \cdot \frac{\partial N^B}{\partial \boldsymbol{X}} \,\mathrm{d}V \;, \tag{5.49}$$

$$\boldsymbol{K}^{e,\,AB}_{\boldsymbol{u}\varphi} = \int\limits_{\mathcal{B}^e} \frac{\partial N^A}{\partial \boldsymbol{X}} \cdot \frac{\mathrm{d}\boldsymbol{\sigma}}{\mathrm{d}\varphi} N^B \,\mathrm{d}V \;, \tag{5.50}$$

$$\boldsymbol{K}^{e,\,AB}_{\boldsymbol{u}\boldsymbol{\chi}} = \boldsymbol{0} \;, \tag{5.51}$$

$$\boldsymbol{K}^{e,\,AB}_{\varphi\boldsymbol{u}} = \int\limits_{\mathcal{B}^e} N^A \frac{\mathrm{d}\omega}{\mathrm{d}\boldsymbol{\varepsilon}} \cdot \frac{\partial N^B}{\partial \boldsymbol{X}} \,\mathrm{d}V \;, \tag{5.52}$$

$$\boldsymbol{K}^{e,\,AB}_{\varphi\varphi} = \int\limits_{\mathcal{B}^e} \left[N^A \frac{\mathrm{d}\omega}{\mathrm{d}\varphi} N^B + \frac{\partial N^A}{\partial \boldsymbol{X}} \cdot \frac{\mathrm{d}\boldsymbol{\Omega}}{\mathrm{d}\nabla\varphi} \cdot \frac{\partial N^B}{\partial \boldsymbol{X}} \right] \mathrm{d}V \;, \tag{5.53}$$

$$\boldsymbol{K}^{e,\,AB}_{\varphi\boldsymbol{\chi}} = \int\limits_{\mathcal{B}^e} \frac{\partial N^A}{\partial \boldsymbol{X}} \cdot \frac{\mathrm{d}\boldsymbol{\Omega}}{\mathrm{d}\boldsymbol{\chi}} N^B \,\mathrm{d}V \;, \tag{5.54}$$

$$\boldsymbol{K}^{e,\,AB}_{\boldsymbol{\chi}\boldsymbol{u}} = \boldsymbol{0} \;, \tag{5.55}$$

$$\boldsymbol{K}^{e,\,AB}_{\boldsymbol{\chi}\varphi} = \int\limits_{\mathcal{B}^e} N^A \frac{\mathrm{d}\boldsymbol{v}}{\mathrm{d}\nabla\varphi} \cdot \frac{\partial N^B}{\partial \boldsymbol{X}} \,\mathrm{d}V \;, \tag{5.56}$$

$$\begin{aligned} \boldsymbol{K}^{e,\,AB}_{\boldsymbol{\chi}\boldsymbol{\chi}} = & \int\limits_{\mathcal{B}^e} \left[N^A \frac{\mathrm{d}\boldsymbol{v}}{\mathrm{d}\boldsymbol{\chi}} N^B + N^A \frac{\mathrm{d}\boldsymbol{v}}{\mathrm{d}\nabla\boldsymbol{\chi}} \cdot \frac{\partial N^B}{\partial \boldsymbol{X}} \right] \mathrm{d}V \\ & + \int\limits_{\mathcal{B}^e} \left[\frac{\partial N^A}{\partial \boldsymbol{X}} \bullet \frac{\mathrm{d}\boldsymbol{\Upsilon}}{\mathrm{d}\boldsymbol{\chi}} N^B + \frac{\partial N^A}{\partial \boldsymbol{X}} \bullet \frac{\mathrm{d}\boldsymbol{\Upsilon}}{\mathrm{d}\nabla\boldsymbol{\chi}} \cdot \frac{\partial N^B}{\partial \boldsymbol{X}} \right] \mathrm{d}V \end{aligned} \tag{5.57}$$

where $\bullet$ indicates a contraction with respect to the second index. Stiffness matrices (5.49), (5.50), (5.52) and (5.53) are directly related to the linearizations of $\boldsymbol{\sigma}$ and ω. For the micromorphic prototype model, cf. Section 3.4, they are given as

$$\mathrm{d}\boldsymbol{\sigma} = \left[\frac{\partial \boldsymbol{\sigma}}{\partial \boldsymbol{\varepsilon}} + \frac{\partial \boldsymbol{\sigma}}{\partial \alpha} \frac{\mathrm{d}\alpha}{\mathrm{d}\boldsymbol{\varepsilon}} \right] : \mathrm{d}\boldsymbol{\varepsilon} + \frac{\partial \boldsymbol{\sigma}}{\partial \alpha} \frac{\mathrm{d}\alpha}{\mathrm{d}\varphi} \,\mathrm{d}\varphi \;, \tag{5.58}$$

$$\mathrm{d}\omega = \frac{\partial \omega}{\partial \alpha} \frac{\mathrm{d}\alpha}{\mathrm{d}\boldsymbol{\varepsilon}} : \mathrm{d}\boldsymbol{\varepsilon} + \left[\frac{\partial \omega}{\partial \varphi} + \frac{\partial \omega}{\partial \alpha} \frac{\mathrm{d}\alpha}{\mathrm{d}\varphi} \right] \mathrm{d}\varphi \;, \tag{5.59}$$

where state variable α is computed by solving optimization problem (3.34). The sensitivities are then computed by a linearization of indicator function Φ at a converged state as

$$\mathrm{d}\alpha = \underbrace{-\left[\frac{\mathrm{d}\Phi}{\mathrm{d}\alpha}\right]^{-1} \frac{\partial\alpha}{\partial\boldsymbol{\varepsilon}}}_{=\dfrac{\mathrm{d}\alpha}{\mathrm{d}\boldsymbol{\varepsilon}}} : \mathrm{d}\boldsymbol{\varepsilon} \underbrace{-\left[\frac{\mathrm{d}\Phi}{\mathrm{d}\alpha}\right]^{-1} \frac{\partial\alpha}{\partial\varphi}}_{=\dfrac{\mathrm{d}\alpha}{\mathrm{d}\varphi}} \mathrm{d}\varphi \,. \tag{5.60}$$

The linearization of $\boldsymbol{\Omega}$, $\boldsymbol{\upsilon}$, $\boldsymbol{\Upsilon}$ depend on the specific choice of curvature-related Helmholtz energy (5.15), which can be rewritten in terms of modified curvature expression $\tilde{r}_\kappa$ as

$$\begin{aligned}\psi^{\mathrm{curv}} &= \frac{c_\chi}{2}\,||\boldsymbol{\chi} - \nabla\varphi||^2 + \frac{L_\chi}{2}\,\left[||\boldsymbol{\chi}||^2\, r_\kappa\right]^2 \\ &= \frac{c_\chi}{2}\,||\boldsymbol{\chi} - \nabla\varphi||^2 + \frac{L_\chi}{2}\,\underbrace{\left[\boldsymbol{\chi}\cdot\nabla\boldsymbol{\chi} - ||\boldsymbol{\chi}||^2\,\mathrm{tr}\,(\nabla\boldsymbol{\chi})\right]}_{=:\tilde{r}_\kappa}^2 \,.\end{aligned} \tag{5.61}$$

The thermodynamic driving forces then read

$$\boldsymbol{\Omega} = \frac{\partial\psi}{\partial\nabla\varphi} = l^\bullet\,\nabla\varphi + c_\chi\,[\nabla\varphi - \boldsymbol{\chi}] \;, \tag{5.62}$$

$$\boldsymbol{\upsilon} = \frac{\partial\psi}{\partial\boldsymbol{\chi}} = c_\chi\,[\boldsymbol{\chi} - \nabla\varphi] + L_\kappa\,\tilde{r}_\kappa\,\frac{\partial\tilde{r}_\kappa}{\partial\boldsymbol{\chi}} \;, \tag{5.63}$$

$$\boldsymbol{\Upsilon} = \frac{\partial\psi}{\partial\nabla\boldsymbol{\chi}} = L_\kappa\,\tilde{r}_\kappa\,\frac{\partial\tilde{r}_\kappa}{\partial\nabla\boldsymbol{\chi}} \;, \tag{5.64}$$

where $\boldsymbol{\upsilon}$ and $\boldsymbol{\Upsilon}$ are energetically dual to micromorphic field $\boldsymbol{\chi}$ and $\nabla\boldsymbol{\chi}$. In order to evaluate stiffness matrices (5.49) – (5.57) the computation of the total derivatives w.r.t. $\nabla\varphi$, $\boldsymbol{\chi}$ and $\nabla\boldsymbol{\chi}$ are required. They follow as

$$\frac{\mathrm{d}\boldsymbol{\Omega}}{\mathrm{d}\nabla\varphi} = [l^\bullet + c_\chi]\,\boldsymbol{I} \;, \tag{5.65}$$

$$\frac{\mathrm{d}\boldsymbol{\Omega}}{\mathrm{d}\boldsymbol{\chi}} = -c_\chi\,\boldsymbol{I} \;, \tag{5.66}$$

$$\frac{\mathrm{d}\boldsymbol{\upsilon}}{\mathrm{d}\nabla\varphi} = -c_\chi\,\boldsymbol{I} \;, \tag{5.67}$$

$$\frac{\mathrm{d}\boldsymbol{\upsilon}}{\mathrm{d}\boldsymbol{\chi}} = c_\chi\,\boldsymbol{I} + L_\kappa\,\left[\frac{\partial\tilde{r}_\kappa}{\partial\boldsymbol{\chi}} \otimes \frac{\partial\tilde{r}_\kappa}{\partial\boldsymbol{\chi}} + \tilde{r}_\kappa\,\frac{\partial^2\tilde{r}_\kappa}{\partial\boldsymbol{\chi}\,\partial\boldsymbol{\chi}}\right] \;, \tag{5.68}$$

$$\frac{\mathrm{d}\boldsymbol{\upsilon}}{\mathrm{d}\nabla\boldsymbol{\chi}} = L_\kappa\,\left[\frac{\partial\tilde{r}_\kappa}{\partial\boldsymbol{\chi}} \otimes \frac{\partial\tilde{r}_\kappa}{\partial\nabla\boldsymbol{\chi}} + \tilde{r}_\kappa\,\frac{\partial^2\tilde{r}_\kappa}{\partial\boldsymbol{\chi}\,\partial\nabla\boldsymbol{\chi}}\right] \;, \tag{5.69}$$

$$\frac{\mathrm{d}\boldsymbol{\Upsilon}}{\mathrm{d}\boldsymbol{\chi}} = L_\kappa \left[\frac{\partial \tilde{r}_\kappa}{\partial \nabla\boldsymbol{\chi}} \otimes \frac{\partial \tilde{r}_\kappa}{\partial \boldsymbol{\chi}} + \tilde{r}_\kappa \frac{\partial^2 \tilde{r}_\kappa}{\partial \nabla\boldsymbol{\chi}\, \partial \boldsymbol{\chi}} \right] , \tag{5.70}$$

$$\frac{\mathrm{d}\boldsymbol{\Upsilon}}{\mathrm{d}\nabla\boldsymbol{\chi}} = L_\kappa \frac{\partial \tilde{r}_\kappa}{\partial \nabla\boldsymbol{\chi}} \otimes \frac{\partial \tilde{r}_\kappa}{\partial \nabla\boldsymbol{\chi}} . \tag{5.71}$$

These derivatives, in turn, depend on the derivatives of $\tilde{r}_\kappa$. A straightforward computation yields

$$\frac{\partial \tilde{r}_\kappa}{\partial \boldsymbol{\chi}} = \nabla\boldsymbol{\chi} \cdot \boldsymbol{\chi} + \boldsymbol{\chi} \cdot \nabla\boldsymbol{\chi} - 2\,\boldsymbol{\chi}\,\mathrm{tr}\,(\nabla\boldsymbol{\chi}) , \tag{5.72}$$

$$\frac{\partial \tilde{r}_\kappa}{\partial \nabla\boldsymbol{\chi}} = \boldsymbol{\chi} \otimes \boldsymbol{\chi} - ||\boldsymbol{\chi}||^2\, \boldsymbol{I} \tag{5.73}$$

and

$$\frac{\partial^2 \tilde{r}_\kappa}{\partial \boldsymbol{\chi} \partial \boldsymbol{\chi}} = \nabla\boldsymbol{\chi} + \nabla^T\boldsymbol{\chi} - 2\,\mathrm{tr}\,(\nabla\boldsymbol{\chi})\, \boldsymbol{I} , \tag{5.74}$$

$$\frac{\partial^2 \tilde{r}_\kappa}{\partial \chi_i\, \partial [\nabla\boldsymbol{\chi}]_{jk}} = \delta_{ij}\,\chi_k + \delta_{ik}\,\chi_j - 2\,\chi_i\,\delta_{kl} , \tag{5.75}$$

$$\frac{\partial^2 \tilde{r}_\kappa}{\partial [\nabla\boldsymbol{\chi}]_{ij}\, \partial \chi_k} = \frac{\partial^2 \tilde{r}_\kappa}{\partial \chi_k\, \partial [\nabla\boldsymbol{\chi}]_{ij}} , \tag{5.76}$$

where the mixed derivatives are given in index notation.

C.3 Implementation details associated with the micro force-based model

The implementation is based on inserting approximations (5.37) – (5.42) into balance equations (2.54), (2.55) and (5.30). The resulting non-linear system of equation (contribution due to element e) reads

$$\boldsymbol{R}^{e,\,A}_{\boldsymbol{u}} = \int_{\mathcal{B}^e} \boldsymbol{\sigma} \cdot \frac{\partial N^A}{\partial \boldsymbol{X}}\, \mathrm{d}V \tag{5.77}$$

$$\boldsymbol{R}^{e,\,A}_{\varphi} = \int_{\mathcal{B}^e} \left[\omega\, N^A - [l^\bullet - l^\bullet_\kappa]\; r_\kappa\, N^A + \boldsymbol{\Omega} \cdot \frac{\partial N^A}{\partial \boldsymbol{X}} - \boldsymbol{\varsigma} \cdot \frac{\partial N^A}{\partial \boldsymbol{X}} \right] \mathrm{d}V \tag{5.78}$$

$$\boldsymbol{R}^{e,\,A}_{\boldsymbol{\chi}} = \int_{\mathcal{B}^e} \boldsymbol{\varsigma}\, N^A\, \mathrm{d}V \tag{5.79}$$

and its corresponding stiffness matrices follow as

$$\boldsymbol{K}^{e,\,AB}_{\boldsymbol{u}\boldsymbol{u}} = \frac{\mathrm{d}\boldsymbol{R}^{e,\,A}_{\boldsymbol{u}}}{\mathrm{d}\boldsymbol{u}^{B}} = \int\limits_{\mathcal{B}^e} \frac{\partial N^A}{\partial \boldsymbol{X}} \cdot \frac{\mathrm{d}\boldsymbol{\sigma}}{\mathrm{d}\boldsymbol{\varepsilon}} \cdot \frac{\partial N^B}{\partial \boldsymbol{X}} \,\mathrm{d}V \;, \tag{5.80}$$

$$\boldsymbol{K}^{e,\,AB}_{\boldsymbol{u}\varphi} = \frac{\mathrm{d}\boldsymbol{R}^{e,\,A}_{\boldsymbol{u}}}{\mathrm{d}\varphi^{B}} = \int\limits_{\mathcal{B}^e} \frac{\partial N^A}{\partial \boldsymbol{X}} \cdot \frac{\mathrm{d}\boldsymbol{\sigma}}{\mathrm{d}\varphi} \, N^B \,\mathrm{d}V \;, \tag{5.81}$$

$$\boldsymbol{K}^{e,\,AB}_{\boldsymbol{u}\boldsymbol{\chi}} = \frac{\mathrm{d}\boldsymbol{R}^{e,\,A}_{\boldsymbol{u}}}{\mathrm{d}\boldsymbol{\chi}^{B}} = \boldsymbol{0} \;, \tag{5.82}$$

$$\boldsymbol{K}^{e,\,AB}_{\varphi\boldsymbol{u}} = \frac{\mathrm{d}\boldsymbol{R}^{e,\,A}_{\varphi}}{\mathrm{d}\boldsymbol{u}^{B}} = \int\limits_{\mathcal{B}^e} N^A \, \frac{\mathrm{d}\omega}{\mathrm{d}\boldsymbol{\varepsilon}} \, \frac{\partial N^B}{\partial \boldsymbol{X}} \,\mathrm{d}V \;, \tag{5.83}$$

$$\boldsymbol{K}^{e,\,AB}_{\varphi\varphi} = \frac{\mathrm{d}\boldsymbol{R}^{e,\,A}_{\varphi}}{\mathrm{d}\varphi^{B}} = \int\limits_{\mathcal{B}^e} \left[N^A \, \frac{\mathrm{d}\omega}{\mathrm{d}\varphi} \, N^B + [l^\bullet + c_\chi] \, \frac{\partial N^A}{\partial \boldsymbol{X}} \cdot \frac{\partial N^B}{\partial \boldsymbol{X}} \right] \mathrm{d}V \;, \tag{5.84}$$

$$\begin{aligned} \boldsymbol{K}^{e,\,AB}_{\varphi\boldsymbol{\chi}} = \frac{\mathrm{d}\boldsymbol{R}^{e,\,A}_{\varphi}}{\mathrm{d}\boldsymbol{\chi}^{B}} = \int\limits_{\mathcal{B}^e} \Bigg[& N^A \, [l^\bullet - l^\bullet_\kappa] \, \frac{\mathrm{d}r_\kappa}{\mathrm{d}\boldsymbol{\chi}} \, N^B - c_\chi \, \frac{\partial N^A}{\partial \boldsymbol{X}} \, N^B \\ & + N^A \, [l^\bullet - l^\bullet_\kappa] \, \frac{\mathrm{d}r_\kappa}{\mathrm{d}\nabla\boldsymbol{\chi}} \cdot \frac{\partial N^B}{\partial \boldsymbol{X}} \Bigg] \,\mathrm{d}V \;, \end{aligned} \tag{5.85}$$

$$\boldsymbol{K}^{e,\,AB}_{\boldsymbol{\chi}\boldsymbol{u}} = \frac{\mathrm{d}\boldsymbol{R}^{e,\,A}_{\chi}}{\mathrm{d}\boldsymbol{u}^{B}} = \boldsymbol{0} \;, \tag{5.86}$$

$$\boldsymbol{K}^{e,\,AB}_{\boldsymbol{\chi}\varphi} = \frac{\mathrm{d}\boldsymbol{R}^{e,\,A}_{\boldsymbol{\chi}}}{\mathrm{d}\varphi^{B}} = \int\limits_{\mathcal{B}^e} -c_\chi \, N^A \, \frac{\partial N^B}{\partial \boldsymbol{X}} \,\mathrm{d}V \;, \tag{5.87}$$

$$\boldsymbol{K}^{e,\,AB}_{\boldsymbol{\chi}\boldsymbol{\chi}} = \frac{\mathrm{d}\boldsymbol{R}^{e,\,A}_{\boldsymbol{\chi}}}{\mathrm{d}\boldsymbol{\chi}^{B}} = \int\limits_{\mathcal{B}^e} c_\chi \, N^A \, \boldsymbol{I} \, N^B \,\mathrm{d}V \;. \tag{5.88}$$

The linearizations of $\boldsymbol{\sigma}$ and ω are identical to those computed in eq. (5.58) – (5.60). Hence, only the linearization of r^χ remains to be derived. It is given in closed format as

$$\frac{\mathrm{d}r_\kappa}{\mathrm{d}\boldsymbol{\chi}} = \frac{1}{||\boldsymbol{\chi}||} \, [\boldsymbol{n}_{\boldsymbol{\chi}} \cdot \nabla\boldsymbol{\chi} + \nabla\boldsymbol{\chi} \cdot \boldsymbol{n}_{\boldsymbol{\chi}} - 2\, \boldsymbol{n}_{\boldsymbol{\chi}} \cdot \nabla\boldsymbol{\chi} \cdot \boldsymbol{n}_{\boldsymbol{\chi}} \, \boldsymbol{n}_{\boldsymbol{\chi}}] \;, \tag{5.89}$$

$$\frac{\mathrm{d}r_\kappa}{\mathrm{d}\nabla\boldsymbol{\chi}} = \boldsymbol{n}_{\boldsymbol{\chi}} \otimes \boldsymbol{n}_{\boldsymbol{\chi}} - \boldsymbol{I} \;, \tag{5.90}$$

so that all residuals (5.77) – (5.79) and stiffness matrices (5.80) – (5.88) can be computed. Eq. (5.90) can be interpreted as the negative unit tensor or projection operator onto the (crack) interface, cf. [166, 173].

C.4 Curvature expression r_κ in axisymmetric coordinates

The special case of rotational symmetry in a two-dimensional space, i.e., the space spanned by radius R and angle Θ, leads to a simplification of curvature expression (5.7). From $\nabla\varphi = \partial_R\varphi\, \boldsymbol{e}_R$ follows $\boldsymbol{\chi} = \chi\, \boldsymbol{e}_R$ with $\boldsymbol{e}_R$ being the unity vector in radial direction and χ being a scalar variable. Therefore $\boldsymbol{n}_{\boldsymbol{\chi}}$ follows as $\boldsymbol{n}_{\boldsymbol{\chi}} = \boldsymbol{e}_R$ and $\nabla\boldsymbol{\chi}$ as

$$\nabla\boldsymbol{\chi} = \frac{\partial\chi}{\partial R}\, \boldsymbol{e}_R \otimes \boldsymbol{e}_R + \frac{\chi}{R}\, \boldsymbol{e}_\Theta \otimes \boldsymbol{e}_\Theta \,. \tag{5.91}$$

Inserting of $\boldsymbol{n}_{\boldsymbol{\chi}}$ and $\nabla\boldsymbol{\chi}$ into curvature expression (5.7) leads to

$$r_\kappa = -\frac{\chi}{R} \tag{5.92}$$

and consequently

$$\frac{\mathrm{d}r_\kappa}{\mathrm{d}\boldsymbol{\chi}} = \boldsymbol{0} \,, \tag{5.93}$$

$$\frac{\mathrm{d}r_\kappa}{\mathrm{d}\nabla\boldsymbol{\chi}} = -\boldsymbol{e}_\Theta \otimes \boldsymbol{e}_\Theta \,. \tag{5.94}$$

6 Modeling anisotropic, ductile damage

In this chapter a prototype model suitable for anisotropic, ductile damage is presented. The underlying framework can be traced back to *Steinmann and Carol* [174]. It provides a basis for the modeling of anisotropic damage by using a second-order damage tensor complying with the principle of strain energy equivalence. That framework was extended to multiplicative elasto-plasticity [105] and adapted to the geometrically linearized theory [51, 106]. The latter models are also based on the principle of Generalized Standard Materials [67, 112]. This chapter briefly recaps the principle of Generalized Standard Materials and the principle of strain energy equivalence according to [174]. Afterwards, a prototype model suitable for anisotropic, ductile damage is presented.

6.1 Fundamentals

6.1.1 Principle of Generalized Standard Materials

In what follows, isothermal constitutive models are considered. In order to capture irreversible effects, the concept of internal variables is adopted. The respective strain-like variables are denoted as $\boldsymbol{q} \in \mathbb{R}^n$. With these assumptions – and focusing on local rate-independent models, Helmholtz energy ψ is of type $\psi = \psi(\boldsymbol{\varepsilon}, \boldsymbol{q})$. In this case, the dissipation inequality follows as

$$\mathcal{D} = \boldsymbol{\sigma} : \dot{\boldsymbol{\varepsilon}} - \dot{\psi} = \left[\boldsymbol{\sigma} - \frac{\partial \psi}{\partial \boldsymbol{\varepsilon}}\right] : \dot{\boldsymbol{\varepsilon}} - \frac{\partial \psi}{\partial \boldsymbol{q}} \bullet \dot{\boldsymbol{q}} \geq 0 \,, \tag{6.1}$$

where the superimposed dot denotes the (material) time derivative, $\bullet$ a suitable contraction and a stress power of type $\mathcal{P} = \boldsymbol{\sigma} : \dot{\boldsymbol{\varepsilon}}$ is chosen. Application of the Coleman

and Noll procedure [37, 38] yields stress response $\boldsymbol{\sigma} = \partial_{\boldsymbol{\varepsilon}} \psi$ as well as reduced dissipation inequality

$$\mathcal{D}_{\text{red}} = -\frac{\partial \psi}{\partial \boldsymbol{q}} \bullet \dot{\boldsymbol{q}} =: \boldsymbol{Q} \bullet \dot{\boldsymbol{q}} \geq 0 \tag{6.2}$$

with $\boldsymbol{Q} := -\partial_{\boldsymbol{q}} \psi$ defining the stress-like internal variables being dual to $\boldsymbol{q}$.

The model is completed by suitable evolution equations governing $\dot{\boldsymbol{q}}$ as well as by proper loading/unloading conditions which are implicitly defined through a yield function. To be more precise, space of admissible stresses

$$\mathbb{E}_{\boldsymbol{\sigma}} = \{(\boldsymbol{\sigma}, \boldsymbol{Q}; \boldsymbol{q}) \in \mathbb{R}^n \,|\, \Phi(\boldsymbol{\sigma}, \boldsymbol{Q}; \boldsymbol{q}) \leq 0\} \tag{6.3}$$

is introduced which is spanned by yield function $\Phi(\boldsymbol{\sigma}, \boldsymbol{Q}; \boldsymbol{q})$. Based on yield function Φ the loading/unloading conditions can be summarized as

$$\lambda \geq 0 \,, \quad \Phi \leq 0 \,, \quad \lambda \, \Phi = 0 \,, \tag{6.4}$$

where $\lambda \geq 0$ is the plastic multiplier. It bears emphasis that parameterization $\Phi = \Phi(\boldsymbol{\sigma}, \boldsymbol{Q}; \boldsymbol{q})$ is not standard, since usually Φ is assumed to depend only on stress-like variables (or only on strain-like variables). By way of contrast, Φ in eq. (6.3) also depends – in addition to stress-like variable $\boldsymbol{Q}$ – on its dual strain-like internal variable $\boldsymbol{q}$. However, by applying the inverse function theorem to $\boldsymbol{Q} = \partial_{\boldsymbol{q}} \psi$, both representations are indeed equivalent, i.e., $\Phi(\boldsymbol{\sigma}, \boldsymbol{Q}; \boldsymbol{q}) = \tilde{\Phi}(\boldsymbol{\sigma}, \boldsymbol{Q})$.

In line with the framework of Generalized Standard Materials, evolution equation $\dot{\boldsymbol{q}}$ is postulated as a (partial) gradient of convex and non-negative plastic potential g (it also has to contain the origin in the sense that $g(\boldsymbol{0}) = 0$). Plastic potential g is not necessarily identical to yield function Φ. For rate-dependent plasticity, i.e., viscoplasticity, a multiplicative ansatz is given as

$$g = f^{\text{vis}} \langle \Phi \rangle^n \,, \tag{6.5}$$

where f^{vis} denotes a suitable factor, which depends on a time scale and might depend on additional internal variables, see, e.g., [31] among others. The expression $\langle \bullet \rangle$ denotes the Macaulay brackets, which excludes elastic stress states from the evolution law. By assuming an associative flow rule ($\dot{\boldsymbol{\varepsilon}}^{\text{p}} = \lambda \, \partial_{\boldsymbol{\sigma}} \Phi$) and focusing on rate-independent models, plastic potential g is oftentimes additively decomposed according to

$$g(\boldsymbol{\sigma}, \boldsymbol{Q}; \boldsymbol{q}) = \Phi(\boldsymbol{\sigma}, \boldsymbol{Q}; \boldsymbol{q}) + \Gamma(\boldsymbol{Q}; \boldsymbol{q}) \,. \tag{6.6}$$

Γ denotes the non-associative part of the potential, which allows to alter the evolution laws of internal variables without modifying the yield criterion, cf. [8]. Hence, it provides the model with an increased flexibility. Again and analogously to yield function Φ, g

is parameterized in terms of $(\boldsymbol{\sigma},\, \boldsymbol{Q};\, \boldsymbol{q})$. Having defined g, the evolution equations are postulated as

$$\dot{\boldsymbol{\varepsilon}}^{\mathrm{p}} = \lambda\, \partial_{\boldsymbol{\sigma}} g = \lambda\, \partial_{\boldsymbol{\sigma}} \Phi \;, \tag{6.7}$$

$$\dot{\boldsymbol{q}} = \lambda\, \partial_{\boldsymbol{Q}} g = \lambda\, \left[\partial_{\boldsymbol{Q}} \Phi + \partial_{\boldsymbol{Q}} \Gamma\right] . \tag{6.8}$$

It is important to note that – in contrast to yield function $\Phi(\boldsymbol{\sigma},\, \boldsymbol{Q};\, \boldsymbol{q})$ – parameterization $g(\boldsymbol{\sigma},\, \boldsymbol{Q};\, \boldsymbol{q})$ indeed adds a certain flexibility to the model. To be more precise, although application of the inverse function theorem results again in $g(\boldsymbol{\sigma},\, \boldsymbol{Q};\, \boldsymbol{q}) = \tilde{g}(\boldsymbol{\sigma},\, \boldsymbol{Q})$, parameterization $g(\boldsymbol{\sigma},\, \boldsymbol{Q};\, \boldsymbol{q})$ affects the evolution equation. More explicitly speaking, the resulting evolution equations differ, i.e., $\partial_{\boldsymbol{Q}} g(\boldsymbol{\sigma},\, \boldsymbol{Q};\, \boldsymbol{q}) \neq \partial_{\boldsymbol{Q}} \tilde{g}(\boldsymbol{\sigma},\, \boldsymbol{Q})$. It will be shown that this flexibility allows the modeling of ductile gradient-enhanced damage evolution by means of a single failure/yield function.

6.1.2 Principle of strain energy equivalence

The principle is based on the introduction of a fictitious undamaged configuration which is connected to the damaged configuration by the so-called damage deformation gradient $\bar{\boldsymbol{F}}_d$. A schematic illustration is provided in Fig. 6.1. Quantities belonging to the

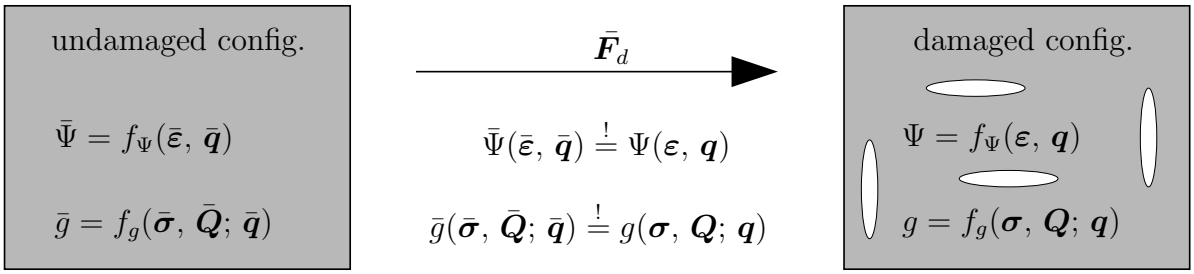

Figure 6.1: Schematic illustration of the principle of strain energy equivalence between the damaged configuration and a fictitious undamaged configuration. The superposed bar signals variables belonging to the fictitious undamaged configuration. The set of internal variables is denoted as $\boldsymbol{q}$.

undamaged configuration are marked as $\bar{\bullet}$. In the spirit of finite strain plasticity the push- and pull operations for co- and contravariant tensors are used. Assuming $\boldsymbol{\varepsilon}$ as covariant, the transformation rule yields

$$\boldsymbol{\varepsilon} = \bar{\boldsymbol{F}}_d^{\,-T} \cdot \bar{\boldsymbol{\varepsilon}} \cdot \bar{\boldsymbol{F}}_d^{\,-1} \;. \tag{6.9}$$

By way of contrast, the transformation rule for contravariant tensors, e.g. for the stress tensor $\boldsymbol{\sigma}$, is given by

$$\boldsymbol{\sigma} = \bar{\boldsymbol{F}}_d \cdot \bar{\boldsymbol{\sigma}} \cdot \bar{\boldsymbol{F}}_d^{\,T} \;. \tag{6.10}$$

As a consequence of both transformation rules (6.9) and (6.10) the double contraction of energetic dual quantities

$$\boldsymbol{\sigma} : \boldsymbol{\varepsilon} = \left[\bar{\boldsymbol{F}}_d \cdot \tilde{\boldsymbol{\sigma}} \cdot \bar{\boldsymbol{F}}_d{}^T\right] : \left[\bar{\boldsymbol{F}}_d{}^{-T} \cdot \bar{\boldsymbol{\varepsilon}} \cdot \bar{\boldsymbol{F}}_d{}^{-1}\right] = \bar{\boldsymbol{\sigma}} : \bar{\boldsymbol{\varepsilon}} \tag{6.11}$$

is independent of the configuration. This allows the principle of strain energy equivalence to be presented as

$$\psi(\boldsymbol{\varepsilon}, \boldsymbol{q}) = \psi(\bar{\boldsymbol{\varepsilon}}, \bar{\boldsymbol{q}}) = \psi(\bar{\boldsymbol{F}}_d{}^T \cdot \boldsymbol{\varepsilon} \cdot \bar{\boldsymbol{F}}_d,\, \bar{\boldsymbol{F}}_d{}^T \cdot \boldsymbol{q} \cdot \bar{\boldsymbol{F}}_d) \quad \forall\, \bar{\boldsymbol{F}}_d\,, \tag{6.12}$$

$$g(\boldsymbol{\sigma}, \boldsymbol{Q}) = g(\bar{\boldsymbol{\sigma}}, \bar{\boldsymbol{Q}}) = g(\bar{\boldsymbol{F}}_d \cdot \bar{\boldsymbol{\sigma}} \cdot \bar{\boldsymbol{F}}_d{}^T,\, \bar{\boldsymbol{F}}_d \cdot \bar{\boldsymbol{Q}} \cdot \bar{\boldsymbol{F}}_d{}^T) \quad \forall\, \bar{\boldsymbol{F}}_d\,. \tag{6.13}$$

The key idea to fulfill these equations, and thus the principle of strain energy equivalence, is to specify Helmholtz energy ψ and plastic potential g solely in terms of invariants in the sense of eq. (6.11). Those invariants for covariant tensors are for instance given in [106] as

$$i_1^{\boldsymbol{\varepsilon}} = \bar{\boldsymbol{I}} : \bar{\boldsymbol{\varepsilon}} = [\bar{\boldsymbol{F}}_d{}^T \cdot \bar{\boldsymbol{F}}_d{}^{-T}] : [\bar{\boldsymbol{F}}_d{}^T \cdot \boldsymbol{\varepsilon} \cdot \bar{\boldsymbol{F}}_d] = \boldsymbol{b} : \boldsymbol{\varepsilon}\,, \tag{6.14}$$

$$i_2^{\boldsymbol{\varepsilon}} = \bar{\boldsymbol{I}} : \bar{\boldsymbol{\varepsilon}}^2 = [\bar{\boldsymbol{F}}_d{}^T \cdot \bar{\boldsymbol{F}}_d{}^{-T}] : [\bar{\boldsymbol{F}}_d{}^T \cdot \boldsymbol{\varepsilon} \cdot \bar{\boldsymbol{F}}_d]^2 = \boldsymbol{b} : [\boldsymbol{\varepsilon} \cdot \boldsymbol{b} \cdot \boldsymbol{\varepsilon}]\,, \tag{6.15}$$

$$i_3^{\boldsymbol{\varepsilon}} = \bar{\boldsymbol{I}} : \bar{\boldsymbol{\varepsilon}}^3 = [\bar{\boldsymbol{F}}_d{}^T \cdot \bar{\boldsymbol{F}}_d{}^{-T}] : [\bar{\boldsymbol{F}}_d{}^T \cdot \boldsymbol{\varepsilon} \cdot \bar{\boldsymbol{F}}_d]^3 = \boldsymbol{b} : [\boldsymbol{\varepsilon} \cdot \boldsymbol{b} \cdot \boldsymbol{\varepsilon} \cdot \boldsymbol{b} \cdot \boldsymbol{\varepsilon}]\,. \tag{6.16}$$

and for contravariant tensors as

$$i_1^{\boldsymbol{\sigma}} = \bar{\boldsymbol{I}} : \bar{\boldsymbol{\sigma}} = [\bar{\boldsymbol{F}}_d{}^T \cdot \bar{\boldsymbol{F}}_d{}^{-T}] : [\bar{\boldsymbol{F}}_d{}^{-1} \cdot \boldsymbol{\sigma} \cdot \bar{\boldsymbol{F}}_d{}^{-T}] = \boldsymbol{b}^{-1} : \boldsymbol{\sigma}\,, \tag{6.17}$$

$$i_2^{\boldsymbol{\sigma}} = \bar{\boldsymbol{I}} : \bar{\boldsymbol{\sigma}}^2 = [\bar{\boldsymbol{F}}_d{}^T \cdot \bar{\boldsymbol{F}}_d{}^{-T}] : [\bar{\boldsymbol{F}}_d{}^{-1} \cdot \boldsymbol{\sigma} \cdot \bar{\boldsymbol{F}}_d{}^{-T}]^2 = \boldsymbol{b}^{-1} : [\boldsymbol{\sigma} \cdot \boldsymbol{b}^{-1} \cdot \boldsymbol{\sigma}]\,, \tag{6.18}$$

$$i_3^{\boldsymbol{\sigma}} = \bar{\boldsymbol{I}} : \bar{\boldsymbol{\sigma}}^3 = [\bar{\boldsymbol{F}}_d{}^T \cdot \bar{\boldsymbol{F}}_d{}^{-T}] : [\bar{\boldsymbol{F}}_d{}^{-1} \cdot \boldsymbol{\sigma} \cdot \bar{\boldsymbol{F}}_d{}^{-T}]^3 = \boldsymbol{b}^{-1} : [\boldsymbol{\sigma} \cdot \boldsymbol{b}^{-1} \cdot \boldsymbol{\sigma} \cdot \boldsymbol{b}^{-1} \cdot \boldsymbol{\sigma}]\,. \tag{6.19}$$

Here, tensor

$$\boldsymbol{b} := \bar{\boldsymbol{F}}_d \cdot \bar{\boldsymbol{F}}_d{}^T = \bar{\boldsymbol{F}}_d \cdot \bar{\boldsymbol{I}} \cdot \bar{\boldsymbol{F}}_d{}^T =: \bar{\boldsymbol{F}}_d \cdot \bar{\boldsymbol{b}} \cdot \bar{\boldsymbol{F}}_d{}^T \qquad \text{with} \qquad \bar{\boldsymbol{b}} = \bar{\boldsymbol{I}} \tag{6.20}$$

can be interpreted as a contra-variant continuity tensor. For instance, an initially undamaged material (at time t_0) corresponds to $\bar{\boldsymbol{F}}_d(t_0) = \boldsymbol{I}$, i.e., the fictitious undamaged configuration is identical to its damaged counterpart and, thus, $\boldsymbol{b}(t_0) = \boldsymbol{I}$. This observation is in line with $\bar{\boldsymbol{b}} = \bar{\boldsymbol{I}}$, since the fictitious configuration is by definition undamaged. By way of contrast, in the case of a fully damaged state, tensor $\bar{\boldsymbol{F}}_d$ and likewise tensor $\boldsymbol{b}$ show, at least, one zero eigenvalue. Focusing on a one-dimensional setting, this property simplifies to $b \to 0$, as required for a continuity measure.
From a differential geometric point of view, eq. (6.20) can be interpreted as a push-

forward transformation of tensor $\bar{\boldsymbol{b}}$. This, in turn, allows the rewriting of eqs. (6.14)-(6.16) as (since $\bar{\boldsymbol{b}} = \bar{\boldsymbol{I}}$)

$$i_1^{\boldsymbol{\varepsilon}} = \boldsymbol{b} : \boldsymbol{\varepsilon} = \bar{\boldsymbol{b}} : \bar{\varepsilon} = \bar{\boldsymbol{I}} : \bar{\varepsilon} \tag{6.21}$$

$$i_2^{\boldsymbol{\varepsilon}} = \boldsymbol{b} : [\boldsymbol{\varepsilon} \cdot \boldsymbol{b} \cdot \boldsymbol{\varepsilon}] = \bar{\boldsymbol{b}} : \left[\bar{\varepsilon} \cdot \bar{\boldsymbol{b}} \cdot \bar{\varepsilon}\right] = \bar{\boldsymbol{I}} : \bar{\varepsilon}^2 \tag{6.22}$$

$$i_3^{\boldsymbol{\varepsilon}} = \boldsymbol{b} : [\boldsymbol{\varepsilon} \cdot \boldsymbol{b} \cdot \boldsymbol{\varepsilon} \cdot \boldsymbol{b} \cdot \boldsymbol{\varepsilon}] = \bar{\boldsymbol{b}} : \left[\bar{\varepsilon} \cdot \bar{\boldsymbol{b}} \cdot \bar{\varepsilon} \cdot \bar{\boldsymbol{b}} \cdot \bar{\varepsilon}\right] = \bar{\boldsymbol{I}} : \bar{\varepsilon}^3 \ . \tag{6.23}$$

Analogously to covariant (strain-like) tensors, invariants are also introduced for contravariant (stress-like) second-order tensors. Again noting identity $\bar{\boldsymbol{b}} = \bar{\boldsymbol{I}}$ and recalling that the product between a contravariant (stress-like) tensor and a covariant tensor is invariant with respect to a superposed isomorphism induced by $\bar{\boldsymbol{F}}_d$ (see eq. (6.11)), invariants of $\bar{\boldsymbol{\sigma}}$ can be introduced according to

$$i_1^{\boldsymbol{\sigma}} = \bar{\boldsymbol{I}} : \bar{\boldsymbol{\sigma}} = \bar{\boldsymbol{b}}^{-1} : \bar{\boldsymbol{\sigma}} = \boldsymbol{b}^{-1} : \boldsymbol{\sigma} \tag{6.24}$$

$$i_2^{\boldsymbol{\sigma}} = \bar{\boldsymbol{I}} : \bar{\boldsymbol{\sigma}}^2 = \bar{\boldsymbol{b}}^{-1} : [\bar{\boldsymbol{\sigma}} \cdot \bar{\boldsymbol{b}}^{-1} \cdot \bar{\boldsymbol{\sigma}}] = \boldsymbol{b}^{-1} : [\boldsymbol{\sigma} \cdot \boldsymbol{b}^{-1} \cdot \boldsymbol{\sigma}] \tag{6.25}$$

$$i_3^{\boldsymbol{\sigma}} = \bar{\boldsymbol{I}} : \bar{\boldsymbol{\sigma}}^3 = \bar{\boldsymbol{b}}^{-1} : [\bar{\boldsymbol{\sigma}} \cdot \bar{\boldsymbol{b}}^{-1} \cdot \bar{\boldsymbol{\sigma}} \cdot \bar{\boldsymbol{b}}^{-1} \cdot \bar{\boldsymbol{\sigma}}] = \boldsymbol{b}^{-1} : [\boldsymbol{\sigma} \cdot \boldsymbol{b}^{-1} \cdot \boldsymbol{\sigma} \cdot \boldsymbol{b}^{-1} \cdot \boldsymbol{\sigma}] \ , \tag{6.26}$$

where $\bar{\boldsymbol{b}}^{-1}$ is a covariant identity tensor belonging to the fictitious undamaged configuration.
As an alternative, invariants (6.14)-(6.16) can also be defined by means of the standard trace operation of mixed-variant tensor $(\boldsymbol{b} \cdot \boldsymbol{\varepsilon})$. To be more explicit,

$$i_1^{\boldsymbol{\varepsilon}} = \mathrm{tr}\left([\boldsymbol{b} \cdot \boldsymbol{\varepsilon}]\right) = \boldsymbol{b} : \boldsymbol{\varepsilon} = \bar{\boldsymbol{b}} : \bar{\varepsilon} = \mathrm{tr}\left([\bar{\boldsymbol{b}} \cdot \bar{\varepsilon}]\right) \tag{6.27}$$

$$i_2^{\boldsymbol{\varepsilon}} = \mathrm{tr}\left([\boldsymbol{b} \cdot \boldsymbol{\varepsilon}]^2\right) = \boldsymbol{b} : [\boldsymbol{\varepsilon} \cdot \boldsymbol{b} \cdot \boldsymbol{\varepsilon}] = \bar{\boldsymbol{b}} : \left[\bar{\varepsilon} \cdot \bar{\boldsymbol{b}} \cdot \bar{\varepsilon}\right] = \mathrm{tr}\left([\bar{\boldsymbol{b}} \cdot \bar{\varepsilon}]^2\right) \tag{6.28}$$

$$i_3^{\boldsymbol{\varepsilon}} = \mathrm{tr}\left([\boldsymbol{b} \cdot \boldsymbol{\varepsilon}]^3\right) = \boldsymbol{b} : [\boldsymbol{\varepsilon} \cdot \boldsymbol{b} \cdot \boldsymbol{\varepsilon} \cdot \boldsymbol{b} \cdot \boldsymbol{\varepsilon}] = \bar{\boldsymbol{b}} : \left[\bar{\varepsilon} \cdot \bar{\boldsymbol{b}} \cdot \bar{\varepsilon} \cdot \bar{\boldsymbol{b}} \cdot \bar{\varepsilon}\right] = \mathrm{tr}\left([\bar{\boldsymbol{b}} \cdot \bar{\varepsilon}]^3\right) \ . \tag{6.29}$$

Likewise, by considering mixed-variant tensor $(\boldsymbol{b}^{-1} \cdot \boldsymbol{\sigma})$, one obtains

$$i_1^{\boldsymbol{\sigma}} = \mathrm{tr}\left([\boldsymbol{b}^{-1} \cdot \boldsymbol{\sigma}]\right) = \boldsymbol{b}^{-1} : \boldsymbol{\sigma} = \bar{\boldsymbol{b}}^{-1} : \bar{\boldsymbol{\sigma}} = \mathrm{tr}\left([\bar{\boldsymbol{b}}^{-1} \cdot \bar{\boldsymbol{\sigma}}]\right) \tag{6.30}$$

$$\begin{aligned} i_2^{\boldsymbol{\sigma}} = \mathrm{tr}\left([\boldsymbol{b}^{-1} \cdot \boldsymbol{\sigma}]^2\right) &= \boldsymbol{b}^{-1} : [\boldsymbol{\sigma} \cdot \boldsymbol{b}^{-1} \cdot \boldsymbol{\sigma}] \\ &= \bar{\boldsymbol{b}}^{-1} : [\bar{\boldsymbol{\sigma}} \cdot \bar{\boldsymbol{b}}^{-1} \cdot \bar{\boldsymbol{\sigma}}] = \mathrm{tr}\left([\bar{\boldsymbol{b}}^{-1} \cdot \bar{\boldsymbol{\sigma}}]^2\right) \end{aligned} \tag{6.31}$$

$$\begin{aligned} i_3^{\boldsymbol{\sigma}} = \mathrm{tr}\left([\boldsymbol{b}^{-1} \cdot \boldsymbol{\sigma}]^3\right) &= \boldsymbol{b}^{-1} : [\boldsymbol{\sigma} \cdot \boldsymbol{b}^{-1} \cdot \boldsymbol{\sigma} \cdot \boldsymbol{b}^{-1} \cdot \boldsymbol{\sigma}] \\ &= \bar{\boldsymbol{b}}^{-1} : [\bar{\boldsymbol{\sigma}} \cdot \bar{\boldsymbol{b}}^{-1} \cdot \bar{\boldsymbol{\sigma}} \cdot \bar{\boldsymbol{b}}^{-1} \cdot \bar{\boldsymbol{\sigma}}] = \mathrm{tr}\left([\bar{\boldsymbol{b}}^{-1} \cdot \bar{\boldsymbol{\sigma}}]^3\right) \ . \end{aligned} \tag{6.32}$$

6.2 Prototype model for anisotropic, ductile damage

The constitutive framework by [51, 106] is solely formulated in terms of the invariants presented in Subsection 6.1.2. The Helmholtz energy is specified as

$$\psi = \psi^{\mathrm{loc}} = \psi^{\mathrm{e}}(\boldsymbol{\varepsilon},\, \boldsymbol{\varepsilon}^{\mathrm{p}},\, \boldsymbol{b}) + \psi^{\mathrm{p}}(\boldsymbol{a},\, \boldsymbol{k},\, \boldsymbol{b}) \;, \tag{6.33}$$

$$\psi^{\mathrm{e}} = \frac{\lambda}{2} \operatorname{tr}\left(\boldsymbol{b} \cdot \boldsymbol{\varepsilon}^{\mathrm{e}}\right)^2 + \mu\, \boldsymbol{b} : \left[\boldsymbol{\varepsilon}^{\mathrm{e}} : \boldsymbol{b} : \boldsymbol{\varepsilon}^{\mathrm{e}}\right] \;, \tag{6.34}$$

$$\psi^{\mathrm{p}} = \frac{H_a}{2}\, \boldsymbol{b} : [\boldsymbol{a} \cdot \boldsymbol{b} \cdot \boldsymbol{a}] + \frac{H_k}{2} \operatorname{tr}\left(\boldsymbol{b} \cdot \boldsymbol{k}\right)^2 \;. \tag{6.35}$$

ψ^{e} denotes the elastic part of Helmholtz energy (6.33) depending on the covariant invariants with respect to strain tensor $\boldsymbol{\varepsilon}^{\mathrm{e}} = \boldsymbol{\varepsilon} - \boldsymbol{\varepsilon}^{\mathrm{p}}$. The plastic part of the energy depends on the strain-like covariant tensors $\boldsymbol{\varepsilon}^{\mathrm{p}}$, $\boldsymbol{k}$ and $\boldsymbol{a}$, where $\boldsymbol{k}$ is associated with isotropic hardening and $\boldsymbol{a}$ with kinematic hardening. Considering dissipation inequality (6.1) and the corresponding set of state variables ($\boldsymbol{\varepsilon}^{\mathrm{p}}$, $\boldsymbol{b}$, $\boldsymbol{a}$, $\boldsymbol{k}$) as well as a stress power of the type $\mathcal{P} = \boldsymbol{\sigma} : \boldsymbol{\varepsilon}$ leads to

$$\mathcal{D} = \mathcal{P} - \dot{\psi} = \boldsymbol{\sigma}^{\mathrm{p}} : \dot{\boldsymbol{\varepsilon}}^{\mathrm{p}} + \boldsymbol{\alpha} : \dot{\boldsymbol{a}} + \boldsymbol{\kappa} : \dot{\boldsymbol{k}} + \boldsymbol{\beta} : \dot{\boldsymbol{b}} \geq 0 \;, \tag{6.36}$$

which has to hold. Consequently, the energetic dual quantities follow from Helmholtz energy (6.33)-(6.35). A straightforward computation results in

$$\boldsymbol{\sigma} = \frac{\partial \psi}{\partial \boldsymbol{\varepsilon}} = \lambda \operatorname{tr}\left(\boldsymbol{b} \cdot \boldsymbol{\varepsilon}^{\mathrm{e}}\right) \boldsymbol{b} + 2\,\mu\, \boldsymbol{b} \cdot \boldsymbol{\varepsilon}^{\mathrm{e}} \cdot \boldsymbol{b} \;, \tag{6.37}$$

$$\boldsymbol{\sigma}^{\mathrm{p}} = -\frac{\partial \psi}{\partial \boldsymbol{\varepsilon}^{\mathrm{p}}} = \lambda \operatorname{tr}\left(\boldsymbol{b} \cdot \boldsymbol{\varepsilon}^{\mathrm{e}}\right) \boldsymbol{b} + 2\,\mu\, \boldsymbol{b} \cdot \boldsymbol{\varepsilon}^{\mathrm{e}} \cdot \boldsymbol{b} \;, \tag{6.38}$$

$$\boldsymbol{\alpha} = -\frac{\partial \psi}{\partial \boldsymbol{a}} = -H_a\, \boldsymbol{b} \cdot \boldsymbol{a} \cdot \boldsymbol{b} \;, \tag{6.39}$$

$$\boldsymbol{\kappa} = -\frac{\partial \psi}{\partial \boldsymbol{k}} = -H_k \operatorname{tr}\left(\boldsymbol{b} \cdot \boldsymbol{k}\right) \boldsymbol{b} \;, \tag{6.40}$$

$$\begin{aligned} \boldsymbol{\beta} = -\frac{\partial \psi}{\partial \boldsymbol{b}} = &-\lambda \operatorname{tr}\left(\boldsymbol{b} \cdot \boldsymbol{\varepsilon}^{\mathrm{e}}\right) \boldsymbol{\varepsilon}^{\mathrm{e}} - 2\,\mu\, \boldsymbol{\varepsilon}^{\mathrm{e}} \cdot \boldsymbol{b} \cdot \boldsymbol{\varepsilon}^{\mathrm{e}} \\ &- H_a\, \boldsymbol{a} \cdot \boldsymbol{b} \cdot \boldsymbol{a} - H_k \operatorname{tr}\left(\boldsymbol{b} \cdot \boldsymbol{k}\right) \boldsymbol{k} \end{aligned} \;, \tag{6.41}$$

where $\boldsymbol{\sigma}$ is the standard stress tensor, $\boldsymbol{\alpha}$ the drag stress tensor, $\boldsymbol{\kappa}$ the back stress tensor and $\boldsymbol{\beta}$ the energy release rate. Quantity $\boldsymbol{\sigma}^{\mathrm{p}}$ is dual to the plastic strains and provides an increased flexibility for the evolution equation of $\boldsymbol{\varepsilon}^{\mathrm{p}}$. It enters plastic potential (6.6) – instead of stress tensor $\boldsymbol{\sigma}$ – and can be utilized to incorporate a Prager-type linear kinematic hardening rule into the constitutive framework, cf. [143]. A suitable method to guarantee the fulfillment of dissipation inequality (6.36) is the principle of General-

ized Standard Materials, see Section 6.1.1. The evolution equations are determined by potential (6.6), which is specified as

$$g = \Phi\left(\boldsymbol{\sigma}^{\mathrm{p}},\, \boldsymbol{\alpha},\, \boldsymbol{\kappa};\, \boldsymbol{b}\right) + \Gamma_{\boldsymbol{\alpha}}(\boldsymbol{\alpha};\, \boldsymbol{b}) + \Gamma_{\boldsymbol{\kappa}}(\boldsymbol{\kappa};\, \boldsymbol{b}) + \Gamma_{\boldsymbol{\beta}}(\boldsymbol{\beta};\, \boldsymbol{b})\ . \tag{6.42}$$

Such a type of potential, where the evolution equation for the integrity tensor $\boldsymbol{b}$, only depends on the non-associative part is typical for ductile damage models of Lemaitre-type, cf. [94]. Additionally, kinematic and isotropic hardening is altered with respect to the non-associative part. The yield function is chosen as

$$\Phi = \sqrt{\tau^{\mathrm{eq}}} - \tau_y - \frac{1}{3}\boldsymbol{b}^{-1} : \boldsymbol{\kappa}\ . \tag{6.43}$$

$$\tau^{\mathrm{eq}} = \frac{3}{2}\,\boldsymbol{b}^{-1} : \left[\boldsymbol{\tau}\cdot\boldsymbol{b}^{-1}\cdot\boldsymbol{\tau}\right] - \frac{1}{2}\,\mathrm{tr}\left(\boldsymbol{b}^{-1}\cdot\boldsymbol{\tau}\right)^2\ , \tag{6.44}$$

$$\boldsymbol{\tau} = \boldsymbol{\sigma}^{\mathrm{p}} - \boldsymbol{\alpha} \tag{6.45}$$

with initial yield stress τ_y. Equivalent stress (6.44) is based on relative stresses (6.45) and chosen as von Mises-type. Furthermore, the non-associative parts of plastic potential (6.42) are adopted as

$$\Gamma = \Gamma_{\boldsymbol{\alpha}} + \Gamma_{\boldsymbol{\kappa}} + \Gamma_{\boldsymbol{\beta}}\ , \tag{6.46}$$

$$\Gamma_{\boldsymbol{\alpha}} = \frac{B_a}{2\,H_a}\boldsymbol{b}^{-1} : \left[\boldsymbol{\alpha}\cdot\boldsymbol{b}^{-1}\cdot\boldsymbol{\alpha}\right]\ , \tag{6.47}$$

$$\Gamma_{\boldsymbol{\kappa}} = \frac{B_k}{2\,H_k}\boldsymbol{b}^{-1} : \left[\boldsymbol{\kappa}\cdot\boldsymbol{b}^{-1}\cdot\boldsymbol{\kappa}\right]\ , \tag{6.48}$$

$$\Gamma_{\boldsymbol{\beta}} = \frac{\eta_1}{2}\,\mathrm{tr}\left(\boldsymbol{b}\cdot\boldsymbol{\beta}\right)^2 + \frac{\eta_2}{2}\,\boldsymbol{b} : \left[\boldsymbol{\beta}\cdot\boldsymbol{b}\cdot\boldsymbol{\beta}\right]\ . \tag{6.49}$$

It consists of potential $\Gamma_{\boldsymbol{\alpha}}$ and $\Gamma_{\boldsymbol{\kappa}}$ which are Armstrong-Frederick-type extensions to non-linear kinematic and non-linear isotropic hardening, cf. [8], and of potential $\Gamma_{\boldsymbol{\beta}}$, which defines the evolution of integrity tensor $\boldsymbol{b}$. The saturation limit of the nonlinear evolution of plastic hardening is set by the ratios $B_\bullet/H_\bullet$ and the slopes by the magnitude of $H_\bullet$, or respectively by the magnitude of $B_\bullet$. Parameters η_1 and η_2 allow to adjust the degree of anisotropy. Particularly, parameter η_1 is responsible for an isotropic evolution of $\boldsymbol{b}$ while parameter η_2 leads to an anisotropic evolution. To be more precise, the second term in potential (6.49) leads to an evolution of $\boldsymbol{b}$ depending on the orientation of $\boldsymbol{\beta}$. A straightforward computation of the evolution equations leads to

$$\dot{\boldsymbol{\varepsilon}}^{\mathrm{p}} = \lambda\,\boldsymbol{\nu}^{\boldsymbol{\sigma}^{\mathrm{p}}}\ , \qquad \boldsymbol{\nu}^{\boldsymbol{\sigma}^{\mathrm{p}}} = \frac{\partial\Phi}{\partial\boldsymbol{\sigma}^{\mathrm{p}}}\ , \tag{6.50}$$

$$\dot{\boldsymbol{a}} = \lambda\,\boldsymbol{\nu}^{\boldsymbol{\alpha}}\ , \qquad \boldsymbol{\nu}^{\boldsymbol{\alpha}} = \frac{\partial g}{\partial\boldsymbol{\alpha}}\ , \tag{6.51}$$

$$\dot{\boldsymbol{k}} = \lambda\,\boldsymbol{\nu}^{\boldsymbol{\kappa}}\ , \qquad \boldsymbol{\nu}^{\boldsymbol{\kappa}} = \frac{\partial g}{\partial\boldsymbol{\kappa}}\ , \tag{6.52}$$

$$\dot{\boldsymbol{b}} = \lambda\, \boldsymbol{\nu}^{\boldsymbol{\beta}} \,, \qquad \boldsymbol{\nu}^{\boldsymbol{\beta}} = \frac{\partial \Gamma_{\boldsymbol{\beta}}}{\partial \boldsymbol{\beta}} \,, \tag{6.53}$$

where $\boldsymbol{\nu}^{\bullet}$ are the corresponding update direction and λ the consistency parameter.
In summary, the model is based on the principle of energy equivalence and formulated in terms of configuration-independent invariants. It is capable of modeling ductile damage, i.e., damage accompanied by plasticity. Both linear and non-linear isotropic as well as linear and non-linear kinematic hardening are included. Furthermore, the presented model automatically fulfills the second law of thermodynamics, since its evolution equations are based on the principle of Generalized Standard Materials.

Remark 2 *Since tensor $\boldsymbol{\tau}$ is of contravariant nature, insertion of contravariant transformation rule* (6.10) *or equivalently insertion of contravariant invariants* (6.17)-(6.19) *leads to*

$$\tau^{eq} = \frac{3}{2} \left[\bar{\boldsymbol{\tau}} : \bar{\boldsymbol{\tau}} - \frac{1}{3} \operatorname{tr} \left(\bar{\boldsymbol{\tau}} \right)^2 \right] = \frac{3}{2} \left[\operatorname{dev} \left(\bar{\boldsymbol{\tau}} \right) : \operatorname{dev} \left(\bar{\boldsymbol{\tau}} \right) \right] \tag{6.54}$$

as an alternative representation of the equivalent stress (6.44)*. It can be seen, that τ^{eq} are indeed the equivalent von Mises stresses.*

Remark 3 *To remain consistent with the framework of material covariance potential* (6.49) *has to depend only on covariant invariants* (6.14)-(6.16)*. However, in [51, 106] it is emphasized that the inclusion of exponent m as*

$$\boldsymbol{\nu}^{\boldsymbol{\beta}} = \eta_1 \operatorname{tr} \left(\boldsymbol{b}^m \cdot \boldsymbol{\beta} \right) \boldsymbol{b}^m + \eta_2\, \boldsymbol{b}^m \cdot \boldsymbol{\beta} \cdot \boldsymbol{b}^m \tag{6.55}$$

is a reasonable extension in order to fit the model to experimental data.

6.3 Prototype model for isotropic, ductile damage

Anisotropic modeling of material degradation is not always necessary. For components which are only loaded proportionally an isotropic model is often sufficient and more efficient – especially for gradient-enhanced constitutive models.

Starting from evolution equation (6.53), which leads to

$$\dot{\boldsymbol{b}} = \lambda \frac{\partial \Gamma_{\boldsymbol{\beta}}}{\partial \boldsymbol{\beta}} = \lambda\, \eta_1 \operatorname{tr} \left(\boldsymbol{b} \cdot \boldsymbol{\beta} \right) \boldsymbol{b} \,, \tag{6.56}$$

shows that the orientation of $\dot{\boldsymbol{b}}$ is coaxial to $\boldsymbol{b}$. Combining this with the assumption of an undamaged initial state, i.e., $\boldsymbol{b}(t = 0) = \boldsymbol{I}$, results in a spherical evolution of the integrity tensor and thus, justifies the scalar representation

$$\boldsymbol{b} = b\, \boldsymbol{I} \tag{6.57}$$

with b being the scalar – isotropic – integrity variable. Insertion of assumption (6.57) into Helmholtz energy (6.33) then leads to its simplified form as

$$\psi = \psi^{\mathrm{loc}} = \psi^{\mathrm{e}}(\boldsymbol{\varepsilon},\, \boldsymbol{\varepsilon}^{\mathrm{p}},\, b) + \psi^{\mathrm{p}}(\boldsymbol{a},\, \boldsymbol{k},\, b)\ , \tag{6.58}$$

$$\psi^{\mathrm{e}} = \frac{\lambda}{2}\, b^2\, \mathrm{tr}\,(\boldsymbol{\varepsilon}^{\mathrm{e}})^2 + \mu\, b^2\, \boldsymbol{\varepsilon}^{\mathrm{e}} : \boldsymbol{\varepsilon}^{\mathrm{e}}\ , \tag{6.59}$$

$$\psi^{\mathrm{p}} = \frac{H_a}{2}\, b^2\, \boldsymbol{a} : \boldsymbol{a} + \frac{H_k}{2}\, b^2\, \mathrm{tr}\,(\boldsymbol{k})^2\ . \tag{6.60}$$

This, in turn, allows the computation of scalar energy release rate β as

$$\begin{aligned} \beta = -\frac{\partial \psi}{\partial b} =& -\lambda\, b\, \mathrm{tr}\,(\boldsymbol{\varepsilon}^{\mathrm{e}})^2 + 2\,\mu\, b\, \boldsymbol{\varepsilon}^{\mathrm{e}} : \boldsymbol{\varepsilon}^{\mathrm{e}} \\ & - H_a\, b\, \boldsymbol{a} : \boldsymbol{a} + H_k\, b\, \mathrm{tr}\,(\boldsymbol{k})^2\ . \end{aligned} \tag{6.61}$$

Inserting assumption (6.57) into evolution equation (6.56) leads to

$$\dot{b} = \lambda\, \eta_1\, b^2\, \mathrm{tr}\,(\boldsymbol{\beta})\ , \tag{6.62}$$

with $\boldsymbol{\beta}$ remaining tensor-valued. A comparison of scalar energy release rate β from eq. (6.61) with

$$\mathrm{tr}\,(\boldsymbol{\beta}) = -\lambda\, b\, \mathrm{tr}\,(\boldsymbol{\varepsilon}^{\mathrm{e}})^2 - 2\,\mu\, b\, \mathrm{tr}\,(\boldsymbol{\varepsilon}^{\mathrm{e}} \cdot \boldsymbol{\varepsilon}^{\mathrm{e}}) - H_a\, b\, \mathrm{tr}\,(\boldsymbol{a} \cdot \boldsymbol{a}) - H_k\, b\, \mathrm{tr}\,(\boldsymbol{k})^2 \tag{6.63}$$

of energy release rate (6.41) and utilizing that $\boldsymbol{\beta}$ only enters the constitutive framework with respect to the trace operator justifies the substitution of $\mathrm{tr}\,(\boldsymbol{\beta})$ with its scalar counterpart resulting in

$$\dot{b} = \lambda\, \eta_1\, b^2\, \beta =: \lambda\, \nu^{\beta}\ . \tag{6.64}$$

Focusing on the isotropic case, a suitable potential for $\Gamma_\beta$is

$$\Gamma_\beta = \frac{\eta_1}{2}\, b^2\, \beta^2\ . \tag{6.65}$$

The scalar representation of integrity b also enables a spherical representation of $\boldsymbol{k}$. To be more precise, analyzing evolution equation (6.52),

$$\dot{\boldsymbol{k}} = \lambda\, \frac{\partial g}{\partial \boldsymbol{\kappa}} = \lambda\, \left[-\frac{1}{3}\, b^{-1}\, \boldsymbol{I} + \frac{B_k}{H_k}\, b^{-2}\, \boldsymbol{\kappa} \right]\ , \tag{6.66}$$

shows that $\boldsymbol{k}$ evolves spherically if $\boldsymbol{\kappa}$ is spherical. This leads to

$$\boldsymbol{k} = k\, \boldsymbol{I}\ , \tag{6.67}$$

where the tensor-valued $\boldsymbol{k}$ is replaced by its scalar counterpart k. Insertion of assumption (6.67) into already reduced plastic part of Helmholtz energy (6.58) leads to

$$\psi^{\mathrm{p}} = \frac{H_a}{2}\, b^2\, \boldsymbol{a} : \boldsymbol{a} + \frac{9\, H_k}{2}\, b^2\, k^2 \tag{6.68}$$

as the isotropic simplified Helmholtz energy. A straightforward computation of back-stress κ yields

$$\kappa = -\frac{\partial \psi}{\partial k} = -9\, H_k\, b^2\, k\ . \tag{6.69}$$

Comparing scalar back stress κ to its tensorial counterpart

$$\mathrm{tr}\,(\boldsymbol{\kappa}) = -9\, H_k\, b^2\, k\ , \tag{6.70}$$

and once again utilizing that $\boldsymbol{\kappa}$ only enters the constitutive equations with respect to the trace operator – if assumption (6.57) is made – leads to the simplified version of evolution equation (6.66)

$$\dot{k} = -\lambda \left[\frac{1}{3}\, b^{-1} + \frac{B_k}{H_k}\, b^{-2}\, \kappa\right] =: \lambda\, \nu^{\kappa}\ . \tag{6.71}$$

A suitable potential in order to achieve $\partial_{\kappa} g = \nu^{\kappa}$ is given by

$$\Phi = \sqrt{\tau^{\mathrm{eq}}} - \tau_y - \frac{1}{3}\frac{\kappa}{b}\ , \tag{6.72}$$

$$\Gamma_{\kappa} = \frac{B_k}{H_k}\, b^{-2}\, \kappa^2\ . \tag{6.73}$$

Since, the remaining quantities remain tensorial the simplification of the associated equations follows jointly by inserting either assumptions (6.57) or assumption (6.67).

Remark 4 *Assumption* (6.67) *leads to a scaling of the isotropic hardening part in Helmholtz energy* (6.68) *with prefactor* 9. *This can be avoided by either assuming* $\boldsymbol{k} = 1/3\, k\, \boldsymbol{I}$ *or by substituting the isotropic hardening modulus with* $\widetilde{H}_k = 9\, H_k$.

D Appendix

D.1 1st and 2nd derivatives of symmetric tensor functions

In this appendix a closed form solution for first and second derivatices of symmetric tensor functions is shown. It is taken from the work by *Miehe and Lambrecht* [108] and its purpose is to visualize the computational algorithm.

The starting point is a symmetric second-order tensor $\boldsymbol{T} \in \mathbb{R}^{3x3}$ and a scalar, twice differentiable function $f \in \mathcal{C}^2$. The eigenvalues of $\boldsymbol{T}$ are real-valued and the left and right eigenvectors are identical. The spectral decomposition allows to rewrite tensor $\boldsymbol{T}$ in terms of its eigenvalues λ^a and its eigenbases $\boldsymbol{P}^a$ with $a \in \{1, 2, 3\}$ as

$$\boldsymbol{T} = \sum_{a=1}^{3} \lambda^a \, \boldsymbol{P}^a \; . \tag{6.74}$$

The tensor function $f(\boldsymbol{T}) \in \mathbb{R}^{3x3}$ then follows by applying scalar function f to the eigenvalues λ^a as

$$f(\boldsymbol{T}) = \sum_{a=1}^{3} f(\lambda^a) \, \boldsymbol{P}^a \; . \tag{6.75}$$

The calculation of the first derivative $\partial_{\boldsymbol{T}} f(\boldsymbol{T})$ requires both the derivative of the eigenvalues as well as the derivative of the eigenbases. Considering *Sylvester Serrin*'s formula, see e.g., [107], to compute the eigenbasis in the case of three different eigenvalues $\lambda^a,\ \lambda^b,\ \lambda^c$ leads to

$$\boldsymbol{P}^a = \frac{\left[\boldsymbol{T} - \lambda^b \, \boldsymbol{I}\right] \cdot \left[\boldsymbol{T} - \lambda^c \, \boldsymbol{I}\right]}{\left[\lambda^a - \lambda^b\right] \, \left[\lambda^a - \lambda^c\right]} \; . \tag{6.76}$$

Exploiting identity $\partial_{\boldsymbol{T}} \lambda^a = \boldsymbol{P}^a$ the derivatives $\partial_{\boldsymbol{T}} f(\boldsymbol{T})$ and $\partial^2_{\boldsymbol{T}} f(\boldsymbol{T})$ can be calculated. For the case of multiple eigenvalues, the algorithm has to be modified. Alternatively, a perturbation of the eigenvalues according to

$$\lambda^a \leftarrow \lambda^a \, \left[1 + \epsilon\right] \; , \qquad \lambda^b \leftarrow \lambda^b \, \left[1 - \epsilon\right] \qquad \lambda^c \leftarrow \frac{\lambda^c}{\left[1 + \epsilon\right] \, \left[1 - \epsilon\right]} \tag{6.77}$$

can be utilized which ensures the determinant to remain unaltered. Due to the perturbation, the algorithm loses accuracy, which sometimes results in divergence of the surrounding algorithms. An analytic computation of the first and second derivatives, which depends on the number of multiple eigenvalues, is presented in [108]. In [108] auxiliary variables ν^{ab}, ξ^{ab} and η with $a, b, c \in \{1, 2, 3\}$ are introduced. Their calculation depends

on the number of multiple eigenvalues and is summarized in Algorithm 1. It is assumed that the eigenvalues are sorted in ascending order, i.e., $\lambda^1 \leq \lambda^2 \leq \lambda^3$, thus, resulting in four different combinations of multiple eigenvalues. Furthermore, the fourth and sixth-order tensors $\mathbb{G}^{ab}$ and $\mathbb{H}^{abc}$ are introduced for all combinations of $a, b, c \in \{1, 2, 3\}$. For the sake of readability they are given in index notation as

$$G^{ab}_{ijkl} = P^a_{ik}\, P^b_{jl} + P^a_{il}\, P^b_{jk} \,, \tag{6.78}$$

$$\begin{aligned} H^{abc}_{ijklmn} &= P^a_{ik}\, P^b_{jm}\, P^c_{ln} + P^a_{ik}\, P^b_{jn}\, P^c_{lm} + P^a_{il}\, P^b_{jm}\, P^c_{kn} + P^a_{il}\, P^b_{jn}\, P^c_{km} \\ &\quad + P^a_{jk}\, P^b_{im}\, P^c_{ln} + P^a_{jk}\, P^b_{in}\, P^c_{lm} + P^a_{jl}\, P^b_{im}\, P^c_{kn} + P^a_{jl}\, P^b_{in}\, P^c_{km} \,. \end{aligned} \tag{6.79}$$

With that quantities at hand, the first derivative of $f(\boldsymbol{T})$ follows by employing the product rule as

$$\begin{aligned} \partial_{\boldsymbol{T}} f(\boldsymbol{T}) &= \sum_{a=1}^{3} \frac{\partial f(\lambda^a)}{\partial \lambda^a}\, \boldsymbol{P}^a \otimes \frac{\partial \lambda^a}{\partial \boldsymbol{T}} + \sum_{a=1}^{3} f(\lambda^a)\, \frac{\partial \boldsymbol{P}^a}{\partial \boldsymbol{T}} \\ &= \sum_{a=1}^{3} \frac{\partial f(\lambda^a)}{\partial \lambda^a}\, \boldsymbol{P}^a \otimes \boldsymbol{P}^a + \frac{1}{2} \sum_{\substack{a,b=1 \\ a \neq b}}^{3} \nu^{ab}\, \mathbb{G}^{ab} \,. \end{aligned} \tag{6.80}$$

The derivative of the eigenbases $\boldsymbol{P}^a$ with respect to tensor $\boldsymbol{T}$ depends on the number of multiple eigenvalues and can be expressed in closed form by inserting the auxiliary variable ν^{ab}, see Algorithm1. In the same manner the second derivative is expressed as

$$\begin{aligned} \partial^2_{\boldsymbol{T}} f(\boldsymbol{T}) &= \sum_{a=1}^{3} \frac{\partial^2 f(\lambda^a)}{\partial {\lambda^a}^2}\, \boldsymbol{P}^a \otimes \boldsymbol{P}^a \otimes \boldsymbol{P}^a + \frac{1}{4} \sum_{\substack{a,b=1 \\ a \neq b}}^{3} \xi^{ab} \left[\mathbb{H}^{abb} + \mathbb{H}^{bab} + \mathbb{H}^{bba} \right] \\ &\quad + \frac{1}{4} \sum_{\substack{a,b,c=1 \\ a \neq b,\, b \neq c,\, c \neq a}}^{3} \eta\, \mathbb{H}^{abc} \,. \end{aligned} \tag{6.81}$$

Here, the auxiliary variables ξ^{ab} and η are inserted.

D.2 Application to tensor power series

The calculation of tensor power series, i.e., $\boldsymbol{T}^n$, may be computed by a series of matrix products as

$$\boldsymbol{T}^n = \underbrace{\boldsymbol{T} \cdot \boldsymbol{T} \cdot \ldots \cdot \boldsymbol{T}}_{n \text{ times}} \,. \tag{6.82}$$

Algorithm 1: Computation of auxiliary variables ν^{ab}, ξ^{ab} and η

Input: Eigenvalues $\lambda^a \in \mathbb{R}$ and scalar function $f \in \mathscr{C}^2$

% Derivatives of f
$f^a = f(\lambda^a), \quad df^a = 2\,\partial_{\lambda^a} f(\lambda^a), \quad ddf^a = 4\,\partial^2_{\lambda^a} f(\lambda^a)$

% Initialization
$\nu^{ab} = 0, \quad \xi^{ab} = 0, \quad \eta = 0$

% Computation of auxiliary variables
if $\lambda^1 \neq \lambda^2 \neq \lambda^3$ **then**
  for $a, b \in \{1,2,3\}$, $a \neq b$ **do**
    $\nu^{ab} = \dfrac{f^a - f^b}{\lambda^a - \lambda^b}$
    $\xi^{ab} = \dfrac{\nu^{ab} - \frac{1}{2}\,df^b}{\lambda^a - \lambda^b}$
    for $c \in \{1,2,3\}$, $c \neq a$, $c \neq b$ **do**
      $\eta \leftarrow \eta + \dfrac{f^a}{2\,[\lambda^a - \lambda^b]\,[\lambda^a - \lambda^c]}$
    end
  end
else if $\lambda^1 = \lambda^2 \neq \lambda^3$ **then**
  $\nu^{12} = \nu^{21} = \frac{1}{2}\,df^1\,, \quad \nu^{13} = \nu^{23} = \nu^{31} = \nu^{32} = \dfrac{f^1 - f^3}{\lambda^a - \lambda^3}$
  $\xi^{12} = \xi^{21} = \frac{1}{8}\,ddf^1, \quad \xi^{13} = \xi^{23} = \dfrac{\nu^{13} - \frac{1}{2}\,df^3}{\lambda^1 - \lambda^3}\,, \quad \xi^{31} = \xi^{32} = \dfrac{\nu^{31} - \frac{1}{2}\,df^1}{\lambda^3 - \lambda^1}$
  $\eta = \xi_{31}$
else if $\lambda^1 \neq \lambda^2 = \lambda^3$ **then**
  $\nu^{23} = \nu^{32} = \frac{1}{2}\,df^1, \quad \nu^{12} = \nu^{13} = \nu^{21} = \nu^{31} = \dfrac{f^2 - f^1}{\lambda^2 - \lambda^1}$
  $\xi^{23} = \xi^{32} = \frac{1}{8}\,ddf^1\,, \quad \xi^{12} = \xi^{13} = \dfrac{\nu^{12} - \frac{1}{2}\,df^2}{\lambda^1 - \lambda^2}, \quad \xi^{21} = \xi^{31} = \dfrac{\nu^{21} - \frac{1}{2}\,df^1}{\lambda^2 - \lambda^1}$
  $\eta = \xi_{12}$
else
  for $a, b \in \{1,2,3\}$, $a \neq b$ **do**
    $\nu^{ab} = \frac{1}{2}\,df^1\,, \qquad \xi^{ab} = \frac{1}{8}\,ddf^1$
  end
  $\eta = \xi^{12}$
end

This implies that the exponent n is a natural number, which may be too restrictive for applications. One method in order to allow real-valued exponents n is given in Appendix D.1. By defining function (6.75) as

$$f(\boldsymbol{T}) = \sum_{a=1}^{3} f(\lambda^a)\, \boldsymbol{P}^a \coloneqq \sum_{a=1}^{3} [\lambda^a]^n = \boldsymbol{T}^n \tag{6.83}$$

shows that exponent n is only applied to the eigenvalues. Hence, formula D.1 is applicable.

D.3 Split of strain tensors in positive and negative parts

A frequently made assumption in the field of damage mechanics is that damage only occurs under tensile loading states. For that purpose, the tensors involved in the model such as the strain or the stress tensor, are often decomposed into a tensile part denoted as $\boldsymbol{T}^+$ and a compression part denoted as $\boldsymbol{T}^-$ such that

$$\boldsymbol{T} = \boldsymbol{T}^+ + \boldsymbol{T}^- \tag{6.84}$$

holds. The tensile part is calculated according to

$$\boldsymbol{T}^+ = \sum_{a=1}^{3} \mathcal{H}(\lambda^a)\, \lambda^a\, \boldsymbol{P}^a \,, \tag{6.85}$$

where

$$\mathcal{H}(x) = \begin{cases} 1 & \text{if } x \geq 0 \\ 0 & \text{else} \end{cases} \tag{6.86}$$

is the Heaviside function. Usually, the derivatives of $\boldsymbol{T}^+$, respectively $\boldsymbol{T}^-$ are required for implementation aspects. Since Heaviside function (6.86) is discontinuous at $x = 0$, a smooth approximation as given in [51] as

$$\mathcal{H}(x) = \frac{1}{2} + \frac{1}{\pi} \arctan\left(\frac{x - x_0}{x_r}\right) \tag{6.87}$$

is often used. Parameter x_0 allows for a horizontal transition and parameter x_r controls the slope of the transition zone at $x = x_0$. Representation (6.85) allows to compute derivatives by means of the methods provided in Appendix D.1. Furthermore,

$$\frac{\mathrm{d}\boldsymbol{T}^-}{\mathrm{d}\boldsymbol{T}} = \mathbb{I}^{\mathrm{sym}} - \frac{\mathrm{d}\boldsymbol{T}^+}{\mathrm{d}\boldsymbol{T}} \,, \tag{6.88}$$

$$\frac{\mathrm{d}^2\boldsymbol{T}^-}{\mathrm{d}\boldsymbol{T}^2} = -\frac{\mathrm{d}^2\boldsymbol{T}^+}{\mathrm{d}\boldsymbol{T}^2} \ . \tag{6.89}$$

D.4 Visualization of anisotropy

A change of integrity tensor $\boldsymbol{b}$ induces a certain anisotropy into the model. In order to visualize the anisotropy of the elasticity, the directional Young's modulus can be plotted, cf. [83]. It is calculated based on the fourth order elasticity tensor $\mathbb{E}$, which is given in terms of Helmholtz energy ψ as $\mathbb{E} = \partial_{\boldsymbol{\varepsilon}\boldsymbol{\varepsilon}}\psi$. The $\boldsymbol{r}$-directional Young's modulus $E_{\boldsymbol{r}}$ then follows as

$$E_{\boldsymbol{r}} = \left[[\boldsymbol{r} \otimes \boldsymbol{r}] : \mathbb{E}^{-1} : [\boldsymbol{r} \otimes \boldsymbol{r}] \right]^{-1} \ . \tag{6.90}$$

Focusing on the model summarized in Section 6.2, fourth-order tensor $\mathbb{E}$ reads in index notation

$$[\mathbb{E}]_{ijkl} = \lambda \, b_{ij} \, b_{kl} + \mu \, \left[b_{ik} \, b_{jl} + b_{il} \, b_{jk} \right] \ . \tag{6.91}$$

For $\boldsymbol{b} = \boldsymbol{I}$ (Fig. 6.2(a)) the elastic material behavior is isotropic. The same holds for

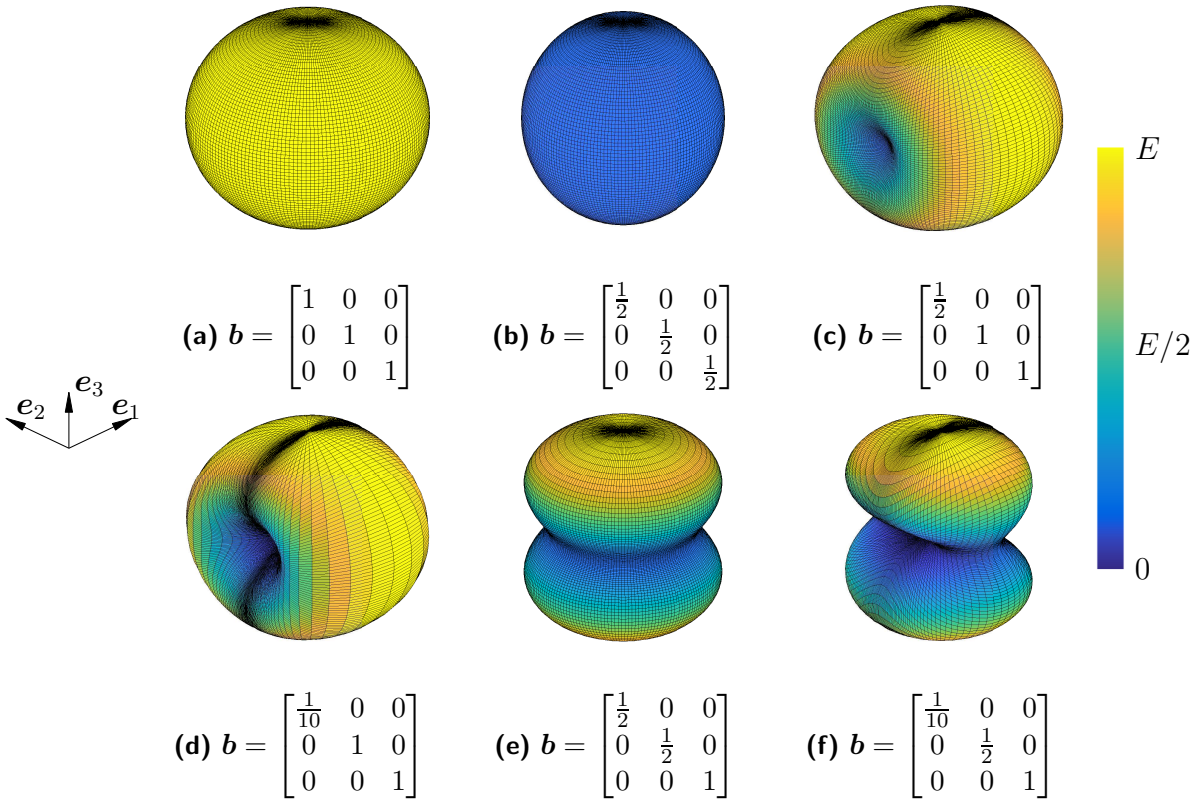

Figure 6.2: Visualization of $\boldsymbol{b}$-induced elastic anisotropy.

spherical degradations of $\boldsymbol{b}$. However, due to the quadratic dependence of $\mathbb{E}$ on $\boldsymbol{b}$ this effect is non-linear.
A reduction of only one component of $\boldsymbol{b}$ leads to a degradation of $\mathbb{E}$ in precisely that direction (Fig. 6.2(c) and (d)) and a degradation of two components leaves the remaining direction unaffected (Fig. 6.2(e) and (f)).

7 Regularization of anisotropic, ductile damage models

In this chapter, the local, anisotropic, ductile damage model presented in the previous chapter is regularized by means of a micromorphic gradient formulation. Such a regularization is indeed required, since the local model – from a mathematical point of view – results in an ill-posed equation which, in turn, leads to a pathological mesh dependence as far as the resulting finite element formulation is concerned. Within this chapter it will be shown, that the micromorphic formulation in its standard form is not suitable to regularize the underlying local model. The origin is analyzed and, based on this, a modified version of the micromorphic regularization is presented. That version is applied to both the anisotropic and the isotropic prototype model.

7.1 Micromorphic gradient regularization

7.1.1 Naive micromorphic extension of the local, anisotropic, ductile damage model

The softening behavior of anisotropic damage model 6.2 is determined by the monotonically decreasing second-order tensor $\boldsymbol{b}$. In order to regularize the local constitutive model, the gradient of $\boldsymbol{b}$ shall be incorporated into the model. Following [48, 54], the regularization is not directly applied to $\boldsymbol{b}$, but to an additional second-order tensor $\boldsymbol{\varphi}$. With this tensor, a micromorphic approximation of a standard gradient regularization is obtained by means of enhanced Helmholtz energy

$$\psi = \psi^{\mathrm{loc}}(\boldsymbol{\varepsilon},\, \boldsymbol{\varepsilon}^{\mathrm{p}},\, \boldsymbol{a},\, \boldsymbol{k},\, \boldsymbol{b}) + \psi^{\mathrm{nloc}}(\boldsymbol{b},\, \boldsymbol{\varphi},\, \nabla\boldsymbol{\varphi}) \;, \tag{7.1}$$

$$\psi^{\mathrm{loc}} = \psi^{\mathrm{e}}(\boldsymbol{\varepsilon},\, \boldsymbol{\varepsilon}^{\mathrm{p}},\, \boldsymbol{b}) + \psi^{\mathrm{p}}(\boldsymbol{\varepsilon}^{\mathrm{p}},\, \boldsymbol{a},\, \boldsymbol{k},\, \boldsymbol{b}) \;, \tag{7.2}$$

$$\psi^{\mathrm{e}} = \frac{\lambda}{2}\,\mathrm{tr}\,(\boldsymbol{b}\cdot\boldsymbol{\varepsilon}^{\mathrm{e}})^2 + \mu\,\boldsymbol{b} : [\boldsymbol{\varepsilon}^{\mathrm{e}}\cdot\boldsymbol{b}\cdot\boldsymbol{\varepsilon}^{\mathrm{e}}] \;, \tag{7.3}$$

$$\psi^{\mathrm{p}} = \frac{H_a}{2}\,\boldsymbol{b} : [\boldsymbol{a}\cdot\boldsymbol{b}\cdot\boldsymbol{a}] + \frac{H_k}{2}\,\mathrm{tr}\,(\boldsymbol{b}\cdot\boldsymbol{k})^2 \;, \tag{7.4}$$

$$\psi^{\mathrm{nloc}} = \frac{c_b}{2}\,||\boldsymbol{\varphi} - \boldsymbol{b}||^2 + \frac{c_b\, l_b^2}{2}\,||\nabla \boldsymbol{b}||^2 \ . \tag{7.5}$$

ψ^{loc} denotes the Helmholtz energy of the underlying local prototype model and ψ^{nloc} the micromorphic extension with penalty parameter c_b and length parameter l_b. The energetically dual quantities to ($\boldsymbol{\varepsilon}$, $\boldsymbol{\varphi}$, $\nabla\boldsymbol{\varphi}$, $\boldsymbol{\varepsilon}^{\mathrm{p}}$, $\boldsymbol{a}$, $\boldsymbol{k}$, $\boldsymbol{b}$) then follow as

$$\boldsymbol{\sigma} = \frac{\partial \psi}{\partial \boldsymbol{\varepsilon}} = \lambda\,\mathrm{tr}\,(\boldsymbol{b}\cdot\boldsymbol{\varepsilon}^{\mathrm{e}})\;\boldsymbol{b} + 2\,\mu\,\boldsymbol{b}\cdot\boldsymbol{\varepsilon}^{\mathrm{e}}\cdot\boldsymbol{b}\ , \tag{7.6}$$

$$\boldsymbol{\omega} = \frac{\partial \psi}{\partial \boldsymbol{\varphi}} = c_b\,[\boldsymbol{\varphi} - \boldsymbol{b}] \tag{7.7}$$

$$\boldsymbol{\Omega} = \frac{\partial \psi}{\partial \nabla\boldsymbol{\varphi}} = c_b\, l_b^2\,\nabla\boldsymbol{\varphi} \tag{7.8}$$

$$\boldsymbol{\sigma}^{\mathrm{p}} = -\frac{\partial \psi}{\partial \boldsymbol{\varepsilon}^{\mathrm{p}}} = \lambda\,\mathrm{tr}\,(\boldsymbol{b}\cdot\boldsymbol{\varepsilon}^{\mathrm{e}})\;\boldsymbol{b} + 2\,\mu\,\boldsymbol{b}\cdot\boldsymbol{\varepsilon}^{\mathrm{e}}\cdot\boldsymbol{b}\ , \tag{7.9}$$

$$\boldsymbol{\alpha} = -\frac{\partial \psi}{\partial \boldsymbol{a}} = -H_a\,\boldsymbol{b}\cdot\boldsymbol{a}\cdot\boldsymbol{b}\ , \tag{7.10}$$

$$\boldsymbol{\kappa} = -\frac{\partial \psi}{\partial \boldsymbol{k}} = -H_k\,\mathrm{tr}\,(\boldsymbol{b}\cdot\boldsymbol{k})\;\boldsymbol{b}\ , \tag{7.11}$$

$$\begin{aligned}\boldsymbol{\beta} = -\frac{\partial \psi}{\partial \boldsymbol{b}} = {} & -\lambda\,\mathrm{tr}\,(\boldsymbol{b}\cdot\boldsymbol{\varepsilon}^{\mathrm{e}})\;\boldsymbol{\varepsilon}^{\mathrm{e}} - 2\,\mu\,\boldsymbol{\varepsilon}^{\mathrm{e}}\cdot\boldsymbol{b}\cdot\boldsymbol{\varepsilon}^{\mathrm{e}} \\ & - H_a\,\boldsymbol{a}\cdot\boldsymbol{b}\cdot\boldsymbol{a} - H_k\,\mathrm{tr}\,(\boldsymbol{b}\cdot\boldsymbol{k})\;\boldsymbol{b} \\ & + c_b\,[\boldsymbol{\varphi} - \boldsymbol{b}]\ .\end{aligned} \tag{7.12}$$

The stress power associated with the model is of type

$$\mathcal{P} = \boldsymbol{\sigma} : \dot{\boldsymbol{\varepsilon}} + \boldsymbol{\omega} : \dot{\boldsymbol{\varphi}} + \boldsymbol{\Omega} \,\vdots\, \nabla\dot{\boldsymbol{\varphi}}\ , \tag{7.13}$$

where operator $\vdots$ denotes a triple contraction. Stress power (7.13) implies reduced dissipation inequality

$$\mathcal{D}^{\mathrm{red}} = \boldsymbol{\sigma} : \dot{\boldsymbol{\varepsilon}}^{\mathrm{p}} + \boldsymbol{a} : \dot{\boldsymbol{a}} + \boldsymbol{\kappa} : \dot{\boldsymbol{k}} + \boldsymbol{\beta} : \dot{\boldsymbol{b}} \geq 0\ . \tag{7.14}$$

The reduced dissipation is formally identical to reduced dissipation (6.36) of the underlying local model. However, energy release rate $\boldsymbol{\beta}$ is affected by the micromorphic regularization. For c_b chosen sufficiently large, $\boldsymbol{\varphi}$ converges towards $\boldsymbol{b}$ and energy release rate (7.12) converges towards its local counterpart. In this case, dissipation inequality (7.14) simplifies to dissipation inequality (6.36) of the underlying local model and thus, the second law of thermodynamics is indeed fulfilled.

According to Section 2.2, the balance law associated with the micromorphic field is the balance of micro forces. It reads

$$\int_{\mathcal{B}} \boldsymbol{\omega} : \delta\boldsymbol{\varphi} + \boldsymbol{\Omega} \vdots \nabla\delta\boldsymbol{\varphi} \, \mathrm{d}V = 0 \, . \tag{7.15}$$

and can be transformed into Laplace-type

$$l_b^2 \, \mathrm{div} \, (\nabla\boldsymbol{\varphi}) = [\boldsymbol{\varphi} - \boldsymbol{b}] \, . \tag{7.16}$$

Its insertion into energy release rate $\boldsymbol{\beta}$ leads to

$$\boldsymbol{\beta} = -\frac{\partial\psi}{\partial\boldsymbol{b}} = \underbrace{-\frac{\partial\psi^{\mathrm{loc}}}{\partial\boldsymbol{b}}}_{=\boldsymbol{\beta}^{\mathrm{loc}}} - \frac{\partial\psi^{\mathrm{nloc}}}{\partial\boldsymbol{b}} = \underbrace{\boldsymbol{\beta}^{\mathrm{loc}}}_{\text{local model}} + c_b \, l_b^2 \, \mathrm{div} \, (\nabla\boldsymbol{\varphi}) \tag{7.17}$$

and, hence, the gradient extension becomes obvious.
Although the model is indeed gradient-enhanced, it does not regularize the local damage model. Within the next section, this problem will be analyzed in detail.

7.1.2 Analysis of the model

Focusing on an isotropic damage evolution, the coupling between plasticity and material degradation was also analyzed in [80]. Within the cited paper, it is mentioned that a micromorphic enhancement of the underlying local model – similar to the modification presented in the previous paragraph – is not able to regularize the local model. In order to solve the problem, two different yield functions are introduced in [80]: one yield function for plasticity and an additional yield/failure function associated with material damage. This modification certainly solves the problem. However, a more detailed analysis of the underlying problem is not given in [80]. Furthermore, classic ductile damage models are usually based on a single yield function, see e.g. [94]. A regularization of ductile damage models based on a single yield function is precisely one of the goals to be achieved in this chapter.

In this section, the naive extension towards a micromorphic regularization as presented in the previous subsection is critically analyzed first. A bar consisting of n (finite) elements with one imperfect element is considered in Subsection 7.3.1. A more complex boundary value problem – a plate with a hole – is investigated in Subsection 7.3.2 and in Subsection 7.4.1. Without anticipating all details provided in Sections 7.3 and 7.4 some of the main findings are already reported here.

Bar with an imperfect element (see Subsection 7.3.1) If loading (such as uniaxial tension) is increased in the bar with an imperfect element (the initial yield stress τ_y of the imperfect element is slightly reduced), the yield stress of the imperfect element is

reached first, resulting in $\dot{\boldsymbol{b}} \neq \boldsymbol{0}$. This, in turn, leads through eq. (7.15) to an evolution of global field $\boldsymbol{\varphi}$. However, $\boldsymbol{\varphi}$ does not influence internal variable $\boldsymbol{b}$ of the remaining finite elements. If loading is further increased, damage evolves in the imperfect element by which $\boldsymbol{\varphi}$ also evolves. The stresses in the imperfect element decrease marginally due to material damage. Due to equilibrium, the stresses in the remaining elements also decrease. However, the integrity tensor of the remaining elements does not evolve. Furthermore, the micromorphic extension eliminates the evolution of $\boldsymbol{b}$ within the localized element. To be more precise, the contribution of micromorphic extension to $\boldsymbol{b}$ shows the same absolute value as that of the local contribution, but a different sign. As a consequence of the aforementioned elimination, the total mechanical response is not characterized by material softening anymore.

Plate with a hole (see Subsections 7.3.2 and 7.4.1) The one-dimensional problem discussed before shows that the naive micromorphic approach cannot capture material softening in general. However, the results seem to be mesh-objective. In order to proof this conjecture (mesh-objectivity) – which is in contrast to the findings reported in [80] – a two-dimensional problem is also analyzed. Without going too much into detail, the results summarized in subsections 7.3.2 and 7.4.1 show that the resulting finite element computations are not mesh-objective, i.e., the naive micromorphic approach does not regularize the underlying ill-posed local constitutive model.

Finally, it is noted that the differences between the one-dimensional and the two-dimensional example seem to be related to the compatibility condition. To be more precise, the kinematics reduced to one dimension are incompatible in the sense that stretches orthogonal to the bar's axis are not subjected to any constraint. By way of contrast, the two-dimensional finite element discretization is automatically compatible. This compatibility leads to a stronger coupling between the neighboring elements and therefore, to a different damage evolution.

7.1.3 Novel micromorphic extension of the local, isotropic, ductile damage model

According to the previous subsection, micromorphic field $\boldsymbol{\varphi}$, which was supposed to regularize the local constitutive model through a gradient-enhancement, affects the yield function of the imperfect element only implicitly. Furthermore, it does not affect the non-imperfect elements. In order to obtain an influence of $\boldsymbol{\varphi}$ on yield function Φ for the neighboring elements as well – and thus on their damage evolution – variable

$$\boldsymbol{\omega} = \frac{\partial \psi}{\partial \boldsymbol{\varphi}} = c_b \, [\boldsymbol{\varphi} - \boldsymbol{b}] \overset{\text{eq. (7.16)}}{=} c_b \, l_b^2 \, \operatorname{div} (\nabla \boldsymbol{\varphi}) \tag{7.18}$$

being dual to $\boldsymbol{\varphi}$ is utilized. Evidently, tensor $\boldsymbol{\omega}$ naturally includes a gradient contribution. Furthermore, $\boldsymbol{\omega}$ connects the local energy release rate tensor $\boldsymbol{\beta}^{\mathrm{loc}}$ and its gradient-enhanced counterpart $\boldsymbol{\beta}$ according to

$$\boldsymbol{\beta} = \boldsymbol{\beta}^{\mathrm{loc}} + \boldsymbol{\omega} \,. \tag{7.19}$$

With this notation, the yield function of the previous micromorphic model is replaced/enhanced by

$$\Phi \leftarrow \Phi(\boldsymbol{\sigma},\, \boldsymbol{\omega},\, \boldsymbol{\alpha},\, \boldsymbol{\kappa};\, \boldsymbol{b}) \,. \tag{7.20}$$

Precisely speaking, the dependency of Φ on $\boldsymbol{\omega}$ is the key idea for the novel micromorphic regularization of the local single yield surface-based ductile damage model. Alternatively, a direct incorporation of $\nabla\boldsymbol{\varphi}$ or $\nabla\boldsymbol{b}$ would be possible as well. However, the choice of $\boldsymbol{\omega}$ is favored, since a direct incorporation of $\nabla\boldsymbol{\varphi}$ or $\nabla\boldsymbol{b}$ would result in high implementation effort – as already explained in Chapter 3. Regarding the numerical examples, the simple choice

$$\Phi = \Phi^{\mathrm{loc}} + f_{\omega} \qquad \text{with} \qquad f_{\omega}(\boldsymbol{\omega}) = -\boldsymbol{b}^{-p} : \boldsymbol{\omega} \,, \tag{7.21}$$

with p being an additional regularization parameter is made. However, it bears emphasis that other functions $\Phi(\boldsymbol{\sigma},\, \boldsymbol{\omega},\, \boldsymbol{\alpha},\, \boldsymbol{\kappa};\, \boldsymbol{b})$ are possible as well and furthermore, the enhancement does not need to be additively in structure. A method for calculation of $\boldsymbol{b}^{-p}$ for real-valued exponents p as well as its first and second derivatives is shown in detail in Appendix D.2.

Choice (7.21) is motivated by the following facts: (i) Within the original model, in which the yield function does not depend on $\boldsymbol{\omega}$, integrity tensor $\boldsymbol{b}$ does not evolve in the elements being neighbors of the imperfect element. However, although $\boldsymbol{b} = \boldsymbol{I}$ in these neighboring elements, field $\boldsymbol{\varphi}$ shows the correct spatial distribution. For this reason, $\boldsymbol{b}$ should follow field $\boldsymbol{\varphi}$. This can be realized by decreasing yield limit τ_y in yield function (6.72). In order to do so, τ_y is replaced by $\tau_y \leftarrow \tau_y - f_{\boldsymbol{\omega}}$. Accordingly, if damage occurs in the imperfect element, the eigenvalues of $\boldsymbol{b}$ and thus also those of $\boldsymbol{\varphi}$ decrease. Through continuity of field $\boldsymbol{\varphi}$, the eigenvalues of $\boldsymbol{\varphi}$ also decrease in the neighboring elements and the coupling becomes active. (ii) Factor $\boldsymbol{b}^{-p}$ increases with respect to damage accumulation. By doing so, the implicit gradient-enhancement becomes more pronounced for material points undergoing localized material damage and thus, localization within a single material point (respectively a finite element) is penalized. It bears emphasis, that the choice of p has a major influence on the results. Increasing parameter p leads to a stronger coupling between $\boldsymbol{\varphi}$ and $\boldsymbol{b}$, but also to an increase in residual forces for lower values of $\boldsymbol{b}$. This will be investigated in detail within Sections 7.3 and 7.4.
Clearly, the yield function of the original local model and that of the modified counterpart according to eq. (7.21) are different – as long as $f_{\boldsymbol{\omega}} \neq 0$, i.e., $\boldsymbol{b} \neq \boldsymbol{\varphi}$. The principle of equi-presence suggests including tensor $\boldsymbol{\omega}$ also into the other constitutive functions such

as the evolution equations and Helmholtz energy ψ. However, concerning the latter, the work-conjugacy between $\boldsymbol{\omega}$ and the already included dependency of ψ on $\boldsymbol{\varphi}$ prohibits this modification. For this reason, only the evolution equations (the respective plastic potentials) have to be modified.
According to the principle of equi-presence, plastic potential $g = g(\boldsymbol{\sigma}, \boldsymbol{\alpha}, \boldsymbol{\kappa}, \boldsymbol{\beta}; \boldsymbol{b})$ (see eq. (6.42)) of the original underlying local model has to be modified by $g \leftarrow g(\boldsymbol{\sigma}, \boldsymbol{\omega}, \boldsymbol{\alpha}, \boldsymbol{\kappa}, \boldsymbol{\beta}; \boldsymbol{b})$. Since only the damage-related part of the local model has to be regularized, ansatz

$$g = \Phi(\boldsymbol{\sigma}, \boldsymbol{\omega}, \boldsymbol{\alpha}, \boldsymbol{\kappa}, \boldsymbol{\beta}; \boldsymbol{b}) + \Gamma_{\boldsymbol{\alpha}}(\boldsymbol{\alpha}; \boldsymbol{b}) + \Gamma_{\boldsymbol{\kappa}}(\boldsymbol{\kappa}; \boldsymbol{b}) + \Gamma_{\boldsymbol{\beta}}(\boldsymbol{\omega}, \boldsymbol{\beta}; \boldsymbol{b}) \tag{7.22}$$

is made. As a consequence, isotropic hardening and kinematic hardening are not modified. In order to keep the plastic potential of the original local model which drives the damage evolution, plastic potential $\Gamma_{\boldsymbol{\beta}}$ is replaced by

$$\begin{aligned} \Gamma_{\boldsymbol{\beta}} &= \frac{\eta_1}{2} \operatorname{tr}\left(\boldsymbol{b} \cdot [\boldsymbol{\beta} - \boldsymbol{\omega}]\right)^2 + \frac{\eta}{2}\, \boldsymbol{b} : [[\boldsymbol{\beta} - \boldsymbol{\omega}] \cdot \boldsymbol{b} \cdot [\boldsymbol{\beta} - \boldsymbol{\omega}]] \\ &= \frac{\eta_1}{2} \operatorname{tr}\left(\boldsymbol{b} \cdot \boldsymbol{\beta}^{\mathrm{loc}}\right)^2 + \frac{\eta}{2}\, \boldsymbol{b} : \left[\boldsymbol{\beta}^{\mathrm{loc}} \cdot \boldsymbol{b} \cdot \boldsymbol{\beta}^{\mathrm{loc}}\right] \ . \end{aligned} \tag{7.23}$$

Again, it is noted that this is indeed a (suitable) constitutive assumption and other choices are possible as well.

Remark 5 *Within the model, the full gradient of second-order tensor $\boldsymbol{b}$ is controlled via the micromorphic approach – in contrast to [10]. Clearly, due to numerical efficiency, regularizing only an effective scalar-valued variable might be tempting. However, second-order tensor $\boldsymbol{b}$ cannot be completely controlled in this case. For this reason, it is currently mathematically an open question, if such a scalar-valued regularization would lead to well-posed mathematical equations.*

7.2 Micromorphic gradient regularization for isotropic, ductile damage models

Following the same line of thoughts, prototype model 6.3 is regularized by means of the novel micromorphic regularization. It is presented here for the sake of completeness. The enhanced Helmholtz energy reads

$$\psi = \psi^{\mathrm{loc}}(\boldsymbol{\varepsilon}, \boldsymbol{\varepsilon}^{\mathrm{p}}, \boldsymbol{a}, k, b) + \psi^{\mathrm{nloc}}(b, \varphi, \nabla\varphi) \tag{7.24}$$

$$\psi^{\mathrm{loc}} = \psi^{\mathrm{e}}(\boldsymbol{\varepsilon}, \boldsymbol{\varepsilon}^{\mathrm{p}}, b) + \psi^{\mathrm{p}}(\boldsymbol{\varepsilon}^{\mathrm{p}}, \boldsymbol{a}, k, b) \tag{7.25}$$

$$\psi^{\mathrm{e}} = \frac{\lambda}{2}\, b^2 \operatorname{tr}\left(\boldsymbol{\varepsilon}^{\mathrm{e}}\right)^2 + \mu\, b^2\, \boldsymbol{\varepsilon}^{\mathrm{e}} : \boldsymbol{\varepsilon}^{\mathrm{e}} \tag{7.26}$$

$$\psi^{\mathrm{p}} = \frac{H_a}{2}\, b^2\, \boldsymbol{a} : \boldsymbol{a} + \frac{H_k}{2}\, b^2\, k^2 \tag{7.27}$$

$$\psi^{\mathrm{nloc}} = \frac{c_b}{2}\,[\varphi - b]^2 + \frac{c_b\, l_b^2}{2}\,||\nabla\varphi||^2 \ . \tag{7.28}$$

By considering a stress power of type (7.13) the reduced dissipation inequality takes the form

$$\mathcal{D}^{\mathrm{red}} = -\boldsymbol{\sigma}^{\mathrm{p}} : \dot{\boldsymbol{\varepsilon}}^{\mathrm{p}} - \beta\,\dot{b} - \boldsymbol{\alpha} : \dot{\boldsymbol{a}} - \kappa\,\dot{k} \geq 0\ , \tag{7.29}$$

which is a priori fulfilled due to the framework of Generalized Standard Materials. Consequently, the thermodynamic forces take the form

$$\boldsymbol{\sigma} = \frac{\partial\psi}{\partial\boldsymbol{\varepsilon}} = \lambda\, b^2\, \mathrm{tr}\,(\boldsymbol{\varepsilon}^{\mathrm{e}})\ \boldsymbol{I} + 2\,\mu\, b^2\, \boldsymbol{\varepsilon}^{\mathrm{e}}\ , \tag{7.30}$$

$$\omega = \frac{\partial\psi}{\partial\varphi} = c_b\ [\varphi - b] \tag{7.31}$$

$$\boldsymbol{\Omega} = \frac{\partial\psi}{\partial\nabla\varphi} = c_b\, l_b^2\, \nabla\varphi \tag{7.32}$$

$$\boldsymbol{\sigma}^{\mathrm{p}} = -\frac{\partial\psi}{\partial\boldsymbol{\varepsilon}^{\mathrm{p}}} = \lambda\, b^2\, \mathrm{tr}\,(\boldsymbol{\varepsilon}^{\mathrm{e}})\ \boldsymbol{I} + 2\,\mu\, b^2\, \boldsymbol{\varepsilon}^{\mathrm{e}}\ , \tag{7.33}$$

$$\boldsymbol{\alpha} = -\frac{\partial\psi}{\partial\boldsymbol{a}} = -H_a\, b^2\, \boldsymbol{a}\ , \tag{7.34}$$

$$\kappa = -\frac{\partial\psi}{\partial k} = -H_k\, b^2\, k\ , \tag{7.35}$$

$$\begin{aligned}\beta = -\frac{\partial\psi}{\partial b} &= -\lambda\, b\, \mathrm{tr}\,(\boldsymbol{\varepsilon}^{\mathrm{e}})^2 - 2\,\mu\, b\, \boldsymbol{\varepsilon}^{\mathrm{e}} : \boldsymbol{\varepsilon}^{\mathrm{e}} - H_a\, b\, \boldsymbol{a} : \boldsymbol{a} - H_k\, b\, k^2 \\ &\quad + c_b\ [\varphi - b]\ .\end{aligned} \tag{7.36}$$

As done for the anisotropic version, the potential associated with the damage evolution is modified by means of penalty contribution ω, reading

$$\Gamma_\beta = \frac{\eta}{2}\, b^2\, [\beta - \omega]^2 = \frac{\eta}{2}\, b^2\, [\beta^{\mathrm{loc}}]^2\ . \tag{7.37}$$

Accordingly, β in potential (6.65) is replaced by β^{loc}. By doing so, the original evolution equation is not affected.

Finally, the yield function of the isotropic model is also given here. Insertion of the aforementioned assumptions eventually yields

$$\Phi = \sqrt{\tau^{\mathrm{eq}}} - \tau_y - \frac{1}{3}\frac{\kappa}{b} + f_\omega \tag{7.38}$$

$$\tau_{\mathrm{eq}} = \frac{3}{2}\, b^{-2}\, \boldsymbol{\tau}_{\mathrm{dev}} : \boldsymbol{\tau}_{\mathrm{dev}} \tag{7.39}$$

$$\boldsymbol{\tau} = \boldsymbol{\sigma}^{\mathrm{p}} - \boldsymbol{\alpha} \tag{7.40}$$

$$f_\omega = -b^{-p}\,\omega. \tag{7.41}$$

7.3 Numerical Examples – Isotropic, ductile damage

7.3.1 Bar with an imperfection

Problem focus The imperfect bar (Fig. 7.1) is ideal in order to analyze the regularization properties of the isotropic, ductile damage model. For the regularized models, the results, i.e., the loading behavior and the distribution of integrity b, should be independent of the underlying element lengths l_e. Therefore, the element length will be varied and the results of the three models (local, naive micromorphic and novel micromorphic) will be compared.

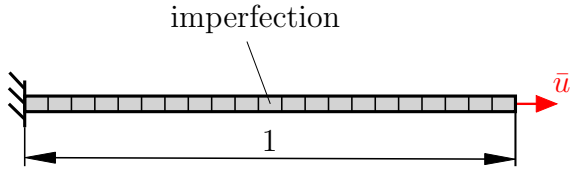

Figure 7.1: Bar with an imperfection: geometry and boundary conditions.

Numerical setup The truss, which is fixed on the left-hand side, is loaded in tension by prescribing the displacement at the right-hand side. The mechanical setup, the finite element discretization by means of (21, 41, 81 and 161) linear displacement-driven finite elements is summarized in Fig. 7.1. The material parameters are shown in Tab. 7.1. In order to trigger localization, the element in the middle of the structure is weakened by reducing its initial yield stress by 5 %. Homogeneous Neumann-boundary conditions have been assumed for the micromorphic field φ.

Results and discussion The mechanical responses as predicted by the three different models are summarized in Fig. 7.2. Accordingly, the underlying local model as well as its novel micromorphic extension capture the desired softening response (Fig. 7.2 (a) and (c)). By way of contrast, the naive micromorphic model (Fig. 7.2 (b)) does not, but shows a plateau in the load-displacement diagram. This can also be seen in the distribution of integrity variable b at the final stage of deformation (Fig. 7.3 (b)). It bears emphasis that the spatial distribution of b is not constant for the naive straightforward micromorphic model, i.e., localized damage indeed occurs within the element showing the imperfection. However, since fields b and φ are only one-directionally coupled, integrity b does not evolve in the neighboring elements. Furthermore, the micromorphic extension eliminates the evolution of b within the localized element such that the total mechanical response is not characterized by material softening anymore.

Name	Symbol	Value	Unit
Young's Modulus	E	400	[MPa]
Initial yield stress	τ_y	1 (0.95)	[MPa]
Hardening modulus (kinematic)	H_a	0	[MPa]
Armstrong Frederick	B_a	0	[-]
Hardening modulus (isotropic)	H_k	0	[MPa]
Armstrong Frederick	B_k	0	[-]
Damage modulus	η	1000	[1/MPa]
Penalty parameter (regularization)	c_b	5	[MPa]
Length parameter	l_b^2	20	[mm^2]
Regularization exponent	p	1	[-]

Table 7.1: Bar with an imperfection: material parameters associated with the regularized anisotropic ductile damage model.

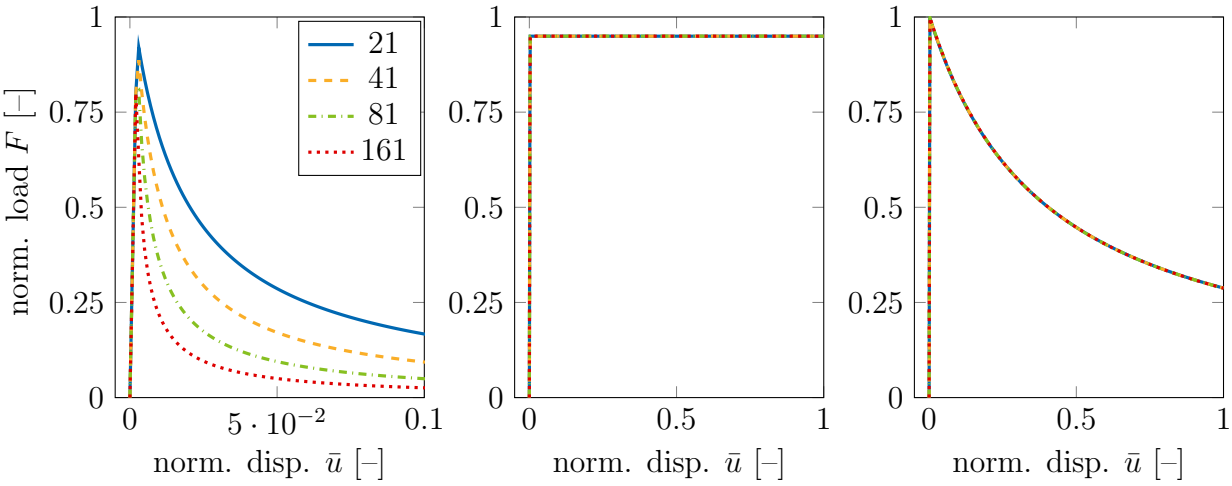

(a) local **(b)** naive **(c)** novel

Figure 7.2: Bar with an imperfection: load-displacement diagrams for the local model, the naive micromorphic model and the novel micromorphic model.

For the sake of completeness, mesh objectivity of the novel model is shown in Fig. 7.3(b). While the load-displacement diagrams associated with the local model depend on the underlying finite element mesh, this pathological behavior is neither observed for the naive micromorphic nor for the novel micromorphic model. However and as already mentioned before, only the novel micromorphic model captures the desired softening response.
Finally, it is noted once again that due to the missing three-dimensional kinematic compatibility of the one-dimensional model, the results obtained from the one-dimensional

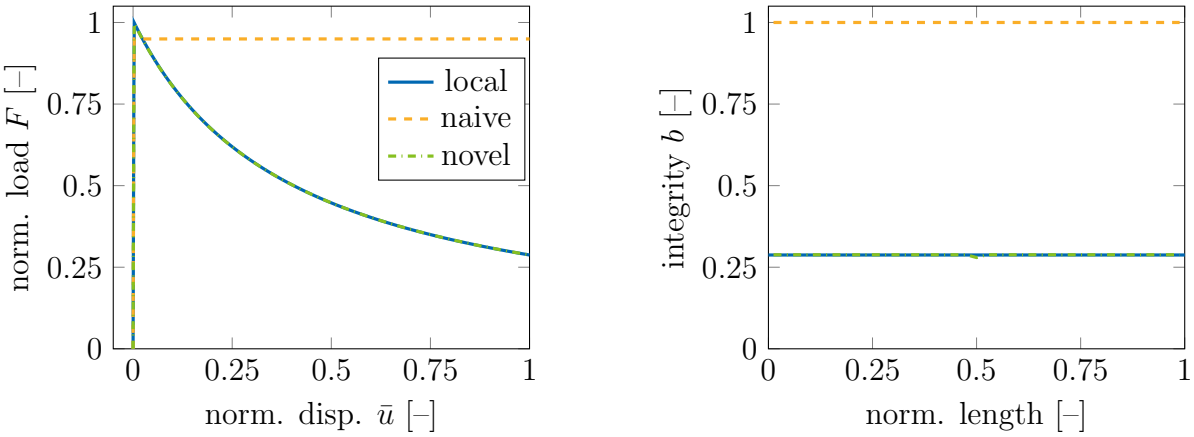

(a) Load-displacement diagram

(b) Distribution of integrity b

Figure 7.3: Bar with an imperfection: load-displacement diagram and distribution of integrity b at the final stage of deformation for the local model, the naive micromorphic model and the novel micromorphic model

example have to be taken with care. For that purpose, spatially more complex boundary value problems are analyzed next.

7.3.2 Plate with a centered hole

Problem focus The predictive capabilities of the novel damage model as well as the mesh objectivity due to the micromorphic gradient regularization are demonstrated here for more complex boundary value problems. Furthermore – and in contrast to the one-dimensional model – the two-dimensional models are kinematically compatible in the sense that lateral contraction effects are modeled in a continuous fashion.

Numerical setup A plate with a centered hole will serve as a benchmark. The geometry and the boundary conditions are given in Fig. 7.4. The displacements at the bottom of the system are fixed to zero, while the displacements at the upper edge are prescribed by $\bar{u}_v$ (vertical direction) and $\bar{u}_h$ (horizontal direction). Due to the symmetry of the system (for vanishing horizontal displacement $\bar{u}_h$), only the blue framed area is discretized by means of finite elements. In order to analyze mesh objectivity of the resulting models, three different finite element discretizations based on bi-linear quadrilateral elements are considered. The discretizations consist of 137 elements (denoted as coarse mesh), 461 elements (denoted as medium mesh) and 991 elements (denoted as fine mesh). The material parameters are given in Tab. 7.2. Different penalty parameters are chosen for the naive and the novel micromorphic approach in order to obtain a similar structural response.

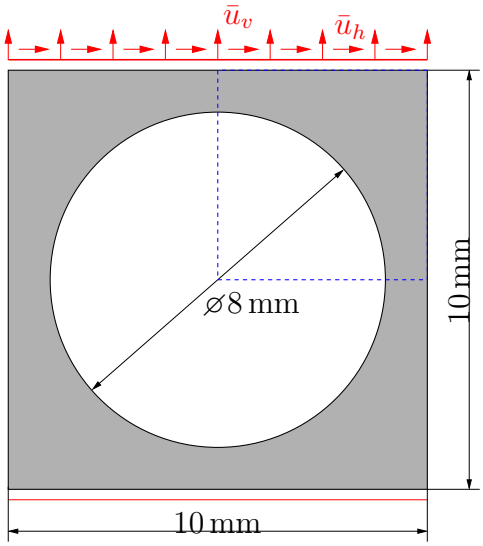

Figure 7.4: Plate with a centered hole: geometry and boundary conditions. Homogeneous Neumann boundary conditions are assumed as far as the gradient-enhanced models are concerned.

Name	Symbol	local	naive	novel		Unit
Young's Modulus	E	400	400	400		[MPa]
Poisson's ratio	ν	0.3	0.3	0.3		[-]
Initial yield stress	τ_y	1	1	1		[MPa]
Hardening modulus (kinematic)	H_a	50	50	50		[MPa]
Armstrong Frederick	B_a	2.5	2.5	2.5		[-]
Hardening modulus (isotropic)	H_k	50	50	50		[MPa]
Armstrong Frederick	B_k	2.5	2.5	2.5		[-]
Damage modulus	η	2000	2000	2000		[1/MPa]
Penalty parameter (regularization)	c_b	–	0.2	15	200	[MPa]
Length parameter	l_b^2	–	5	1/15	1/200	[mm^2]
Regularization exponent	p	–	–	0.5	0	[-]

Table 7.2: Plate with a centered hole: material parameters associated with the isotropic models.

Results and discussion Fig. 7.5 shows the load-displacement diagrams for the three different finite element triangulations (prescribed displacement $\bar{u}_v$ versus corresponding reaction force F_v ($\bar{u}_h$ is not prescribed)). According to Fig. 7.5, the softening response as predicted by the novel micromorphic model is indeed mesh objective. Furthermore, the sensitivity of the softening response with respect to exponent p is evident: the smaller p, the faster the softening. In contrast to the novel model, the underlying local model as well as its naive micromorphic extension show a pathological mesh dependence. Concerning the naive micromorphic extension, a very fine finite element triangulation

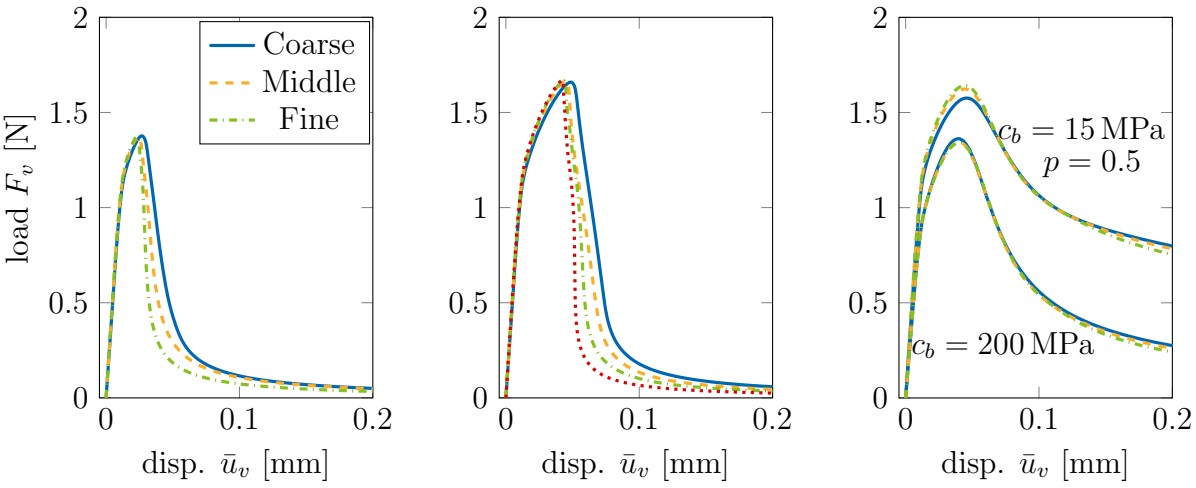

(a) local **(b)** naive **(c)** novel

Figure 7.5: Plate with a centered hole: load-displacement diagrams for the local model, the naive micromorphic model and the novel micromorphic model.

has been additionally considered (red-colored dots).

The distribution of integrity variable b is shown in Fig. 7.6 - Fig. 7.8 for the final displacement amplitudes $\bar{u}_v = 0.2\,\mathrm{mm}$, ($\bar{u}_h$ is not prescribed). In order to highlight the missing mesh-objectivity associated with the local and the naive micromorphic extension, the distribution of integrity variable b predicted by the local and the naive micromorphic model are shown in Fig. 7.6 and Fig. 7.7. Both models predict not only a varying crack thickness, but also a varying crack path. The missing interaction between local field b and non-local field φ becomes evident, since φ shows the expected spatial distribution, but does not affect the local field.

In contrast, the novel micromorphic model (Fig. 7.8) shows the expected smeared spatial distribution for both fields b and φ. For the chosen length parameter, the damage evolution does not resemble a sharp crack anymore, which can be achieved by choosing a smaller length parameter (and a finer discretization). Furthermore, it can be seen that the difference between the fine and the medium mesh is smaller than that between the coarse and the medium mesh, which is an indicator for mesh convergence. In line with the load-displacement diagram, the predicted distribution of b is mesh objective.

7.4 Numerical Examples – Anisotropic, ductile damage

The plate with a centered hole (Fig. 7.4) is re-analyzed with respect to anisotropic material degradation and two different load-cases.

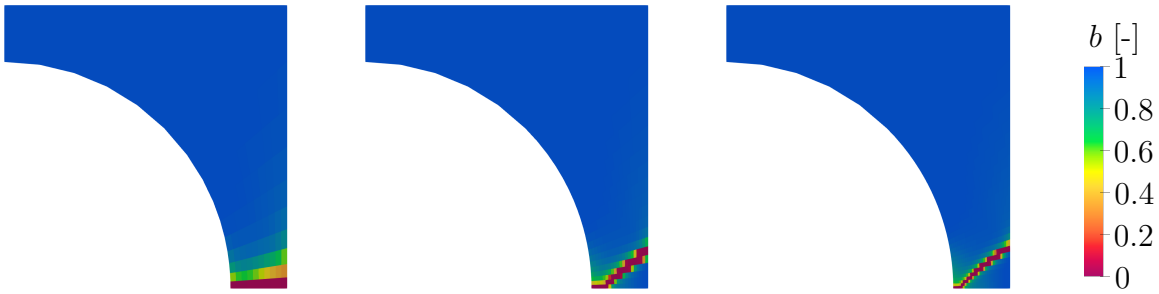

(a) Coarse mesh **(b)** Medium mesh **(c)** Fine mesh

Figure 7.6: Plate with a centered hole: distribution of integrity b associated with the local model.

Name	Symbol	Tension		Tension and shear		Unit
Young's Modulus	E	400		400		[MPa]
Poisson's ratio	ν	0.3		0.3		[-]
Initial yield stress	τ_y	1		1		[MPa]
Hardening modulus (kinematic)	H_a	50		50		[MPa]
Armstrong Frederick	B_a	2.5		2.5		[-]
Hardening modulus (isotropic)	H_k	50		50		[MPa]
Armstrong Frederick	B_k	2.5		2.5		[-]
Damage modulus (isotropic)	η_1	500		1000	0	[1/MPa]
Damage modulus (anisotropic)	η_2	500		0	1000	[1/MPa]
Penalty parameter (regularization)	c_b	10	50	50		[MPa]
Length parameter	l_b^2	0.1	0.02	0.02		[mm^2]
Regularization exponent	p	0.5	0	0		[-]

Table 7.3: Plate with a centered hole: material parameters associated with the anisotropic models.

7.4.1 Plate with a centered hole under tension

Two different sets of material parameters are considered, cf. Tab. 7.3. In comparison to set $p = 0.5$ and $c_b = 10\,\text{MPa}$, set $p = 0$ and $c_b = 50\,\text{MPa}$ is characterized by faster material softening. The structure is loaded first by prescribing only the vertical displacement $\bar{u}_v$. Due to the missing mesh-objectivity, results associated with the underlying local model as well as with its naive micromorphic extension are not presented.

Results and discussion In comparison to the isotropic case, the differences between the different load-displacement diagrams (Fig. 7.9) corresponding to the underlying finite element meshes is even smaller. Furthermore, the influence of material parameter p on the softening behavior is evident.

The distribution of the integrity is given in Fig. 7.10 as well as in Fig. 7.11. All

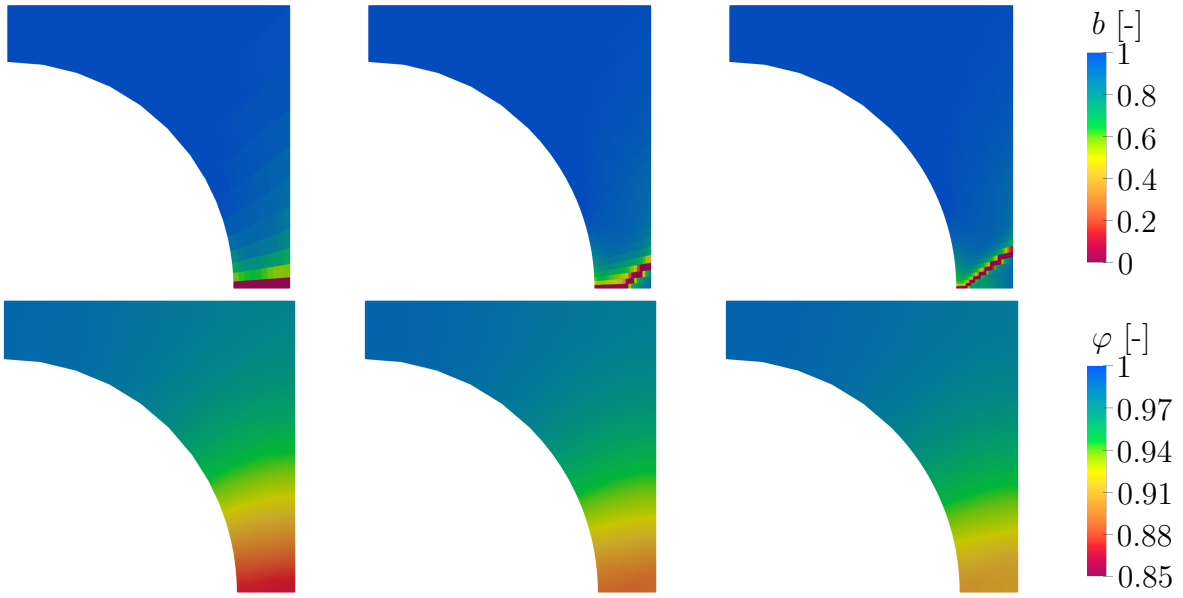

(a) Coarse mesh **(b)** Medium mesh **(c)** Fine mesh

Figure 7.7: Plate with a centered hole: distribution of integrity b associated with the naive regularized micromorphic model.

distributions correspond to the set of material parameters $p = 0$ and $c_b = 50\,\mathrm{MPa}$. Since integrity $\boldsymbol{b}$ is now a second-order tensor, its scalar-valued graphical representation is more difficult. Since loading is in line with the y-axis, the two representative coordinates b_{xx} and b_{yy} are chosen.

The distributions are analyzed for two different loading amplitudes $\bar{u}_v = 0.1\,\mathrm{mm}$ and $\bar{u}_v = 0.2\,\mathrm{mm}$ which correspond to the peak load and the final displacement amplitude.

The distributions of the b_{yy} coordinate is given in Fig. 7.10 for three different finite element triangulations. Accordingly, all meshes predict the same response, i.e., only marginal differences can be seen. As a consequence, objectivity of the results is confirmed.

The distribution of the b_{xx} coordinate of the integrity tensor is shown in Fig. 7.11. Clearly, due to the underlying anisotropic damage model, the b_{xx} coordinate is not identical to coordinate b_{yy}. As expected, the degradation in loading direction is more advanced compared to the degradation in orthogonal direction. Again, mesh objectivity is observed.

7.4.2 Plate with a centered hole under tension followed by shear

In order to highlight the importance of considering damage evolution as an anisotropic process, the plate with a hole is re-analyzed. Within the re-analysis, uniaxial loading in vertical direction is again applied first. However, the loading amplitude is subsequently

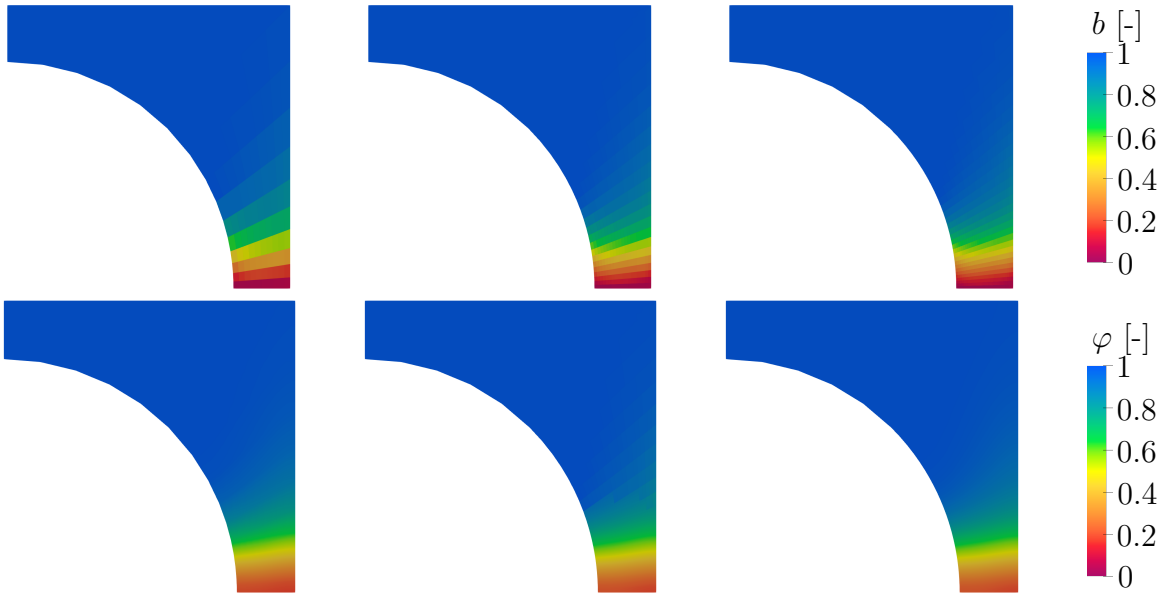

(a) Coarse mesh **(b)** Medium mesh **(c)** Fine mesh

Figure 7.8: Plate with a centered hole: distribution of integrity b associated with the novel regularized isotropic model with parameter $p = 0$ and $c_b = 200\,\mathrm{MPa}$

decreased. By doing so, the evolution of the overall structural elasticity is visualized. Finally, loading is applied in a shear mode. This allows to investigate the influence of the previous damage evolution on a different direction. A summary of the loading history in terms of a normalized time is given in Fig. 7.12(a). The corresponding material parameters are summarized in Tab. 7.3. Accordingly, $\eta_1 = 1000\,\mathrm{MPa}^{-1}$ and $\eta_2 = 0\,\mathrm{MPa}^{-1}$ defines an isotropic damage model, while an anisotropic model is obtained for $\eta_1 = 0\,\mathrm{MPa}^{-1}$ and $\eta_2 = 1000\,\mathrm{MPa}^{-1}$.

Results and discussion From Fig. 7.12(b) it can be concluded that both models (isotropic and the anisotropic model) lead to a similar damage evolution in loading direction, since both curves agree very well during the first two loading stages. Clearly, the isotropic model predicts an identical damage evolution in all directions. By way of contrast, the anisotropic model shows the highest damage accumulation in loading direction. As a consequence, the structural stiffness in horizontal direction is higher for the anisotropic model — as shown in Fig. 7.12(c). This effect can be seen in brittle-materials due to the anisotropy induced by micro-cracks or in ductile materials due to the evolution of elongated and distorted pores.

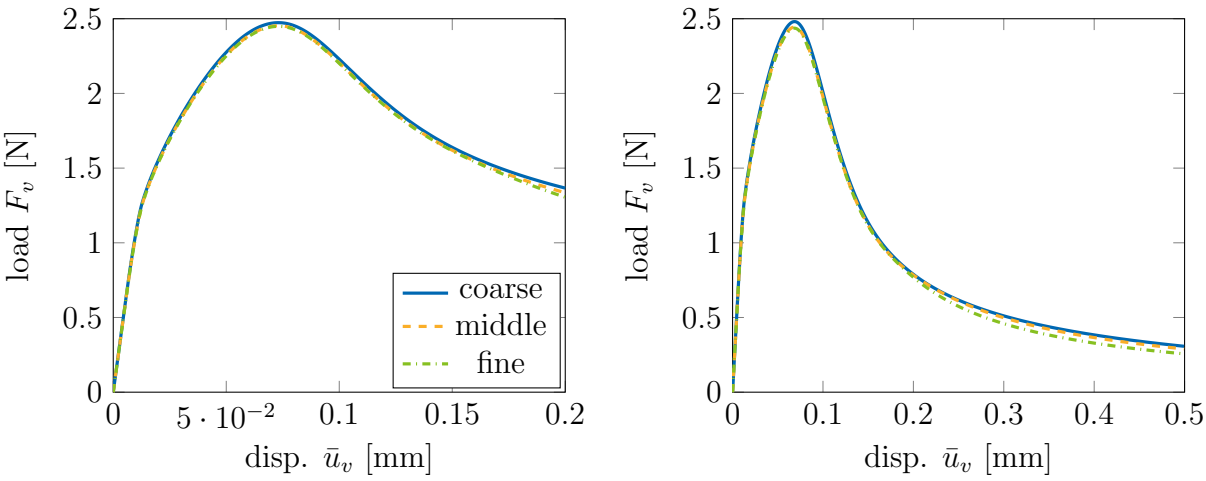

(a) $p = 0.5$, $c_b = 10\,\mathrm{MPa}$ **(b)** $p = 0$, $c_b = 50\,\mathrm{MPa}$

Figure 7.9: Plate with a centered hole: novel regularized anisotropic model. Prescribed displacement $\bar{u}_v$ versus corresponding reaction force F_v ($\bar{u}_h$ is not prescribed). Material parameters according to Tab. 7.3.

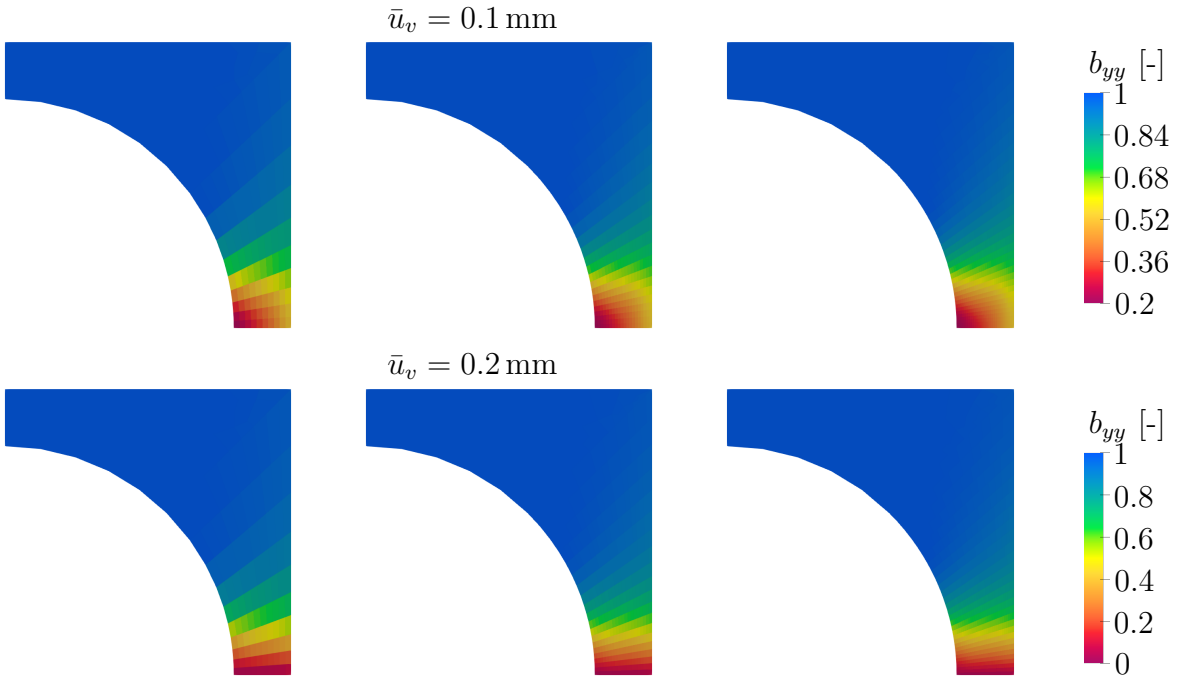

(a) Coarse mesh **(b)** Medium mesh **(c)** Fine mesh

Figure 7.10: Plate with a centered hole: novel regularized anisotropic model. Distributions of component b_{yy} of integrity tensor $\boldsymbol{b}$. Material parameters according to Tab. 7.3 ($p = 0$ and $c_b = 50\,\mathrm{MPa}$).

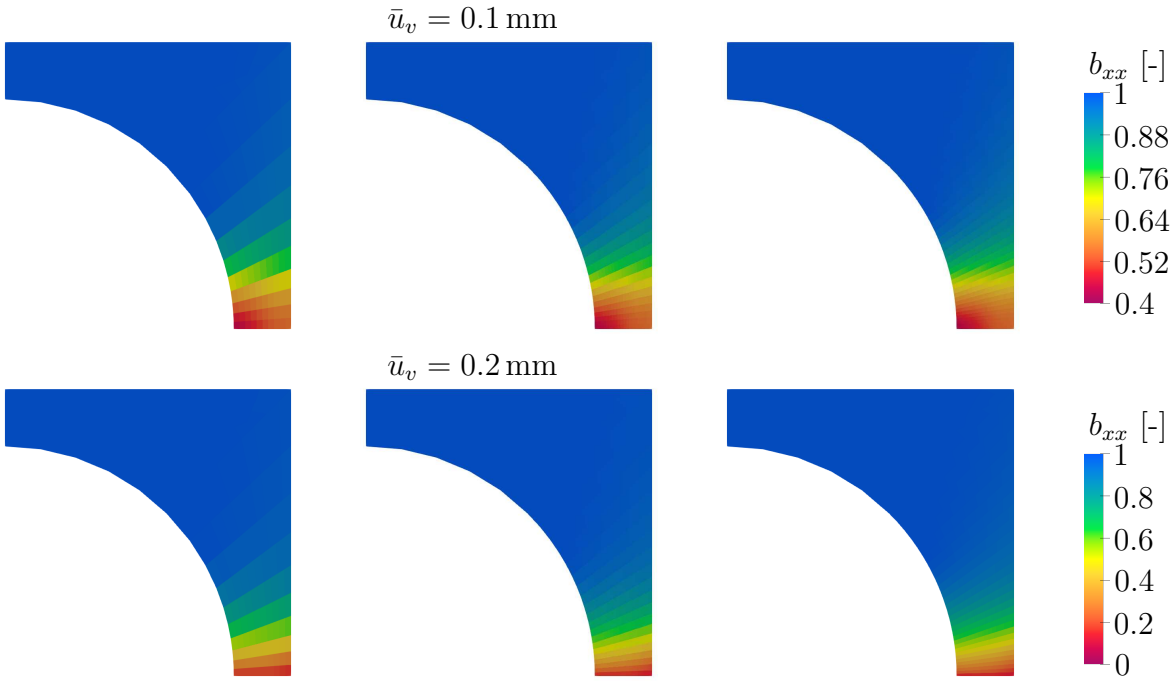

(a) Coarse mesh **(b)** Medium mesh **(c)** Fine mesh

Figure 7.11: Plate with a centered hole: anisotropic damage model: distributions of coordinate b_{xx} of integrity tensor $\boldsymbol{b}$. Material parameters according to Tab. 7.3 ($p = 0$ and $c_b = 50\,\mathrm{MPa}$)

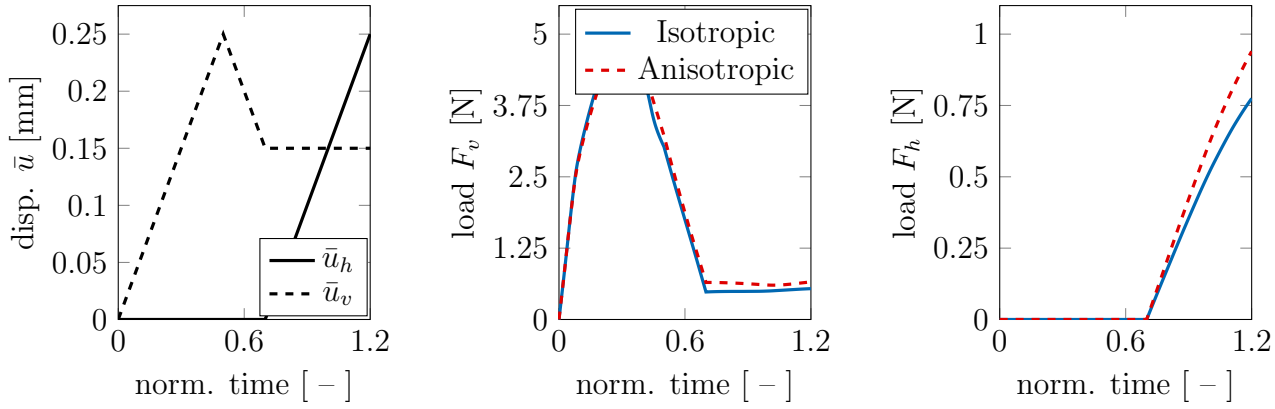

(a) prescribed loading **(b)** vertical reaction force **(c)** horizontal reaction force

Figure 7.12: Plate with a centered hole: novel regularized anisotropic model. Material parameters according to Tab. 7.3.

E Appendix

E.1 Numerical implementation

This section deals with the effective numerical implementation of the regularized anisotropic ductile damage model according to Section 6.2 and 7.1.3. In line with the standard approximations of the finite element method, global field variables $\boldsymbol{u}$ and $\boldsymbol{\varphi}$ are approximated by

$$\boldsymbol{u} = \sum_{A=1}^{n_{\text{en}}} \boldsymbol{u}^A \, N^A \quad \Rightarrow \quad \nabla \boldsymbol{u} = \sum_{A=1}^{n_{\text{en}}} \boldsymbol{u}^A \otimes \frac{\partial N^A}{\partial \boldsymbol{X}} \tag{7.42}$$

$$\boldsymbol{\varphi} = \sum_{A=1}^{n_{\text{en}}} \boldsymbol{\varphi}^A \, N^A \quad \Rightarrow \quad \nabla \boldsymbol{\varphi} = \sum_{A=1}^{n_{\text{en}}} \boldsymbol{\varphi}^A \otimes \frac{\partial N^A}{\partial \boldsymbol{X}} \, , \tag{7.43}$$

where N^A are shape functions and $\boldsymbol{u}^A$ as well as $\boldsymbol{\varphi}^A$ are nodal degrees of freedom associated with node $A \in \{1, ..., n_{\text{en}}\}$. Accordingly, the same shape functions are used for both fields. This choice is clearly not mandatory. Adopting a Bubnov-Galerkin-Ansatz, test functions $\delta\boldsymbol{u}$ and $\delta\boldsymbol{\varphi}$ are spanned by the same shape functions. They read

$$\delta\boldsymbol{u} = \sum_{A=1}^{n_{\text{en}}} \delta\boldsymbol{u}^A \, N^A \quad \Rightarrow \quad \nabla\delta\boldsymbol{u} = \sum_{A=1}^{n_{\text{en}}} \delta\boldsymbol{u}^A \otimes \frac{\partial N^A}{\partial \boldsymbol{X}} \tag{7.44}$$

$$\delta\boldsymbol{\varphi} = \sum_{A=1}^{n_{\text{en}}} \delta\boldsymbol{\varphi}^A \, N^A \quad \Rightarrow \quad \nabla\delta\boldsymbol{\varphi} = \sum_{A=1}^{n_{\text{en}}} \delta\boldsymbol{\varphi}^A \otimes \frac{\partial N^A}{\partial \boldsymbol{X}} \, . \tag{7.45}$$

By inserting these approximations into balance of linear momentum (2.12) and balance of micro forces (2.21), respectively, one obtains the contribution of element e and node A as

$$\boldsymbol{R}_{\boldsymbol{u}}^{e,A} = \int_{V^e} \boldsymbol{\sigma} \cdot \frac{\partial N^A}{\partial \boldsymbol{X}} \, \mathrm{d}V \tag{7.46}$$

$$\boldsymbol{R}_{\boldsymbol{\varphi}}^{e,A} = \int_{V^e} \boldsymbol{\omega} \, N^A \, \mathrm{d}V + \int_{V^e} \boldsymbol{\Omega} \cdot \frac{\partial N^A}{\partial \boldsymbol{X}} \, \mathrm{d}V \, . \tag{7.47}$$

Clearly, if body forces are present, the respective terms have to be added. For solving the resulting assembled non-linear system of equations in an efficient manner, the standard

Newton-Raphson-method is applied. Therefore, the linearizations of residuals (7.46) and (7.47) are required. They are given by

$$\boldsymbol{K}_{\boldsymbol{uu}}^{e,AB} := \frac{\mathrm{d}\boldsymbol{R}_{\boldsymbol{u}}^{e,A}}{\mathrm{d}\boldsymbol{u}^B} = \int_{V^e} \frac{\partial N^A}{\partial \boldsymbol{X}} \cdot \frac{\mathrm{d}\boldsymbol{\sigma}}{\mathrm{d}\boldsymbol{\varepsilon}} \cdot \frac{\partial N^B}{\partial \boldsymbol{X}} \,\mathrm{d}V \tag{7.48}$$

$$\boldsymbol{K}_{\boldsymbol{u\varphi}}^{e,AB} := \frac{\mathrm{d}\boldsymbol{R}_{\boldsymbol{u}}^{e,A}}{\mathrm{d}\boldsymbol{\varphi}^B} = \int_{V^e} \frac{\partial N^A}{\partial \boldsymbol{X}} \cdot \frac{\mathrm{d}\boldsymbol{\sigma}}{\mathrm{d}\boldsymbol{\varphi}} N^B \,\mathrm{d}V \tag{7.49}$$

$$\boldsymbol{K}_{\boldsymbol{\varphi u}}^{e,AB} := \frac{\mathrm{d}\boldsymbol{R}_{\boldsymbol{\varphi}}^{e,A}}{\mathrm{d}\boldsymbol{u}^B} = \int_{V^e} N^A \frac{\mathrm{d}\boldsymbol{\omega}}{\mathrm{d}\boldsymbol{\varepsilon}} \cdot \frac{\partial N^B}{\partial \boldsymbol{X}} \,\mathrm{d}V \tag{7.50}$$

$$\boldsymbol{K}_{\boldsymbol{\varphi\varphi}}^{e,AB} := \frac{\mathrm{d}\boldsymbol{R}_{\boldsymbol{\varphi}}^{e,A}}{\mathrm{d}\boldsymbol{\varphi}^B} = \int_{V^e} N^A \frac{\mathrm{d}\boldsymbol{\omega}}{\mathrm{d}\boldsymbol{\varphi}} N^B \,\mathrm{d}V + l_b \int_{V^e} \mathbb{I}^{\mathrm{sym}} \left[\frac{\partial N^A}{\partial \boldsymbol{X}} \cdot \frac{\partial N^B}{\partial \boldsymbol{X}}\right] \mathrm{d}V \;, \tag{7.51}$$

where $\mathbb{I}^{\mathrm{sym}}$ denotes the fourth-order symmetric identity tensor.

Stiffness matrices $\boldsymbol{K}_{\bullet\bullet}^{e,AB}$ are directly related to linearizations

$$\begin{aligned} \mathrm{d}\boldsymbol{\sigma} = &\left[\frac{\partial \boldsymbol{\sigma}}{\partial \boldsymbol{\varepsilon}} + \frac{\partial \boldsymbol{\sigma}}{\partial \boldsymbol{\varepsilon}^{\mathrm{p}}} : \frac{\partial \boldsymbol{\varepsilon}^{\mathrm{p}}}{\partial \boldsymbol{\varepsilon}} + \frac{\partial \boldsymbol{\sigma}}{\partial \boldsymbol{b}} : \frac{\partial \boldsymbol{b}}{\partial \boldsymbol{\varepsilon}}\right] : \mathrm{d}\boldsymbol{\varepsilon} \\ &+ \left[\frac{\partial \boldsymbol{\sigma}}{\partial \boldsymbol{\varepsilon}^{\mathrm{p}}} : \frac{\partial \boldsymbol{\varepsilon}^{\mathrm{p}}}{\partial \boldsymbol{\varphi}} + \frac{\partial \boldsymbol{\sigma}}{\partial \boldsymbol{b}} : \frac{\partial \boldsymbol{b}}{\partial \boldsymbol{\varphi}}\right] : \mathrm{d}\boldsymbol{\varphi} \end{aligned} \tag{7.52}$$

$$\begin{aligned} \mathrm{d}\boldsymbol{\omega} = &\left[\frac{\partial \boldsymbol{\omega}}{\partial \boldsymbol{b}} : \frac{\partial \boldsymbol{b}}{\partial \boldsymbol{\varepsilon}}\right] : \mathrm{d}\boldsymbol{\varepsilon} \\ &\left[\frac{\partial \boldsymbol{\omega}}{\partial \boldsymbol{\varphi}} + \frac{\partial \boldsymbol{\omega}}{\partial \boldsymbol{b}} : \frac{\partial \boldsymbol{b}}{\partial \boldsymbol{\varphi}}\right] : \mathrm{d}\boldsymbol{\varphi} \;. \end{aligned} \tag{7.53}$$

Here, (local) state variables $\boldsymbol{\Xi} = [\boldsymbol{\varepsilon}^{\mathrm{p}}, \boldsymbol{b}, \boldsymbol{a}, \boldsymbol{k}, \Delta\lambda]$ are computed by means of a return-mapping scheme. The residuals corresponding to this scheme are (implicit backward Euler integration of evolution equations (6.50) – (6.53))

$$\boldsymbol{r} = \boldsymbol{r}(\boldsymbol{\varepsilon}, \boldsymbol{\varphi}, \boldsymbol{\Xi}) = \begin{bmatrix} \boldsymbol{r}^{\boldsymbol{\varepsilon}^{\mathrm{p}}} \\ \boldsymbol{r}^{\boldsymbol{b}} \\ \boldsymbol{r}^{\boldsymbol{a}} \\ \boldsymbol{r}^{\boldsymbol{k}} \\ r^{\Phi} \end{bmatrix} = \begin{bmatrix} \boldsymbol{\varepsilon}^{\mathrm{p}} - \boldsymbol{\varepsilon}_n^{\mathrm{p}} - \Delta\lambda \dfrac{\partial g}{\partial \boldsymbol{\sigma}} \\ \boldsymbol{b} - \boldsymbol{b}_n - \Delta\lambda \dfrac{\partial g}{\partial \boldsymbol{\beta}} \\ \boldsymbol{a} - \boldsymbol{a}_n - \Delta\lambda \dfrac{\partial g}{\partial \boldsymbol{\alpha}} \\ \boldsymbol{k} - \boldsymbol{k}_n - \Delta\lambda \dfrac{\partial g}{\partial \boldsymbol{\kappa}} \\ \Phi \end{bmatrix} \;. \tag{7.54}$$

Index $(\bullet)_n$ in these equations signals time t_n, while for time t_{n+1} the index is omitted. For fixed global fields $\boldsymbol{\varepsilon}$ and $\boldsymbol{\varphi}$, state variables $\boldsymbol{x}$ are again computed by solving $\boldsymbol{r} = \mathbf{0}$ by employing Newton's method, i.e.,

$$\boldsymbol{\Xi}^{k+1} \leftarrow \boldsymbol{\Xi}^{k} - \left[\left. \frac{\partial \boldsymbol{r}}{\partial \boldsymbol{\Xi}} \right|_{\boldsymbol{\Xi}=\boldsymbol{\Xi}^k} \right]^{-1} \bullet \boldsymbol{r}|_{\boldsymbol{\Xi}=\boldsymbol{\Xi}^k} \ , \tag{7.55}$$

where k denotes the current iteration and $\bullet$ a suitable contraction. The sensitivities of state variables $\boldsymbol{\Xi}$ are calculated through a linearization of residual $\boldsymbol{r}$ at a converged state, i.e., from linearizing $\mathrm{d}\boldsymbol{r} = \mathbf{0}$. By doing so, sensitivity

$$\mathrm{d}\boldsymbol{\Xi} = -\left[\frac{\partial \boldsymbol{r}}{\partial \boldsymbol{\Xi}}\right]^{-1} \bullet \frac{\partial \boldsymbol{r}}{\partial \boldsymbol{\varepsilon}} : \mathrm{d}\boldsymbol{\varepsilon} - \left[\frac{\partial \boldsymbol{r}}{\partial \boldsymbol{\Xi}}\right]^{-1} \bullet \frac{\partial \boldsymbol{r}}{\partial \boldsymbol{\varphi}} : \mathrm{d}\boldsymbol{\varphi} \tag{7.56}$$

is derived. This equation can finally be decomposed into derivatives (sensitivities)

$$\frac{\mathrm{d}\boldsymbol{\Xi}}{\mathrm{d}\boldsymbol{\varepsilon}} = -\left[\frac{\partial \boldsymbol{r}}{\partial \boldsymbol{\Xi}}\right]^{-1} \bullet \frac{\partial \boldsymbol{r}}{\partial \boldsymbol{\varepsilon}} \tag{7.57}$$

$$\frac{\mathrm{d}\boldsymbol{\Xi}}{\mathrm{d}\boldsymbol{\varphi}} = -\left[\frac{\partial \boldsymbol{r}}{\partial \boldsymbol{\Xi}}\right]^{-1} \bullet \frac{\partial \boldsymbol{r}}{\partial \boldsymbol{\varphi}} \ . \tag{7.58}$$

These derivatives, in turn, allow the computation of linearizations (7.52) and (7.53) in terms of global fields $\boldsymbol{\varepsilon}$ (of $\boldsymbol{u}$) and $\boldsymbol{\varphi}$ and therefore all stiffness matrices (7.48) - (7.51) can be evaluated.

8 Modeling low cycle fatigue

Fatigue in materials can be classified by the number of cycles until failure and the respective underlying mechanisms into either low cycle fatigue or high cycle fatigue. A mechanism associated with low cycle fatigue is the nucleation of micro cavities as a result of irreversible plastic deformation, i.e., ductile damage [122]. These micro cavities then grow and coalesce until failure of the structure. Therefore, the ductile damage model in Chapter 7 is suitable for the modeling of this type of fatigue. However, it turns out that the behavior of the present model is not sufficient in order to capture the low cycle fatigue experiments accurately. Therefore the model will be extended accordingly within this chapter.

Furthermore, the model is embedded within a thermomechanically coupled framework. The change of temperature allows to assess the dissipation, since a direct measurement of dissipation is hardly possible [71].

8.1 Experimental data

The tests have been performed with the *Walter+Bai* combined tension/compression/torsion testing machine (Fig. 8.1). The experimental data is shown in Fig. 8.2. The specimens are manufactured from a hardened-steel 16MnCrS5, have a length of 90 mm and a diameter of 2.5 mm in the rejuvenated area. A strain ratio of -0.5 has been chosen in order to prevent buckling of the specimens. The displacement has been measured by means of a tactile extensometer with a gauge length of 10 mm and the corresponding reaction force with a force load cell. The amplitude of the prescribed displacement has been adjusted to obtain fatigue failure below 250 cycles. This allows a modeling of the complete experiment without the necessity of time homogenization schemes, such as for instance presented in [36].

8.2 Constitutive modeling

The following section is associated with the extension of the regularized, anisotropic, ductile damage model as presented in Chapter 7 in order to model low cycle fatigue. For this purpose, the elasto-plastic behavior of the model will be extended first to fit

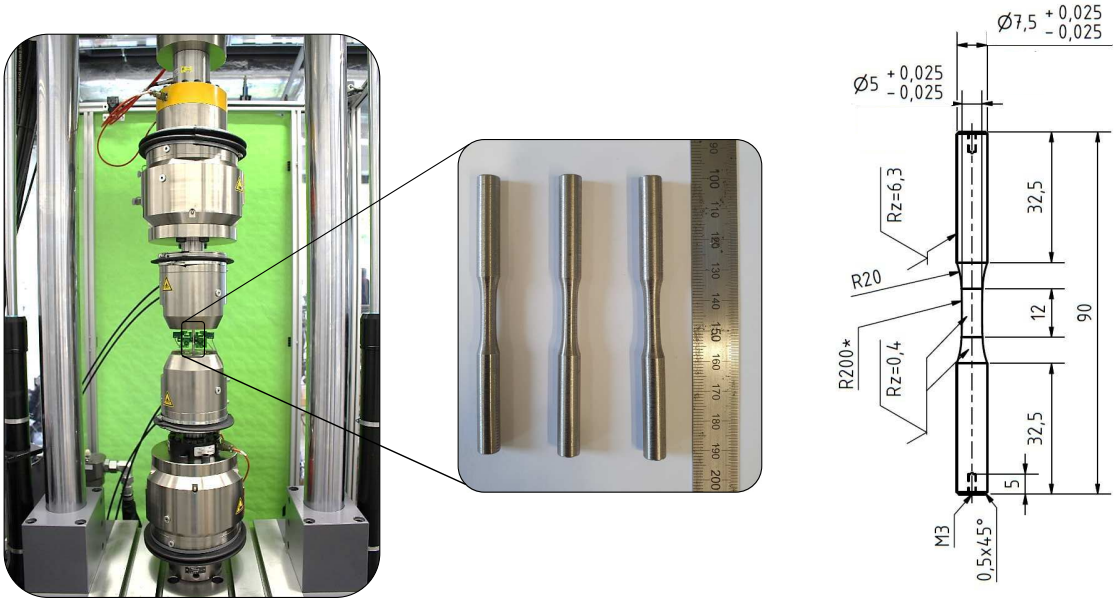

(a) Walter+Bai combined tension/compression/torsion testing machine

(b) Technical drawing

Figure 8.1: Cyclic tensile test: experimental setup.

the experiments better. Subsequently, a thermomechanically coupled setting is adopted. Lastly, a novel damage initiation criterion is developed to predict the onset of fatigue-related damage.

8.2.1 Elasto-plasticity: extension to superposed linear and non-linear hardening

The experimental data (Fig. 8.2) shows a combination of linear and non-linear hardening. The non-linear part corresponds to hardening within a single cycle, while the linear part characterizes hardening between cycles. The hardening law as adopted in Chapter 6 is of Armstrong-Frederick type only non-linear hardening behavior. Therefore, the hardening behavior of the anisotropic, ductile damage model has to be extended in order to calibrate the material model as accurately as possible. One possibility is the introduction of additional internal variables that govern the linear evolution of isotropic and kinematic hardening, as done for instance in [81]. This would require at least two additional symmetric state tensors and thus additional 12 degrees of freedom. In order to avoid these additional costs, an alternative method is proposed.

For that purpose, yield function (7.21) and plastic non-associative potential (6.48) are modified. To be more precise and focusing on isotropic hardening, the non-linearity

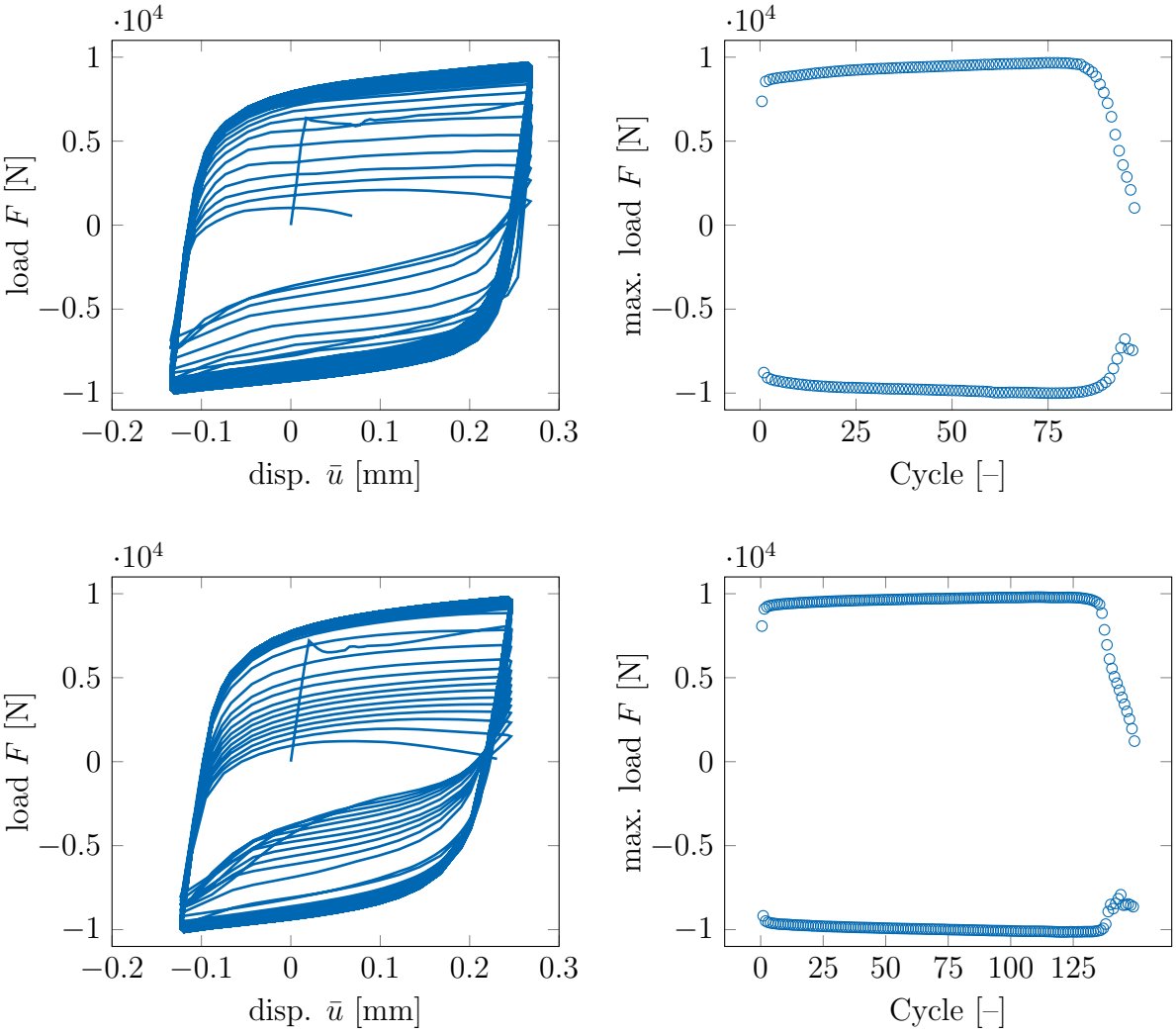

(a) Load-displacement diagram **(b)** Maximum and minimum load per cycle

Figure 8.2: Cyclic tensile test: experimental data. Strain ratio of -0.5 and amplitude of $\bar{u}_{\text{amp}} = 0.27\,\text{mm}$ (top row) and $\bar{u}_{\text{amp}} = 0.245\,\text{mm}$ (bottom row).

due to Armstrong-Frederick type extension (6.48) is shifted into the yield function. Mathematically speaking, the yield function is modified into

$$\Phi = \sqrt{\tau^{\text{eq}}} - \tau_y - \frac{1}{3}\,\boldsymbol{b}^{-1} : \boldsymbol{\kappa} - \Delta\tau \left[1 - \exp\left(\frac{-\boldsymbol{b}^{-1} : \boldsymbol{\kappa}}{\kappa_u}\right)\right] + f_\omega \tag{8.1}$$

and plastic potential Γ_κ vanishes, i.e., $\Gamma_\kappa \equiv 0$. By doing so, material parameter B_k is replaced by parameters $\Delta\tau$ and κ_u, which define the increase of isotropic hardening and the degree of non-linearity, respectively. Since the linear and the non-linear part are both based on state tensor $\boldsymbol{\kappa}$ no additional degrees of freedom have to be introduced.

A Prager-type hardening law [143] will be utilized for the linear increase of kinematic hardening, cf. [46] for further alternatives. The Prager-type hardening law incorporates no additional internal variables in the present framework, since it is based on the plastic strain tensor $\boldsymbol{\varepsilon}^{\mathrm{p}}$. From an implementation point of view, this requires the extension of the plastic part of Helmholtz energy (7.4) as

$$\psi^{\mathrm{p}} = \frac{H_a}{2}\,\boldsymbol{b} : [\boldsymbol{a}\cdot\boldsymbol{b}\cdot\boldsymbol{a}] + \frac{H_k}{2}\,\mathrm{tr}\,(\boldsymbol{b}\cdot\boldsymbol{k})^2 + \frac{H_p}{2}\,\boldsymbol{b} : [\boldsymbol{\varepsilon}^{\mathrm{p}}\cdot\boldsymbol{b}\cdot\boldsymbol{\varepsilon}^{\mathrm{p}}]\ , \tag{8.2}$$

where parameter H_p is the Prager-type hardening modulus. Furthermore, it motivates the introduction of thermodynamic driving force $\boldsymbol{\sigma}^{\mathrm{p}}$, being dual to plastic strain tensor $\boldsymbol{\varepsilon}^{\mathrm{p}}$. The thermodynamic driving forces are given by

$$\boldsymbol{\sigma}^{\mathrm{p}} = -\frac{\partial\psi}{\partial\boldsymbol{\varepsilon}^{\mathrm{p}}} = \lambda\,\mathrm{tr}\,(\boldsymbol{b}\cdot\boldsymbol{\varepsilon}^{\mathrm{e}})\ \boldsymbol{b} + 2\,\mu\,\boldsymbol{b}\cdot\boldsymbol{\varepsilon}^{\mathrm{e}}\cdot\boldsymbol{b} - H_p\,\boldsymbol{b}\cdot\boldsymbol{\varepsilon}^{\mathrm{p}}\cdot\boldsymbol{b}\ , \tag{8.3}$$

$$\begin{aligned}\boldsymbol{\beta} = -\frac{\partial\psi}{\partial\boldsymbol{b}} &= -\lambda\,\mathrm{tr}\,(\boldsymbol{b}\cdot\boldsymbol{\varepsilon}^{\mathrm{e}})\ \boldsymbol{\varepsilon}^{\mathrm{e}} - 2\,\mu\,\boldsymbol{\varepsilon}^{\mathrm{e}}\cdot\boldsymbol{b}\cdot\boldsymbol{\varepsilon}^{\mathrm{e}}\\ &\quad - H_a\,\boldsymbol{a}\cdot\boldsymbol{b}\cdot\boldsymbol{a} - H_k\,\mathrm{tr}\,(\boldsymbol{b}\cdot\boldsymbol{k})\ \boldsymbol{b} - H_p\,\boldsymbol{\varepsilon}^{\mathrm{p}}\cdot\boldsymbol{b}\cdot\boldsymbol{\varepsilon}^{\mathrm{p}}\\ &\quad + c_b\,l_b^2\ [\boldsymbol{\varphi}-\boldsymbol{b}]\ .\end{aligned} \tag{8.4}$$

The only difference between stress tensors $\boldsymbol{\sigma}$ and $\boldsymbol{\sigma}^{\mathrm{p}}$ is the last term of eq. (8.3). The relative stress $\boldsymbol{\tau}$ now reads

$$\boldsymbol{\tau} = \boldsymbol{\sigma}^{\mathrm{p}} - \boldsymbol{\alpha}\ , \tag{8.5}$$

where $\boldsymbol{\sigma}^{\mathrm{p}}$ replaces stress tensor $\boldsymbol{\sigma}$. As a consequence, dissipation inequality (7.14) is affected. It results in

$$\mathcal{D}^{\mathrm{red}} = \boldsymbol{\sigma}^{\mathrm{p}} : \dot{\boldsymbol{\varepsilon}}^{\mathrm{p}} + \boldsymbol{a} : \dot{\boldsymbol{a}} + \boldsymbol{\kappa} : \dot{\boldsymbol{k}} + \boldsymbol{\beta} : \dot{\boldsymbol{b}} \geq 0 \tag{8.6}$$

and is still a priori fulfilled due to application of the principle of Generalized Standard Materials.

8.2.2 Thermomechanical coupling

8.2.2.1 Fundamentals

This section deals with the extension of the regularized, anisotropic, ductile damage model to thermomechanics. On the one hand, the temperature affects hardening/softening while on the other hand, the temperature allows to estimate the dissipa-

tion induced by plasticity and damage. For that reason, the caloric Helmholtz energy contribution

$$\psi^{\Theta} = -3\,K\,\alpha_{\Theta}\,\left[\Theta - \Theta_0\right]\,\boldsymbol{b} : \boldsymbol{\varepsilon}^{\mathrm{e}} + c_{\Theta}\,\left[\Theta - \Theta_0 - \Theta \ln\left(\frac{\Theta}{\Theta_0}\right)\right] \tag{8.7}$$

is appended to Helmholtz energy (7.1). It is adopted from [12] and reformulated in terms of invariants (6.14). Θ denotes the temperature, Θ_0 the reference temperature, K is the bulk modulus, α_0 the thermal expansion coefficient and c_{Θ} the heat capacity. This leads to entropy

$$s = -\frac{\partial \psi^{\Theta}}{\partial \Theta} = 3\,K\,\alpha_{\Theta}\,\boldsymbol{b} : \boldsymbol{\varepsilon}^{\mathrm{e}} + c_{\Theta} \ln\left(\frac{\Theta}{\Theta_0}\right) \tag{8.8}$$

$$\dot{s} = \qquad 3\,K\,\alpha_{\Theta}\,\left[\dot{\boldsymbol{b}} : \boldsymbol{\varepsilon}^{\mathrm{e}} + \boldsymbol{b} : \dot{\boldsymbol{\varepsilon}}^{\mathrm{e}}\right] + c_{\Theta}\,\frac{\dot{\Theta}}{\Theta} \tag{8.9}$$

being dual to temperature Θ. The first term in entropy (8.8) and in caloric Helmholtz energy (8.7) leads to a structural heating effect, also referred to as Gough-Joule-effect. Evidently, stress tensors $\boldsymbol{\sigma}$, $\boldsymbol{\sigma}^{\mathrm{p}}$ and energy release rate $\boldsymbol{\beta}$ are affected by energy contribution (8.7). They result in

$$\boldsymbol{\sigma} = \frac{\partial \psi}{\partial \boldsymbol{\varepsilon}} = \lambda\,\mathrm{tr}\left(\boldsymbol{b}\cdot\boldsymbol{\varepsilon}^{\mathrm{e}}\right)\,\boldsymbol{b} + 2\,\mu\,\boldsymbol{b}\cdot\boldsymbol{\varepsilon}^{\mathrm{e}}\cdot\boldsymbol{b} - 3\,K\,\alpha_{\Theta}\,\left[\Theta - \Theta_0\right]\,\boldsymbol{b}\,, \tag{8.10}$$

$$\begin{aligned}\boldsymbol{\sigma}^{\mathrm{p}} = -\frac{\partial \psi}{\partial \boldsymbol{\varepsilon}^{\mathrm{p}}} = {} & \lambda\,\mathrm{tr}\left(\boldsymbol{b}\cdot\boldsymbol{\varepsilon}^{\mathrm{e}}\right)\,\boldsymbol{b} + 2\,\mu\,\boldsymbol{b}\cdot\boldsymbol{\varepsilon}^{\mathrm{e}}\cdot\boldsymbol{b} \\ & - H_p\,\boldsymbol{b}\cdot\boldsymbol{\varepsilon}^{\mathrm{p}}\cdot\boldsymbol{b} - 3\,K\,\alpha_{\Theta}\,\left[\Theta - \Theta_0\right]\,\boldsymbol{b}\,,\end{aligned} \tag{8.11}$$

$$\begin{aligned}\boldsymbol{\beta} = -\frac{\partial \psi}{\partial \boldsymbol{b}} = {} & -\lambda\,\mathrm{tr}\left(\boldsymbol{b}\cdot\boldsymbol{\varepsilon}^{\mathrm{e}}\right)\,\boldsymbol{\varepsilon}^{\mathrm{e}} - 2\,\mu\,\boldsymbol{\varepsilon}^{\mathrm{e}}\cdot\boldsymbol{b}\cdot\boldsymbol{\varepsilon}^{\mathrm{e}} \\ & - H_a\,\boldsymbol{a}\cdot\boldsymbol{b}\cdot\boldsymbol{a} - H_k\,\mathrm{tr}\left(\boldsymbol{b}\cdot\boldsymbol{k}\right)\,\boldsymbol{b} - H_p\,\boldsymbol{\varepsilon}^{\mathrm{p}}\cdot\boldsymbol{b}\cdot\boldsymbol{\varepsilon}^{\mathrm{p}} \\ & + c_b\,l_b^2\,\left[\boldsymbol{\varphi} - \boldsymbol{b}\right] + 3\,K\,\alpha_0\,\left[\Theta - \Theta_0\right]\,\boldsymbol{\varepsilon}^{\mathrm{e}}\,.\end{aligned} \tag{8.12}$$

The associated balance equation is the first law of thermodynamics, i.e., balance of energy (2.30). It reads

$$\underbrace{\dot{\psi} + \dot{\Theta}\,s - \boldsymbol{\sigma} : \dot{\boldsymbol{\varepsilon}} - \boldsymbol{\Omega}\cdot\nabla\dot{\varphi} - \omega\,\dot{\varphi}}_{=:\,-\mathcal{D}^{\mathrm{mec}}} + \Theta\,\dot{s} + \mathrm{div}\left(\boldsymbol{q}\right) - \rho\,r = 0\,, \tag{8.13}$$

where $\mathcal{D}^{\text{mec}}$ is mechanical dissipation (7.14), r the source term and $\boldsymbol{q}$ the heat flux, which is chosen as of Fourier type $\boldsymbol{q} = -k_\Theta \nabla\Theta$. By multiplying strong form (8.13) with test function $\delta\Theta$ and integrating over body $\mathcal{B}$ leads to

$$\int_{\mathcal{B}} \left[\Theta\,\dot{s} - \mathcal{D}^{\text{mec}} - \rho\, r^{\Theta}\right]\,\delta\Theta \,+ k_\Theta\,\nabla\Theta\cdot\nabla\delta\Theta\,\mathrm{d}V = 0 \tag{8.14}$$

as the weak form of the balance of energy. Although dissipation inequality (7.14) is formally identical to dissipation inequality (6.36), the micromorphic enhancement still effects the energy release rate $\boldsymbol{\beta}$, since $\boldsymbol{\varphi} - \boldsymbol{b} = l_b^2\,\mathrm{div}\,(\nabla\varphi)$. This, in turn, affects the temperature distribution due to balance of energy (8.14). In order to remedy this effect, mechanical dissipation $\mathcal{D}^{\text{mec}}$ is estimated according to

$$\begin{aligned}\mathcal{D}^{\text{mec}} &= \boldsymbol{\sigma} : \dot{\boldsymbol{\varepsilon}}^{\text{p}} + \boldsymbol{\alpha} : \dot{\boldsymbol{a}} + \boldsymbol{\kappa} : \dot{\boldsymbol{k}} + \boldsymbol{\beta} : \dot{\boldsymbol{b}} \\ &= \boldsymbol{\sigma} : \dot{\boldsymbol{\varepsilon}}^{\text{p}} + \boldsymbol{\alpha} : \dot{\boldsymbol{a}} + \boldsymbol{\kappa} : \dot{\boldsymbol{k}} + \left[\boldsymbol{\beta}^{\text{loc}} + \boldsymbol{\omega}\right] : \dot{\boldsymbol{b}} \qquad (8.15a)\\ &\approx \boldsymbol{\sigma} : \dot{\boldsymbol{\varepsilon}}^{\text{p}} + \boldsymbol{\alpha} : \dot{\boldsymbol{a}} + \boldsymbol{\kappa} : \dot{\boldsymbol{k}} + \boldsymbol{\beta}^{\text{loc}} : \dot{\boldsymbol{b}}\,. \qquad (8.15b)\end{aligned}$$

Alternatively, by choosing stress power

$$\mathcal{P} = \boldsymbol{\sigma} : \boldsymbol{\varepsilon} + \boldsymbol{\Omega} \,\vdots\, \nabla\boldsymbol{\varphi}\,, \tag{8.16}$$

where only the gradient part is assumed as an energetic contribution, leads to

$$\begin{aligned}\mathcal{D}^{\text{mec}} &= \boldsymbol{\sigma} : \dot{\boldsymbol{\varepsilon}}^{\text{p}} + \boldsymbol{\alpha} : \dot{\boldsymbol{a}} + \boldsymbol{\kappa} : \dot{\boldsymbol{k}} + \boldsymbol{\beta} : \dot{\boldsymbol{b}} + \boldsymbol{\omega} : \dot{\boldsymbol{\varphi}} \\ &= \boldsymbol{\sigma} : \dot{\boldsymbol{\varepsilon}}^{\text{p}} + \boldsymbol{\alpha} : \dot{\boldsymbol{a}} + \boldsymbol{\kappa} : \dot{\boldsymbol{k}} + \boldsymbol{\beta}^{\text{loc}} : \dot{\boldsymbol{b}} + \boldsymbol{\omega} : \underbrace{[\dot{\boldsymbol{\varphi}} - \dot{\boldsymbol{b}}]}_{=\dot{\boldsymbol{\omega}}} \qquad (8.17a)\\ &\approx \boldsymbol{\sigma} : \dot{\boldsymbol{\varepsilon}}^{\text{p}} + \boldsymbol{\alpha} : \dot{\boldsymbol{a}} + \boldsymbol{\kappa} : \dot{\boldsymbol{k}} + \boldsymbol{\beta}^{\text{loc}} : \dot{\boldsymbol{b}}\,. \qquad (8.17b)\end{aligned}$$

Since penalty expression $\boldsymbol{\omega}$ is generally small and evolves slightly, expression $\boldsymbol{\omega} : \dot{\boldsymbol{\omega}}$ is very small and, thus, assumption (8.17b) and consequently (8.15b) are justified.

8.2.2.2 Numerical results: loading path dependence

The tensile specimen (Fig. 8.3) is ideal in order to highlight the loading path dependency. The tensile specimen is loaded in tensile and in circumferential direction. Thereby, the order of the applied deformation is varied.

Numerical setup The axisymmetric tensile specimen is fixed at the bottom and loaded at the top with the final deformation $\bar{u}_z = 1.2\,\text{mm}$, $\bar{u}_\vartheta = 45°$ (torsion). This deformation is applied in three different orders: (i) $\bar{u}_z$ and subsequently $\bar{u}_\vartheta$, (ii) $\bar{u}_\vartheta$ and subsequently $\bar{u}_z$ and (iii) $\bar{u}_z$ and $\bar{u}_\vartheta$ simultaneously. The model is extended to finite strains in order to capture the large twist angle. Implementation details regarding the modeling of

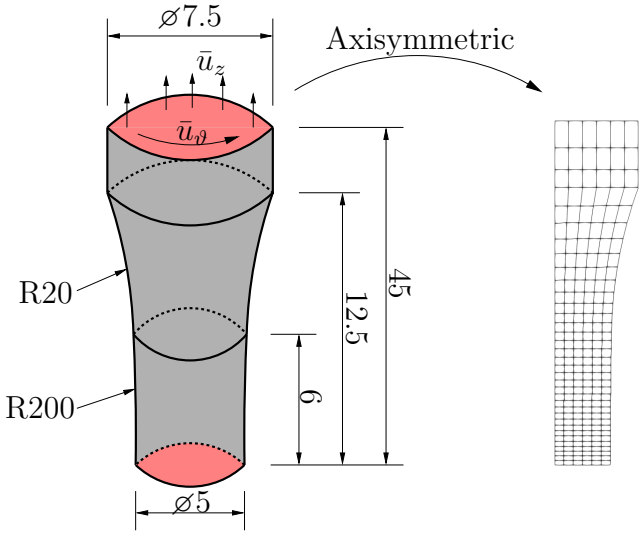

Figure 8.3: Tensile specimen: geometry and discretization.

axisymmetric is given in Appendix F.1 and regarding the extension of the model to finite strains are provided in Appendix F.2. The material parameters are given in Tab. 8.1.

Name	Symbol	Value	Unit
Young's modulus	E	400	[MPa]
Poisson's ratio	ν	0.3	[–]
Initial yield stress	τ_y	1	[MPa]
Hardening modulus (kinematic)	H_a	50	[MPa]
Armstrong Frederick (kinematic)	B_a	20	[–]
Hardening modulus (isotropic)	H_k	50	[MPa]
Hardening increment (isotropic)	$\Delta\tau_y$	2	[MPa]
Hardening slope (isotropic)	κ_u	10	[MPa]
Damage modulus (isotropic)	η_1	0	[MPa^{-1}]
Damage modulus (anisotropic)	η_2	4	[MPa^{-1}]
Damage slope	m	-1	[–]
Damage initiation threshold	W_s	0	[MPa]
Penalty parameter (regularization)	$c_{\boldsymbol{b}}$	100	[MPa]
Length parameter (regularization)	$l^2_{\boldsymbol{b}}$	0.5	[mm^2]
Reference temperature	Θ_0	293	[K]
Thermal expansion	α_Θ	$2 \cdot 10^{-5}$	[K^{-1}]
Heat capacity	c_Θ	0.1	[MPa/K]
Thermal conductivity	k_Θ	10	[W/(m K)]

Table 8.1: Loading path dependence: material parameters associated with the thermo-mechanically coupled anisotropic, ductile damage model

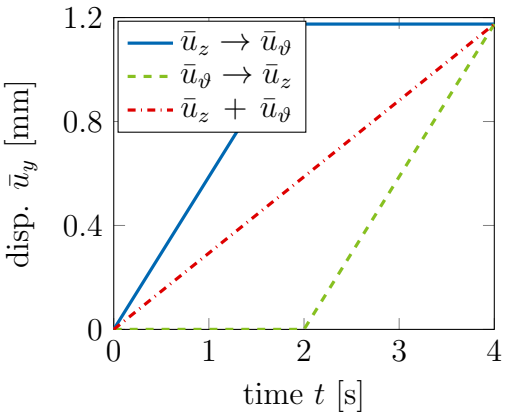

(a) Loading path for displacement $\bar{u}_z$

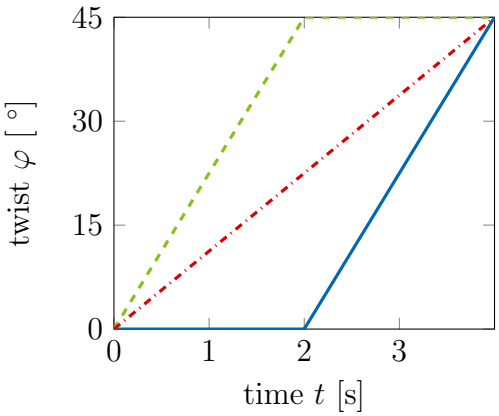

(b) Loading path for twist angle $\bar{u}_\vartheta$

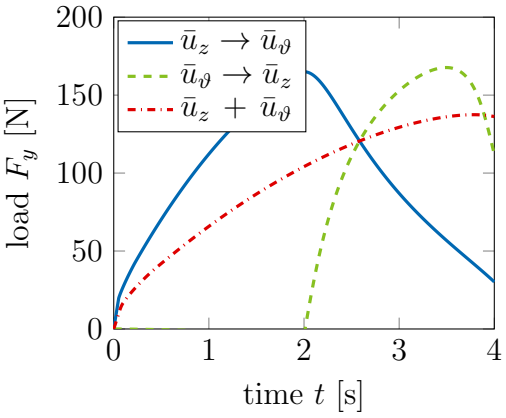

(c) Load-displacement diagrams

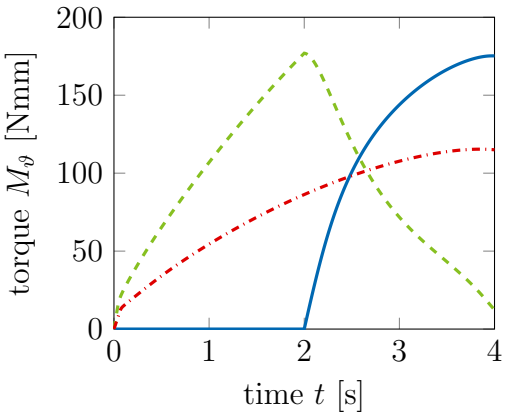

(d) Twist-torque diagrams

Figure 8.4: Loading path dependence: load-displacement and torque-twist diagrams.

Results and discussion The load-displacement diagrams and torque-twist diagrams (Fig. 8.4) show a clear loading path dependency. The forces vary between 20 N (path (i)) and 136.2 N (path(iii)) at the final stage of deformation. The torque-twist diagrams show a different behavior. Path (ii) shows the lowest torque with $M_\vartheta = 12.3\,\mathrm{N\,mm}$ and path (i) the highest torque with $M_\vartheta = 175.2\,\mathrm{N\,mm}$. This leads to a factor of 6.8 associated with the axial behavior and to a factor of 14.2 associated with the torsional behavior. The behavior of path (i) indicates high damage in axial direction (b_{zz}) and low damage in circumferential direction ($b_{\vartheta\vartheta}$) while path (ii) indicates the opposite behavior, i.e., low damage in axial direction (b_{zz}) and high damage in circumferential direction ($b_{\vartheta\vartheta}$) and path (iii) shows low damage in both directions. The distributions of integrity tensor components b_{zz} and $b_{\vartheta\vartheta}$ (Fig. 8.5) do not confirm this observation though. Therefore, the strong softening behavior associated with path (i) and path (ii) is mainly related to geometric effects. Path (i) and (iii) are associated with low damage in axial direction

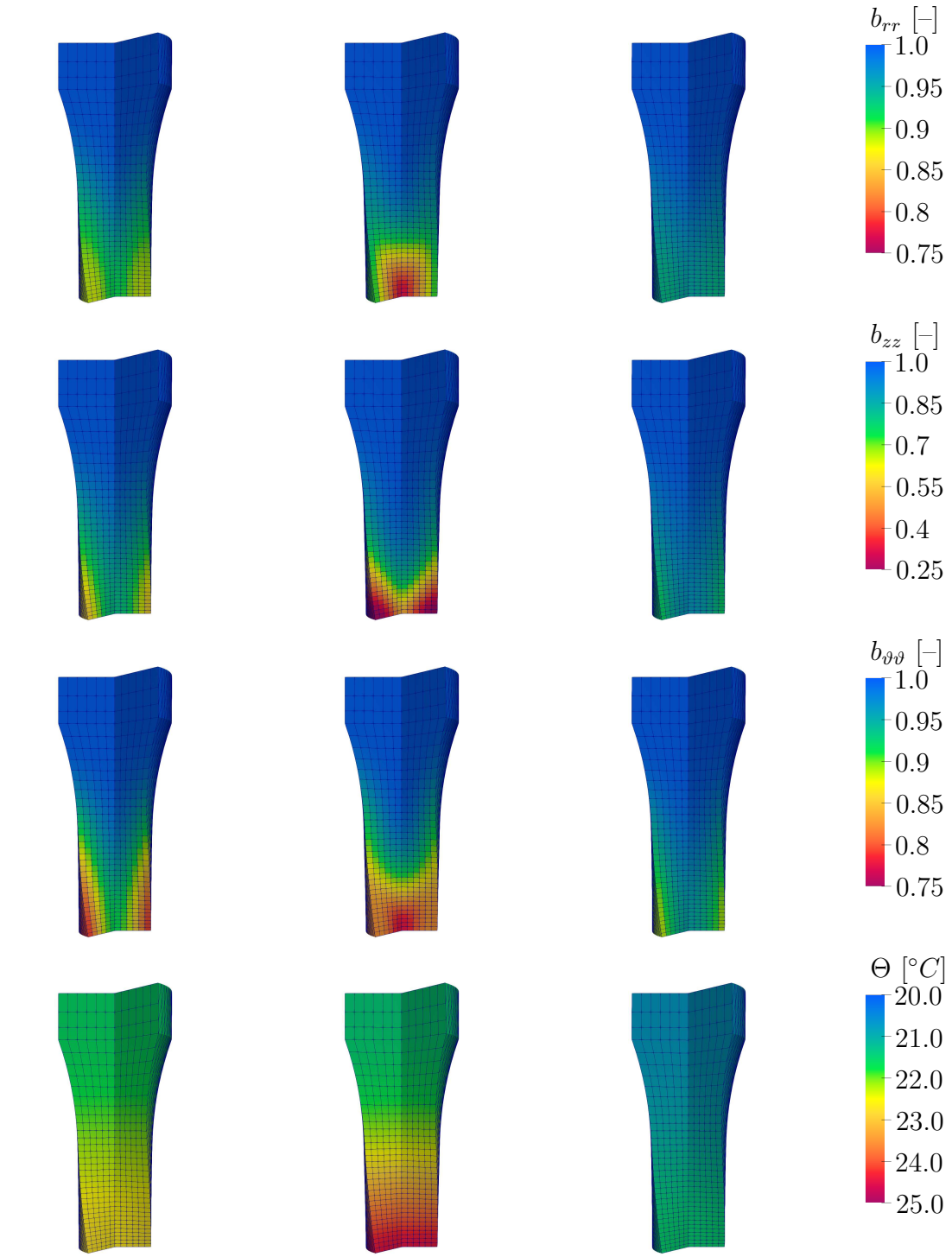

(a) (i): $\bar{u}_z \rightarrow \bar{u}_\vartheta$ **(b)** (ii): $\bar{u}_\vartheta \rightarrow \bar{u}_z$ **(c)** (iii): $\bar{u}_z + \bar{u}_\vartheta$

Figure 8.5: Loading path dependence: distribution of integrity tensor-components b_{rr} , b_{zz}, $b_{\vartheta\vartheta}$ and distribution of temperature Θ.

compared to path (iii). The damage patterns in circumferential direction associated with path (i) and (ii) are on a similar level. The highest damage occurs at the surface of the specimen for path (i) and in the center for path (ii). Usually, the highest damage occurs in the center for tensile tests and on the surface for torsion tests. This indicates that the first loading stage highly influences the position of maximum damage. The temperature distribution highlights the overall dissipation associated with the three loading paths, since all integrity tensor components enter mechanical dissipation (8.15b) and thus the temperature increase. For the prescribed final deformation, path (iii) shows the smallest amount of dissipation while path (ii) leads to the largest amount.

8.2.3 Damage initiation criterion associated with low cycle fatigue

8.2.3.1 Fundamentals

For the modeling of low cycle fatigue, elasto-plasticity is usually assumed within the first loading stage. Subsequently and postponed, damage evolves. Thus, the onset of damage initiation has to be captured precisely, see Fig. 8.2 and [96, 155].

By following that line of thought, damage evolves in a material point as soon as the material dependent threshold value w_s is exceeded by energetic driving force w^{p}. The driving force w^{p} is given in terms of the plastic part of the Helmholtz energy scaled with correction function $z(k)$ as

$$w^{\mathrm{p}} = \int \kappa\, z(k)\, \dot{k} + \boldsymbol{\alpha} : \dot{\boldsymbol{a}} + [\boldsymbol{\sigma}^{\mathrm{p}} - \boldsymbol{\sigma}] : \dot{\boldsymbol{\varepsilon}}^{\mathrm{p}}\, \mathrm{d}t \qquad \text{with} \quad z(k) = \frac{A}{n}\, k^{\frac{1-n}{n}} \,. \tag{8.18}$$

This model, originally proposed in [96], is based on isotropic hardening though. An option in order to extend this criterion to the present anisotropic, ductile damage model is the replacement of scalar variable k by $\mathrm{tr}\,(\boldsymbol{k})$. The additional material parameters A and n are then subject to the calibration of the damage initiation criterion according to experiments.

Alternatively, initiation criterion (8.18) can be rewritten into the more general format

$$w^{\mathrm{p}} = f^{\mathrm{p}}(\boldsymbol{\varepsilon}^{\mathrm{p}},\, \boldsymbol{b})\, \psi^{\mathrm{p}}(\boldsymbol{\varepsilon}^{\mathrm{p}},\, \boldsymbol{a},\, \boldsymbol{k},\, \boldsymbol{b}) \tag{8.19}$$

where not only the isotropic part is scaled by a correction function, but also the complete plastic part of the Helmholtz energy. The dependence of scaling function f^{p} on plastic strain tensor $\boldsymbol{\varepsilon}^{\mathrm{p}}$ is motivated by the Coffin-Manson-model, cf. [35, 70, 101]. Thermodynamic driving force (8.19) has to fulfill the properties

$$\varepsilon^{\mathrm{p,eq}} \uparrow \quad \Rightarrow \quad w_p \uparrow, \qquad \psi^{\mathrm{p}} \uparrow \quad \Rightarrow \quad w_p \uparrow \tag{8.20}$$

since the increase of both the equivalent plastic strain and the plastic energy contribution leads to an earlier initiation of damage. A suitable choice is

$$f^{\mathrm{p}} = \frac{1}{c_1 - c_2 \max\left(\varepsilon^{\mathrm{p,eq}}\right)} \qquad \text{with} \quad \varepsilon^{\mathrm{p,eq}} = \frac{3}{2}\,\boldsymbol{\varepsilon}^{\mathrm{p}} : [\boldsymbol{b} \cdot \boldsymbol{\varepsilon}^{\mathrm{p}} \cdot \boldsymbol{b}] - \frac{1}{2}\,[\boldsymbol{b} : \boldsymbol{\varepsilon}^{\mathrm{p}}]^2 \tag{8.21}$$

and positive parameters c_1 and c_2. Here, function f^{p} only depends on the maximum equivalent plastic strain. That dependence on the maximum plastic strain enables the distinction between different loading amplitudes. Since function (8.21) has a singularity at

$$\max\left(\varepsilon^{\mathrm{p,eq}}\right) = \frac{c_1}{c_2} \tag{8.22}$$

parameter c_1 and c_2 have to be chosen such that

$$\max\left(\varepsilon^{\mathrm{p,eq}}\right) < \frac{c_1}{c_2} \tag{8.23}$$

holds. In practice, this only needs to be considered for the experiment with the highest loading amplitude, since this is (usually) the experiment with the largest amount of plastic strain.

8.2.3.2 Calibration of the damage initiation criterion

The calibration has been done in multiple steps. First, the material parameters τ_y, H_a, H_k, H_p and B_a associated with the elasto-plastic model behavior are calibrated. The kinematic hardening parameters H_a, H_p and B_a mainly control the non-linear increase in

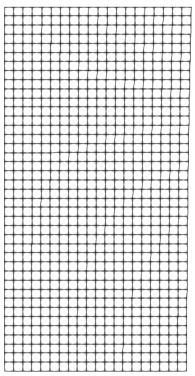

Figure 8.6: Cyclic tensile test: discretization of the tensile specimen with 800 elements.

Name	Symbol	Value	Unit
Young's modulus	E	210000	[MPa]
Poisson's ratio	ν	0.3	[–]
Initial yield stress	τ_y	206.78	[MPa]
Hardening modulus (kinematic)	H_a	177750	[MPa]
Armstrong Frederick (kinematic)	B_a	1344.3	[–]
Hardening modulus (prager-type)	H_p	3354.8	[MPa]
Hardening modulus (isotropic)	H_k	7.1154	[MPa]
Hardening increment (isotropic)	$\Delta\tau_y$	0	[MPa]
Hardening slope (isotropic)	κ_u	1	[MPa]
Damage initiation threshold	w_s	100	[MPa]
Damage initiation parameter	c_1	10.167	[–]
Damage initiation parameter	c_2	5608.7	[–]
Damage modulus (isotropic)	η_1	0.00125	[MPa^{-1}]
Damage modulus (anisotropic)	η_2	0	[MPa^{-1}]
Damage slope	m	-2.1978	[–]
Penalty parameter	c_b	100	[MPa]
Length parameter	l_b^2	0.1	[mm]
Reference temperature	Θ_0	293	[K]
Thermal expansion	α_Θ	0	K^{-1}
Heat capacity	c_Θ	100	[MPa/K]
Thermal conductivity	k_Θ	0	[W/(m K)]

Table 8.2: Cyclic tensile test: material parameters associated with the softening behavior.

hardening during each cycle, and isotropic hardening parameter H_k controls the increase in hardening between cycles. The goal function is chosen as

$$f^{\mathrm{LCF}} = \sum_{\text{steps}} w_{\text{step}} \left[F^{\text{sim}}_{\text{step}} - F^{\text{exp}}_{\text{step}}\right]^2 + \sum_{\text{cycles}} w_{\text{cycle}} \left[F^{\text{sim}}_{\text{max,cycle}} - F^{\text{exp}}_{\text{max,cycle}}\right]^2 \tag{8.24}$$

where $F^{\text{exp}}_{\text{step}}$ is the interpolated force at the same time as $F^{\text{sim}}_{\text{step}}$. Analogously, $F^{\text{exp}}_{\text{max,cycle}}$ and $F^{\text{sim}}_{\text{max,cycle}}$ are the maximum forces of each cycle. w_{step} and w_{cycle} scale the respective force differences separately. The optimization is performed by means of the Nelder-Mead simplex-algorithm as it requires no gradients and is very robust. The displacement is measured with an extensometer with a gauge length of 10 mm at positions ± 5 mm from the center, cf. Fig. 8.3. The displacement in the simulations is prescribed directly at the measurement points of the extensometer for the sake of simplicity. Due to symmetry, only one half has been discretized based on an axisymmetric simplification (Fig. 8.6).

The results of the first calibration step are given in Fig. 8.7. According to the experimental data (Fig. 8.2) the softening behavior starts at 74 cycles and at 128 cycles,

respectively. The calibration of the elasto-plastic model parameters considers only the loading behavior up to these transition points and are given in Tab. 8.2.

The subsequent calibration of damage initiation criterion 8.19 and the choice of threshold value $w_s = 100\,\mathrm{MPa}$ leads to parameters c_1 and c_2 as $c_1 = 10.167$ and $c_2 = 5608.7$. A graphical representation of the damage initiation criterion is given in Fig. 8.8. As soon as the energetic driving force w^{p} exceeds the chosen threshold value damage is activated.

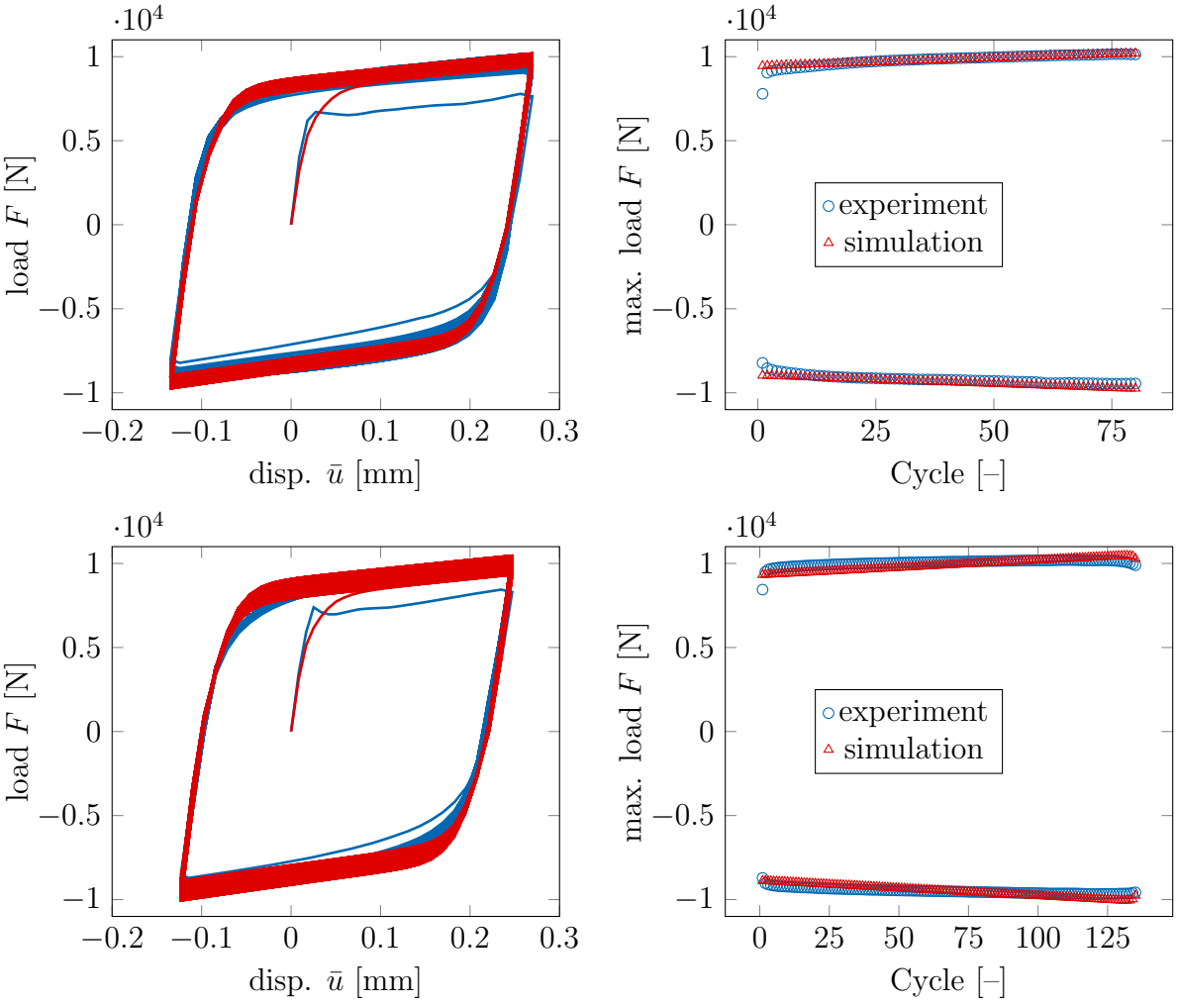

(a) Load-displacement diagram **(b)** Maximum and minimum load per cycle

Figure 8.7: Cyclic tensile test: experiment vs. simulation. Strain ratio of -0.5 and amplitude $\bar{u}_{\mathrm{amp}} = 0.27\,\mathrm{mm}$ (top row) and $\bar{u}_{\mathrm{amp}} = 0.245\,\mathrm{mm}$ (bottom row).

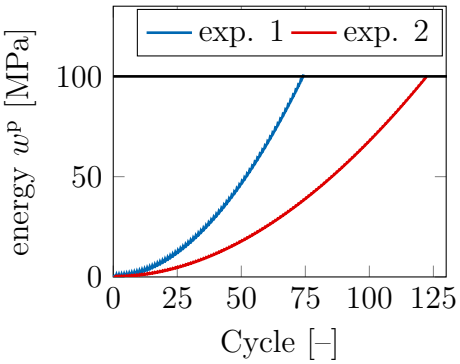

(a) Driving force w^{p} vs. number of cycles

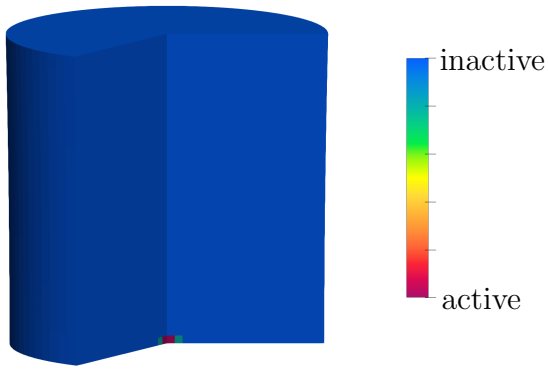

(b) First damage activated elements

Figure 8.8: Cyclic tensile test: visualization of the damage initiation criterion.

8.2.3.3 Damage evolution

Penalty and length parameter c_b and l_b are chosen similar to material parameter set 8.1. The thermal expansion coefficient and the thermal conductivity have been set to zero (adiabatic setting). Therefore the temperature at each material point is only related to the dissipated mechanical work at that material point. Due to the consideration of a one-axial load path an isotropic damage evolution is sufficient. Therefore, damage modulus η_2 has been set to zero while damage modulus η_1 and exponent m have been identified by means of the calibration process.

The results are given in terms of the loading and softening behavior (Fig. 8.9) and in terms of the distribution of integrity component b_{zz} as well as the temperature distribution (Fig. 8.10). The softening behavior of both simulations starts similar to the experiments at either 74 cycles (amplitude $\bar{u}_{\mathrm{amp}} = 0.27\,\mathrm{mm}$) or at 128 cycles (amplitude $\bar{u}_{\mathrm{amp}} = 0.245\,\mathrm{mm}$ mm). Damage starts to evolve slowly since only a few elements soften first. While only the central element shows damage behavior at the beginning (Fig. 8.8), the damage behavior is activated in all elements in the lower third along from the center to the specimen surface at the end of the simulations (Fig. 8.10). In contrast to experimental observation, damage does not start at the surface. In line with the experiment, where damage starts at the surface due to surface roughness, a slight imperfection could be used within the numerical model. This would also lead to damage initiation at the surface.

In summary, the extended ductile damage model is suitable to model the cyclic loading behavior. It covers kinematic hardening within individual cycles as well as isotropic hardening between cycles. Furthermore, the novel damage initiation criterion appears to be sufficient in order to predict the onset of softening.

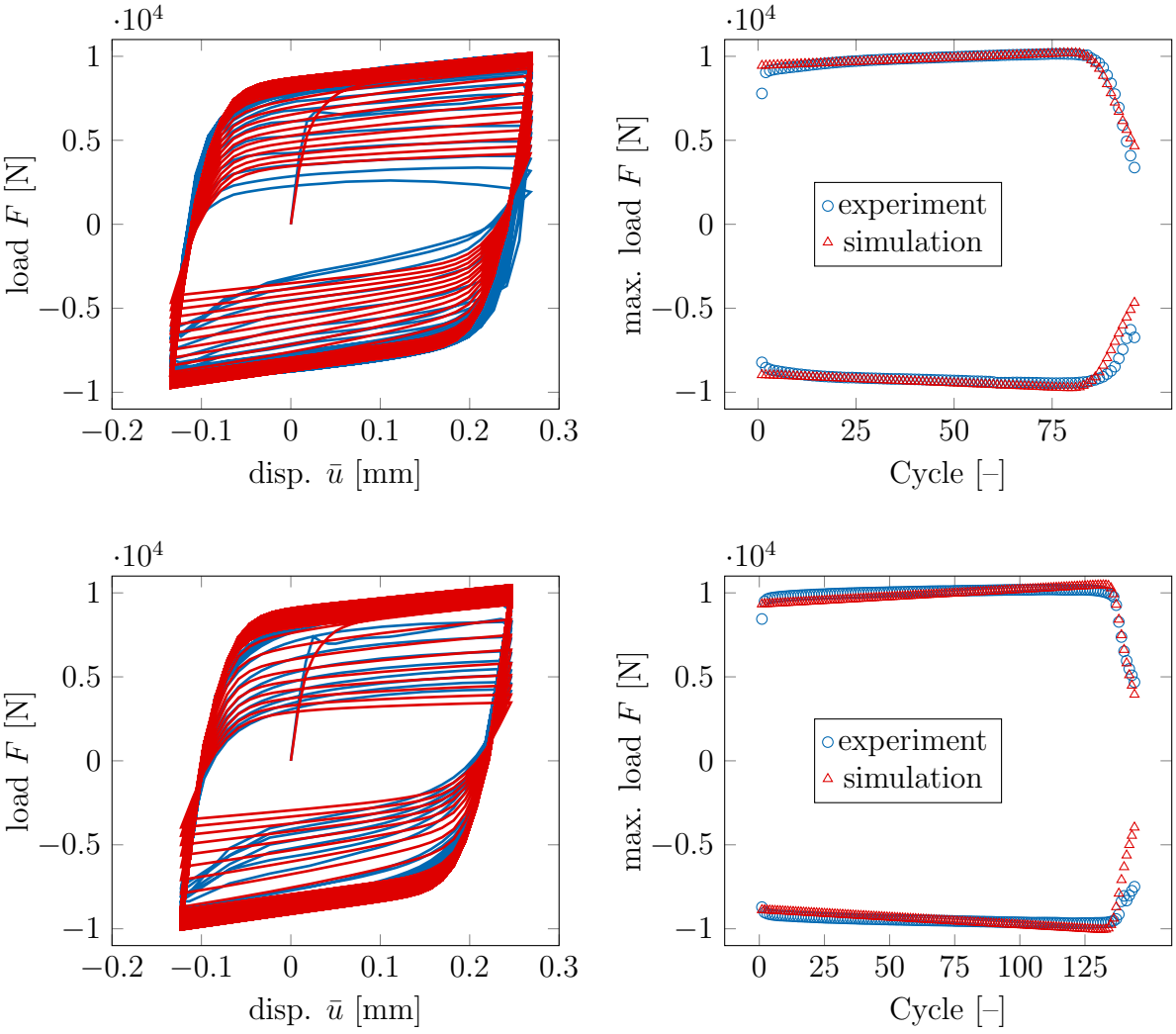

(a) Load-displacement diagram **(b)** Maximum and minimum load per cycle

Figure 8.9: Cyclic tensile test: experiment vs. simulation. Strain ratio of -0.5 and amplitude of $\bar{u}_{\text{amp}} = 0.27\,\text{mm}$ (top row) and $\bar{u}_{\text{amp}} = 0.245\,\text{mm}$ (bottom row).

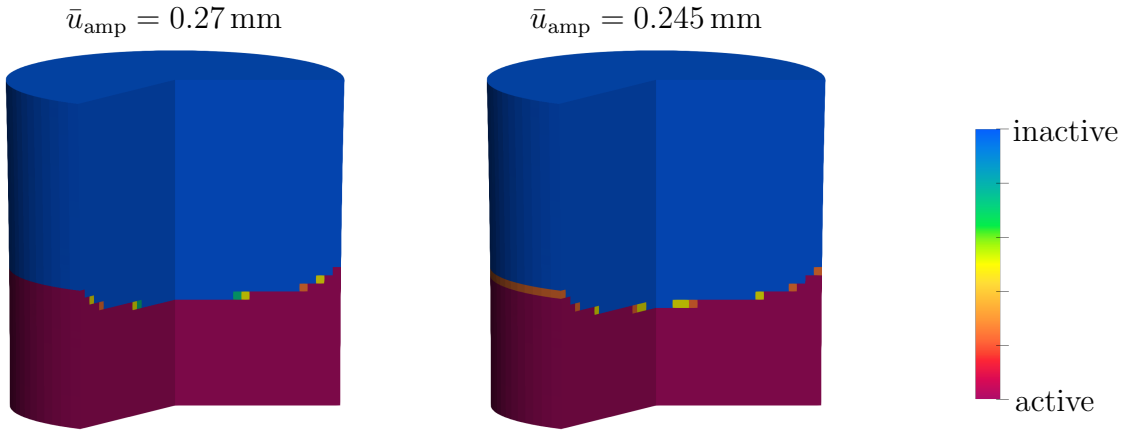

(a) Active and inactive softening behavior

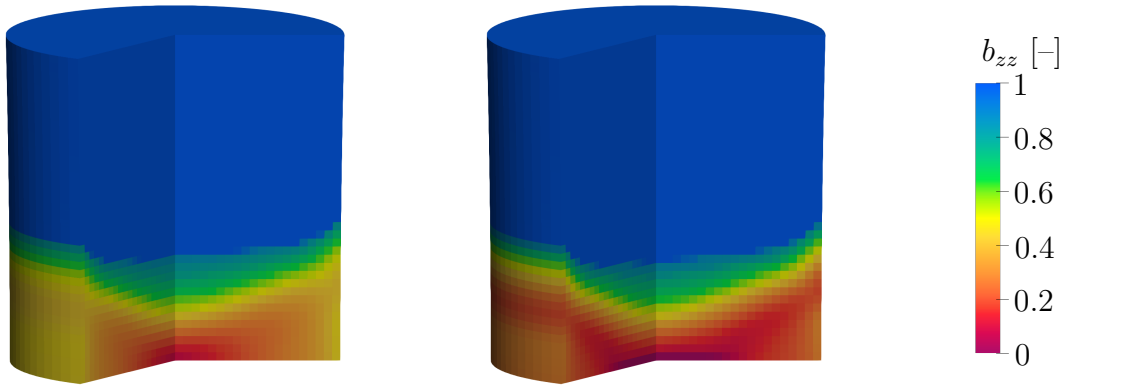

(b) Distribution of integrity component b_{zz}

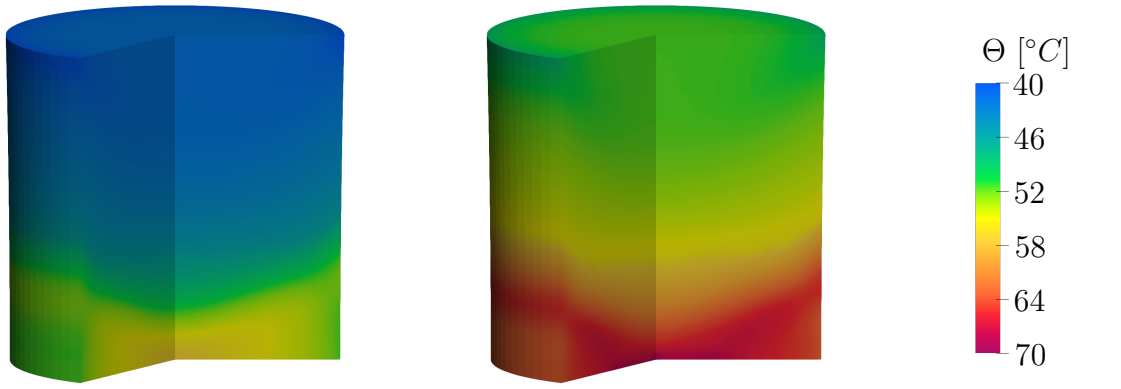

(c) Distribution of temperature

Figure 8.10: Cyclic tensile test: final stage of deformation. Strain ratio of -0.5 and amplitude of $\bar{u}_{\text{amp}} = 0.27\,\text{mm}$ (left column) and $\bar{u}_{\text{amp}} = 0.245\,\text{mm}$ (right column).

F Appendix

F.1 Axisymmetric finite element formulation with torsional degree of freedom

This appendix shows implementation details for modeling of axisymmetric problems combined with torsional loading in a two-dimensional setting. First, the geometrically linearized theory will be shown and afterwards the geometrically exact theory.

Geometrically linearized theory The rotation is assumed to be small. This allows the approximation of the rotational degree of freedom as a tangential displacement with respect to the initial configuration. Thus, the displacement vector takes the form

$$\boldsymbol{u} = u_R\,\boldsymbol{e}_R + u_Z\,\boldsymbol{e}_Z + u_\theta\,\boldsymbol{e}_\theta\ , \tag{8.25}$$

leading to $\nabla\boldsymbol{u}$ and $\delta_{\boldsymbol{u}}\nabla\boldsymbol{u}$ given as

$$\begin{aligned}\nabla\boldsymbol{u} = &\frac{\partial u_R}{\partial R}\,\boldsymbol{e}_R\otimes\boldsymbol{e}_R + \frac{\partial u_R}{\partial Z}\,\boldsymbol{e}_R\otimes\boldsymbol{e}_T - \frac{u_\theta}{R}\,\boldsymbol{e}_T\otimes\boldsymbol{e}_\theta\\ &+\frac{\partial u_Z}{\partial R}\,\boldsymbol{e}_Z\otimes\boldsymbol{e}_R + \frac{\partial u_Z}{\partial Z}\,\boldsymbol{e}_Z\otimes\boldsymbol{e}_Z\\ &+\frac{\partial u_\theta}{\partial R}\,\boldsymbol{e}_\theta\otimes\boldsymbol{e}_R + \frac{\partial u_\theta}{\partial Z}\,\boldsymbol{e}_\theta\otimes\boldsymbol{e}_Z + \frac{u_R}{R}\,\boldsymbol{e}_\theta\otimes\boldsymbol{e}_\theta\ .\end{aligned} \tag{8.26}$$

$$\begin{aligned}\delta_{\boldsymbol{u}}\nabla\boldsymbol{u} = &\frac{\partial\delta u_R}{\partial R}\,\boldsymbol{e}_R\otimes\boldsymbol{e}_R + \frac{\partial\delta u_R}{\partial Z}\,\boldsymbol{e}_R\otimes\boldsymbol{e}_Z - \frac{\delta u_\theta}{R}\,\boldsymbol{e}_R\otimes\boldsymbol{e}_\theta\\ &+\frac{\partial\delta u_Z}{\partial R}\,\boldsymbol{e}_Z\otimes\boldsymbol{e}_R + \frac{\partial\delta u_Z}{\partial Z}\,\boldsymbol{e}_Z\otimes\boldsymbol{e}_Z\\ &+\frac{\partial\delta u_\theta}{\partial R}\,\boldsymbol{e}_\theta\otimes\boldsymbol{e}_R + \frac{\partial\delta u_\theta}{\partial Z}\,\boldsymbol{e}_\theta\otimes\boldsymbol{e}_Z + \frac{\delta u_R}{R}\,\boldsymbol{e}_\theta\otimes\boldsymbol{e}_\theta\ .\end{aligned} \tag{8.27}$$

The linearized strain tensor and its variation follow as

$$\boldsymbol{\varepsilon} = \frac{1}{2}\left[\nabla\boldsymbol{u} + \nabla^T\boldsymbol{u}\right] \quad\Rightarrow\quad \delta_{\boldsymbol{u}}\boldsymbol{\varepsilon} = \frac{1}{2}\left[\delta_{\boldsymbol{u}}\nabla\boldsymbol{u} + \delta_{\boldsymbol{u}}\nabla^T\boldsymbol{u}\right]\ . \tag{8.28}$$

Insertion into the weak form of balance of linear momentum leads to

$$\boldsymbol{R} = \int_{\mathcal{B}} \boldsymbol{\sigma} : \delta_{\boldsymbol{u}}\boldsymbol{\varepsilon}\,\mathrm{d}V = \boldsymbol{0}\ , \tag{8.29}$$

where body forces and surface loads have been neglected. By applying Newton's method the linearization $\boldsymbol{K} = \mathrm{d}_{\boldsymbol{u}}\boldsymbol{R}$ is required. For the purpose of clarity it is given in index notation with the subscripts being element of $\{R,\, Z,\, \theta\}$ as

$$K_{ij} = \int_{\mathcal{B}} \delta_{u_i}\varepsilon_{pq} : \frac{\mathrm{d}\sigma_{pq}}{\mathrm{d}\varepsilon_{rs}} : \Delta_{u_j}\varepsilon_{rs}\,\mathrm{d}V \ . \tag{8.30}$$

Geometrically exact theory The presented formulation is adopted from [2]. The position of a point $\boldsymbol{X}$ in the reference configuration and of point $\boldsymbol{x}$ in the current configuration is given by

$$\boldsymbol{X} = R\,\boldsymbol{e}_R + Z\,\boldsymbol{e}_Z \ , \qquad \boldsymbol{x} = r\,\boldsymbol{e}_r + z\,\boldsymbol{e}_z \ . \tag{8.31}$$

The vectors $\boldsymbol{e}_\bullet$ are the corresponding unit vectors and $(R,\, Z,\, \theta)$ and $(r,\, z,\, \vartheta)$, respectively denote the polar coordinates with respect to the reference and the deformed configuration, i.e., R is the radius, Z the height and θ the angle of considered point $\boldsymbol{X}$. The dependency between both sets of coordinates reads

$$r(R,\, Z) = R + u_R(R,\, Z) \tag{8.32}$$
$$z(R,\, Z) = Z + u_Z(R,\, Z) \tag{8.33}$$
$$\vartheta(R,\, Z,\, \theta) = \theta + u_\theta(R,\, Z) \ . \tag{8.34}$$

It bears emphasis that u_θ is an angle. Applying the gradient operator with respect to cylindrical coordinates and the identities $\partial_\vartheta \boldsymbol{e}_r = \boldsymbol{e}_\vartheta$ and $\partial_\vartheta \boldsymbol{e}_\vartheta = -\boldsymbol{e}_r$ leads to the deformation gradient $\boldsymbol{F} = \partial_{\boldsymbol{X}}\boldsymbol{x}$ as

$$\begin{aligned}\boldsymbol{F} = {} & \frac{\partial r}{\partial R}\,\boldsymbol{e}_r \otimes \boldsymbol{e}_R + \frac{\partial r}{\partial Z}\,\boldsymbol{e}_r \otimes \boldsymbol{e}_Z \\ & + \frac{\partial z}{\partial R}\,\boldsymbol{e}_z \otimes \boldsymbol{e}_R + \frac{\partial z}{\partial Z}\,\boldsymbol{e}_z \otimes \boldsymbol{e}_Z \\ & + r\,\frac{\partial \vartheta}{\partial R}\,\boldsymbol{e}_\vartheta \otimes \boldsymbol{e}_R + r\,\frac{\partial \vartheta}{\partial Z}\,\boldsymbol{e}_\vartheta \otimes \boldsymbol{e}_Z + \frac{r}{R}\,\frac{\partial \vartheta}{\partial \theta}\,\boldsymbol{e}_\vartheta \otimes \boldsymbol{e}_\theta \ .\end{aligned} \tag{8.35}$$

Consequently, the first variation of the deformation gradient with respect to the displacement $\boldsymbol{u} = (u_R,\, u_Z,\, u_\theta)$ follows as

$$\begin{aligned}\delta_{\boldsymbol{u}}\boldsymbol{F}\cdot\delta\boldsymbol{u} = {} & \left[\frac{\partial \delta u_R}{\partial R} - r\,\frac{\partial u_\theta}{\partial R}\,\delta u_\theta\right]\boldsymbol{e}_r \otimes \boldsymbol{e}_R + \left[\frac{\partial \delta u_R}{\partial Z} - r\,\frac{\partial u_\theta}{\partial Z}\,\delta u_\theta\right]\boldsymbol{e}_r \otimes \boldsymbol{e}_Z \\ & - \frac{r}{R}\,\delta u_\theta\,\boldsymbol{e}_r \otimes \boldsymbol{e}_\theta + \frac{\partial \delta u_Z}{\partial R}\boldsymbol{e}_z \otimes \boldsymbol{e}_R + \frac{\partial \delta u_Z}{\partial Z}\boldsymbol{e}_z \otimes \boldsymbol{e}_Z \\ & + \left[\delta u_R\,\frac{\partial u_\theta}{\partial R} + r\,\frac{\partial \delta u_\theta}{\partial R} + \left[1 + \frac{\partial u_R}{\partial R}\right]\,\delta u_\theta\right]\boldsymbol{e}_\vartheta \otimes \boldsymbol{e}_R\end{aligned} \tag{8.36}$$

$$+\left[\delta u_R \frac{\partial u_\theta}{\partial Z} + r \frac{\partial \delta u_\theta}{\partial Z} + \frac{\partial u_R}{\partial Z}\delta u_\theta\right] \boldsymbol{e}_\vartheta \otimes \boldsymbol{e}_Z + \delta u_R \frac{1}{R} \boldsymbol{e}_\vartheta \otimes \boldsymbol{e}_\theta \ .$$

Insertion of of eq. (8.35) – (8.36) into the weak form of linear momentum and neglecting again contributions due to body forces and surface loads leads to nodal residual vector $\boldsymbol{R}$ as

$$\boldsymbol{R} = \int_{\mathcal{B}} \delta_{\boldsymbol{u}} \boldsymbol{F} : \boldsymbol{P} \, \mathrm{d}V = \boldsymbol{0} \ . \tag{8.37}$$

By applying Newton's method for solving the resulting set of equations, the linearization $\boldsymbol{K} = \mathrm{d}_{\boldsymbol{u}} \boldsymbol{R}$ is required. For the purpose of clarity it is given in index notation with the subscripts being element of $\{R, Z, \theta\}$ as

$$K_{ij} = \int_V \delta_{u_i} F_{pq} : \frac{\mathrm{d}P_{pq}}{\mathrm{d}F_{rs}} : \Delta_{u_j} F_{rs} + P_{pq} : \Delta_{u_j} \left[\delta_{u_i} F_{pq}\right] \mathrm{d}V \ . \tag{8.38}$$

The only new expression is the lineraization of the variation of the deformation gradient. By making the assumption of linear shape functions, it reads

$$\begin{aligned}
&\left[\Delta_{\boldsymbol{u}} \left[\delta_{\boldsymbol{u}} \boldsymbol{F}\right] \cdot \delta \boldsymbol{u}\right] \cdot \Delta \boldsymbol{u} = \\
&- \left[\Delta u_R \frac{\partial u_\theta}{\partial R} \delta u_\theta + r \frac{\partial \Delta u_\theta}{\partial R} \delta u_\theta + \delta r \frac{\partial u_\theta}{\partial R} \Delta u_\theta + r \frac{\partial \delta u_\theta}{\partial R} \Delta u_\theta + [1 + \frac{\partial u_R}{\partial R}] \delta u_\theta \Delta u_\theta\right] \boldsymbol{e}_r \otimes \boldsymbol{e}_R \\
&- \left[\Delta r \frac{\partial u_\theta}{\partial Z} \delta u_\theta + r \frac{\partial \Delta u_\theta}{\partial Z} \delta u_\theta + \delta u_R \frac{\partial u_\theta}{\partial Z} \Delta u_\theta + r \frac{\partial \delta u_\theta}{\partial Z} \Delta u_\theta + \frac{\partial u_R}{\partial Z} \delta u_\theta \Delta u_\theta\right] \boldsymbol{e}_r \otimes \boldsymbol{e}_Z \\
&- \left[\frac{\Delta u_R}{R} \delta u_\theta + \frac{\delta u_R}{R} \Delta u_\theta\right] \boldsymbol{e}_r \otimes \boldsymbol{e}_\theta \\
&+ \left[\frac{\partial \delta u_R}{\partial R} \Delta u_\theta - r \frac{\partial u_\theta}{\partial R} \delta u_\theta \Delta u_\theta + \delta u_R \frac{\Delta u_\theta}{R} + \Delta r \frac{\partial \delta u_\theta}{\partial R} + \frac{\partial \Delta u_R}{\partial R} \delta u_\theta\right] \boldsymbol{e}_\vartheta \otimes \boldsymbol{e}_R \\
&+ \left[\frac{\partial \delta u_R}{\partial Z} \Delta u_\theta - r \frac{\partial u_\theta}{\partial Z} \delta u_\theta \Delta u_\theta + \delta u_R \frac{\partial \Delta u_\theta}{\partial Z} + \Delta u_R \frac{\partial \delta u_\theta}{\partial Z} + \frac{\partial \Delta u_R}{\partial Z} \delta u_\theta\right] \boldsymbol{e}_\vartheta \otimes \boldsymbol{e}_Z \\
&- \frac{r}{R} \delta u_\theta \Delta u_\theta \, \boldsymbol{e}_\vartheta \otimes \boldsymbol{e}_\theta \ ,
\end{aligned} \tag{8.39}$$

such that residual vector (8.37) and stiffness matrix (8.39) can be evaluated.

F.2 Extension to finite strains

The starting point of the extension is a constitutive framework for a themomechanically coupled, regularized constitutive model based on geometrically linearized kinematics. In

what follows, this constitutive routine will be considered as a black box. It is expressed as a function of the type

$$\left[\boldsymbol{\sigma}, \frac{\mathrm{d}\boldsymbol{\sigma}}{\mathrm{d}\boldsymbol{\varepsilon}}, \frac{\mathrm{d}\boldsymbol{\sigma}}{\mathrm{d}\boldsymbol{\varphi}}, \frac{\mathrm{d}\boldsymbol{\sigma}}{\mathrm{d}\Theta}, \boldsymbol{\omega}, \frac{\mathrm{d}\boldsymbol{\omega}}{\mathrm{d}\boldsymbol{\varepsilon}}, \frac{\mathrm{d}\boldsymbol{\omega}}{\mathrm{d}\boldsymbol{\varphi}}, \frac{\mathrm{d}\boldsymbol{\omega}}{\mathrm{d}\Theta}, r^{\Theta}, \frac{\mathrm{d}r^{\Theta}}{\mathrm{d}\boldsymbol{\varepsilon}}, \frac{\mathrm{d}r^{\Theta}}{\mathrm{d}\boldsymbol{\varphi}}, \frac{\mathrm{d}r^{\Theta}}{\mathrm{d}\Theta}\right] = \boldsymbol{f}^{\mathrm{Mat}}\left(\boldsymbol{\varepsilon}, \boldsymbol{\varphi}, \Theta, \boldsymbol{q}\right) \ . \tag{8.40}$$

The function depends on the small strain tensor $\boldsymbol{\varepsilon}$, an additional global field $\boldsymbol{\varphi}$ and the temperature Θ. Internal variables and material parameter are stored in the array $\boldsymbol{q}$. The output of the routine are the dual variables $\boldsymbol{\sigma}$, $\boldsymbol{\omega_b}$ and r^{Θ} together with their corresponding derivatives. The linearized strain tensor $\boldsymbol{\varepsilon}$ will be substituted by a large strain tensor $\boldsymbol{E}$ belonging to the Seth-Hill family in order to extend the constitutive framework to finite strains. This preserves the additive decomposition of the strains into an elastic part and a plastic part as $\boldsymbol{E} = \boldsymbol{E}^{\mathrm{e}} + \boldsymbol{E}^{\mathrm{p}}$. Logarithmic strains of the type

$$\boldsymbol{E} = \frac{1}{2}\ln\left(\boldsymbol{C}\right), \quad \boldsymbol{C} = \boldsymbol{F}^{T} \cdot \boldsymbol{F} \tag{8.41}$$

have been chosen, which can be computed by means of algorithm 1. Certainly other choices are also admissible. The logarithmic strains guarantee realistic material behavior even for strong compression, which is a typical disadvantage by considering a Helmholtz energy of St. Venant type. Substituting $\boldsymbol{E}$ in black box (8.40) yields

$$\left[\boldsymbol{T}, \frac{\mathrm{d}\boldsymbol{T}}{\mathrm{d}\boldsymbol{E}}, \frac{\mathrm{d}\boldsymbol{T}}{\mathrm{d}\boldsymbol{\varphi}}, \frac{\mathrm{d}\boldsymbol{T}}{\mathrm{d}\Theta}, \boldsymbol{\omega}, \frac{\mathrm{d}\boldsymbol{\omega}}{\mathrm{d}\boldsymbol{E}}, \frac{\mathrm{d}\boldsymbol{\omega}}{\mathrm{d}\boldsymbol{\varphi}}, \frac{\mathrm{d}\boldsymbol{\omega}}{\mathrm{d}\Theta}, r^{\Theta}, \frac{\mathrm{d}r^{\Theta}}{\mathrm{d}\boldsymbol{E}}, \frac{\mathrm{d}r^{\Theta}}{\mathrm{d}\boldsymbol{\varphi}}, \frac{\mathrm{d}r^{\Theta}}{\mathrm{d}\Theta}\right] = \boldsymbol{f}^{\mathrm{Mat}}\left(\boldsymbol{E}, \boldsymbol{\varphi}, \Theta, \boldsymbol{q}\right) \ , \tag{8.42}$$

where the energetic dual variable to $\boldsymbol{E}$ is denoted as stress tensor $\boldsymbol{T} = \partial_{\boldsymbol{E}}\psi$. In what follows, balance of linear momentum is expressed in terms of the first Piola-Kirchhoff stress tensor $\boldsymbol{P}$ and the deformation gradient $\boldsymbol{F}$. The first Piola-Kirchhoff stress tensor is computed according to

$$\boldsymbol{P} = \frac{\partial\psi}{\partial\boldsymbol{F}} = \frac{\partial\psi}{\partial\boldsymbol{E}} : \frac{\partial\boldsymbol{E}}{\partial\boldsymbol{C}} : \frac{\partial\boldsymbol{C}}{\partial\boldsymbol{F}} \quad \Leftrightarrow \quad P_{ij} = 2\,T_{ab}\,\frac{\partial E_{ab}}{\partial C_{jc}}\,F_{ic} \ . \tag{8.43}$$

The derivatives with respect to $\boldsymbol{F}$ have to be computed since the considered weak form of equilibrium is based on $\boldsymbol{P}$. The derivatives follow in the same spirit as the first Piola-Kirchhoff stress tensor $\boldsymbol{P}$ and read in index notation

$$\frac{\mathrm{d}P_{ij}}{\mathrm{d}F_{kl}} = 2\,T_{ab}\,\frac{\partial E_{ab}}{\partial C_{jl}}\,\delta_{ik} + 2\,\frac{\partial T_{ab}}{\partial F_{kl}}\,\frac{\partial E_{ab}}{\partial C_{jc}}\,F_{ic} + 4\,F_{ic}\,T_{ab}\,\frac{\partial^2 E_{ab}}{\partial C_{jc}\,\partial C_{ld}}\,F_{kd} \ , \tag{8.44}$$

$$\frac{\mathrm{d}P_{ij}}{\mathrm{d}\varphi_{kl}} = 2\,\frac{\mathrm{d}T_{ab}}{\mathrm{d}\varphi_{kl}}\,\frac{\partial E_{ab}}{\partial C_{jc}}\,F_{ic} \ , \tag{8.45}$$

$$\frac{\mathrm{d}P_{ij}}{\mathrm{d}\Theta} = 2\,\frac{\mathrm{d}T_{ab}}{\mathrm{d}\Theta}\,\frac{\partial E_{ab}}{\partial C_{jc}}\,F_{ic}\,. \tag{8.46}$$

Here, identity

$$\frac{\mathrm{d}T_{ij}}{\mathrm{d}F_{kl}} = 2\,\frac{\mathrm{d}T_{ij}}{\mathrm{d}E_{ab}}\,\frac{\partial E_{ab}}{\partial C_{lc}}\,F_{kc} \tag{8.47}$$

is utilized. Finally, the derivatives of $\boldsymbol{\omega}$ and r^{Θ} with respect to the deformation gradient are given according to

$$\frac{\mathrm{d}\omega_{ij}}{\mathrm{d}F_{kl}} = 2\,\frac{\mathrm{d}\omega_{ij}}{\mathrm{d}E_{ab}}\,\frac{\partial E_{ab}}{\partial C_{lc}}\,F_{kc}\,, \tag{8.48}$$

$$\frac{\mathrm{d}r^{\Theta}}{\mathrm{d}F_{ij}} = 2\,\frac{\mathrm{d}r^{\Theta}}{\mathrm{d}E_{ab}}\,\frac{\partial E_{ab}}{\partial C_{jc}}\,F_{ic}\,. \tag{8.49}$$

9 Conclusion and outlook

The work of this thesis can be categorized in two major topics. The first part, Chapter 2 – Chapter 5 dealt with the modeling of brittle damage and the second part, Chapter 6 – Chapter 8 dealt with ductile damage.

9.1 Brittle damage

9.1.1 Conclusion

In Chapter 2 two prototype models suitable for isotropic, brittle damage have been derived: a local model and a gradient damage model. On the basis of that local model, three different regularization methods – fracture energy concept, viscous regularization and micromorphic gradient regularization – have been compared to each other in Chapter 3. They follow jointly from the same variational framework. Undesired side effects of these regularization methods have been analyzed and compared to the underlying local model. The micromorphic gradient regularization has shown the most promising results. Hence, the micromorphic gradient regularization (and also general gradient continua) have been further analyzed in Chapter 4. It was pointed out that most gradient models are curvature-dependent. While, for many models that curvature dependence is intended, it is at least for the models in Chapter 4 an undesired side effect. The origin of the curvature dependence has been traced back to the balance law associated with the non-local damage field. It was shown that the width of the softening zone and the curvature of the softening zone cannot be controlled simultaneously and hence, independently. Therefore, two enhanced models were proposed in Chapter 5 in order to eliminate the undesired curvature dependence of gradient continua. By splitting the gradient into its magnitude and its direction and introducing an additional length (or curvature parameter) to scale both the magnitude and the direction independently, an explicit expression associated with the curvature dependence has been derived. Two enhanced models were proposed on the basis of this expression: a curvature-superposed potential-based model and a non-potential model relying on a direct modification of the balance law. The first model follows from the variational formulation by extending the Helmholtz energy by a curvature-dependent contribution. From an implementation point of view the finite element formulation of both aforementioned models had to be

extended since both models are explicitly dependent on the hessian of the non-local damage field. A second micromorphic (vector) field $\boldsymbol{\chi}$ has been introduced and coupled to the non-local damage field φ for this purpose.

9.1.2 Outlook

The focus of Chapter 2 – Chapter 5 lied on the analysis of three (mathematically two) different regularization methods. One may include further regularization methods in this comparison, e.g., a non-local regularization [17, 138]. The non-local regularization naturally contains higher derivatives, e.g., the hessian. It is interesting to analyze whether this regularization also shows a curvature dependence. Furthermore, more sophisticated choices of Helmholtz energies in order to capture the curvature dependence shall be investigated in future work.

9.2 Ductile damage

9.2.1 Conclusion

The second part of this thesis is associated with the modeling of ductile damage and starts in Chapter 6. A prototype model suitable for anisotropic, ductile material degradation was taken from the literature, cf. [51, 106], in order to investigate numerical aspects. An isotropic version has been derived, which served as a basis to simplify the fourthcoming analyses. It was shown that a naive micromorphic regularization is not suitable for ductile damage models of Lemaitre-type. This is due to a one-directional coupling between local integrity field $\boldsymbol{b}$ and auxiliary field $\boldsymbol{\varphi}$. In order to achieve a stronger, two-directional coupling the yield function has been modified. A comparison between the underlying local model, the naive regularized model and the novel regularized model on the basis of one- and two-dimensional examples showed that only the novel regularized model leads to mesh-independent numerical results.

The extensions of the model to low cycle fatigue were finally discussed in Chapter 8. For that purpose, the evolution equations were modified. They now account for superposed linear and non-linear isotropic and kinematic hardening. Subsequently a thermomechanical setting was adopted. It allowed to study different damage states by means of the scalar quantity temperature. Finally, an energetic damage initiation criterion was extended by the influence of the plastic loading amplitude in line with the well-known Coffin-Manson-relation. The resulting model was calibrated to the underlying experimental data.

9.2.2 Outlook

Up to this point the damage initiation criterion has only been calibrated to cyclic tensile test. For this reason, its applicability to fatigue simulations has to be further inves-

tigated. The anisotropy of the ductile damage model was of minor importance since the fatigue experiments only involved axial loading paths. Cyclic torsion experiments shall be considered additionally to investigate the loading path dependence. Likewise, the thermomechanically coupled setting has to be compared to experiments, e.g., by spatially resolved temperature measurements. Eventually, the model has to be extended to high cycle fatigue, since operating loads are more frequently in the high cycle fatigue range. Due to the increased number of cycles, the explicit calculation of each individual cycle by means of standard time discretization is not feasible anymore. In this case, time extrapolation algorithms, e.g., cycle extrapolation [36], the LaTIn-method [87] or finite elements in time and space might turn out beneficial and, thus, shall be linked to the model.

Bibliography

[1] Wolfram Alpha LLC. 2022. Wolfram|Alpha. https://www.wolframalpha.com/input/?i=y-y%27%27-y%27%2Fx-1x%5E2%3D0%2C+y%27%280%29%3D0%2C+y%27%28100%29%3D0%2C+x%3E%3D0. Accessed: 2022-Jan-05.

[2] *Abaqus Theory Guide*. Abaqus 6.14 Documentation. Dassault Systèmes Simulia Corp., Providence, RI, USA., 2014.

[3] W. A. J. Albert. Uber Treibseile am Harz. Archiv fur Mineralogie, Georgnosie. *Bergbau und Huttenkunde*, 10:215, 1837.

[4] R. Alessi, S. Vidoli, and L. De Lorenzis. A phenomenological approach to fatigue with a variational phase-field model: The one-dimensional case. *Engineering Fracture Mechanics*, 190:53–73, 2018. doi:10.1016/j.engfracmech.2017.11.036.

[5] H. Altenbach, W. H. Müller, and B. E. Abali. *Higher Gradient Materials and Related Generalized Continua*. Springer, 2019. doi:10.1007/978-3-030-30406-5.

[6] L. Ambrosio and V. M. Tortorelli. On the approximation of free discontinuity problems. *Bollettino della Unione Matematica Italiana*, 6:105–123, 1992.

[7] T. L. Anderson. *Fracture mechanics: fundamentals and applications*. CRC press, 2017. doi:10.1201/9781315370293.

[8] P. J. Armstrong and C. Frederick. *A mathematical representation of the multiaxial Bauschinger effect*, volume 731. Central Electricity Generating Board [and] Berkeley Nuclear Laboratories, 1966.

[9] M. Artina, M. Fornasier, S. Micheletti, and S. Perotto. Anisotropic mesh adaptation for crack detection in brittle materials. *SIAM Journal on Scientific Computing*, 37(4):B633–B659, 2015. doi:10.1137/140970495.

[10] O. Aslan, S. Quilici, and S. Forest. Numerical modeling of fatigue crack growth in single crystals based on microdamage theory. *International Journal of Damage Mechanics*, 20(5):681–705, 2011. doi:10.1177/1056789510395738.

[11] T. Asmanoglo and A. M. Menzel. Fibre-reinforced composites with fibre-bending stiffness under azimuthal shear – comparison of simulation results with analytical solutions. *International Journal of Non-linear Mechanics*, 91:128–139, 2017. doi:10.1016/j.ijnonlinmec.2017.01.001.

[12] A. Bartels, T. Bartel, M. Canadija, and J. Mosler. On the thermomechanical coupling in dissipative materials: a variational approach for generalized standard

materials. *Journal of the Mechanics and Physics of Solids*, 82:218–234, 2015. doi:10.1016/j.jmps.2015.04.011.

[13] A. Bartels, P. Kurzeja, and J. Mosler. Cahn–hilliard phase field theory coupled to mechanics: Fundamentals, numerical implementation and application to topology optimization. *Computer Methods in Applied Mechanics and Engineering*, 383: 113918, 2021. doi:10.1016/j.cma.2021.113918.

[14] J. Bauschinger. Über die veränderungen der elastizitatsgrenze und der festigkeit des eisens und stahls durch strecken, quetschen, erwärmen abkühlen und durch oftmals wiederholte belastung, vol. *XIII. Munchen: Mitt. Mech-Tech Lab*, 1886.

[15] Z. P. Bažant and B. H. Oh. Crack band theory for fracture of concrete. *Matériaux et Construction*, 16(3):155–177, 1983. doi:10.1007/BF02486267.

[16] Z. P. Bažant, T. B. Belytschko, and T. Chang. Continuum theory for strain-softening. *Journal of Engineering Mechanics*, 110(12):1666–1692, 1984. doi:10.1061/(ASCE)0733-9399(1984)110:12(1666).

[17] Z. Bažant and M. Jirásek. Nonlocal integral formulations of plasticity and damage: Survey of progress. *Journal of Engineering Mechanics*, 128(11):1119–1149, 2002. doi:10.1061/(ASCE)0733-9399(2002)128:11(1119).

[18] J. Besson. Continuum models of ductile fracture: A review. *International Journal of Damage Mechanics*, 19(1):3–52, 2010. doi:10.1177/1056789509103482.

[19] M. Bhattacharyya, A. Fau, R. Desmorat, S. Alameddin, D. Néron, P. Ladevèze, and U. Nackenhorst. A kinetic two-scale damage model for high-cycle fatigue simulation using multi-temporal latin framework. *European Journal of Mechanics-A/Solids*, 77:103808, 2019. doi:10.1016/j.euromechsol.2019.103808.

[20] D. Bigoni. *Nonlinear solid mechanics: bifurcation theory and material instability*. Cambridge University Press, 2012. doi:10.1017/CBO9781139178938.

[21] M. A. Biot. *Mechanics of incremental deformations*. John Wiley & Sons, Inc., NewYork/London/Sydney, 1965. doi:10.1063/1.3047001.

[22] W. A. M. Brekelmans, P. J. G. Schreurs, and J. H. P. de Vree. Continuum damage mechanics for softening of brittle materials. *Acta Mechanica*, 93(1):133–143, 1992. doi:10.1007/BF01182579.

[23] M. Burger, F. Haußer, C. Stöcker, and A. Voigt. A level set approach to anisotropic flows with curvature regularization. *Journal of computational physics*, 225(1):183–205, 2007. doi:10.1016/j.jcp.2006.11.026.

[24] J. W. Cahn and J. E. Hilliard. Free energy of a nonuniform system. i. interfacial free energy. *The Journal of chemical physics*, 28(2):258–267, 1958. doi:10.1063/1.1744102.

[25] A. Carpinteri and G. Colombo. Numerical analysis of catastrophic softening behaviour (snap-back instability). *Computers & Structures*, 31(4):607–636, 1989.

doi:10.1016/0045-7949(89)90337-4.

[26] C. Carstensen, K. Hackl, and A. Mielke. Non-Convex Potentials and Microstructures in Finite-Strain Plasticity. *Proceedings: Mathematical, Physical and Engineering Sciences*, 458(2018):299–317, 2002. doi:10.1098/rspa.2001.0864.

[27] A. Cauvin and R. B. Testa. Damage mechanics : basic variables in continuum theories. *International Journal of Solids and Structures*, 36(5):747–761, 1999. doi:10.1016/S0020-7683(98)00044-4.

[28] J. L. Chaboche and P. M. Lesne. A non-linear continuous fatigue damage model. *Fatigue & Fracture of Engineering Materials & Structures*, 11(1):1–17, 1988. doi:10.1111/j.1460-2695.1988.tb01216.x.

[29] J. L. Chaboche, P. M. Lesne, and J. F. Maire. Continuum damage mechanics, anisotropy and damage deactivation for brittle materials like concrete and ceramic composites. *International Journal of Damage Mechanics*, 4(1):5–22, 1995. doi:10.1177/105678959500400102.

[30] J. Chaboche. Continuum damage mechanics: Present state and future trends. *Nuclear Engineering and Design*, 105(1):19–33, 1987. doi:10.1016/0029-5493(87)90225-1.

[31] J. Chaboche. A review of some plasticity and viscoplasticity constitutive theories. *International Journal of Plasticity*, 24(10):1642–1693, 2008. doi:10.1016/j.ijplas.2008.03.009.

[32] P. Chhapadia, P. Mohammadi, and P. Sharma. Curvature-dependent surface energy and implications for nanostructures. *Journal of the Mechanics and Physics of Solids*, 59(10):2103–2115, 2011. doi:10.1016/j.jmps.2011.06.007.

[33] C. Chow and J. Wang. An anisotropic theory of elasticity for continuum damage mechanics. *International Journal of fracture*, 33(1):3–16, 1987. doi:10.1007/BF00034895.

[34] J. H. Claudio Findeisen, Samuel Forest and P. Gumbsch. Discrete and continuum modelling of size effects in architectured unstable metamaterials. *Continuum Mechanics and Thermodynamics*, 32:1629–1645, 2020. doi:10.1007/s00161-020-00870-8.

[35] L. F. Coffin Jr. A study of the effects of cyclic thermal stresses on a ductile metal. *Transactions of the American Society of Mechanical Engineers, New York*, 76: 931–950, 1954.

[36] D. Cojocaru and A. Karlsson. A simple numerical method of cycle jumps for cyclically loaded structures. *International Journal of Fatigue*, 28(12):1677–1689, 2006. doi:10.1016/j.ijfatigue.2006.01.010.

[37] B. D. Coleman and M. E. Gurtin. Thermodynamics with internal state variables. *Journal of Chemical Physics*, 47(2):597–613, 1967. doi:10.1063/1.1711937.

[38] B. D. Coleman and W. Noll. The thermodynamics of elastic materials with heat conduction and viscosity. *Archive for Rational Mechanics and Analysis*, 13(1): 167–178, 1963. doi:10.1007/BF01262690.

[39] C. D. Coman. Linear elasticity: General considerations and boundary-value problems. In *Continuum Mechanics and Linear Elasticity*, pages 243–280. Springer, 2020. doi:10.1007/978-94-024-1771-5_5.

[40] C. Comi and U. Perego. A unified approach for variationally consistent finite elements in elastoplasticity. *Computer Methods in Applied Mechanics and Engineering*, 121(1):323–344, 1995. doi:10.1016/0045-7825(94)00703-P.

[41] J. Cordebois and F. Sidoroff. Damage induced elastic anisotropy. In *Mechanical behavior of anisotropic solids/comportment méchanique des solides anisotropes*, pages 761–774. Springer, 1982. doi:10.1007/978-94-009-6827-1_44.

[42] M. A. Crisfield. An arc-length method including line searches and accelerations. *International Journal for Numerical Methods in Engineering*, 19(9):1269–1289, 1983. doi:10.1002/nme.1620190902.

[43] G. S. Cunningham, A. Lehovich, and K. M. Hanson. Bayesian estimation of regularization parameters for deformable surface models. In *Medical Imaging 1999: Image Processing*, volume 3661, pages 562–573. International Society for Optics and Photonics, 1999. doi:10.1117/12.348612.

[44] V. D. da Silva. A simple model for viscous regularization of elasto-plasticconstitutive laws with softening. *Communications in Numerical Methods in Engineering*, 20:547–568, 2004. doi:10.1002/cnm.700).

[45] P.-G. De Gennes, F. Brochard-Wyart, D. Quéré, et al. *Capillarity and wetting phenomena: drops, bubbles, pearls, waves*, volume 336. Springer, 2004. doi:10.1007/978-0-387-21656-0.

[46] R. Desmorat. Non-saturating nonlinear kinematic hardening laws. *Comptes Rendus Mécanique*, 338(3):146–151, 2010. doi:10.1016/j.crme.2010.02.007.

[47] R. Desmorat, A. Kane, M. Seyedi, and J. P. Sermage. Two scale damage model and related numerical issues for thermo-mechanical high cycle fatigue. *European Journal of Mechanics-A/Solids*, 26(6):909–935, 2007. doi:10.1016/j.euromechsol.2007.01.002.

[48] B. Dimitrijevic and K. Hackl. A method for gradient enhancement of continuum damage models. *Technische Mechanik*, 1:43–52, 2008.

[49] J. Dold and D. Crighton. Non-monotonic curvature-dependent propagation. *Philosophical Transactions of the Royal Society of London. Series A: Mathematical, Physical and Engineering Sciences*, 357(1764):3553–3566, 1999. doi:10.1098/rsta.1999.0509.

[50] G. Duvant and J. L. Lions. *Inequalities in Mechanics and Physics*. Grundlehren der mathematischen Wissenschaften. Springer-Verlag, Berlin Heidelberg, 1976. doi:10.1007/978-3-642-66165-5.

[51] M. Ekh, A. Menzel, K. Runesson, and P. Steinmann. Anisotropic damage with the mcr effect coupled to plasticity. *International Journal of Engineering Science*, 41(13):1535–1551, 2003. doi:10.1016/S0020-7225(03)00032-6.

[52] M. Fassin, R. Eggersmann, S. Wulfinghoff, and S. Reese. Gradient-extended anisotropic brittle damage modeling using a second order damage tensor – Theory, implementation and numerical examples. *International Journal of Solids and Structures*, 167:93–126, 2019. doi:10.1016/j.ijsolstr.2019.02.009.

[53] N. Fleck, G. Muller, M. F. Ashby, and J. W. Hutchinson. Strain gradient plasticity: theory and experiment. *Acta Metallurgica et materialia*, 42(2):475–487, 1994. doi:10.1016/0956-7151(94)90502-9.

[54] S. Forest. Micromorphic Approach for Gradient Elasticity, Viscoplasticity, and Damage. *Journal of Engineering Mechanics*, 135(3):117–131, 2009. doi:10.1061/(ASCE)0733-9399(2009)135:3(117).

[55] S. Forest, K. Ammar, B. Appolaire, N. Cordero, and A. Gaubert. Micromorphic approach to crystal plasticity and phase transformation. In J. Schröder and K. Hackl, editors, *Plasticity and Becond, CISM International Centre for Mechanical Sciences*. Springer, Vienna, 2014. doi:10.1007/978-3-7091-1625-8.

[56] G. Francfort and J.-J. Marigo. Revisiting brittle fracture as an energy minimization problem. *Journal of the Mechanics and Physics of Solids*, 46(8):1319–1342, 1998. ISSN 0022-5096. doi:10.1016/S0022-5096(98)00034-9.

[57] W. Garrison and N. Moody. Ductile fracture. *Journal of Physics and Chemistry of Solids*, 48(11):1035–1074, 1987. doi:10.1016/0022-3697(87)90118-1.

[58] M. Geers, W. Brekelmans, and R. de Borst. Viscous Regularization of Strain-Localisation for Damaging Materials. In H. M. Kusters G.M.A., editor, *DIANA Computational Mechanics ´94*, pages 127–138. Springer, Dordrecht, 1994. doi:10.1007/978-94-011-1046-4_12.

[59] T. Gerasimov, U. Römer, J. Vondřejc, H. G. Matthies, and L. De Lorenzis. Stochastic phase-field modeling of brittle fracture: computing multiple crack patterns and their probabilities. *Computer Methods in Applied Mechanics and Engineering*, 372:113353, 2020. doi:10.1016/j.cma.2020.113353.

[60] Y. Gong. Bernstein filter: A new solver for mean curvature regularized models. In *2016 IEEE International Conference on Acoustics, Speech and Signal Processing (ICASSP)*, pages 1701–1705. IEEE, 2016. doi:10.1109/ICASSP.2016.7471967.

[61] A. E. Green and P. M. Naghdi. A general theory of an elastic-plastic continuum. Technical report, California Univ Berkeley Inst Of Engineering Research, 1964.

[62] A. A. Griffith and G. I. Taylor. Vi. the phenomena of rupture and flow in solids. *Philosophical Transactions of the Royal Society of London. Series A, Containing Papers of a Mathematical or Physical Character*, 221(582-593):163–198, 1921. doi:10.1098/rsta.1921.0006.

[63] D. Gross and T. Seelig. *Fracture mechanics: with an introduction to micromechanics*. Springer, 2017.

[64] A. L. Gurson. Continuum Theory of Ductile Rupture by Void Nucleation and Growth: Part I –Yield Criteria and Flow Rules for Porous Ductile Media. *Journal of Engineering Materials and Technology*, 99(1):2–15, 1977. doi:10.1115/1.3443401.

[65] M. E. Gurtin. Generalized ginzburg-landau and cahn-hilliard equations based on a microforce balance. *Physica D: Nonlinear Phenomena*, 92(3):178–192, 1996. doi:10.1016/0167-2789(95)00173-5.

[66] M. R. Hajidehi and S. Stupkiewicz. Gradient-enhanced model and its micromorphic regularization for simulation of lüders-like bands in shape memory alloys. *International Journal of Solids and Structures*, 135:208–218, 2018. doi:10.1016/j.ijsolstr.2017.11.021.

[67] B. Halphen and Q. Nguyen. On Generalized Standard Materials. *Journal de Mécanique*, 14:39–63, 1975.

[68] R. W. Hertzberg. *Deformation and fracture mechanics of engineering materials*. Wiley, 1989. doi:10.1115/1.3264456.

[69] B. S. Hosseini and M. Möller. Phase field-based incompressible two-component liquid flow simulation. In *Numerical Methods for Flows*, pages 165–176. Springer, Cham, 2020. doi:10.1007/978-3-030-30705-9_15.

[70] ISO 12106:2017. Metallic materials - Fatigue testing - Axial-strain-controlled method. Standard, International Organization for Standardization, March 2017.

[71] L. Jiang, H. Wang, P. Liaw, C. Brooks, and D. Klarstrom. Temperature evolution during low-cycle fatigue of ultimetÂ® alloy: experiment and modeling. *Mechanics of Materials*, 36(1):73–84, 2004. doi:10.1016/S0167-6636(03)00032-2.

[72] H. Jin, Y. Liu, H. Li, and Q. Fu. Numerical analysis of the flow field in a sloshing tank with a horizontal perforated plate. *Journal of Ocean University of China*, 16 (4):575–584, 2017. doi:10.1007/s11802-017-3369-6.

[73] M. Jirásek and M. Bauer. Numerical aspects of the crack band approach. *COMPUTERS & STRUCTURES*, 110:60–78, 11 2012. doi:10.1016/j.compstruc.2012.06.006.

[74] J. Ju. Isotropic and anisotropic damage variables in continuum damage mechanics. *Journal of Engineering Mechanics*, 116(12):2764–2770, 1990. doi:10.1061/(ASCE)0733-9399(1990)116:12(2764).

[75] L. M. Kachanov. Rupture time under creep conditions. *International Journal of Fracture*, 97:11–18, 1999. doi:10.1023/A:1018671022008.

[76] M. Kachanov. Continuum model of medium with cracks. *Journal of the engineering mechanics division*, 106(5):1039–1051, 1980. doi:10.1061/JMCEA3.0002642.

[77] A. Karolczuk and E. Macha. A review of critical plane orientations in multiaxial fatigue failure criteria of metallic materials. *International Journal of Fracture*, 134 (3):267–304, 2005. doi:10.1007/s10704-005-1088-2.

[78] M. Kass, A. Witkin, and D. Terzopoulos. Snakes: Active contour models. *International journal of computer vision*, 1(4):321–331, 1988. doi:10.1007/BF00133570.

[79] V. Kazymyrovych. Very high cycle fatigue of engineering materials: A literature review. Technical report, Karlstad University, 2009.

[80] B. Kiefer, T. Waffenschmidt, L. Sprave, and A. Menzel. A gradient-enhanced damage model coupled to plasticity – multi-surface formulation and algorithmic concepts. *International Journal of Damage Mechanics*, 27(2):253–295, 2018. doi:10.1177/1056789516676306.

[81] O. Kintzel and J. Mosler. An incremental minimization principle suitable for the analysis of low cycle fatigue in metals: A coupled ductile–brittle damage model. *Computer methods in applied mechanics and engineering*, 200(45-46):3127–3138, 2011. doi:10.1016/j.cma.2011.07.006.

[82] B. Klusemann and S. Bargmann. Modeling and simulation of size effects in metallic glasses with a nonlocal continuum mechanics theory. *Journal of the Mechanical Behavior of Materials*, 22(1-2):51–66, 2013. doi:10.1515/jmbm-2013-0009.

[83] F. Kocks, C. Tomé, and H.-R. Wenk. *Texture and Anisotropy. Preferred Orientations in Polycrystals and Their Effect on Material Properties*. Cambridge University Press, 2000.

[84] D. Krajcinovic, editor. *Damage Mechanics*. North-Holland, 1996.

[85] C. Kuhn and R. Müller. A new finite element technique for a phase field model of brittle fracture. *Journal of Theoretical and Applied Mechanics*, 49(4):1115–1133, 2011.

[86] P. Kurzeja and H. Steeb. Variational formulation of oscillating fluid clusters and oscillator-like classification. i. theory. *Physics of Fluids*, 26(4):042106, 2014. doi:10.1063/1.4871486.

[87] P. Ladevèze. *Nonlinear Computational Structural Mechanics – New Approaches and Non-Incremental Methods of Calculation*. Springer, New York, 1999.

[88] K. Langenfeld and J. Mosler. A micromorphic approach for gradient-enhanced anisotropic ductile damage. *Computer Methods in Applied Mechanics and Engineering*, 360:112717, 2020. doi:10.1016/j.cma.2019.112717.

[89] K. Langenfeld, P. Junker, and J. Mosler. Quasi-brittle damage modeling based on incremental energy relaxation combined with a viscous-type regularization. *Continuum Mechanics and Thermodynamics*, 30(5):1125–1144, 2018. doi:10.1007/s00161-018-0669-z.

[90] K. Langenfeld, P. Kurzeja, and J. Mosler. On the curvature dependence of gradient damage models: Control and opportunities. *Computer Methods in Applied Mechanics and Engineering*, 410:115987, 2023. doi:https://doi.org/10.1016/j.cma.2023.115987.

[91] K. Langenfeld, A. Schowtjak, R. Schulte, O. Hering, K. Möhring, T. Clausmeyer, R. Ostwald, F. Walther, A. Tekkaya, and J. Mosler. Influence of anisotropic damage evolution on cold forging. *Production Engineering*, 14, 2020. doi:10.1007/s11740-019-00942-y.

[92] K. Langenfeld, P. Kurzeja, and J. Mosler. How regularization concepts interfere with (quasi-)brittle damage: A comparison based on a unified variational framework. *Continuum Mechanics and Thermodynamics*, 2022 – accepted for publication.

[93] U. Lee, G. A. Lesieutre, and L. Fang. Anisotropic damage mechanics based on strain energy equivalence and equivalent elliptical microcracks. *International Journal of Solids and Structures*, 34(33):4377–4397, 1997. doi:10.1016/S0020-7683(97)00022-X.

[94] J. Lemaitre. A Continuous Damage Mechanics Model for Ductile Fracture. *Journal of Engineering Materials and Technology*, 107(1):83–89, 1985. doi:10.1115/1.3225775.

[95] J. Lemaitre. *A course on damage mechanics*. Springer Science & Business Media, 1996.

[96] J. Lemaitre and R. Desmorat. *Engineering Damage Mechanics: Ductile, Creep, Fatigue and Brittle Failures*. Springer-Verlag Berlin Heidelberg, 2005.

[97] B. Li and C. Maurini. Crack kinking in a variational phase-field model of brittle fracture with strongly anisotropic surface energy. *Journal of the Mechanics and Physics of Solids*, 125:502–522, 2019. doi:10.1016/j.jmps.2019.01.010.

[98] T. Li and R. Abdelmoula. Gradient damage analysis of a cylinder under torsion: Bifurcation and size effects. *Journal of Elasticity*, 143(2):209–237, 2021. doi:10.1007/s10659-021-09815-x.

[99] T. Lu and C. Chow. On constitutive equations of inelastic solids with anisotropic damage. *Theoretical and Applied Fracture Mechanics*, 14(3):187–218, 1990. doi:10.1016/0167-8442(90)90020-Z.

[100] P. Luo, W. Yao, L. Susmel, Y. Wang, and X. Ma. A survey on multiaxial fatigue damage parameters under non-proportional loadings. *Fatigue & Fracture of Engineering Materials and Structures*, 40, 06 2017. doi:10.1111/ffe.12659.

[101] S. Manson. Behaviour of materials under conditions of thermal stress, 1953, naca tn-2933 and coffin lf jr. *Transactions of the ASME*, 76:931, 1954.

[102] J.-J. Marigo, C. Maurini, and K. Pham. An overview of the modelling of fracture by gradient damage models. *Meccanica*, 51(12):3107–3128, 2016. doi:10.1007/s11012-016-0538-4.

[103] A. Matzenmiller, J. Lubliner, and R. L. Taylor. A constitutive model for anisotropic damage in fiber-composites. *Mechanics of Materials*, 20(2):125–152, 1995. doi:10.1016/0167-6636(94)00053-0.

[104] F. A. McClintock. A criterion for ductile fracture by the growth of holes. *Journal of Applied Mechanics*, 35(2):363–371, 1968. doi:10.1115/1.3601204.

[105] A. Menzel and P. Steinmann. A theoretical and computational framework for anisotropic continuum damage mechanics at large strains. *International Journal of Solids and Structures*, 38(52):9505–9523, 2001. doi:10.1016/S0020-7683(01)00136-6.

[106] A. Menzel, M. Ekh, P. Steinmann, and K. Runesson. Anisotropic damage coupled to plasticity: Modelling based on the effective configuration concept. *International Journal for Numerical Methods in Engineering*, 54:1409 – 1430, 08 2002. doi:10.1002/nme.470.

[107] C. Miehe. Computation of isotropic tensor functions. *Communications in Numerical Methods in Engineering*, 9(11):889–896, 1993. doi:10.1002/cnm.1640091105.

[108] C. Miehe and M. Lambrecht. Algorithms for computation of stresses and elasticity moduli in terms of Seth-Hill's family of generalized strain tensors. *Communications in Numerical Methods in Engineering*, 17(5):337–353, 2001. doi:10.1002/cnm.404.

[109] C. Miehe, J. Schotte, and M. Lambrecht. Homogenization of inelastic solid materials at finite strains based on incremental minimization principles. application to the texture analysis of polycrystals. *Journal of the Mechanics and Physics of Solids*, 50(10):2123–2167, 2002. doi:10.1016/S0022-5096(02)00016-9.

[110] C. Miehe, F. Welschinger, and M. Hofacker. Thermodynamically consistent phase-field models of fracture: Variational principles and multi-field FE implementations. *International Journal for Numerical Methods in Engineering*, 83(10):1273–1311, 2010. doi:10.1002/nme.2861.

[111] C. Miehe, E. Gürses, and M. Birkle. A computational framework of configurational-force-driven brittle fracture based on incremental energy minimization. *International Journal of Fracture*, 145(4):245–259, 2007. doi:10.1007/s10704-007-9078-1.

[112] A. Mielke. A Mathematical Framework for Generalized Standard Materials in the rate-independent case. In R. Helmig, A. Mielke, and B. Wohlmuth, editors, *Multifield Problems in Solid and Fluid Mechanics*. Springer, Berlin, Heidelberg, 2006. doi:10.1007/978-3-540-34961-7_12.

[113] R. D. Mindlin. Second gradient of strain and surface-tension in linear elasticity. *International Journal of Solids and Structures*, 1(4):417–438, 1965. doi:10.1016/0020-7683(65)90006-5.

[114] R. D. Mindlin. Micro-structure in linear elasticity. *Archive for Rational Mechanics and Analysis*, 16(1):51–78, 1963. doi:10.1007/BF00248490.

[115] L. Modica. The gradient theory of phase transitions and the minimal interface criterion. *Archive for Rational Mechanics and Analysis*, 98(2):123–142, 1987. doi:10.1007/BF00251230.

[116] D. Mokbel, H. Abels, and S. Aland. A phase-field model for fluid–structure interaction. *Journal of Computational Physics*, 372:823–840, 2018. doi:10.1016/j.jcp.2018.06.063.

[117] R. Moser. Singular perturbation problems involving curvature. In *Differential Geometry and Continuum Mechanics*, pages 49–75. Springer, 2015. doi:10.1007/978-3-319-18573-6_3.

[118] J. Mosler. On variational updates for non-associative kinematic hardening of armstrong-frederick-type. *Technische Mechanik*, 30:1–3, 11 2010.

[119] J. Mosler and G. Meschke. Embedded crack vs. smeared crack models: A comparison of elementwise discontinuous crack path approaches with emphasis on mesh bias. *Computer Methods in Applied Mechanics and Engineering*, 193:3351–3375, 2004. doi:10.1016/j.cma.2003.09.022.

[120] A. P. Mouritz. *Introduction to aerospace materials*. Elsevier, 2012.

[121] S. Murakami. Mechanical Modeling of Material Damage. *Journal of Applied Mechanics*, 55(2):280–286, 1988. doi:10.1115/1.3173673.

[122] S. Murakami. *Continuum Damage Mechanics*. Springer Netherlands, 2012.

[123] S. Murakami and N. Ohno. A continuum theory of creep and creep damage. In A. R. S. Ponter and D. R. Hayhurst, editors, *Creep in Structures*, pages 422–444, Berlin, Heidelberg, 1981. Springer Berlin Heidelberg.

[124] P. Neff. A finite-strain elastic–plastic cosserat theory for polycrystals with grain rotations. *International Journal of Engineering Science*, 44(8-9):574–594, 2006. doi:10.1016/j.ijengsci.2006.04.002.

[125] M. Neuner, P. Gamnitzer, and G. Hofstetter. A 3d gradient-enhanced micropolar damage-plasticity approach for modeling quasi-brittle failure of cohesive-frictional materials. *Computers & Structures*, 239:106332, 2020. doi:10.1016/j.compstruc.2020.106332.

[126] E. Oñate, S. Oller, J. Oliver, and J. Lubliner. A constitutive model for cracking of concrete based on the incremental theory of plasticity. *Engineering Computations*, 5(4):309–319, 1988. doi:10.1108/eb023750.

[127] J. Oliver. A consistent characteristic length for smeared cracking models. *International Journal for Numerical Methods in Engineering*, 28(2):461–474, 1989. doi:10.1002/nme.1620280214.

[128] M. Ortiz. A method of homogenization of elastic media. *International Journal of Engineering Science*, 25(7):923–934, 1987. doi:10.1016/0020-7225(87)90125-X.

[129] M. Ortiz and A. Pandolfi. Finite-deformation irreversible cohesive elements for three-dimensional crack-propagation analysis. *International Journal for Numerical Methods in Engineering*, 44(9):1267–1282, 1999. doi:10.1002/(SICI)1097-0207(19990330)44:9<1267::AID-NME486>3.0.CO;2-7.

[130] M. Ortiz and E. Repetto. Nonconvex energy minimization and dislocation structures in ductile single crystals. *Journal of the Mechanics and Physics of Solids*, 47 (2):397–462, 1999. doi:10.1016/S0022-5096(97)00096-3.

[131] M. Ortiz and L. Stainier. The variational formulation of viscoplastic constitutive updates. *Computer Methods in Applied Mechanics and Engineering*, 171(3):419–444, 1999. doi:10.1016/S0045-7825(98)00219-9.

[132] N. S. Ottosen, R. Stenström, and M. Ristinmaa. Continuum approach to high-cycle fatigue modeling. *International Journal of Fatigue*, 30(6):996–1006, 2008. doi:10.1016/j.ijfatigue.2007.08.009.

[133] J. T. Overvelde, J. C. Weaver, C. Hoberman, and K. Bertoldi. Rational design of reconfigurable prismatic architected materials. *Nature*, 541(7637):347–352, 2017. doi:10.1038/nature20824.

[134] P. C. Paris. A rational analytic theory of fatigue. *The trend in engineering*, 13:9, 1961.

[135] S. Park, S. H. Jung, and P. M. Pardalos. Combining stochastic adaptive cubic regularization with negative curvature for nonconvex optimization. *Journal of Optimization Theory and Applications*, 184(3):953–971, 2020. doi:10.1007/s10957-019-01624-6.

[136] R. H. J. Peerlings, R. de Borst, W. A. M. Brekelmans, and J. H. P. de Vree. Gradient enhanced damage for quasi-brittle materials. *International Journal for Numerical Methods in Engineering*, 39(19):3391–3403, 1996. doi:10.1002/(SICI)1097-0207(19961015)39:19<3391::AID-NME7>3.0.CO;2-D.

[137] R. Peerlings. Gradient Damage for Quasi-Brittle Materials. Master's thesis, Eindhoven University of Technology, 1994.

[138] R. Peerlings, M. Geers, R. de Borst, and W. Brekelmans. A critical comparison of nonlocal and gradient-enhanced softening continua. *International Jornal of Solids and Structures*, 38(44–45):7723–7746, 2001. doi:10.1016/S0020-7683(01)00087-7.

[139] R. Peerlings, L. Poh, and M. Geers. An implicit gradient plasticity-damage theory for predicting size effects in hardening and softening. *Engineering Fracture*

Mechanics, 95:2–12, 2012. doi:10.1016/j.engfracmech.2011.12.016.

[140] H. Petryk. A consistent energy approach to defining stability of plastic deformation processes. In *Stability in the mechanics of continua (ed. FH Schroeder) Proc. IUTAM Symp. Nümbrecht*, volume 1981, pages 262–272, 1982.

[141] H. Petryk. Incremental energy minimization in dissipative solids. *Comptes Rendus Mécanique*, 331(7):469–474, 2003. doi:10.1016/S1631-0721(03)00109-8.

[142] P. Piovano. Evolution of elastic thin films with curvature regularization via minimizing movements. *Calculus of Variations and Partial Differential Equations*, 49 (1):337–367, 2014. doi:10.1007/s00526-012-0585-1.

[143] W. Prager. A new method of analyzing stresses and strains in work-hardening plastic solids. *Journal of Applied Mechanics*, 23:493–496, 1956. doi:10.1115/1.4011389.

[144] Y. N. Rabotnov. Creep rupture. In M. Hetényi and W. G. Vincenti, editors, *Applied Mechanics*, pages 342–349. Springer Berlin Heidelberg, 1969. doi:10.1007/978-3-642-85640-2_26.

[145] R. Radulovic, O. Bruhns, and J. Mosler. Effective 3d failure simulations by combining the advantages of embedded strong discontinuity approaches and classical interface elements. *Engineering Fracture Mechanics*, 78(12):2470–2485, 2011. doi:10.1016/j.engfracmech.2011.06.007.

[146] E. Ramm. Strategies for tracing the nonlinear response near limit points. In *Nonlinear Finite Element Analysis in Structural Mechanics*. Springer, 1981. doi:10.1007/978-3-642-81589-8_5.

[147] W. J. M. Rankine. On the causes of the unexpected breakage of the journals of railway axles; and on the means of preventing such accidents by observing the law of continuity in their construction. In *Minutes of the Proceedings of the Institution of Civil Engineers*, volume 2, pages 105–107. Thomas Telford-ICE Virtual Library, 1843. doi:10.1680/imotp.1843.24600.

[148] J. Rice and D. Tracey. On the ductile enlargement of voids in triaxial stress fields. *Journal of the Mechanics and Physics of Solids*, 17(3):201–217, 1969. doi:10.1016/0022-5096(69)90033-7.

[149] Ridwan, T. Putranto, F. B. Laksono, and A. R. Prabowo. Fracture and damage to the material accounting for transportation crash and accident. *Procedia Structural Integrity*, 27:38–45, 2020. doi:10.1016/j.prostr.2020.07.006.

[150] E. Riks. An incremental approach to the solution of snapping and buckling problems. *International Journal of Solids and Structures*, 15(7):529–551, 1979. doi:10.1016/0020-7683(79)90081-7.

[151] G. Rousselier. Ductile fracture models and their potential in local approach of fracture. *Nuclear Engineering and Design*, 105(1):97–111, 1987. doi:10.1016/0029-5493(87)90234-2.

[152] R. Russo, F. A. Girot Mata, S. Forest, and D. Jacquin. A review on strain gradient plasticity approaches in simulation of manufacturing processes. *Journal of Manufacturing and Materials Processing*, 4(3):87, 2020. doi:10.3390/jmmp4030087.

[153] M. Ryś, S. Forest, and H. Petryk. A micromorphic crystal plasticity model with the gradient-enhanced incremental hardening law. *International Journal of Plasticity*, 128:102655, 2020. doi:10.1016/j.ijplas.2019.102655.

[154] K. Saanouni and M. Hamed. Micromorphic approach for finite gradient-elastoplasticity fully coupled with ductile damage: Formulation and computational aspects. *International Journal of Solids and Structures*, 50(14):2289–2309, 2013. doi:10.1016/j.ijsolstr.2013.03.027.

[155] O. Sally, C. Julien, F. Laurin, R. Desmorat, and F. Bouillon. Fatigue lifetime modeling of oxide/oxide composites. *Procedia engineering*, 213:797–803, 2018. doi:10.1016/j.proeng.2018.02.075.

[156] E. Sánchez-Palencia. Non-homogeneous media and vibration theory. *Lecture notes in physics*, 127, 1980. doi:10.1007/3-540-10000-8.

[157] A. K. Saxena, S. Brinckmann, B. Völker, G. Dehm, and C. Kirchlechner. Experimental conditions affecting the measured fracture toughness at the microscale: Notch geometry and crack extension measurement. *Materials & Design*, 191: 108582, 2020. doi:10.1016/j.matdes.2020.108582.

[158] J. Schijve. Fatigue damage in aircraft structures, not wanted, but tolerated? *International Journal of Fatigue*, 31(6):998–1011, 2009. doi:10.1016/j.ijfatigue.2008.05.016.

[159] T. Schoenemann and D. Cremers. Introducing curvature into globally optimal image segmentation: Minimum ratio cycles on product graphs. In *2007 IEEE 11th International Conference on Computer Vision*, pages 1–6. IEEE, 2007. doi:10.1109/ICCV.2007.4408973.

[160] J. Schröder. A numerical two-scale homogenization scheme: the fe 2-method. In *Plasticity and beyond*, pages 1–64. Springer, 2014. doi:10.1007/978-3-7091-1625-8_1.

[161] W. Schütz. A history of fatigue. *Engineering Fracture Mechanics*, 54(2):263–300, 1996. ISSN 0013-7944. doi:10.1016/0013-7944(95)00178-6.

[162] M. Seiler, T. Linse, P. Hantschke, and M. Kästner. An efficient phase-field model for fatigue fracture in ductile materials. *Engineering Fracture Mechanics*, 224: 106807, 2020. doi:10.1016/j.engfracmech.2019.106807.

[163] B. Seth. Generalized strain measure with applications to physical problems. Technical report, Wisconsin Univ-Madison Mathematics Research Center, 1961.

[164] J. Y. Shu, W. E. King, and N. A. Fleck. Finite elements for materials with strain gradient effects. *International Jour-*

nal for Numerical Methods in Engineering, 44(3):373–391, 1999. doi:10.1002/(SICI)1097-0207(19990130)44:3<373::AID-NME508>3.0.CO;2-7.

[165] C. Sievers, J. Mosler, L. Brendel, and P. Kurzeja. Computational homogenization of material surfaces: From atomistic simulations to continuum models. *Computational Materials Science*, 175:109431, 2020. doi:10.1016/j.commatsci.2019.109431.

[166] C. Sievers, J. Mosler, and P. Kurzeja. Projection vs. relaxation of adjacent bulk deformation for surface modeling: Theoretical and numerical aspects. *International Journal of Solids and Structures*, 226-227:111084, 2021. doi:10.1016/j.ijsolstr.2021.111084.

[167] J. C. Simo, J. Oliver, and F. Armero. An analysis of strong discontinuities induced by strain-softening in rate-independent inelastic solids. *Computational Mechanics*, 12(5):277–296, 1993. doi:10.1016/0020-7683(79)90081-7.

[168] J. Simo and J. Ju. Strain- and stress-based continuum damage models – i. formulation. *International Journal of Solids and Structures*, 23(7):821–840, 1987. doi:10.1016/0020-7683(87)90083-7.

[169] D. Socie and G. B. Marquis. *Multiaxial fatigue*. Society of Automotive Engineers Warrendale, PA, 2000.

[170] R. Souchet. Equivalence principles in continuum damage mechanics. *International Journal of Engineering Science*, 43(17):1313–1322, 2005. doi:10.1016/j.ijengsci.2005.06.003.

[171] L. Sprave and A. Menzel. A large strain gradient-enhanced ductile damage model: finite element formulation, experiment and parameter identification. *Acta Mechanica*, 231(12):5159–5192, 2020. doi:10.1007/s00707-020-02786-5.

[172] D. Steigmann. Fluid films with curvature elasticity. *Archive for Rational Mechanics and Analysis*, 150(2):127–152, 1999. doi:10.1007/s002050050183.

[173] P. Steinmann. On boundary potential energies in deformational and configurational mechanics. *Journal of the Mechanics and Physics of Solids*, 56(3):772–800, 2008. doi:10.1016/j.jmps.2007.07.001.

[174] P. Steinmann and I. Carol. A framework for geometrically nonlinear continuum damage mechanics. *International Journal of Engineering Science*, 36(15):1793–1814, 1998. doi:10.1016/S0020-7225(97)00116-X.

[175] N. Sukumar, N. Moës, B. Moran, and T. Belytschko. Extended finite element method for three-dimensional crack modelling. *International Journal for Numerical Methods in Engineering*, 48(11):1549–1570, 2000. doi:10.1002/1097-0207(20000820)48:11<1549::AID-NME955>3.0.CO;2-A.

[176] S. Suresh. *Fatigue of Materials*. Cambridge University Press, 2 edition, 1998. doi:10.1017/CBO9780511806575.

[177] E. Tanné, T. Li, B. Bourdin, J.-J. Marigo, and C. Maurini. Crack nucleation in variational phase-field models of brittle fracture. *Journal of the Mechanics and Physics of Solids*, 110:80–99, 2018. doi:10.1016/j.jmps.2017.09.006.

[178] R. C. Tolman. The effect of droplet size on surface tension. *The journal of chemical physics*, 17(3):333–337, 1949. doi:10.1063/1.1747247.

[179] C. Truesdell and W. Noll. The non-linear field theories of mechanics. In *The non-linear field theories of mechanics*, pages 1–579. Springer, 2004. doi:10.1007/978-3-662-10388-3.

[180] V. Tvergaard and A. Needleman. Analysis of the cup-cone fracture in a round tensile bar. *Acta Metallurgica*, 32(1):157–169, 1984. doi:10.1016/0001-6160(84)90213-X.

[181] V. Tvergaard. Influence of voids on shear band instabilities under plane strain conditions. *International Journal of Fracture*, 17(4):389–407, 1981. doi:10.1007/BF00036191.

[182] V. Tvergaard. On localization in ductile materials containing spherical voids. *International Journal of Fracture*, 18(4):237–252, 1982. doi:10.1007/BF00015686.

[183] A. Vidyasagar, S. Krödel, and D. M. Kochmann. Microstructural patterns with tunable mechanical anisotropy obtained by simulating anisotropic spinodal decomposition. *Proceedings of the Royal Society A: Mathematical, Physical and Engineering Sciences*, 474(2218):20180535, 2018. doi:10.1098/rspa.2018.0535.

[184] B. Winkler, G. Hofstetter, and H. Lehar. Application of a constitutive model for concrete to the analysis of a precast segmental tunnel lining. *International Journal for Numerical and Analytical Methods in Geomechanics*, 28(7–8):797–819, 2004. doi:10.1002/nag.362.

[185] A. Wöhler. Versuche zur ermittlung der auf die eisenbahnwagenachsen einwirkenden kräfte und die widerstandsfähigkeit der wagen-achsen. *Zeitschrift für Bauwesen*, 10(1860):583–614, 1860.

[186] P. Wriggers. *Nonlinear Finite Element Methods*. Springer-Verlag Berlin Heidelberg, 2008. doi:10.1007/978-3-540-71001-1.

[187] Y. Zhang, A. S. Shedbale, Y. Gan, J. Moon, and L. H. Poh. Size effect analysis of quasi-brittle fracture with localizing gradient damage model. *International Journal of Damage Mechanics*, 30(7):1012–1035, 2021. doi:10.1177/1056789520983872.

[188] Q. S. Zheng and J. Betten. On damage effective stress and equivalence hypothesis. *International Journal of Damage Mechanics*, 5(3):219–240, 1996. doi:10.1177/105678959600500301.

[189] O. Zienkiewicz, R. Taylor, and D. Fox. *The Finite Element Method for Solid and Structural Mechanics*. Elsevier Butterworth- Heinemann, 2014. doi:10.1016/C2009-0-26332-X.

Publication series of the Institute of Mechanics

published to date:

2010/01 Palnau, V.: Implementierung eines netzfreien Diskretisierungsverfahrens und seine Anwendung auf die Scherbandanalyse.
ISBN 978-3-921823-51-4

2010/02 Klusemann, B.: Application of homogenization methods and crystal plasticity to the modeling of heterogeneous materials of technological interest.
ISBN 978-3-921823-53-8

2011/01 Hortig, C.: Local and non-local thermomechanical modeling and finite-element simulation of high-speed cutting.
ISBN 978-3-921823-54-5

2011/02 Parvizian, F.: Modeling of microstructure evolution in aluminum alloys during hot extrusion.
ISBN 978-3-921823-56-9

2011/03 Noman, M.: Characterization and model identification for the simulation of the forming behavior of ferritic steels.
ISBN: 978-3-921823-55-2

2011/04 Kayser, T.: Characterization of microstructure in aluminum alloys based on electron backscatter diffraction.
ISBN: 978-3-921823-57-6

2011/05 Bargmann, S.: Computational modeling of material behavior on different scales based on continuum mechanics.
ISBN: 978-3-921823-58-3

2013/01 Waffenschmidt, T.: Modelling and simulation of adaptation and degradation in anisotropic biological tissues.
ISBN: 978-3-921823-61-3

2015/01 Ostwald, R.: Modelling and simulation of phase-transformations in elastoplastic polycrystals.
ISBN: 978-3-921823-66-8

2016/01 Subramanian, M.: Phenomenological modelling and simulation of ferroelectric ceramics.
ISBN: 978-3-921823-74-3

2016/02 Clausmeyer, T.: Evolution of plastic anisotropy in metals.
ISBN: 978-3-921823-76-7

2017/01 Holtermann, R.: Computational multiscale modelling of grinding processes.
ISBN: 978-3-921823-86-6

2017/02 Bartels, A.: Modelling of evolving microstructures at different scales.
ISBN: 978-3-921823-93-4

2017/03 Dusthakar Kumar Rao, D. K.: Computational modelling of single and polycrystalline ferroelectric materials.
ISBN 978-3-921823-94-1

2019/01 Buckmann, K.: Microstructure evolution in functional magnetic materials.
ISBN 978-3-947323-09-8

2019/02 Kaiser, T.: Computational modelling of non-simple and anisotropic materials.
ISBN 978-3-947323-14-2

2019/03 Heitbreder, T.: Modelling of material interfaces at different length scales.
ISBN 978-3-947323-18-0

2020/01 Berthelsen, R.: Computational homogenisation of thermomechanical problems.
ISBN 978-3-947323-19-7

2020/02 Sievers, C.: Describing the macroscopic behavior of surfaces based on atomistic models.
ISBN 978-3-947323-24-1

2022/01 Rose, L.: Optimisation based parameter identification using optical field measurements.
ISBN 978-3-947323-31-9

2023/01 Langenfeld, K.: Continuum modeling of brittle and ductile damage: theory and computational frameworks.
ISBN 978-3-947323-41-8